An investigation of galaxy evolution with H-ATLAS and gravitational lenses

By

ARISTEIDIS AMVROSIADIS

School of Physics and Astronomy
CARDIFF UNIVERSITY

A thesis submitted to Cardiff University in accordance
with the requirements of the degree of
DOCTOR OF PHILOSOPHY

MAY 2019

DEDICATION

This thesis is dedicated to a number of people in my life, without who I could not have done this.

First of all I would like to thank both my parents, Litsa and Ioannis. You were both by my side and supported me since I first announced to you that I wanted to be a physicist.

A massive thanks goes to my beatiful girlfriend Penny. Thank you for putting up with me all these years. You were always there when I needed you.

Of course a big thanks goes to my friends here in Cardiff, Greg, Chinmay, Max, Ruth, Danny. Thank you for all these wonderfull moments we had all these years. Also a big thanks to my friend back in Greece, Kanlis, Andy, Gour, Harris, Kribas, Nikos, Georgiou. Altough I only got to see guys during holidays you were exactly the people I needed to see to make forget of all the problems I was having and have a great time alltogether as if nothing had changed.

Lastly, but definitely not least, to both my supervisors Stephen Eales and Mattia Negrello. You are the best possible mentors I could have asked for to go through this journey.

ACKNOWLEDGEMENTS

This Thesis makes use of the following software packages: matplotlib (Hunter, 2007), numpy (van der Walt et al., 2011), scipy (Jones et al. 2001), Astropy (Astropy Collaboration et al., 2013), APLpy (Robitaille and Bressert, 2012), emcee (Foreman-Mackey et al., 2013), HMFcalc (Murray et al., 2013), HALOMOD (Murray et al., in prep.), GALPAK3D Bouché et al. (2015), AutoLens Nightingale et al. (2018), TOPCAT (Taylor, 2005), scikit-learn (Pedregosa et al., 2011).

This Thesis makes use of the following ALMA data: ADS/JAO.ALMA # 2015.1.01362.S and ADS/JAO.ALMA 2016.1.00282.S. ALMA is a partnership of ESO (representing its member states), NSF (USA) and NINS (Japan), together with NRC (Canada), MOST and ASIAA (Taiwan), and KASI (Republic of Korea), in cooperation with the Republic of Chile. The Joint ALMA Observatory is operated by ESO, AUI/NRAO and NAOJ.

This Thesis makes use of data which are part of the Herschel-ATLAS project (http://www.h-atlas.org). The Herschel-ATLAS is a project with Herschel, which is an ESA space observatory with science instruments provided by European-led Principal Investigator consortia and with impor- tant participation from NASA. The data that have been used in this Thesis we taken with the PACS and SPIRE instruments. PACS has been developed by a consortium of institutes led by MPE (Germany) and including UVIE (Austria); KU Leuven, CSL, IMEC (Belgium); CEA, LAM (France); MPIA (Germany); INAF-IFSI/OAA/OAP/OAT, LENS, SISSA (Italy); IAC (Spain). This development has been supported by the funding agencies BMVIT (Austria), ESAPRODEX (Belgium), CEA/CNES (France), DLR (Germany), ASI/INAF (Italy), and CICYT/MCYT (Spain). SPIRE has been developed by a consortium of institutes led by Cardiff University (UK) and including Univ. Lethbridge (Canada); NAOC (China); CEA, LAM (France); IFSI, Univ. Padua (Italy); IAC (Spain); Stockholm Observatory (Sweden); Imperial College London, RAL, UCL-MSSL, UKATC, Univ. Sussex (UK); and Caltech, JPL, NHSC, Univ. Colorado (USA). This development has been supported by national funding agencies: CSA (Canada); NAOC (China); CEA, CNES, CNRS (France); ASI (Italy); MCINN (Spain); SNSB (Sweden); STFC, UKSA (UK); and NASA (USA).

ABSTRACT

This thesis presents a collection of studies which mainly focus on the population of high-redshift dusty star-forming galaxies (DSFGs) in the context of galaxy evolution. The sample of DSFGs that is used in this thesis was discovered as part of the Herschel-Astrophysical Terahertz Large Area Survey (H-ATLAS; Eales et al., 2010) which is the largest area extragalactic survey undertaken with the Herschel Space Telescope.

One Chapter of this Thesis studies the clustering statistics, i.e. the angular correlation function (ACF), of this population demonstrating that when selected on the basis of their flux density (i.e. $S_{250\mu m} > 30$ mJy) they exhibit a higher clustering strength at high redshift ($z > 1$; $r_0 = 8 - 14$ Mpc/h) than at low redshfit ($z < 0.3$; $r_0 = 1 - 2$ Mpc/h). From a galaxy evolution point of view this it is evident that we are dealing with two different galaxy populations, where the later is consistent with being the progenitors of massive early-type galaxies in the local Universe. This study uses that largest sample of DSFGs (discovered in the H-ATLAS survey) that has even been used to perform the measurement of their ACF.

Another Chapter of this Thesis studies the properties of the Interstellar medium (ISM) of one of these high redshift DSFGs (HATLAS J091043.0−000322) using a suite of multiwavelength observations. As this object is strongly lensed, we combined the resolving power of (ALMA) with the enchanced resolution offered by strong lensing to probe scales down to $300 - 700$ pc. Our morphological and kinematical analysis of the ISM components led us to conclude that this object is more likely undergoing a major-merger event.

Finally, another chapter of this thesis utilizes a sample of Herschel-selected strongly-lensed galaxies to study the density profiles of the lens population in a statistical manner. Using both numerically and analytically-derived density distributions we were able to reproduce the observed distribution of image separations. Although we were not able to distinguish between the two profiles, we showed that with a sample ~200 lenses that would become possible, highlighting that the simplicity of our selection of our sample does not introduce any additional systematics.

TABLE OF CONTENTS

LIST OF TABLES

LIST OF FIGURES

FIGURE **Page**

CHAPTER 1

INTRODUCTION

According to the Λ Cold Dark Matter (ΛCDM) cosmological model, the present day richness of structures in our Universe resulted from the hierarchical growth of tiny matter inhomogeneities that were in place shortly after the Big Bang (Peebles, 1980). These tiny inhomogeneities grow in time under the influence of gravity and in addition their growth is also regulated by the interplay between dark-matter and baryons, where several astrophysical processes take place, some yet to be fully understood.

The star formation history of galaxies is one of the key processes we need to understand in order to reconstruct how the Universe evolved since the Big Bang (~13.8 Gyr; Planck Collaboration et al., 2016). Figure 1.1 shows results from a compilation of studies which measure the star formation rate (SFR) volume density[1] as a function of redshift (or lookback time) using observations conducted from far ultraviolet (FUV) to infrared (IR) wavelengths. These two different wavelength regimes probe the un-obscured (directly) and dust obscured (indirectly) star formation activity, respectively, where the two seem to equally contribute to the total as long as we correct the former for the fact that some UV photons have been absorbed by dust and were re-emmited at IR wavelengths (and effect also known as dust attenuation). It is clear from this figure that the peak of the cosmic star formation activity in our Universe occurred in the redshift range $1 < z < 3$ (Madau and Dickinson, 2014) and was characterized by severe dust obscuration (see inset plot in Figure 1.1).

---

[1] The star formation rate of all galaxies contained within a cosmological volume, which in turn corresponds to a redshift slice.

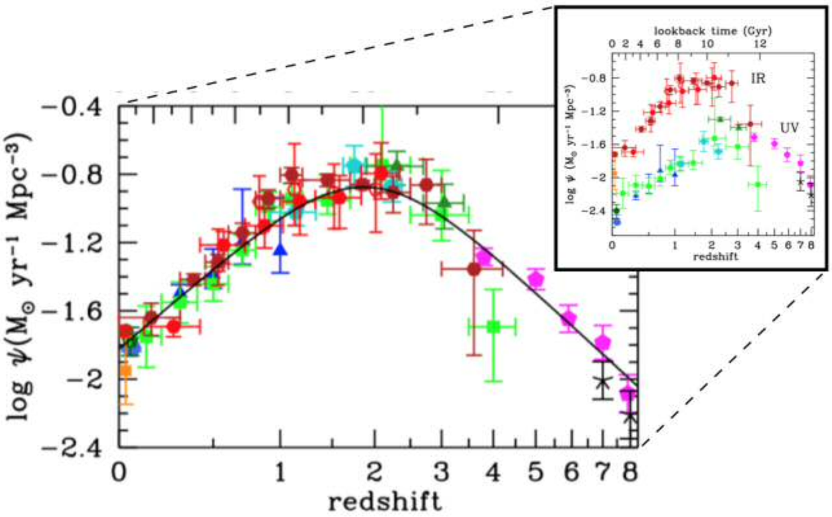

Figure 1.1: Figure adapted from Madau and Dickinson (2014). The star formation rate volume density (ψ) as a function of redshift. The various data points come from a compilation of multiple galaxy surveys which were conducted from the rest-frame UV (green, blue and magenta data points) to IR (orange, dark and light red data points) wavelengths. The right panel is the same as the left but the UV data points have been corrected for dust attenuation. The black curve shows the best-fit model, which is given by Eq. 15 in Madau and Dickinson (2014), and shows a strong peak at $z \sim 2$.

Given that ~50% of the present day stellar mass in galaxies was assembled during the peak of star formation activity (Madau and Dickinson, 2014), it is important to understand the physical conditions in galaxies at that epoch. In the following sections we will focus our discussion on the population of dusty star-forming galaxies (DSFGs), which is among these high redshift galaxy populations that contribute significantly to the rapid stellar mass build-up at that epoch.

1.1 The discovery of dusty star forming galaxies at high-redshifts

DSFGs are among the most intensively star-forming objects in the Universe (Blain et al., 2002; Casey et al., 2014, , and references therein). The ultraviolet (UV) radiation from their newly born hot OB stars is absorbed by the copious amount of dust in these objects and then re-emmited at far-infrared (FIR) / sub-millimetre (sub-mm) / millimeter (mm) wavelengths.

The population of DSFGs was first discovered in the 850 μm sub-mm band using the Submillimeter Common-User Bolometer Array (SCUBA, Holland et al.,

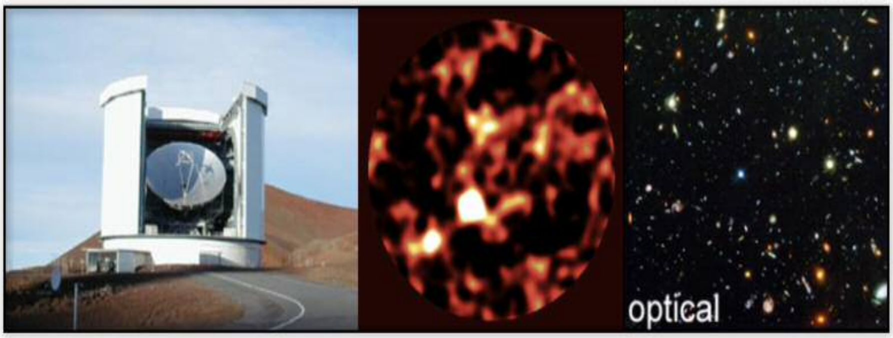

Figure 1.2: *Left panel:* The James Clerk Maxwell Telescope (JCMT) on which the Submillimeter Common-User Bolometer Arra (SCUBA) instrument is mounted. *Middle panel:* The Hubble Deep Field (HDF) as seen at 850 μm with SCUBA (~15$''$ resolution at 850 μm). *Right panel:* The same as the previous field but now as seen in optical with the Hubble Deep field (HST)

1999) onboard the James Clerk Maxwell Telescope (JCMT; see left panel of Figure 1.2). This is why they are also commonly referred to as submillimeter galaxies (SMGs)[2]. These first deep observations targeted both cluster (Smail et al., 1997) and blank fields (Barger et al., 1998), among which was the the Hubble Deep Field (HDF; Hughes et al., 1998, see middle panel of Figure 1.2). The right panel of the same figure shows again the HDF but this time as viewed in optical wavelengths with the Hubble Space Telescope (HST). What's incredible is that the ~1000 galaxies identified in optical image of the HDF have about the same energy output as the few blobs that can be seen in the corresponding sub-mm image (~5 were identified above the rms noise level of the SCUBA image; Hughes et al., 1998). It's no surprise that the discovery of this population marked the beginning of a new era in the field of galaxy formation and evolution.

Since their discovery, a number of surveys have been conducted in other sub-mm/mm bands with either ground or space based facilities. A few notable examples of such surveys are:

- The LABOCA Extended Chandra Deep Field South (ECDFS) Submillimetre Survey (LESS; Weiß et al., 2009) was conducted at 870 μm using the Large Apex BOlometer CAmera (LABOCA; Siringo et al., 2009) on the APEX telescope and has an area of ~0.25 deg^2.
- The Herschel Astrophysical Terahertz Large Area Survey (*H*-ATLAS; Eales et al., 2010) was conducted at 100 and 160 μm using the Photoconductor

---

[2] The term dusty star forming galaxies (DSFGs) refers to the bulk of this population discovered at 850 μm (1 mJy<$S_{850\mu m}$<5 mJy), while submillimeter galaxies (SMGs) are considered to be the most luminous subset of these objects ($S_{850\mu m} > 5$ mJy).

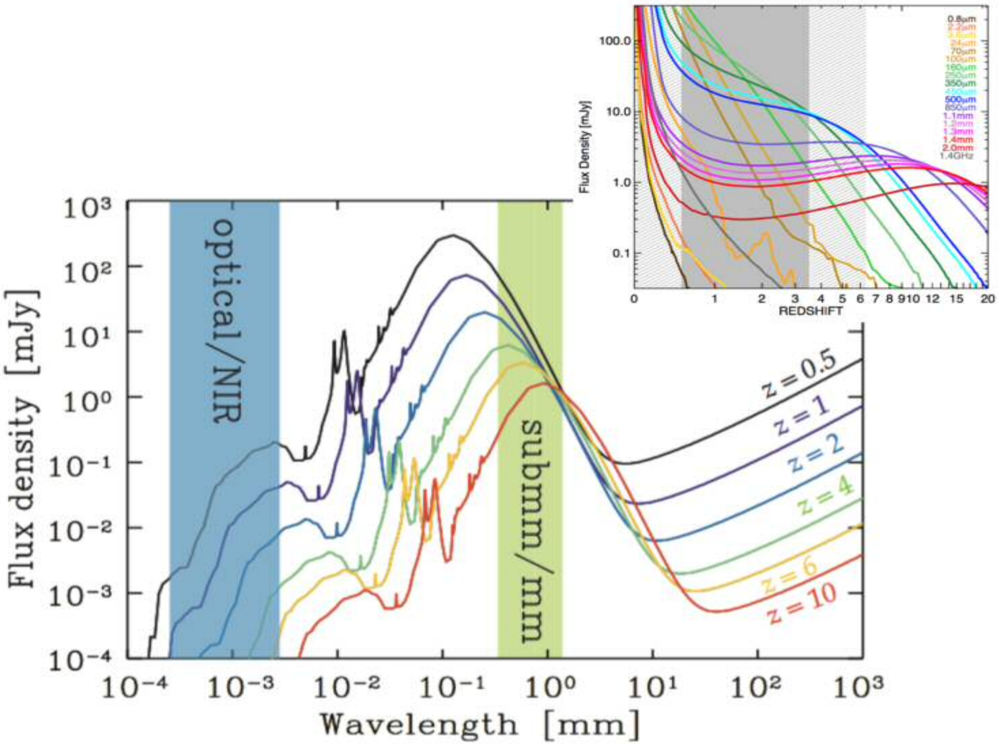

Figure 1.3: Figures are taken from Yang et al. (2016) and Casey et al. (2014). The flux density (i.e. the radiation power per unit area) as a function of wavelength (from optical to radio), of the widely used SED template of Arp 220, at different redshifts. The inset plot at the right top corner shows how the flux density at different observing wavebands change as a function of redshift, using the same SED template.

Array Camera and Spectrometer (PACS; Poglitsch et al., 2010) and at 250, 350 and 500 μm using the Spectral and Photometric Imaging Receiver (SPIRE; Griffin et al., 2010) instruments, both on-board the Herschel Space Telescope (Pilbratt et al., 2010), and has an area of ~660 deg^2. *H*-ATLAS is the widest of the *Herschel* surveys, some of which we are going to discuss in Chapter 2.

- The South Pole Telescope Survey (SPT; Vieira et al., 2010) was conducted at 1.4 and 2.0 mm using the South Pole Telescope (Carlstrom et al., 2011) and has an area of ~1300 deg^2.
- The SCUBA-2 Cosmology Legacy Survey (S2CLS; Geach et al., 2013, 2017) was conducted at 450 and 850 μm using the SCUBA-2 camera on JCMT and has an area of ~5 deg^2.
- The Atacama Cosmology Telescope (ACT; Marsden et al., 2014) survey was conducted at 1.1, 1.4 and 2.0 mm.

Surveys such as the *H*-ATLAS survey, led to the discovery of hundreds of thousands of high redshift SMGs due to their superior area coverage. The success of these surveys is partially due to the negative K-correction (Blain et al., 2002; Casey et al., 2014), which makes observations of high redshift sources ($z \sim 5$) at these wavelengths as easy as their relatively lower redshift counterparts ($z \sim 1$). This type of correction is applied in order to convert an object's flux density from the observed to the rest frame. It strongly depends on the shape of the object's spectral energy distribution (SED) at these wavelengths (i.e. more precisely on the properties of the dust; see Section 1.3.1) and it's redshift, z. Figure 1.3 demonstrates this effect more clearly, showing the the observed flux density as a function of wavelength for the Arp220[3] SED template at different redshifts. As can be seen from the shaded green region, corresponding to submillimeter (submm)/millimeter (mm) wavelengths, the observed flux density of the source changes very slightly with increasing redshift. The effect is more pronounced at wavelengths between 1.0 - 2.0 mm, as seen from the inset plot of Figure 1.3, resulting in an almost constant flux density over a wide range of redshifts.

1.2 The redshift distribution of SMGs

Now that we have these large samples of SMGs (see previous subsection) the next step is to try and characterize their physical properties, however, in order to do that we first need to determine their redshifts. Determining the redshifts of SMGs has been a very challenging task as the large beam sizes of single dish sub-mm observations make the SMG counterpart identification in other wavelengths very ambiguous (Bourne et al., 2016; Furlanetto et al., 2018). Although, since the advent of the Atacama Large Millimeter Array (ALMA) this longstanding problem is beginning to be resolved (e.g. Karim et al., 2013; Hodge et al., 2013; Simpson et al., 2015; Bussmann et al., 2015).

In the case where an SMG has no identified counterparts in other wavelengths, measuring its redshift can be performed with two main methods. The first method is to obtain follow-up spectroscopic data and look for various molecular lines (e.g. CO, C_I, C_{II}, H_2O; Omont et al., 2011, 2013; Harris et al., 2012; Lupu et al., 2012) in their spectra (spectroscopic redshift). This method gives very accurate redshifts, but its observationally expensive. The second method is to fit an appropriate FIR spectral energy distribution (SED) template to the sub-mm/mm fluxes

---

[3] Arp 220 is the closest Ultraluminous Infrared Galaxy to Earth and is the result of the collision between two galaxies.

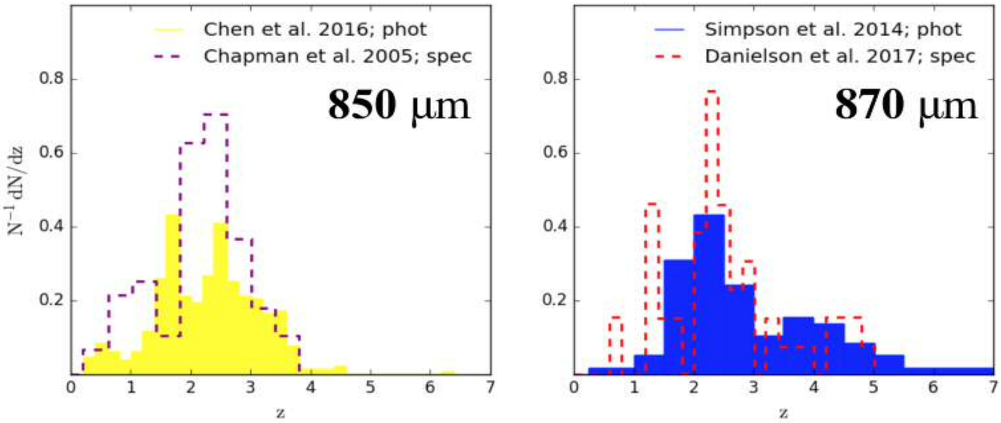

Figure 1.4: Figures are adapted from Chapman et al. (2005); Simpson et al. (2014); Chen et al. (2016a); Danielson et al. (2017). The normalised redshift distributions of SMGs selected at 850 μm (left panel) and 870 μm (right panel), using either spectroscopic or photometric redshifts (where N is the number of sources used to construct the distributions).

(photometric redshift; as the one shown in Figure 1.3, however see Section 1.3.1 for more details), allowing only the redshift to vary as a free parameter (e.g. Lapi et al., 2011; González-Nuevo et al., 2012; Pearson et al., 2013; Bakx et al., 2018). This method can be very inaccurate due to the intrinsic variation of SEDs (i.e. dust temperatures) in the SMG population (Casey, 2012) but is observationally much cheaper than carrying out follow-up spectroscopic observations (this method will be applied in Chapter 3 and more details will be discussed there).[4]

The first dedicated study to determine the redshift distribution for this population of galaxies was conducted by Chapman et al. (2005). Although this study had a few biases folded in the SMG selection as well as the spectroscopic follow-up observations, it provided the first compelling evidence that SMGs lie at high redshifts with a median redshift of 2.2 and an interquartile range of $z = 1.7 - 2.8$, which coincides with the peak of the cosmic star formation activity. Several other studies have tried to determine the redshift distribution of SMGs selected at different wavelengths using either photometric or spectroscopic redshifts. In the same waveband Chen et al. (2016a) using a sample of 523 SMGs with photometrically determined redshifts, identified in the S2CLS survey, found a median of $z = 2.3 \pm 0.1$. At 870 μm Simpson et al. (2014) used a sample of 77 SMGs from the LESS survey with photometric redshifts and found a median $z = 2.3 \pm 0.1$, which is in excellent agreement with the finding of Danielson et al. (2017) who used a subsample of 55

---

[4] It is important to note that the fewer the bands that are used in the SED fitting are, the less reliable this method becomes.

of these sources with spectroscopic redshifts. All these aforementioned redshift distributions are shown in Figure 1.4 for the 850 μm-selected *(left panel)* and 870 μm-selected *(right panel)* samples.

One common characteristic of these redshift distributions is that the space density (i.e. the number of source per unit of cosmological volume) of SMGs drops rapidly from $z \sim 2$ up to the present day (~3 orders of magnitude; Smail et al., 1997; Chapman et al., 2005), where Ultraluminous Infrared Galaxies (ULIRGs) are used as their present day analogues to make that statement. Considering that just the bright SMGs ($S_{870\mu m} > 1$ mJy) contribute ~20% of the total star formation rate density around the peak ($z \sim 1-4$ Swinbank et al., 2014), it is clear that this population plays an important role in our understanding of how galaxies evolve. Therefore, characterizing their properties is essential in order to reveal the physical mechanisms that take place in these systems.

1.3 Properties of the ISM components in SMGs

Several studies have been conducted in an effort to characterize the properties of the different components of the interstellar medium (ISM) in SMGs (see Blain et al., 2002; Casey et al., 2014, for a reviews). In this section we are going to focus mainly on the global properties of this population, with particular emphasis on results coming from the *H*-ATLAS survey.

1.3.1 Dust

As mentioned before, most the sub-mm emission is a result of the reprocessing of stellar radiation by dust[5], and therefore a probe of the dust properties. In order to characterize the properties of the emitting dust, a SED needs to be fitted to the observed data (i.e. the flux densities form far-IR to mm wavelengths).

Since the dust emits thermal radiation, the traditional method is to fit a modified blackbody SED with either one component (accounting for the bulk of the dust emission) or two components (treating the cold and hot dust separately). Following Pearson et al. (2013), the latter is given by,

$$S_\nu = A_{off}\left[B_\nu(T_h)\nu^\beta + \alpha B_\nu(T_c)\nu^\beta\right] , \tag{1.1}$$

---

[5] The presence of an active galactic nuclei (AGN) in some SMGs could be contributing to the sub-mm emission output.

where S_ν is the flux at the rest-frame frequency ν, A_{off} is the normalisation factor, β is the dust emissivity index, T_h and T_c are the temperatures of the hot and cold dust components, respectively, α is the ratio of the mass of the cold to hot dust and B_ν is the *Planck* blackbody function[6].

1.3.1.1 Far Infrared Luminosities & Star Formation Rates

Once a SED template, S_ν, is fitted to a given source, the total infrared luminosity can be computed by integrating the SED over the rest-frame 8−1000 μm range, as

$$L_{IR}(8-1000\mu m) = 4\pi D_L^2(z)\int S_\nu d\nu, \tag{1.3}$$

where D_L is the luminosty distance (Hogg, 1999). There is a plethora of studies that measure total IR luminosities for SMGs. The bulk of currently detected SMGs have IR luminosities, $10^{12} \leq (L_{IR}/L_\odot) \leq 10^{13}$ (e.g. Rowlands et al., 2014; Swinbank et al., 2014), otherwise known as Ultra-Luminous Infrared Galaxies (ULIRGs; Sanders and Mirabel, 1996) the majority of which are major mergers (e.g. the Antennae galaxy). Few rare cases, however, have IR luminosities exceeding, $L_{IR} \geq 10^{13} L_\odot$ (e.g. Ivison et al., 2013; Fu et al., 2013; Bussmann et al., 2015). These sources are classified as Hyper-Luminous Infrared Galaxies (HyLIRGs; Rowan-Robinson and Wang, 2010).

Under the assumption that all the IR emission comes from the reprocessing of stellar radiation by dust (i.e. from dust-obscured regions), their derived star-formation rates (SFRs) are of of the order of SFR ~ 10^2–10^3 M$_\odot$ yr^{-1} (Chapman et al., 2005; Riechers et al., 2013), where the SFR is computed using the Kennicutt and Evans (2012) relation,

$$\left(\frac{SFR}{M_\odot yr^{-1}}\right) \sim 1.3\times10^{-10}\left(\frac{L_{IR}}{L_\odot}\right), \tag{1.4}$$

which assumes a Kroupa initial mass function (Kroupa IMF; Kroupa, 2001). Understanding such environments at high redshift (i.e. the mechanisms responsible for the extreme star formation rates) is fundamental in building a complete picture of how galaxies form and evolve. The two possible explanations that justify such extreme conditions are either that these object have massive reservoir of cold gas

---

[6] The Planck function is given by,

$$B_\nu(T) = \frac{2h\nu^3}{c^2}\frac{1}{e^{h\nu/(k_B T)}-1} \tag{1.2}$$

where where k_B is the Boltzmann constant, h is the Planck constant, and c is the speed of light in the vacuum.

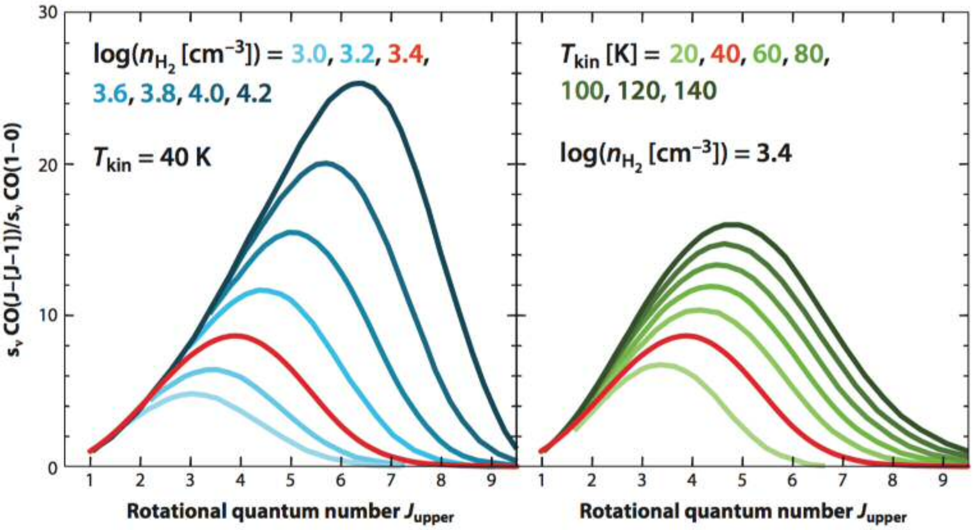

Figure 1.5: Figure is taken from Carilli and Walter (2013). The CO SLED (where s_ν is the flux of the J CO transition) based on a fixed gas temperature, T_{kin}, and a varying gas density, n_{H_2} *(left panel)*, and on a fixed gas density and a varying gas temperature *(right panel)*. The $J_{\rm upper}$ indicates which CO transition is being measured (e.g $J_{\rm upper}$=1 corresponds to the CO(1-0) transition, $J_{\rm upper}$=2 corresponds to the CO(2-1) transition. etc.)

that fuels the rapid stellar mass build-up or that they are very efficient at turning gas into stars (e.g. via major-mergers).

1.3.2 Gas

As mentioned before, one way of understanding the prodigious star formation rates in SMGs is to measure their molecular gas mass, M$_{gas}$. This is because molecular gas is the fuel for the formation of new stars (Carilli and Walter, 2013). Carbon Monoxide (CO) is considered to be an excellent tracer of the molecular gas in galaxies. Molecular gas masses are traditionally computed from the CO$(1-0)$ line luminosity, $L^{'}_{\rm CO(1-0)}$ (in units of K km s^{-1} pc^2), where the latter is computed following Solomon and Vanden Bout (2005),

$$L^{'}_{line} = 3.25 \times 10^7 \, S_{line}\Delta_v \, \frac{D_L^2(z)}{v_{obs}^2 (z+1)^3}, \tag{1.5}$$

where $S_{line}\Delta_v$ is the observed line flux density (in units of Jy km s^{-1}), v_{obs} and is the observed frequency of the line (in unit of GHz). The molecular gas mass can then be derived from the linear relation, M$_{gas}$ = $\alpha_{CO} L^{'}_{CO(1-0)}$, where α_{CO} is the CO-to-H$_2$ conversion factor (Bolatto et al., 2013). Besides CO, there are other atomic and molecular lines that can be used to trace the gas in high redshift SMGs, such as C_I, C_{II} and water (H_20) lines. Using all these different gas tracers, many previous studies have shown that SMGs possess massive reservoirs of molecular gas (e.g. a few times 10^{11} $M_\odot$; Bothwell et al., 2013; Yang et al., 2016, 2017).

In addition, measuring multiple CO lines allow us to probe the physical condition of the gas by means of modeling the CO spectral line energy distribution (SLED). En example of a SLED is shown in Figure 1.5, which demonstrates how the shape of the SLED is changing by varying either the density (left panel) or the temperature (right panel) of the gas. Such analysis in high redshift SMGs has only become possible over the last few years (e.g. (Riechers et al., 2013; Yang et al., 2017; Dong et al., 2019).

Finally, obtaining spatially resolved spectra of these various molecular lines gives us insights into the dynamical state of these galaxies. Revealing the kinematical structure of these systems allows us to determine if the system in question is a clumpy rotating disk (Dye et al., 2015; Swinbank et al., 2015) or a major-merger (Engel et al., 2010; Riechers et al., 2011). Once the dynamics of the system are determined, an estimate of their dynamical mass, which is the sum of all the different components that make up the ISM, can be derived (Bothwell et al., 2013).

1.3.3 Stars

Another diagnostic of the extreme star formation rates in SMGs is to measure their stellar masses, $M_\star$. That would allow us to determine where these galaxies lie on the $M_\star - SFR$ plane with respect to main-sequence (MS) galaxies. The galaxy MS is a power law relation (Speagle et al., 2014),

$$\log\left(\frac{SFR}{M_\odot\, yr^{-1}}\right) = \alpha \log\left(\frac{M_\star}{M_\odot}\right) + b\,, \tag{1.6}$$

where α is the slope and b the normalisation. Various studies (e.g. Rodighiero et al., 2011; Speagle et al., 2014) have shown that the majority of star-forming galaxies follow this correlation (see Figure 1.6). In addition, the normalisation is found to increase with redshift (Speagle et al., 2014; Tomczak et al., 2016). This increase is attributed to higher cold gas fractions in galaxies as we move to higher redshift (Tacconi et al., 2010; Scoville et al., 2016). Regardless of redshift, however, objects ×10 above the main sequence are characterized as starburst galaxies and are believed to follow a different evolutionary path than normal MS galaxies.

Measuring stellar masses for SMGs, however, is a challenging task as most the UV radiation is absorbed by dust and re-emitted at longer wavelengths. In addition, different assumptions on the parametrization of the star formation

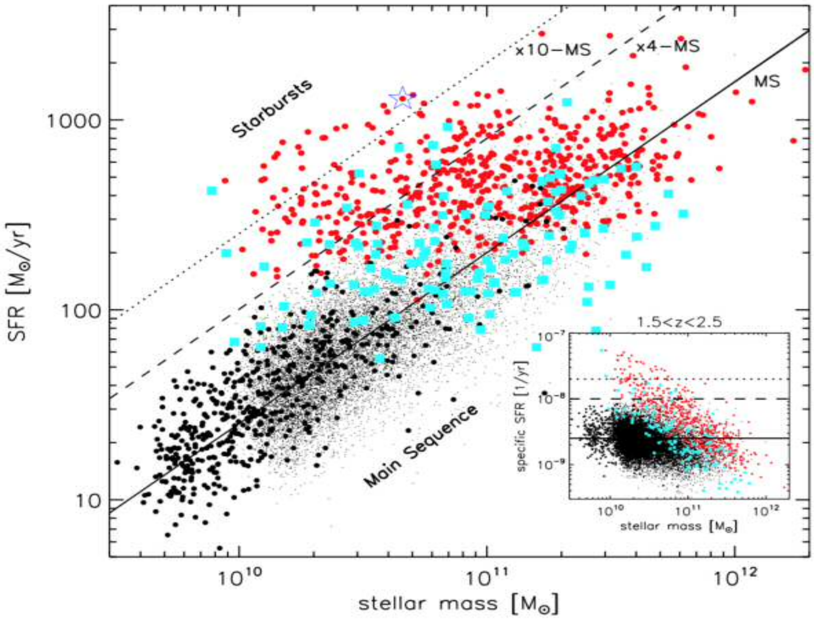

Figure 1.6: Figure is taken from Rodighiero et al. (2011). The star formation rate - stellar mass relation for galaxies selected at redshifts $1.5 < z < 2.5$. The different color points come from the shallow PACS-COSMOS sources (red), the deeper PACS-GOODS South (cyan), the BzK-GOODS sample (black filled circles), and the BzK-COSMOS sources (black dots). The black solid line correspond to the main sequence for star-forming galaxies at z~2, while the dashed and dotted lines correspond to 4 and 10 times above the main sequence, respectively.

histories in the SED modelling of SMGs or their initial mass function can lead to large discrepancies on the inferred stellar masses. By reviewing the various assumptions that go into the calculation of stellar masses and consulting results of hydrodynamical simulations, Michałowski et al. (2012) concludes to a set of sensible assumptions for the above ingredients. Using these assumptions the authors provide the most accurate determination of stellar masses of SMGs for a sample of 349 source selected from the S2CLS, finding a median of $\sim 10^{11}$ $M_{\odot}$. This and many other studies that followed (e.g. Scoville et al., 2016, 2017; Tacconi et al., 2018) have determined that the majority of SMGs lie at the high-mass end of the main sequence. But even for those that lie above the MS, Scoville et al. (2016) found that their primary difference is their increased gas content rather than higher efficiency of gas conversion into stars (e.g. due to a major-merger). In fact, their gas mass fractions range between 50-80%, meaning that their gas masses can reach up to ~ 4 times their stellar mass. All these evidence suggest that the primary drive of the extreme star-formation rates in SMGs is the excess of cold gas reservoir in these objects.

1.4 Models of SMGs

Despite the great effort in characterizing the properties of the different components of the ISM in high redshift SMGs (as demonstrated from the compilation of studies in the previous section), the evolutionary stages and nature of these galaxies is still hottly debated.

The most prevailing scenarios are merger-driven galaxy evolution models, which follow the evolution of both the disc and the spheroidal components of galaxies (Baugh et al., 2005; Almeida et al., 2011), models where the star formation is fuelled by steady accretion of large amounts of cold gas (Davé et al., 2010; Narayanan et al., 2015) and a self-regulated galaxy evolution model where proto-spheroidal galaxies are the dominant population at z>1.5 while below that IR galaxies are dominated by normal star-forming and starburst galaxies, with the two populations being distinct in terms of their properties (Granato et al., 2004; Lapi et al., 2011; Cai et al., 2013).

1.4.1 Evolution of SMGs

Besides understanding the mechanisms responsible for the formation of SMGs, it is also important to understand how these galaxies will evolve over time. Assuming that an SMG at $z\sim2$ is forming stars at a rate of ~500 M$_\odot$ yr^{-1} and has a gas reservoir of $M_{gas}\sim5\times10^{11}$ M$_\odot$ then in ~1 Gyr it will have exhausted all its gas and turned it into stars. Assuming that this SMG had initially a stellar mass of $\sim10^{11}$ M$_\odot$, its stellar mass at $z\sim0$ will be of the order of a few times 10^{12} M$_\odot$.

Stellar masses of this order are typically found in massive elliptical galaxies in the local Universe (Lapi et al., 2011), hinting to a potential link between these two galaxy populations. Strengthening this link further is also the fact that the space density of SMGs at $z\sim2$ is comparable to that of local elliptical galaxies (Simpson et al., 2014). These observational evidence, along with a few other arguments (Lapi et al., 2011), point to the direction that SMGs are the progenitors of massive elliptical galaxies that we see in our local Universe.

An alternative way to examine the evolutionary linkage between galaxy populations identified at different redshifts is to measure their clustering properties. Estimates of their clustering strength[7] allow us to measure the masses of dark matter halos in which these galaxies reside. Previous studies on the topic have shown that SMGs at $z>1$ reside in dark matter halos of the order of 10^{13} M$_\odot$

---

[7] The clustering strength, defined as r_0, sets the scale at which the excess probability ($P(r)=N[1+\xi(r)]$, where N is the volume density of galaxy; see section 3.3.1) of finding a pair of galaxies is unity $\xi(r=r_0)=1$.

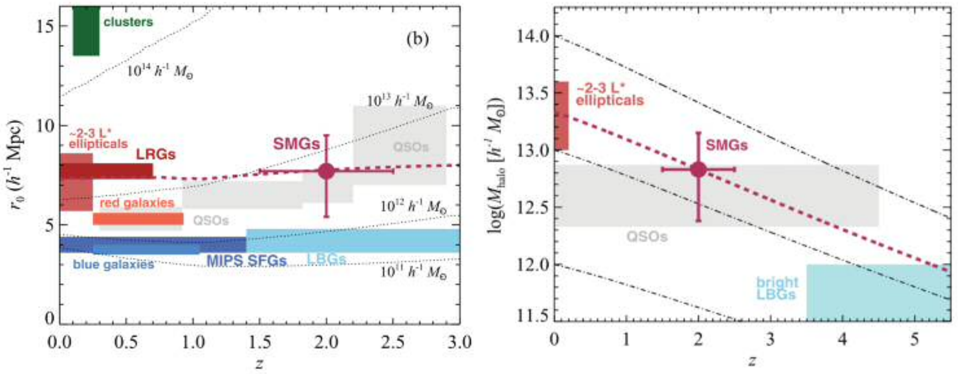

Figure 1.7: Figures are taken from Hickox et al. (2012). The evolution based on the measurement of the correlation length (r_0; *left panel*) and halo mass (M_{halo}; *right panel*) of the SMG population selected at 870 μm in comparison to other galaxy populations (e.g. QSOs; Myers et al., 2006; Ross et al., 2009), early-type (Wake et al., 2008) and late-type (Hickox et al., 2009) galaxies, among others).

Cooray et al. (2010); Maddox et al. (2010); Hickox et al. (2012); Chen et al. (2016b); Wilkinson et al. (2017). This is demonstrated in Figure 1.7 which shows theoretical predictions for the clustering strength of dark matter halos at different masses *(as black dotted lines)* against observational results from Hickox et al. (2012). However, this and other studies that followed were either limited by small number statistics (Chen et al., 2016b; Wilkinson et al., 2017) leading to large uncertainties on the derived properties or the results from similar data sets were proven contradictory (Cooray et al., 2010; Maddox et al., 2010). In Chapter 3 we measure the clustering properties of SMGs selected at 250 μm from the *H*-ATLAS survey, finding that they reside in dark matter halos of the order of ~ $10^{12.5} - 10^{13.2}$ h^{-1} $\mathrm{M}_{\odot}$ which is consistent with them being the progenitors of massive elliptical galaxies that we see in the local Universe. This work resulted in a publication entitled "Herschel-ATLAS: The spatial clustering of low and high redshift submillimetre galaxies" (Amvrosiadis et al., 2018)

1.5 Strong Gravitational Lensing

In Section 1.3, we mentioned that a great effort has been put into investigating the global properties of the different components of the ISM (i.e. dust, gas and stars) for the population of SMGs. However, in order to fully understand the mechanism that drive the star-burst phase in these object we need to map these properties at scales where star formation takes place.

In local galaxies the typical scale of Giant Molecular Clouds, which is where

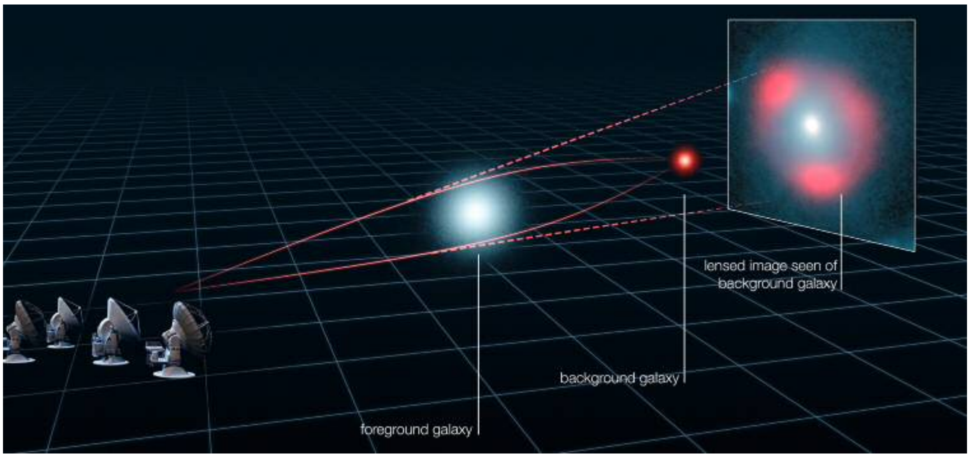

Figure 1.8: Typical strong lensing configuration, where a background galaxy is lensed by a foreground galaxy (elliptical) forming multiple images.

gas condenses to form stars, is between 10 – 100 pc. Resolving the properties of the ISM down to such scales in high redshift DSFGs, however, is very challenging. With our current facilities, this can only become possible with the aid from strong gravitational lensing. Strong gravitational lensing can magnify the images of the background sources by large factors, increasing their observed flux, effectively working as a natural telescope. In the section that follows we will give a brief overview of this effect and later on discuss some of it's applications.

1.5.1 Basic principles of strong gravitational lensing

In the framework of general relativity (GR), as photons travel from a distant background source and through the vicinity of massive objects, such as galaxies or groups/clusters of galaxies, their trajectories get distorted by the presence of these matter inhomogeneities (as shown in Figure 1.8). If the background source and the foreground object are well aligned with the observer, we have the creation of multiple images and/or arc-like features. This effect is called strong gravitational lensing (Schneider et al., 1992). In the thin screen approximation (i.e., when the size of the deflector is much smaller than the distances between the deflector and the observer, D_d, and the deflector and the source, D_{ds}), we can assume that lensing occurs instantaneously when the light crosses the lens plane (see Figure 1.9). Under this assumption we derive the following properties (see Bartelmann and Schneider, 2001, for reviews).

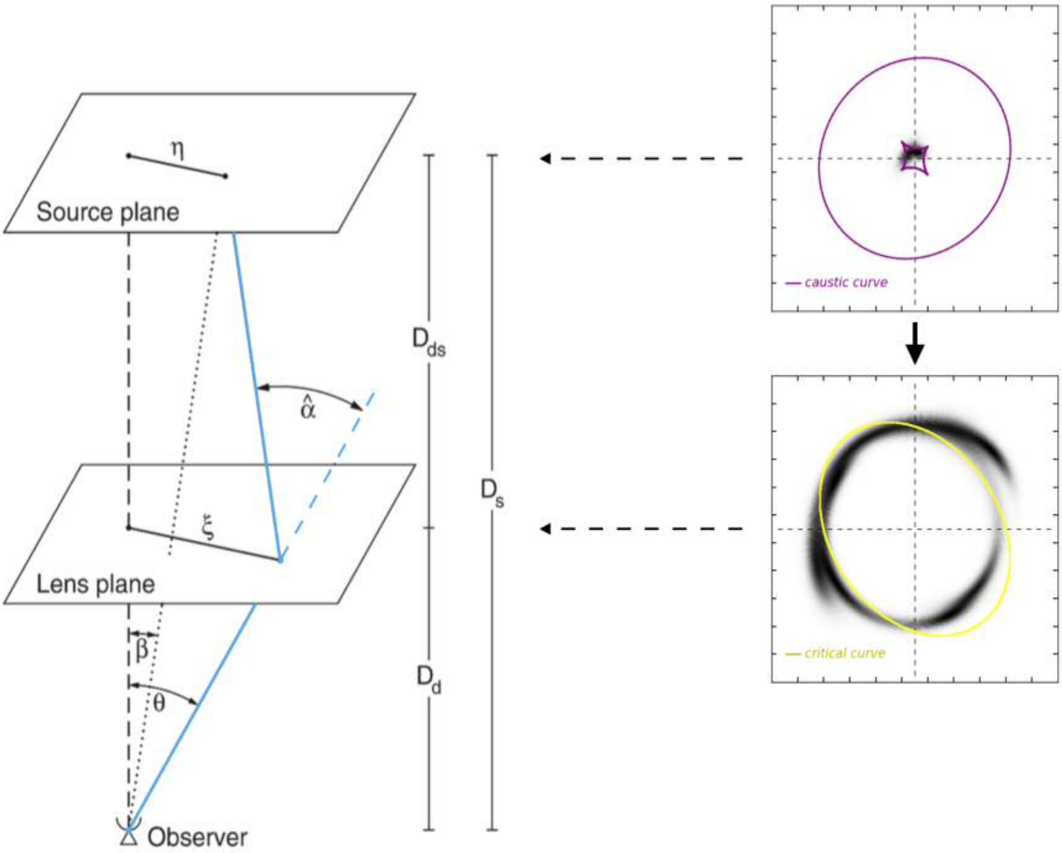

Figure 1.9: Figure adapted from Bartelmann and Schneider (2001) showing a typical lensing configuration. *(Left panel):* The blue lines show the actual path of a light ray coming from the source to the observer, as it gets deflected by an angle $\hat{\alpha}$ due to strong gravitational lensing. The angular diameter distances between the observer and the deflector, the observer and the source and the deflector and the source are denoted as D_d, D_s and D_{ds}, respectively. *(Right panel):* The top row shows the emission of the background galaxy in the source-plane (SP), which is composed of two elliptical Gassian profiles. The bottom row shows the emission of the background galaxy in the lens-plane (LP) after it has been lensed by Spherical Isothermal Ellipsoid (SIE; Kormann et al., 1994) mass distribution (typical of early-type galaxies). The purple (in the SP) and yellow (in the LP) curves correspond to the caustic and critical curve, respectively (see main text for more details on the definition of these curves).

1.5.1.1 The deflection angle

The deflection angle caused by an extended mass distribution can be calculated by breaking the mass into many small ("point-like") segments and summing over the individual deflection angles as

$$\hat{\vec{\alpha}} = \frac{4G}{c^2}\int d^2\xi^{'}\Sigma(\vec{\xi}^{'})\frac{\vec{\xi}-\vec{\xi}^{'}}{\left|\vec{\xi}-\vec{\xi}^{'}\right|} \tag{1.7}$$

where G is the gravitational constant, c is the speed of light, $\Sigma(\vec{\xi})$ is the surface mass density along the line-of-sight (LOS) of the object acting as the lens and $\vec{\xi}$ is a vector from the center of the mass distribution to each mass segment.

Knowing the deflection angle, the relationship between the true position of the source in the sky, β, and of it's lensed images relative to the observer, θ, is described by the lens equation,

$$\vec{\beta} = \vec{\theta} - \vec{\alpha}(\vec{\theta}), \tag{1.8}$$

which is derived from simple trigonometric arguments as seen from Figure 1.9. We are in the strong lensing regime when the lens equation has multiple solutions, θ_i, in the lens plane for a given position, β in the source plane.

1.5.1.2 The magnification factor

If we now define ψ as the two-dimensional lensing potential, the *Jacobian* of the transformation from the image to the source plane can be written as

$$A = \frac{\partial\vec{\beta}}{\partial\vec{\theta}} = \delta_{ij} - \frac{\partial^2\psi}{\partial\vec{\theta}_i\partial\vec{\theta}_j} = \begin{pmatrix} 1-\kappa-\gamma_1 & -\gamma_2 \\ -\gamma_2 & 1-\kappa+\gamma_1 \end{pmatrix} \tag{1.9}$$

where κ gives the convergence of the image

$$\kappa(\vec{\theta}) = \frac{\Sigma(D_d\vec{\theta})}{\Sigma_{cr}} \quad with \;\; \Sigma_{cr} = \frac{c^2}{4\pi G}\frac{D_s}{D_d D_{ds}} \tag{1.10}$$

being the critical surface mass density which defines the condition for strong lensing to occur. The vector quantity, γ, describes the shear which has two components γ_1 and γ_2 so that

$$\gamma = \gamma_1 + i\gamma_2 = |\gamma|e^{2i\phi} \tag{1.11}$$

and gives the distortion of the source along a privileged direction, ϕ.

The inverse of the determinant of the *Jacobian* matrix gives the magnification factor, μ, which for a point-like source is given from

$$\mu = \frac{1}{detA} = \frac{1}{(1-\kappa)^2 - |\gamma|^2} \,. \tag{1.12}$$

In real lensed systems, as the example shown in Figure 1.9, the fact that the background source is extended means that the magnification is finite and it generally takes values in the range 10-25 for galaxy-scale lenses (e.g. Bussmann et al., 2013; Enia et al., 2018; Dye et al., 2018).

1.5.1.3 The critical and caustic curves

We can clearly see from Eq. 1.12 that the magnification becomes infinite when $detA = 0$. The positions in the image and source planes corresponding to this condition define critical and caustic curves, respectively. The purple and yellow curves in Figure 1.9 show the caustic and critical curves, respectively, for a simulated lensed system.

In the example of Figure 1.9 we see that there are two distinct caustic curves in the source plane. These two correspond to the radial (inside) and tangential (outside) caustic, which are defined as

$$\begin{aligned} 1-\kappa-\gamma &= 0 \\ 1-\kappa+\gamma &= 0 \end{aligned} \tag{1.13}$$

respectively. A point source will be quadruply lensed if it's located within the radial caustic and doubly lensed if it's outside [8]. For an extended source, as the one shown in Figure 1.9, we have the creation of rings and arcs, respectively.

1.6 Modelling strongly lensed systems

In the previous section, we described the basic formalism for strong gravitational lensing and how to compute various lensing quantities given the surface mass distribution of the lens, Σ. In practice, however, we are looking to solve the inverse problem when presented with an observed lensed system. The methodology on the modeling of strongly lensed galaxies has been thoroughly described in the

---

[8] In theory, strong lensing always produced an odd number of multiple images (unless the central density of the lens is infinite). However, the additional image that is formed, whether the source is within or outside the radial caustic, is always de-magnified.

literature (Warren and Dye, 2003; Suyu et al., 2006; Nightingale and Dye, 2015) of which the general aim is to reconstruct the intrinsic light profile of the background lensed galaxy, while simultaneously trying to constrain the mass distribution of the foreground object acting as the lens.

1.6.1 Modelling in the *uv-plane*

Traditionally, the modeling is performed in the image plane (e.g. Dye et al., 2014) with observations carried out at optical wavelengths (e.g. HST or Keck). However, recent advances in imaging capabilities, with interferometric facilities such as the Atacama Large Millimeter/submillimeter Array (ALMA), the Submillimeter Array (SMA) and the Plateau de Bure Interferometer (PdBI/NOEMA), have opened a new window.

An interferometer is an array of antennas, where the maximum resolving power is set by the maximum distances between two antennas, $\theta \propto \lambda B$, where B is usually refereed to as the baseline and λ is the wavelength of the observation. In interferometric observations, we do not directly measure the source's surface brightness, $I(x,y)$, but rather a complex quantity called the *visibility function*, $V(u,v)$, which is its Fourier transform and is computed from,

$$V(u,v) = \int\int A(x,y) I(x,y) e^{-2\pi i(ux+vy)} dx dy, \tag{1.14}$$

where $A(x,y)$ is the effective collective area of each antenna (otherwise known as the primary beam). The uv-plane represents a coordinate system in the Fourier domain where visibilities are measured at distinct (u,v) locations. Each pair of antennas records one visibility point where the location of this point in the uv-plane is determined by their baseline (see left panel of Figure 1.10).

Although interferometric observations offer significant improvement in spatial resolution, there is a caveat when it comes to strong-lens modeling. As we show in Figure 1.10, a good sampling of the uv-plane results in a good-quality image and the more the antennas of an interferometer the better the uv-coverage will be. Insufficient uv-plane coverage can lead to artifacts such as side lobes and correlated noise (Hezaveh et al., 2013), which if not treated properly can bias the lens model parameter inference. For that purpose, the modelling of these observations needs to be carried out in the uv-plane rather than the image-plane, where the noise of the visibilities is Gaussian and no artifacts are in place. In a recent work, Dye et al. (2018) showed that with sufficient uv-covarage, modelling in the image-plane can still be viable in order to recovered the lens model parameters to first order. This

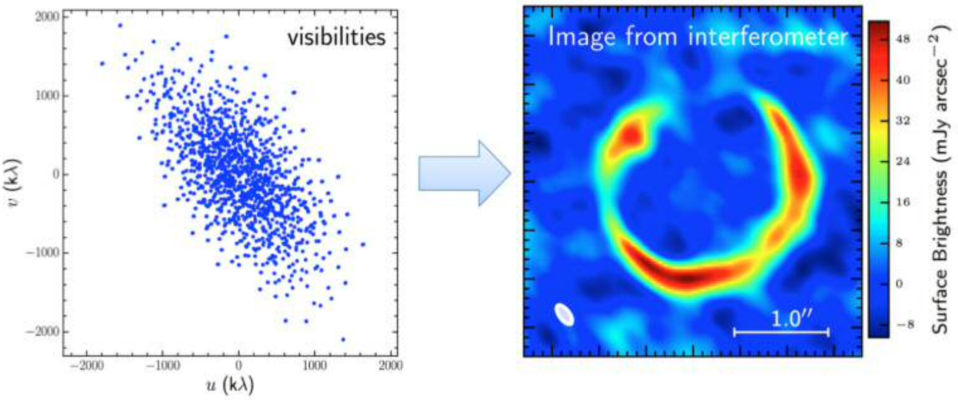

Figure 1.10: Simulation of an ALMA observation where the left panel shows the coverage in the uv-plane and the right panel the image that results from the Fourier Transform of the visibilities.

can be very useful so as to reduce the parameter space that needs to be searched during the non-linear search using the uv-data, where the latter is several times more time consuming that the first (e.g. ALMA interferometric observations can have up to 10^8-10^9 individual visibilities).

The formalism for modeling strongly lensed systems in the uv-plane was first introduced in Bussmann et al. (2012). Over the past few years, modeling strongly lensed systems in the *uv-plane* has become a common practice (Bussmann et al., 2013, 2015; Rybak et al., 2015a,b; Hezaveh et al., 2016; Spilker et al., 2016; Dye et al., 2018; Enia et al., 2018; Litke et al., 2019; Dong et al., 2019, Negrello et al., in prep., Amvrosiadis et al., in prep.) for studying high-redshift SMGs.

1.6.2 Applications using Strong Gravitational Lensing

There are numerous applications of strong gravitational lensing in the literature. The three main categories include the use of strong lensing to study either the background or the foreground population and to infer cosmological parameters. In the following sections I discuss the first two categories which are more relevant to the content of this Thesis.

1.6.2.1 Studying the background population with strong lensing

In this section I discuss the use of strong lensing to study the lensed population and in particular that of SMGs. I only focus on one study that uses observations that were conducted in the sub-mm wavelength regime. An important advantage at this wavelength regime is that the emission from the lens itself (typically an early-type galaxy with very little dust) is negligible, thus alleviating any biases due

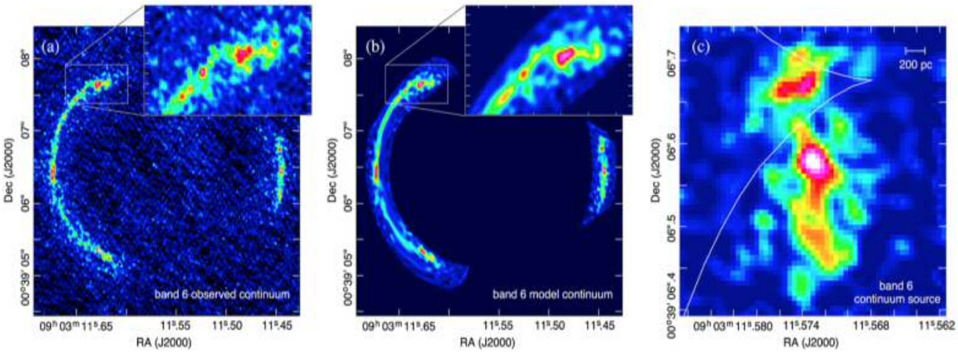

Figure 1.11: Figure adapted from Dye et al. (2015). Panel (a) shows the observed image of the dust continuum emission in the ALMA band 6 (~1.3 mm), panel (b) shows the model image of the reconstructed source in panel (c). The white line in panel (c) shows the radial caustic curve while the image scale is indicated at the top right corner of the same panel.

to the removal of the lens's emission (Dye et al., 2014; Nightingale et al., 2018). In addition, the bulk of the sub-mm emission in SMGs comes from compact regions (~3 times smaller compared to the rest optical/UV emission Simpson et al., 2015; Hodge et al., 2018) and hence experiences higher magnifications (Hezaveh et al., 2012, see also Section 1.5.1.2).

Typical magnification factors for SMGs, where the lensing object is a galaxy-scale lens, range between $\mu \sim 5 - 15$ (Bussmann et al., 2013; Enia et al., 2018). Observing an SMG at $z \sim 2$ at an angular resolution $\sim 0.1''$ and adopting a spatially-flat Λ Cold Dark Matter (Λ-CDM) cosmology with $\mathrm{H}_0 = 67.8 \pm 0.9$ km s^{-1} Mpc^{-1} and $\Omega_M = 0.308 \pm 0.012$ (Planck Collaboration et al., 2016, where H_0 and Ω_M are the cosmological parameters of this model) means that we can probe scales down to ~850 pc. If we now factor in the increase in angular resolution offered by strong lenisng[9] we can reach scales down to ~200-300 pc, comparable to GMCs that we see in local star-forming galaxies.

The increase in angular resolution that strong gravitational lensing offers coupled with the power of ALMA (reaching angular resolutions ~0.02-0.04″ in its most extended configuration), allows the investigation of the ISM properties in SMGs down to tens of pc. One of the most well studied cases is the strongly lensed $z = 3.042$ galaxy J090311.6+003906 (SDP.81; Dye et al., 2015), which was discovered in the *H*-ATLAS survey (Negrello et al., 2010) and was followed-up with ALMA (ALMA Partnership et al., 2015) in Bands 4 (~2.0 mm; rest-frame

---

[9] The average resolution that we can achieve in the source plane is compute as $FWHM_{beam}/\sqrt{\mu}$, where $FWHM_{beam}$ is the angular resolution of our telescope and μ is the magnification of the strongly lensed system.

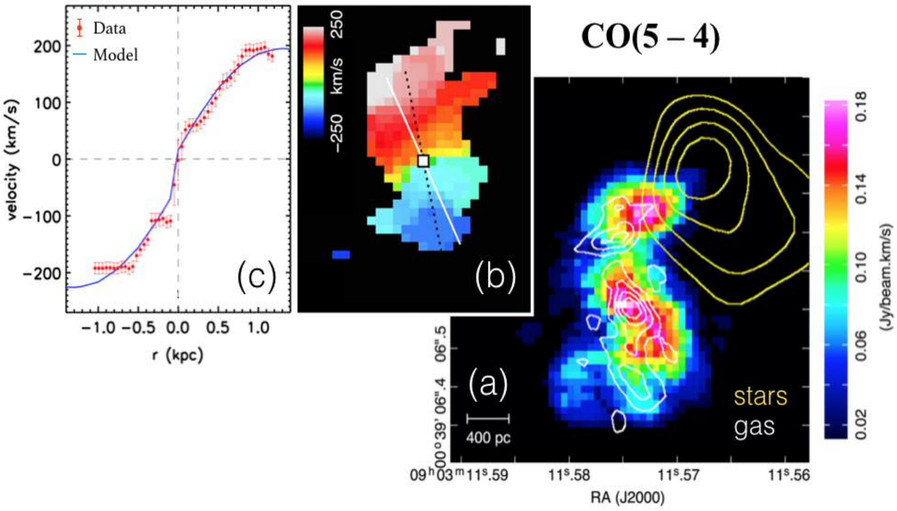

Figure 1.12: Figure adapted from Dye et al. (2015) and Swinbank et al. (2015). Panel (a) shows the reconstructed CO(5-4) line emission where the white contours correspond to the reconstructed dust continuum emission and the yellow contours to the stellar emission. Panel (b) show the reconstructed kinematics of the reconstructed source as traced by the CO(5-4) emission line, which is well fitted by a rotating disk model shown as the blue curve in panel (c).

~500 μm), 6 (~1.3 mm; rest-frame ~320 μm) and 7 (~1.0 mm; rest-frame ~250 μm), probing not only the dust continuum emission but also several emission lines (e.g. CO J=5-4, J=8-7, J=10-9 and H_2O).

Modeling of the dust continuum in these bands 6 and 7 revealed a clumpy distribution of dust (Dye et al., 2015) on scales of 50 – 100 pc (Swinbank et al., 2015). The best-fit model along with the reconstructed source from the modelling of the dust continuum in band 6 are shown in Figure 1.11. Studying the individual clumps, Swinbank et al. (2015) showed that their scaling relations between luminosity, line widths and sizes (Larson's relations; Larson, 1981) are significantly offset from those of typical molecular clouds in the local Universe. This study revealed the extreme physical conditions of the star forming ISM in this object which is similar to the densest environments in the local Universe (e.g. the galactic center of the Milky Way) .

The best-fit lens model, that was derived from modeling the dust continuum emission, was then used to reconstruct the CO(5-4) and CO(8-7) emission lines in each velocity slice of the ~21 km s^{-1} resolution cubes[10]. Collapsing the reconstructed cube along the velocity axis gives the velocity integrated flux density

---

[10] ALMA records visibilities over a bandwidth of ~2GHz per spectral window. Therefore the resulting product of these observations is a cube of the submm emission over different slices of frequencies (or radio velocities equivalently).

(zeroth moment) of the different emission lines. This is shown in panel (a) of Figure 1.12 and reveals that the gas also has a clumpy distribution. The reconstructed CO(4-3) emission line is shown in panel (a) of Figure 1.12 and shows the same clumpy morphology as the dust continuum emission. In the same figure, panel (b) shows the velocity field of the line, which shows a smooth gradient. The kinematics of the background source are best described by a rotating disk model, as shown in panel (c) of Figure 1.12. Finally, by measuring the Toomre parameter [11](Toomre, 1964) the authors concluded that the disk is in the process of collapse.

Such a wealth of information can only be accessible though the magnifying power of strong lenses. It has now become common practice (e.g. Dye et al., 2015; Spilker et al., 2015; Geach et al., 2018; Litke et al., 2019; Yang et al., 2019, Amvrosiadis et al., in prep.) to perform this kind of analysis to study the dust and gas distribution in strongly lensed SMGs. In Chapter 4, I perform a similar analysis for the strongly lensed $z = 1.783$ galaxy J091043.0−000322 (SDP.11), which was discovered in the SDP field of the *H*-ATLAS survey (Negrello et al., 2010).

1.6.2.2 Studying the foreground population with strong lensing

In the previous section we focused our discussion on the advantages strong lensing has to offer when it comes to studying the background population that is being lensed. However, another use of strong lensing is to study the properties of the population of objects acting as lenses. In fact strong lensing offers the most reliable method for inferring the density profiles of galaxies, from which measurements of total masses (dark + baryonic matter) in galaxies can be performed with great accuracy within the central few kpc regions (i.e. within the Einstein radius[12], θ_E).

Since the majority of objects acting as lenses are massive early-type galaxies, most of the studies have focused on characterizing this population; although a great effort has been put into determining the mass profiles of cluster-scale lenses. Some interesting results that came out from such studies include the determination of the average slope, γ, of the total density profile, $\rho_{tot} \propto r^{-\gamma}$, to be $\gamma \sim 2$ (Ruff et al., 2011) which also appears to steepen with increasing redshift (Ruff et al., 2011; Bolton et al., 2012); the fraction of dark matter within half the effective radius, R_{eff}, increases with increasing mass and size of the galaxy (Auger et al., 2010;

---

[11] In the case of a differentially rotating disk, the Toomre parameter, Q, is used to determine the stability of the disk. For $Q > 1$ the disk is considered to be stable against collapse.

[12] In the ideal case where the background source is located along the line of sight of the object acting as the lens, then the Einstein radius is defined as the radius of the ring that is formed due to strong lensing. Alternatively, if two images are formed in a strong lensing event then half the separation between these multiple images are approximately equal to the Einstein radius.

Ruff et al., 2011); the characterization of the subhalo population around massive elliptical galaxies (Vegetti et al., 2010; Hezaveh et al., 2016) among others.

Another such application is the use of strong gravitational lens statistics, a method introduced by Turner et al. (1984) to study the surface mass density distribution on the population of objects acting as lenses in a statistical manner. The quantity of interest here is the separation, θ, between the multiple images that are formed (or the Einstein radius, θ_E, in the cases where arc-like features are formed) in a strong lensing event. It has been predicted that its distribution, $P(\theta)$, depends strongly on the adopted density profile of the lens population as well as the number density of dark matter halos (i.e. the halo mass function; HMF) and the adopted cosmological model. Assuming that we have a good knowledge of the latter two, we can infer the former. In Chapter 5, I use both analytical and numerical density profiles to compute the distribution of image separations and compare it with the one produced from a sample of Herschel-selected strongly lensed galaxies. This work resulted in a publication entitled: "ALMA observations of lensed Herschel sources : Testing the dark-matter halo paradigm".

1.7 Thesis outline

In Chapter 2, I describe the methodology we use in order to select candidate strongly lensed galaxies from sub-mm surveys and it's application to the *H*-ATLAS survey (Negrello et al., 2017). We show that the observed number counts of our candidate sample can be reproduced by our model assuming a maximum magnification of $\mu_{max} \sim 10-20$.

In Chapter 3, I study the clustering properties for a sample of 250 μm selected SMGs from the *H*-ATLAS survey. I model the clustering signal and determine that SMGs reside in dark matter halos of the order of 10^{13} $M_\odot$, consistent with being the progenitors of massive elliptical galaxies that we see in the local Universe (Amvrosiadis et al., 2018). I further split the sample into redshift slices and show that SMGs reside in dark matter halos of the same order across all $z > 1$ slices.

In Chapter 4, I use high resolution ALMA observations to study the dust and gas distribution in the strongly lensed galaxy SDP.11. I further reconstruct the kinematics of the background lensed source and determine that its velocity field has a smooth gradient, possible reminiscent of a rotating disk. However, my analysis indicates that the lensed system is most probably a merger, possibly in the second or third close-by merging (Amvrosiadis et al., in prep.).

In Chapter 5, I argue that lensing statistics can be a powerful tool to study the density profiles of galaxies when applied to samples of strong lenses selected at sub-mm wavelengths as they do not suffer from the same difficulty to account for biases as samples selected at optical/radio wavelengths. I then use numerical and analytic models for the mass distribution of the lens population and show that samples of ~200 lenses will be sufficient to discriminate between these models (Amvrosiadis et al., 2019).

In Chapter 6, I give a summary of the thesis and briefly discuss the current status of our ongoing project to study the dust and gas in SMGs at scales down to ~100 pc with high resolution ($\sim 35-37$ mas) ALMA observations of strongly-lensed galaxies from the Amvrosiadis et al. (2018) sample.

CHAPTER 2

SOURCE SELECTION AND FOLLOW-UP OBSERVATIONS

In this chapter I will focus the discussion on the method we use to select candidate strongly lensed galaxies from wide-area extragalactic surveys conducted at sub-mm/mm wavelengths. In particular, I will emphasize on the application of this method to the *H*-ATLAS and HELMS surveys, which constitute the basis of this work. Finally, I will discuss the modeling of the observed number counts. This chapter is intended as an extension to the previous chapter and does not contain any original work that is part of this Thesis.

2.1 Identifying candidate strongly lensed galaxies in sub-mm surveys

It has long been proposed that large samples of gravitationally lensed galaxies, lying preferentially at high redshifts, can be efficiently selected by searching for bright sources in wide-area extragalactic surveys conducted at sub-mm/mm wavelengths (Blain, 1996; Negrello et al., 2007). This selection is supported by the prediction that the number counts (i.e. the number of sources at a given flux density) of the un-lensed population of SMGs are expected to drop very steeply above 100 mJy at 500 μm. This prediction comes from models for the formation and evolution of this population of sources (e.g. Blain, 1996; Perrotta et al., 2002, 2003; Lapi et al., 2006; Lapi and Cavaliere, 2011; Negrello et al., 2007, 2010; Cai et al., 2013), which assume that their luminosity function is intrinsically steep and that the majority of these sources are found at high redshifts ($z > 1.5$).

The potential of this method was first demonstrated in Negrello et al. (2010)

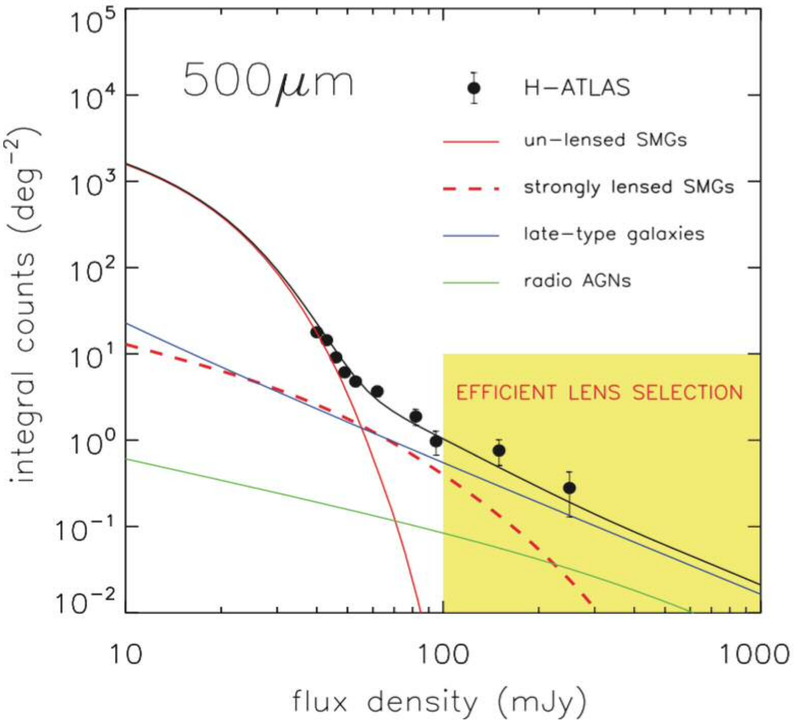

Figure 2.1: Figure adapted from Negrello et al. (2010). This figure displays the number counts of different types of galaxies at 500μm: green solid curve corresponds to radio-loud active galactic nuclei (AGNs), the blue solid curve corresponds to local late-type galaxies and the red solid and dashed curves correspond to unlensed and lensed submillimeter galaxies (SMGs), respectively. The black solid curve shows the total predicted number counts which is the sum of AGNs, late-type galaxies and lensed SMGs while the black points are the observed number counts which were derived from the *H*-ATLAS maps. Finally, the yellow square region indicates the flux density range at 500 μm where the selection of candidate strongly lensed galaxies is more efficient.

using the source catalogue from the Science Demonstration Phase (SDP) field of the *H*-ATLAS survey. The authors of this work showed that out of the 10 extragalactic sources with $F_{500\,\mu m}$ > 100 mJy, 5 were identified as high redshift strongly lensed galaxies while the remainder were either local (z<0.1) spiral galaxies (Baes et al., 2010) or flat spectrum AGNs (González-Nuevo et al., 2010). The findings of this work can be summarized in Figure 2.1. This figure shows that the model number counts of the un-lensed population of SMGs (red solid curve) drop below 10^{-2} deg^{-2} at ~100 mJy, meaning that we expect almost none of these source to be intrinsically brighter that this limit. However, several of these sources will go through an event of lensing which will increase their apparent luminosity boosting them above the 100 mJy limit. The number counts of the strongly lensed population of SMGs are now given by the red dashed line in Figure 2.1, which have a characteristic bright end tail above the 100 mJy limit.

Other types of galaxies that contribute to this bright end tail of the number counts are radio-loud active galactic nuclei (AGNs) and local (z<0.1) late-type galaxies, which are shown in Figure 2.1 as the green and blue curves, respectively. However, these type of sources can be easily identified in relatively shallow radio (e.g. NRAO VLA Sky Survey (NVSS); Condon et al., 1998) and optical (e.g. Sloan Digital Sky Survey (SDSS); Abazajian et al., 2009) surveys and therefore removed from our candidate sample.

We expect a large fraction of this list to be strongly lensed (~100%), with a small fraction made up of bright SMG−SMG mergers (e.g. Ivison et al., 2013) that appear as hyper-luminous infrared galaxies ($L_{IR} > 10^{13}$ M$_{\odot}$). The statement that this method has an ~100% efficiency is based on the sample after local contaminants have been removed.

Although strongly lensed SMGs are rare (~0.13−0.21 deg^{-2}, when selected at 500 μm; Wardlow et al., 2013; Nayyeri et al., 2016; Negrello et al., 2017), statistically significant samples have recently become available due to the advent of multiple wide-area extragalactic surveys conducted at sub-mm/mm wavelengths. Examples of such surveys include:

- The Herschel-Astrophysical Terahertz Large Area Survey (H-ATLAS; Eales et al., 2010) covering an area of 660 deg^2, led to the identification of 80 candidate strongly-lensed galaxies (sources are selected at 500 μm; Negrello et al., 2017) where 20 of them have been subsequently confirmed as lensed sources (Negrello et al., 2017) and one source is an SMG-SMG merger (Ivison et al., 2013). Another 3 sources have also been confirmed using Submillimeter Array (SMA) observations (Enia et al., 2018). The source selection is the same for all Herschel surveys that follow.

- The Herschel Multi-tiered Extragalactic Survey (HerMES; Oliver et al., 2012) covering an area of 95 deg^2, identified 13 candidates, with 11 confirmed strong lenses (Wardlow et al., 2013) and 2 sources that are luminous SMG−SMG mergers (Fu et al., 2013; Bussmann et al., 2015).

- The HerMES Large Mode Survey (HeLMS; Oliver et al., 2012) and the Herschel Stripe 82 Survey (HerS; Viero et al., 2014) covering a total area of 372 deg^2, identified 77 candidates (Nayyeri et al., 2016), with >10 so far confirmed (Amvrosiadis et al., 2018, Marchetti et al., in prep.).

- The South Pole Telescope (SPT; Carlstrom et al., 2011) covering an area of 1300 deg^2, identified 47 candidates (sources are selected at 1.4 and 2.0 mm;

Vieira et al., 2013) and for 38 of which strong lensing is the most plausible explanation (Spilker et al., 2016).

- The Planck all-sky survey (e.g., Planck Collaboration et al., 2015; Cañameras et al., 2015; Harrington et al., 2016).

These surveys have enabled the identification of hundreds of candidate strongly lensed galaxies altogether. However, the large beam sizes of the facilities used to identify the candidates (e.g. the full width at half maximum (FWHM) of the SPIRE instrument's point spread function (PSF) even at 250 μm is ~15″; Griffin et al., 2010) means that follow-up observations are required in order to confirm the strong lensing nature of these systems.

2.2 Candidate selection and follow-up observations for the *H*-ATLAS survey

The*H*-ATLAS survey, which was introduced in the previous chapter, is the widest area extragalactic survey undertaken with *Herschel* (~ 660 deg^2). The survey is comprised of five different fields, three of which are located on the celestial equator (GAMA fields; Valiante et al., 2016) covering in total an area of 161.6 deg^2. The other two fields are centred on the North and South Galactic Poles (NGP and SGP fields; Smith et al., 2017) covering areas of 180.1 deg^2 and 317.6 deg^2, respectively. The source catalogues of the H-ATLAS fields were presented in Valiante et al. (2016) and Maddox et al. (2018) for the GAMA and NGP/SGP fields respectively. A more in depth description of the H-ATLAS survey will be given in Chapter 3.

In order to build our sample of candidate strongly lensed galaxies we start from these source catalogues and select only sources with $F_{500} \geq$100 mJy, which are 325 in total. Out of these sources, a fraction will be low-redshift spiral galaxies or flat spectrum radio source. 11 were identified as blazars from having intense radio emission ($F_{1.4GHz}$ >100 mJy) and rising/flat SEDs. 231 were identified as spiral galaxies all of which have confirmed spectroscopic redhisfts below $z < 0.1$ (except two, which could be acting as lenses). 3 were identified as dusty stars. The remaining 80 sources are classified as candidate strongly lensed galaxies. In Figure 2.2 we show the distribution of our final sample of 80 candidate strongly lensed galaxies (yellow dots), across the five different *H*-ATLAS fields.

Follow-up observations were carried out with various facilities such as the Hubble Space Telescope (HST), Keck Observatory and the UK Infrared Telescope (UKIRT) in the optical and submillimeter Array (SMA) in the sub-mm wavebands.

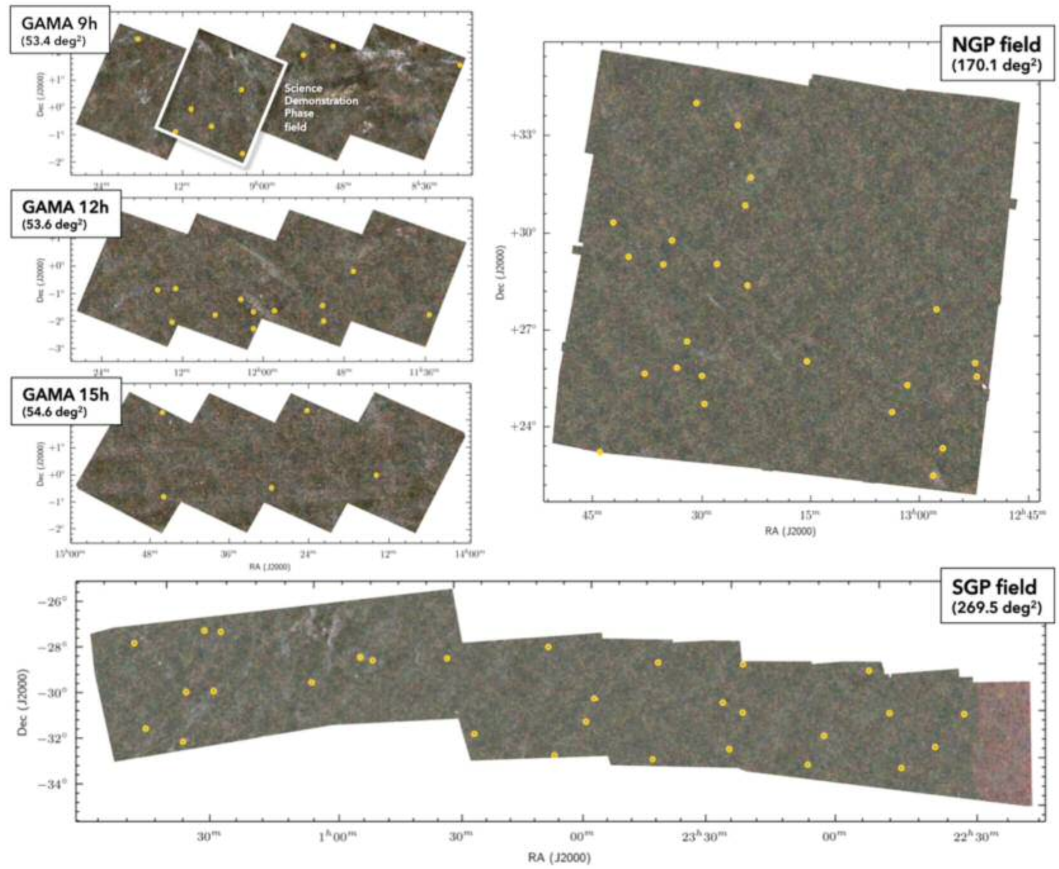

Figure 2.2: Figure adapted from Negrello et al. (2017). This figure displays the *Herschel*/SPIRE color maps of the *H*-ATLAS fields where the yellow circles indicate the position of the 80 candidate strongly lensed galaxies with flux densities $F \geq 500$ mJy at 500 μm.

These observations have allowed us to confirm, so far, that >20 of these sources are strongly lensed by a foreground object (Negrello et al., 2010, 2014, 2017; Cox et al., 2011; Fu et al., 2012; Bussmann et al., 2012, 2013, 2015; Calanog et al., 2014; Messias et al., 2014; Amvrosiadis et al., 2018; Enia et al., 2018, Marchetti et al., in prep., Negrello et al., in prep.). Postage stamps for 20 of these sources are shown in Figure 2.3, which all show arc-like features or multiple images, indicative of the strong lensing nature of these system.

These sources are excellent target for high-resolution follow-up observations with ALMA to study the distribution of dust and gas at sub-kpc scales (see Section 4). Among these objects is the well studied example of SDP.81 (ALMA Partnership et al., 2015), which demonstrated the power of this technique.

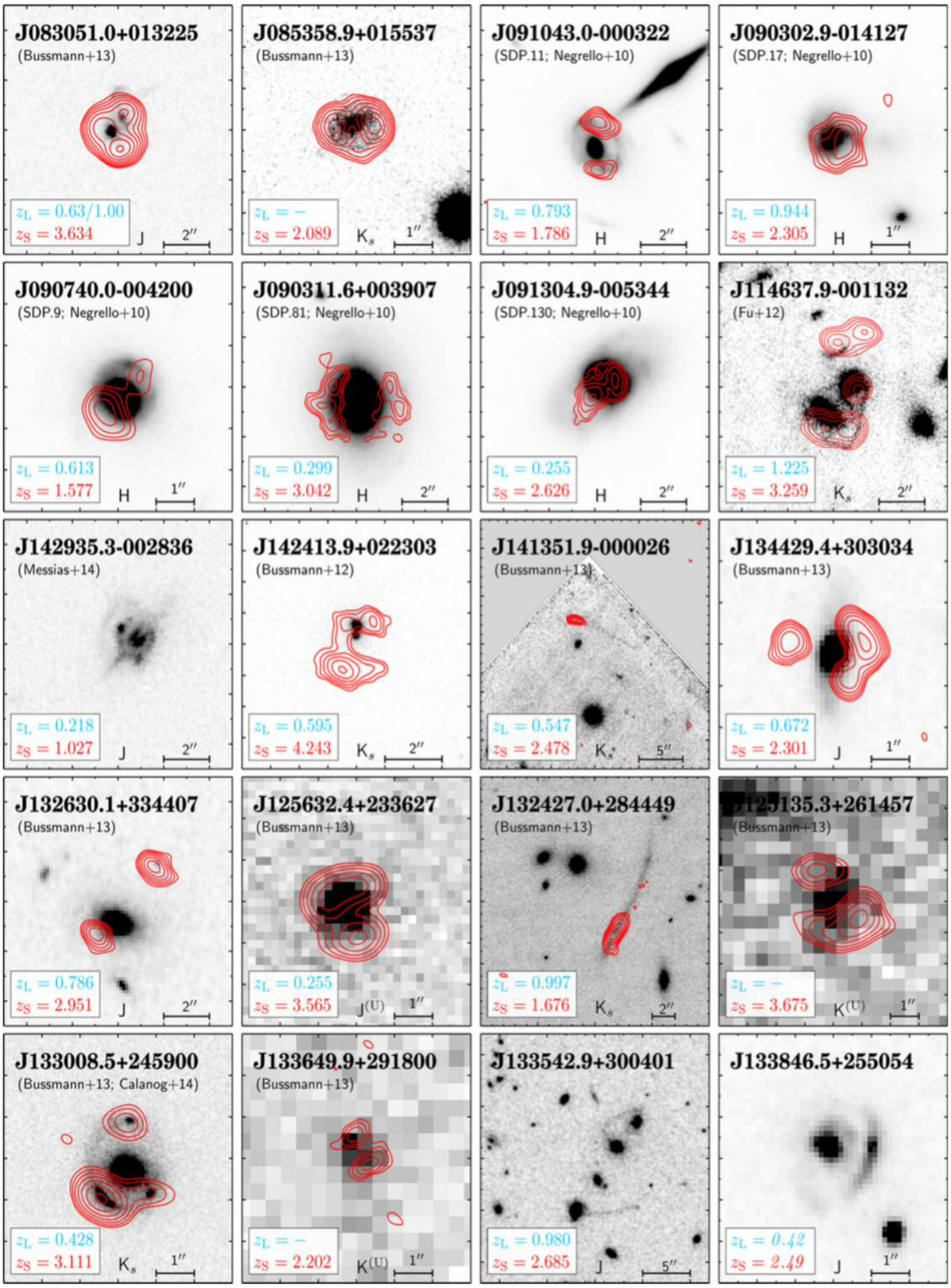

Figure 2.3: Figure adapted from Negrello et al. (2017). Postage stamps of the 20 confirmed strongly lensed galaxies in the *H*-ATLAS fields. The redshifts of the foreground (z_L) and background (z_S) sources are shown in the bottom left corner with blue and red, respectively (some of which are photometrically determined).

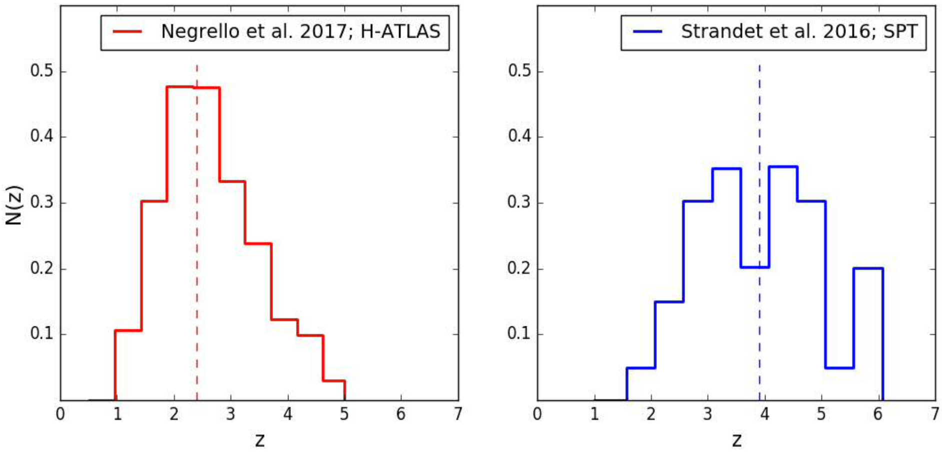

Figure 2.4: Figures are adapted from Negrello et al. (2017) and Strandet et al. (2016). The redshift distributions of candidate strongly lensed galaxies selected at 500 μm from the *H*-ATLAS survey and at 1.4 mm from the SPT survey.

2.3 Redshift distribution

The majority of sources in our sample of candidate strong lenses have photometric redshifts. These were determined by fitting the Herschel/SPIRE photometry with the Pearson et al. (2013) template, which is the sum of two modified blackbody SEDs with temperatures $T_{cold} = 23.9$ K and $T_{hot} = 46.9$ K, dust emissivity index of $\beta = 2$ and a ratio of $\alpha = 30.1$ between the normalization of the two dust components.

Several sources, however, have confirmed spectroscopic redshifts. These were determined through the detection of various emission lines using the *Z*-spec presented in Lupu et al. (2012), the GBT/Zspectrometer presented in Frayer et al. (2011) and Harris et al. (2012), the (PdBI) presented in Negrello et al. (2010); Omont et al. (2011, 2013); Yang et al. (2016), the CARMA presented in Riechers et al., in prep. and finally the Herschel/SPIRE Fourier Transform Spectrometer presented in (Valtchanov et al., 2011; George et al., 2013).

The redshift distribution of our candidate sample of strong lenses is shown in the left panel of Figure 2.4 while in the right panel of the same figure is the redshift distribution from the SPT survey (Strandet et al., 2016). The difference in the median redshift for samples selected at 500 μm and 1.4 mm is a selection effect (Béthermin et al., 2012).

In addition, we find that the median of the redshift distribution of lensed SMGs is slightly higher compared to the one derived from samples of unlensed SMGs (Chapman et al., 2005; Simpson et al., 2014). This is because the probability of having a lensing event increases with increasing redshift of the background source

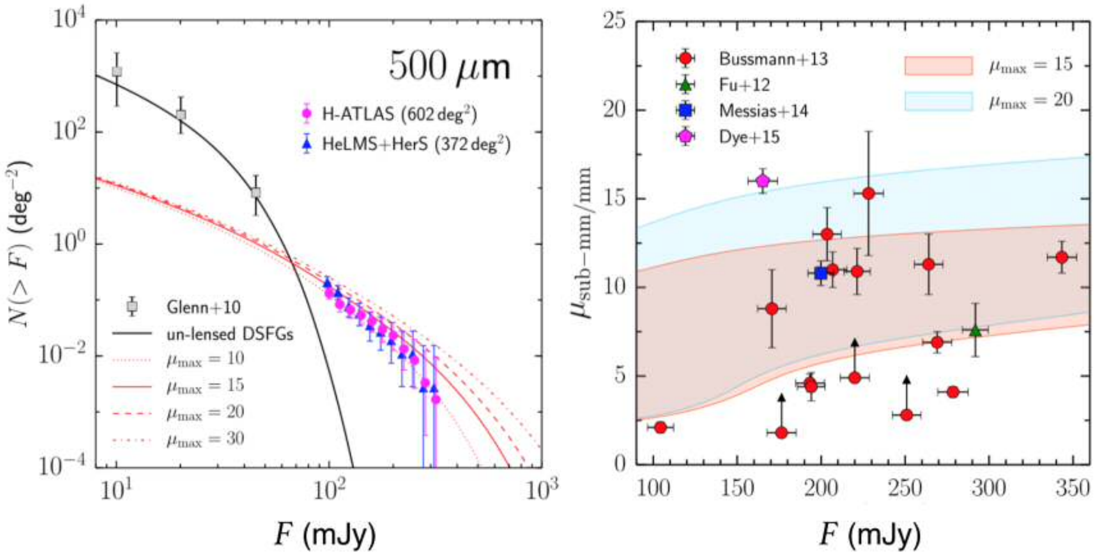

Figure 2.5: Figure are taken from Negrello et al. (2017). *(Left panel):* Observed (from *H*-ATLAS and HeLMES surveys; magenta and blue points) and modeled (red curves) number counts (i.e. number of sources above a certain flux-density, $N(>F)$, divided by the area of the survey, as a function of flux density) of candidate lensed SMGs (see main text for details on how the modelled number counts were estimated). The solid black curve is the prediction for the abundance of unlensed DSFGs at $z > 1.5$, based on the model of Cai et al. (2013). *(Right panel):* Magnification factors derived from modeling of the confirmed strong lenses in the *H*-ATLAS survey. The shaded regions show the 68 per cent confidence interval around the mean of the magnification distributions for $\mu_{max} = 15$ (red) and $\mu_{max} = 20$ (blue).

(Amvrosiadis et al., 2018).

2.4 Number counts of lensed galaxies

Galaxy number counts can be used as one of the most simplistic yet powerful tools to put to the test various galaxy evolution models. Number counts of lensed galaxies, however, fold in a few assumptions (e.g. their redshift distribution and their luminosity function, both of which are not well constrained) about the lensing population that can potentially complicate the comparison. The statistics of lensing at sub-millimeter wavelengths have been discussed extensively in the literature (Perrotta et al., 2002, 2003; Negrello et al., 2007, 2010, 2017; Lima et al., 2010a,b; Hezaveh and Holder, 2011; Lapi et al., 2012; Wardlow et al., 2013; Nayyeri et al., 2016).

The measured integral number counts (i.e. the number density of sources above a flux density as a function of flux density) are shown in the left panel of Figure 2.5.

The blue points correspond to the measured number counts from the H-ATLAS survey, while the purple points from the HeLMES survey. The two measurements agree very well within the measured errors (corresponding to the 95 per cent confidence interval, derived following the Gehrels (1986) prescriptions).

2.4.1 Modelling

Given the number density of unlensed SMGs per unit of logarithmic interval in flux density and redshift interval, $d^2N/d\ \log S\, dz_s$ (Lapi et al., 2012; Cai et al., 2013), the corresponding number counts of lensed SMGs are computed as (Lapi et al., 2012; Negrello et al., 2017)

$$\frac{dN}{d\log S} = \int dz_s \int_{\mu_{min}}^{\mu_{max}} d\mu \frac{dp}{d\mu}(\mu|z_s) \frac{d^2N}{d\ \log S\, dz_s} \tag{2.1}$$

where $dp/d\mu$ is the propability distribution of lensing magnifications which takes into account that higher redshift sources have a higher probability of being strongly lensed (Oguri et al., 2002; Kuhlen et al., 2004; Lapi et al., 2012; Amvrosiadis et al., 2018, see chapter 5 for more details).

In the above equation the integral over the magnifications refers to total magnifications, since the typical separation between multiple images (of the order of $\sim 1''$) are below the resolution capabilities of *Herschel*. We fix the $\mu_{min} = 2$, which according to a Singular Isothermal Ellipsoid (SIS) density profile, which is typical for galaxy scale lenses (see Amvrosiadis et al., 2018), is the minimum magnification in the strong lensing regime. In the left panel of Figure 2.5 we plot the model number counts for strongly lensed galaxies using different values for the maximum magnification, μ_{max}. This value mainly depends on the intrinsic angular size of the background source (Lapi et al., 2012; Hezaveh et al., 2012). We find that maximum magnifications between $\mu_{max} = 10 - 20$, result in predictions that are consistent with the data, within the errors. They are also broadly consistent with magnification factors that were derived from the modeling of high resolution sub-mm/mm imaging of confirmed strong lenses in the H-ATLAS survey, as shown in the right panel of Figure 2.5.

CHAPTER

3

HERSCHEL-ATLAS : THE SPATIAL CLUSTERING OF LOW AND HIGH REDSHIFT SUBMILLIMETRE GALAXIES

ABSTRACT

We present measurements of the angular correlation function of sub-millimeter (sub-mm) galaxies (SMGs) identified in four out of the five fields of the *H-ATLAS survey* – *GAMA-9h*, *GAMA-12h*, *GAMA-15h* and *NGP* – with flux densities $S_{250\mu m}$>30 mJy at 250 μm. We show that galaxies selected at this wavelength trace the underlying matter distribution differently at low and high redshifts. We study the evolution of the clustering finding that, at low redshift, sub-mm galaxies exhibit clustering strengths of $r_0 \sim 2-3\ h^{-1}$Mpc, below $z < 0.3$. At high redshifts, on the other hand, we find that sub-mm galaxies are more strongly clustered with correlation lengths $r_0 = 8.1 \pm 0.5$, 8.8 ± 0.8 and $13.9 \pm 3.9\ h^{-1}$Mpc at $z = 1-2$, $2-3$ and $3-5$, respectively. We show that sub-mm galaxies across the redshift range $1 < z < 5$, typically reside in dark-matter halos of mass of the order of $\sim 10^{12.5} - 10^{13.0} h^{-1} M_{\odot}$ and are consistent with being the progenitors of local massive elliptical galaxies that we see in the local Universe. The content of this Chapter was published in Amvrosiadis et al. (2019).

3.1 Introduction

The evolution of a galaxy population can be constrained from the measurement of its clustering strength, which provides information on the the masses of dark matter halos that these galaxies reside in. There have been numerous clustering studies of SMG's identified in the short (250-500 μm; Cooray et al., 2010; Maddox et al., 2010; Mitchell-Wynne et al., 2012; van Kampen et al., 2012) and long (850-1100 μm; Webb et al., 2003; Blain et al., 2004; Webb et al., 2003; Weiß et al., 2009; Williams et al., 2011; Hickox et al., 2012; Chen et al., 2016a,b; Wilkinson et al., 2017) submillimetre bands. Similar information can be extracted from the clustering of the unresolved FIR/sub-mm galaxies, through the measurement of the angular power spectrum of Cosmic Infrared Background (CIB) anisotropies (Viero et al., 2009; Amblard et al., 2011; Viero et al., 2013; Planck Collaboration et al., 2014) which is the cumulative infrared radiation caused by the reprocessing of stellar radiation by dust.

The most accurate determination of the clustering properties of SMGs up to date has been performed by Chen et al. (2016b). The authors used a sample of ~3000 SMGs with redshifts in the range $z \sim 1-5$, which were selected using a color selection technique (Chen et al., 2016a), Optical-Infrared Triple Color (OIRTC), to preferentially select faint SMGs ($S_{850} < 2\,\mathrm{mJy}$) in the K-band from the UKIRT Infrared Deep Sky Survey (UKIDSS; Lawrence et al., 2007) Ultra Deep Survey (UDS). In their study they concluded that SMGs, selected with the OIRTC technique, are strongly clustered residing in halos with typical halo masses of the order of $M_h \sim 10^{13} h^{-1} M_{\odot}$ across the probed redshift range. However, these sources were not individually detected in the sub-mm wavebands and the evidence that these galaxies are SMGs was based on observations with an ALMA training set (a subset of the objects predicted to be brighter sub-mm sources), which implied that the OIRTC method is 87% efficient.

More recently, Wilkinson et al. (2017) studied the clustering properties of SMG's which were identified using the 850-μm maps of the UDS field from the SCUBA-2 Cosmology Legacy Survey (S2CLS; Geach et al., 2013). The authors used a sample of 610 SMGs for which they found counterparts using a combination of radio imaging and the optical/infrared selection technique of Chen et al. (2016a). Using ALMA observations of the brightest sources, they estimate an 80% successful SMG counterpart identification. However, due to the sparse number density of SMGs the authors relied on a cross-correlation technique, with a more abundant K-band selected sample, to measure their clustering properties. Their analysis yield similar results to Chen et al. (2016b) for $z > 2$ SMGs, in terms of the halo masses that these galaxies reside in, but for SMGs found in the redshift range $1 < z < 2$ they reported a downsizing effect where the SMG activity is shifted to halos with typical halo masses of the order of $M_h \sim 10^{12} h^{-1} M_{\odot}$.

In addition, both Chen et al. (2016b) and Wilkinson et al. (2017) performed the clustering analysis for typical star-forming and passive galaxies, identified in the same field using their colors. This is important in order to place the clustering results of SMGs in the broader context of galaxy evolution. However, both these studies were unable to significantly differentiate SMG clustering properties from more typical star-forming galaxies identified in the same redshift range. In addition, Hickox et al. (2012) using a sample of 126 SMGs selected at 870μm from the *Large APEX Bolometer Camera (LABOCA)* sub-mm survey of the *Extended Chandra Deep Field-South (ECDFS)* concluded that the clustering properties of high redshift SMGs are consistent with measurements for optically-selected quasi-stellar objects

(QSOs). Their findings support evolutionary scenarios in which powerful starburst and QSOs occur in the same systems. In all these studies, high-redshift SMGs reside in dark-matter halos of the order of $\sim 10^{13} h^{-1} M_{\odot}$ and seem to be consistent with being the progenitors of massive elliptical galaxies that we see in the local universe.

In order to improve the already existing measurements of the angular clustering signal of SMG we need much larger survey areas to increase the number of detected sources and to obtain accurate redshift information. Concerning the first requirement, the *H-ATLAS* (which cover an area of more than ~600 deg^2) provides almost 3 orders of magnitude improvement in covered area compared to surveys conducted at 850μm (Chen et al., 2016a,b; Wilkinson et al., 2017). As for the latter requirement, the challenge is to identify optical/near-infrared (NIR) counterparts to the sub-mm sources in order to obtain relatively well-constrained photometric or spectroscopic redshifts. This is especially challenging due to the low angular resolution at sub-mm wavelengths, which results in large positional uncertainties for the sub-mm sources. We thoroughly discuss in Section 3.2 how we approach this issue.

Nevertheless, these aforementioned studies provide a unique contribution to the field, enabling for the first time the characterisation of the clustering properties of SMGs as a function of redshift and their role in galaxy evolution scenarios. However, they do not provide a complete picture as they fold in biases linked to the selection of SMGs at these particular wavelengths, rendering it essential to conduct similar studies at different sub-mm wavebands. In this Chapter we will study the clustering properties of SMG's identified at 250μm in the H-ATLAS survey, with flux densities $S_{250\mu m} > 30\,\mathrm{mJy}$. Throughout this Chapter, we assume a flat ΛCDM cosmological model with the best-fit parameters derived from the Planck Observatory (Planck Collaboration et al., 2016), which are $\Omega_m = 0.307$, $H_0 = 69.3$ km s^{-1} Mpc^{-1} and $\sigma_8 = 0.816$.

3.2 H-ATLAS Data

The H-ATLAS fields were selected to minimise bright continuum emission from dust in the Galaxy, as seen by the *Infrared Astronomical Satellite* (IRAS) at 100 μm. Complementary multi-wavelength data for these fields are provided by surveys spanning ultraviolet (UV) to mid-infrared (mid-IR) regimes. In particular for the GAMA fields – *GAMA-9h*, *GAMA-12h*, *GAMA-15h* – optical spectroscopic data are provided by the Galaxy and Mass Assembly survey (GAMA; Driver et al., 2009), the Sloan Digital Sky Survey (SDSS; Abazajian et al., 2009) and the 2-Degree-Field Galaxy Redshift Survey (2dFGRS; Colless et al., 2001), while optical photometric data are provided by the Galaxy Evolution Explorer (GALEX; Martin et al., 2005) and the Kilo-Degree Survey (KiDS; de Jong et al., 2015). Besides optical imaging and spectroscopy, imaging data at near-infrared (near-IR) wavelengths are available from the UKIRT Infrared Deep Sky Survey Large Area Survey (UKIDSS-LAS; Lawrence et al., 2007), the Wide-field Infrared Survey Explorer (WISE; Wright et al., 2010) and the VISTA Kilo-Degree Infrared Galaxy Survey (VIKING; Edge et al., 2013). In addition, radio-imaging data in the fields are provided by the Faint Images of the Radio Sky at Twenty-cm survey and the NRAO Very Large Array Sky Survey. The multi-wavelength coverage of the *NGP* and *SGP* fields is less extensive. The *NGP* field is covered in the optical by the SDSS and in near-IR by the UKIDSS-LAS while the *SGP* field is covered in the optical by KiDS and in the near-IR by VIKING.

The source catalogues of the H-ATLAS fields, which are presented in Valiante et al. (2016) and Maddox et al. (2018) for the GAMA and NGP/SGP fields respectively, are created in three stages. Firstly, the emission from dust in our Galaxy, which is contained in all *Herschel* images, needs to be removed before the source extraction process. The *Nebuliser*[1] algorithm was used in order to remove this emission from the SPIRE images in all the three wavebands (more details can be found in Valiante et al. (2016) for how the algorithm works). Secondly, the Multiband Algorithm for source Detection and eXtraction (MADX; Maddox et al., in prep.) was used to identify 2.5σ peaks in the 250 μm maps and to measure the flux densities at the position of those peaks in all the SPIRE bands. Before the source extraction, however, the maps were filtered with a matched-filter technique (Chapin et al., 2011) in order to reduce instrumental and confusion noise with respect to the raw maps (see Table 3 in Valiante et al. (2016)). Finally, only sources with a signal-to-noise ratio ≥ 4 in at least one of the three SPIRE bands were kept in the final catalogue. The 4σ detection limit at 250 μm for a point source ranges from 20mJy in the deepest regions of the maps (where tiles overlap) to 36mJy in the non-overlapping regions.

Having extracted our sub-mm sources from our *Herschel* maps, ideally we would like to find the counterparts of these sources in other wavelengths. Identifying counterparts to these sub-mm sources, however, is a challenging task. Using likelihood ratio techniques Bourne et al. (2016) identified SDSS optical counter-

---

[1] The *Nebuliser* algorithm was developed by the Cambridge Astronomical Survey Unit, which can be found at http://casu.ast.cam.ac.uk/surveys-projects/software-release/background-filtering

parts to the sub-mm sources in the *GAMA* fields, using sources with a magnitude in the r band of $r < 22.4$ and with a 4σ detection at $250\,\mu$m. The quantity R *(reliability)* corresponds to the probability that a potential counterpart is associated with a *Herschel* source. They find reliable counterparts ($R \geq 0.8$) for 44,835 sources (39 per cent). In addition, Dye et al. (2018) performed the same analysis for the *NGP* field and obtained optical counterparts for 42,429 sources (37.8 per cent). One potential caveat of this methodology however, is that it gives a artificially higher likelihood of association for high-z sub-mm sources that are gravitationally lensed by local galaxies or large-scale structure (Bourne et al., 2014). This is because for strong lensing to occur the foreground and the background sources need to be very well alligned and so the lens if is detected in the r band will be very close to the submm source in the 250 μm image and therefore be assigned a high R value.

Finally, we removed local extended sources from our final extracted source catalogue. These sources were selected from the *Herschel* catalogues for having a non-zero aperture radius in either of the three *SPIRE* wavebands. For these sources, custom apertures were generated whithin which the flux of these source was measured (see Valiante et al. (2016) for the *GAMA* fields and Maddox et al. (2018) for the *NGP* and *SGP* fields). The number of local extended sources are 231, 226, 284, 889 and1452 in the *GAMA-9h*, *GAMA-12h*, *GAMA-15h*, *NGP* and *SGP* fields, respectively.

3.2.1 Redshift distribution of sub-mm sources

The redshift distribution of our sources is an essential ingredient in our clustering analysis. It is used to project the angular correlation function, $w(\theta)$, in order to recover the spatial correlation function, $\xi(r)$, from which the clustering properties of our galaxy population are determined.

The standard approach used to estimate photometric redshifts, when only IR to sub-mm photometric data are available (in this case the SPIRE *250, 350 & 500 μm* flux densities), is to fit a *calibrated* SED template (i.e. whose parameters have been determined from fitting to sources with spectroscopic redshifts) to each source in our sample. This approach has been adopted in many previous studies (Pearson et al., 2013; Ivison et al., 2016; Bakx et al., 2018).

We adopt as our SED template a modified blackbody spectral energy distribution, consisting of two dust components with different temperatures, which is given by Eq 1.1. In that expression, the flux density, S_v is given in terms of the rest-frame wavelength, which is related to the observed wavelength from the

Table 3.1: Herschel-ATLAS sources with measured spectroscopic redshift from CO observations.

H-ATLAS ID	z_{spec}	z_{phot}	Ref.
J134429.5+303034	2.30	2.31	H12
J114637.9−001132	3.26	2.81	H12
J132630.1+334408	2.95	3.89	H-p
J083051.0+013225	3.63	3.19	R-p
J125632.5+233627	3.57	3.56	R-p
J132427.0+284450	1.68	2.32	G13
J132859.2+292327	2.78	2.81	K-p
J084933.4+021442	2.41	2.91	L-p
J125135.3+261458	3.68	3.63	K-p
J113526.2−014606	3.13	2.28	H12
J133008.6+245900	3.11	2.36	R-p
J142413.9+022303	4.28	4.24	C11
J141351.9−000026	2.48	285	H12
J090311.6+003907	3.04	3.54	F11
J132504.4+311534	1.84	2.12	R-p
J133846.5+255055	2.34	2.69	R-p
J132301.7+341649	2.19	2.58	R-p
J091840.8+023048	2.58	3.06	H12
J133543.0+300402	2.68	2.76	H-p
J091304.9−005344	2.63	2.73	N10
J115820.1−013752	2.19	3.21	H-p
J113243.0−005108	2.58	3.92	R-p
J142935.3−002836	1.03	0.56	P13
J090740.0−004200	1.58	1.05	L12
J085358.9+015537	2.09	1.84	P13
J090302.9-014127	2.31	1.97	L12

Notes: The last column corresponds to references for the CO spectroscopic redshifts: N10 = Negrello et al. (2010), C11 = Cox et al. (2011), F11 = Frayer et al. (2011), H12 = Harris et al. (2012), L12 = Lupu et al. (2012), B13 = Bussmann et al. (2013), G13 = George et al. (2013), P13 = Pearson et al. (2013), H-p = Harris et al. (prep), R-p = Riechers et al. (prep), K-p = Krips et al. (prep), L-p = Lupu et al. (prep).

following relation,

$$\nu_{rest} = \nu_{obs}(1+z).$$

Fixing the parameters of the SED template to the values determined by Pearson et al. (2013), which are $T_h = 46.9$, $T_c = 23.9$, $\alpha = 30.1$ and $\beta = 2$, we can then fit our template to our data (only the SPIRE flux densities) allowing only the redshift and the normalisation factor, A_{off} to vary. In this way we can estimate the photometric redshifts for our sources.

We evaluate the accuracy of our sub-mm photometric redshift estimates using the sources presented in Table 3.1 for which we have spectroscopic redshifts. In Figure 3.1 we show $(z_{spec} - z_{phot})/(1 + z_{spec})$ vs z_{spec}, finding that the template performs reasonably well and does not introduce any systematic offset. Fitting a Gaussian distribution to the histogram of $\Delta z/(1+z)$, shown in the lower right corner of Figure 3.1, we find a mean of -0.03 with a standard deviation of $\sigma_{\Delta z/(1+z)} = 0.157$ and no outliers. Similar conclusions were drown by Ivison et al. (2016), where the authors used different templates to evaluate their performance. In the top panel of Figure 3.1 we see that higher redshift sub-mm sources have preferentially redder colors as expected, where the points are color-coded based on the flux density ratio S_{500}/S_{250} at 500 and 250 μm, respectively.

Finally, in order to construct the redshift distributions we adopted the following procedure (i) if R < 0.8 we used the sub-mm photometric redshifts that were determined from our SED fitting methodology. (ii) if R ≥ 0.8 we further applied an additional cut in redshift quality parameter Q[2] (see Driver et al., 2011, for a detailed definition of the redshift quality parameter Q). If Q ≥ 3 we used the optical spectroscopic redshift, otherwise we used the optical photometric redshift. In some few cases where R ≥ 0.8 but none of the above information was available we used sub-mm photometric redshifts. We need to note here that this selection only concerns the clustering analysis of our low redshift sample since the completeness of our counterpart identification method drops significantly above $z > 0.3$ to the point where our high redshift sample ($z > 1$) is completely dominated by sub-mm sources with no counterparts.

Figure 3.2 shows the redshift distribution of our sub-mm sources for all H-ATLAS fields, following the procedure outlined above. The inset plot in each panel shows a zoom into the low redshift range of the redshift distribution of our sub-mm sources with identified counterparts. The grey histogram corresponds to sources with either an optical photometric or spectroscopic redshift while the black histogram corresponds to sources with only optical spectroscopic redshift of

---

[2] The parameter, Q is a measure of the redshift's reliability.

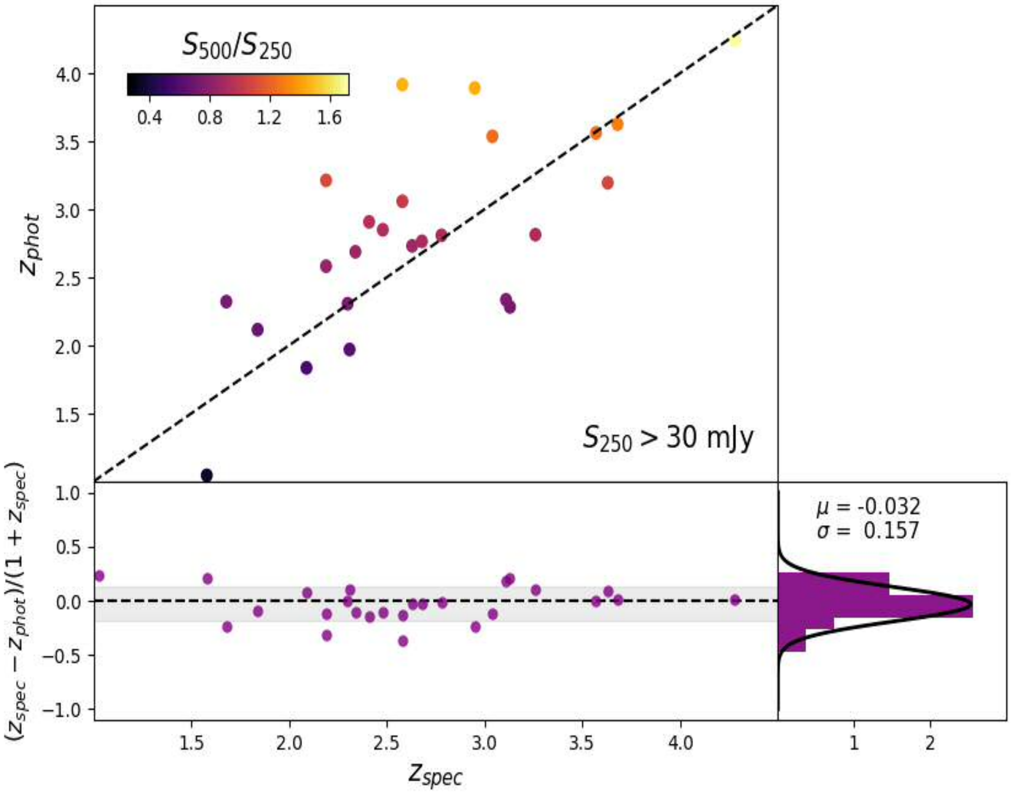

Figure 3.1: Scatter plot of $(z_{spec} - z_{phot})/(1 + z_{spec})$ against the spectroscopic redshift, z_{spec}, for sources with CO spectroscopic redshifts in the redshift range, $1 < z < 5$, which are listed in Table 3.1. For this comparison we exclude identified QSOs, as it has been shown that the photometric redshift estimation methodology is only reliable for starburst galaxies (Pearson et al., 2013). In the lower right corner we show the histogram of $\Delta z/(1+z)$ values, as well as the mean and standard deviation from fitting a Gaussian distribution (black curve) to this histogram. Finally, in the upper panel we show a scatter plot of z_{spec} vs z_{phot}, where the points are color-coded based on the flux density ratio S_{500}/S_{250} at 500 and 250 μm, respectively. The black dashed line shows the 1:1 relation.

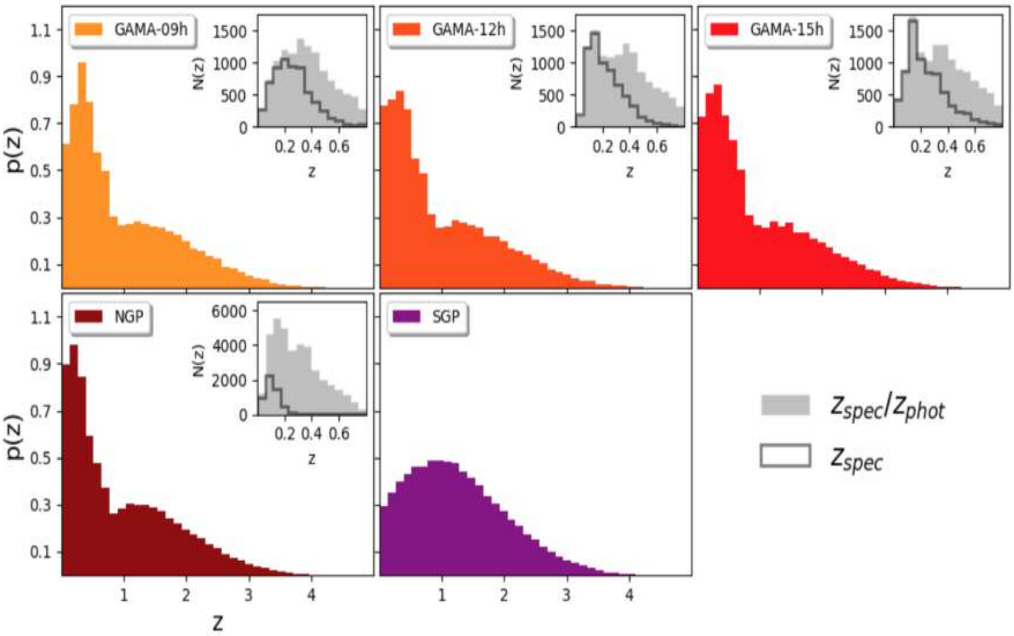

Figure 3.2: The redshift distribution of sub-mm sources detected in the five fields of the *H-ATLAS* survey: *GAMA-09h* (top-left), *GAMA-12h* (top-middle), *GAMA-15h* (top-right), *NGP* (bottom-left) and *SGP* (bottom-middle). The histograms are normalised so that the area is equal to unity. The inset plot in each panel shows a zoom into the low redshift range of the redshift distribution of our sub-mm sources with identified counterparts. The grey histogram corresponds to sources with either an optical photometric or spectroscopic redshift (see the main text for more details) while the black histogram corresponds to sources with only optical spectroscopic redshift of quality $Q \geq 3$. For the case of the *SGP* field, no counterpart identification analysis has been performed as yet and so the distribution shown in this figure is produced using only the submm photometric redshifts for all sources (which for low-z sources are strongly biased).

quality $Q \geq 3$. The counterpart identification analysis has not been performed as yet for the SGP field and so in this case we only show the redshift distribution of sub-mm photometric redshifts. One thing to note here is the lack of spectroscopic redshifts in the *NGP* field compared to the *GAMA* fields, which are complemented by the GAMA survey (Driver et al., 2009).

We can clearly see that our sample of 250μm selected sub-mm galaxies contains different galaxy populations at low and high redshifts (see Pearson et al. (2013) where the authors performed simulations to show that these are in fact two different galaxy populations rather than being a bias of the sub-mm photometric redshift estimation methodology). On the one hand, the low redshift peak around z ~ 0.2 - 0.3 is mostly associated with typical star-forming galaxies (see Bourne et al.

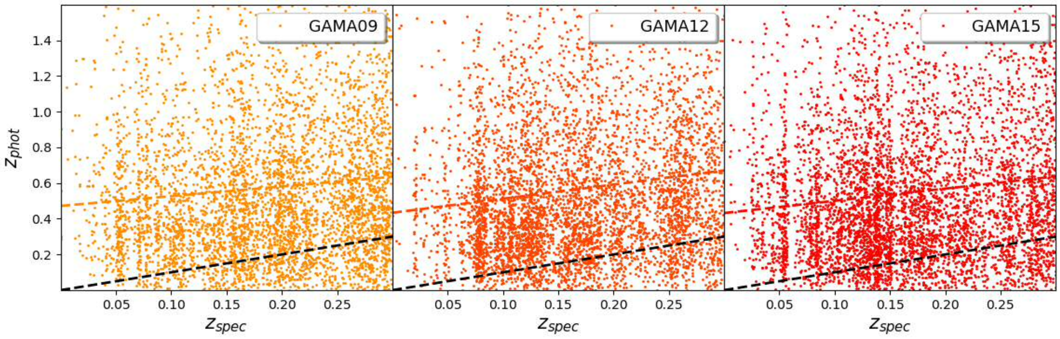

Figure 3.3: Comparison of spectroscopic, z_{spec}, and photometric, z_{phot}, redshifts in the redshift range $z < 0.3$, for submillimeter sources with identified counterparts. The black dashed lines show the 1:1 relation, while the colored dashed lines show the best-fit line that goes through the data points.

(2016) for more details on the multi-wavalength properties of H-ATLAS galaxies with identified counterpart), while 15-30% would be classified as passive galaxies based on their optical colors (Eales et al., 2018). On the other hand, the broader part of the distribution in the redshift range $z > 1$ is associated with sub-mm galaxies (Chapman et al., 2005).

3.2.2 Efftects of sub-mm photometric redshifts

One caveat of using a FIR/sub-mm SED template fitting approach to estimate photometric redshifts for our sub-mm sources, is that the redshifts of low-redshift sources are significantly overestimated. As mentioned in the previous section, our sample is comprised of different galaxy populations at low and high redshifts which have different physical conditions (e.g. temperature). As a result the same SED template can not simultaneously fit the fluxes of sources at these different redshift regimes. This is clearly demonstrated in Figure 3.3, where we show the comparison of z_{spec} vs z_{phot} for sources in the three GAMA fields in the redshift range $z < 0.3$, with optically identified counterparts. This comparison highlights the importance of identifying the optical counterparts of low-redshift sub-mm galaxies, when one wishes to measure the clustering properties of high-redshift ($z > 1$) sub-mm galaxies. This is the main reason why we choose not to include the SGP field in the analysis that follows.

In addition, the errors of our sub-mm photometric redshifts, z_{phot}, which are derived from the SED fitting methodology, are in most cases quite large. This means that when a tomographic analysis of the clustering is performed, a single source can be found in more than one redshift bin. If this effect is not accounted for properly, it can lead to severe biases. Cowley et al. (2017) demonstrated that seemingly similar correlation functions (from observations and simulations of SMGs) result in significantly different clustering properties due to the incorrect normalisation of the correlation function of the underlying dark-matter distribution that these galaxies are tracing (the normalization depends of the redshift distribution, e.g. a broader redshift distribution will result in a larger normalisation than a narrow one).

In order to account for the effect of random errors in photometric redshift estimates on dN/dz, following the analysis by Budavári et al. (2003), we estimate the redshift distribution $p(z|W)$ of galaxies selected by our window function $W(z_{ph})$, as

$$p(z|W) = p(z) \int dz_{ph} W(z_{ph}) p(z_{ph}|z) \tag{3.1}$$

where $p(z)$ is the initial redshift distribution (the one shown in Figure 3.2), $W(z_{ph})$ is a top-hat window function where $W = 1$ for z_{ph} in the selected redshift interval $z_{min} < z < z_{max}$ and $W = 0$ otherwise, and $p(z_{ph}|z)$ is the probability that a source with true redshift z has a photometric redshift z_{ph}. The function $p(z_{ph}|z)$ is parametrised as a Gaussian distribution with a zero mean and variance $(1+z)\sigma_{\Delta z/(1+z)}$,

$$p(z_{ph}|z) = \frac{1}{\sqrt{2\pi(1+z)^2\sigma^2_{\Delta z/(1+z)}}} \exp\left\{ -\frac{\left(z - z_{ph}\right)^2}{2(1+z)^2\sigma^2_{\Delta z/(1+z)}} \right\} \tag{3.2}$$

where the dispersion is taken to be $\sigma_{\Delta z/(1+z)} = 0.15$ as determined from the comparison our sub-mm photometric redshifts and a sample of 26 sources with reliable CO spectroscopic redshifts.

This correction is only relevant for the clustering analysis of our high redshift sample ($z > 1$) and will be used in Section 3.4.2 and on-words. This is because our high-redshift sample is completely dominated by sources with only sub-mm photometric redshift information. Therefore, in this case, the initial redshift distribution, $p(z)$, is estimated by excluding sources with identified counterparts (i.e. those with reliability $R \geq 0.8$).

3.3 Clustering Analysis

In this section we describe the methodology we followed in order to measure the angular clustering signal.

3.3.1 The Angular two-point correlation function

The angular two-point auto-correlation function (ACF), $w(\theta)$, is a measure of the excess probability, compared with a random distribution, of finding a galaxy at an angular separation θ from another, $P(\theta) = N[1 + w(\theta)]$, where N is the surface density of galaxies. To calculate the angular two-point autocorrelation function we use the Landy and Szalay (1993) estimator,

$$w(\theta) = \frac{DD(\theta) - 2DR(\theta) + RR(\theta)}{RR(\theta)}, \tag{3.3}$$

where $DD(\theta)$ is the number of data-data pairs, $DR(\theta)$ is the number of data-random pairs and $RR(\theta)$ is the number of random-random pairs, each at separation θ. By construction, the $DR(\theta)$ and $RR(\theta)$ are normalised to have the same number of total pairs as $DD(\theta)$, so that given N_D sample sources and N_R random points then $DR(\theta) = [(N_D - 1)/2N_R]N_{DR}(\theta)$ and $RR(\theta) = [N_D(N_D - 1)/N_R(N_R - 1)]N_{RR}(\theta)$, where $N_{DR}(\theta)$ and $N_{RR}(\theta)$ are the original counts.

The error on $w(\theta)$ at each angular separation, which is associated with the Landy and Szalay (1993) estimator, is defined as

$$\sigma_w^2 = \frac{(1+w)^2}{DD}. \tag{3.4}$$

However, these errors are considerably underestimated as the variance only accounts for the shot noise from the sample of the random points (which is folded in the measurement of w) and the Poisson uncertainties of the DD counts. For a more accurate representation of the errors we consider a 'delete one jackknife' resampling method (Norberg et al., 2009), which also account for systematic uncertainties due to the field-to-field variations.

In order to implement this approach the area of each field was divided into N_{sub} circular sub-regions (as seen in Figure 3.4), each with a radius of ~120 arcmin. Similarly to González-Nuevo et al. (2017) we allowed for a 30% overlap between sub-regions and about less than 10% of each sub-region did not contain any sources (essentially falling outside of the image). These constraints were introduced in order to maximise the usable area and resulted in 4 independent sub-regions in each of the GAMA fields and 15 for the NGP field (as shown in Figure 3.4).

Each jackknife sample is defined by discarding, in turn, each of the N_{sub} subregions into which each field has been split. The covariance matrix for the N_{sub} jackknife resamplings is then estimated using,

$$C_{i,j} = \frac{N_{sub}-1}{N_{sub}} \sum_{k=1}^{N_{sub}} \left(w(\theta_i)^k - \bar{w}(\theta_i) \right) \left(w(\theta_j)^k - \bar{w}(\theta_j) \right), \tag{3.5}$$

where $w(\theta_{i,j})^k$ are the auto-correlation functions measured in each jackknife realisation and $\bar{w}(\theta_{i,j})$ is the average auto-correlation function from all jackknife realisations.

We also corrected the measured correlation function for the integral constraint (IC; Roche and Eales, 1999). Assuming that the true correlation function $w(\theta)$ can be described as a power-law model, $w_{model}(\theta) = A\theta^{-\gamma}$, the observed one will be given by

$$w(\theta) = w_{model}(\theta) - IC, \tag{3.6}$$

where the IC can be numerically evaluated (Adelberger et al., 2005) using the RR counts from,

$$IC = \frac{\sum_i RR(\theta_i) w_{model}(\theta_i)}{\sum_i RR(\theta_i)}. \tag{3.7}$$

The best-fit values for the power-law model, w_{model}, from which the IC correction was evaluated, were determined by restricting the angular distance range to $\theta > 4\,\mathrm{arcmin}$.

3.3.2 Construction of the random catalogues

In this section we describe the methodology we use to construct our random catalogues, which are used to compute the RR and DR pairs of Eq. 3.3. We mentioned is Section 3.2 that local extended sources were removed from our *Herschel* catalogues, prior to calculating $w(\theta)$. Consequently, we need to account for the removal of these sources when constructing our random catalogues. This is accomplished by masking out the regions covered by extended source in order to avoid placing random sources in those regions. The masked regions were elliptical in the case where a custom aperture was created (using the minor semi-axis as well as the position angle; see section 5.2 in Valiante et al. (2016) for details), otherwise they

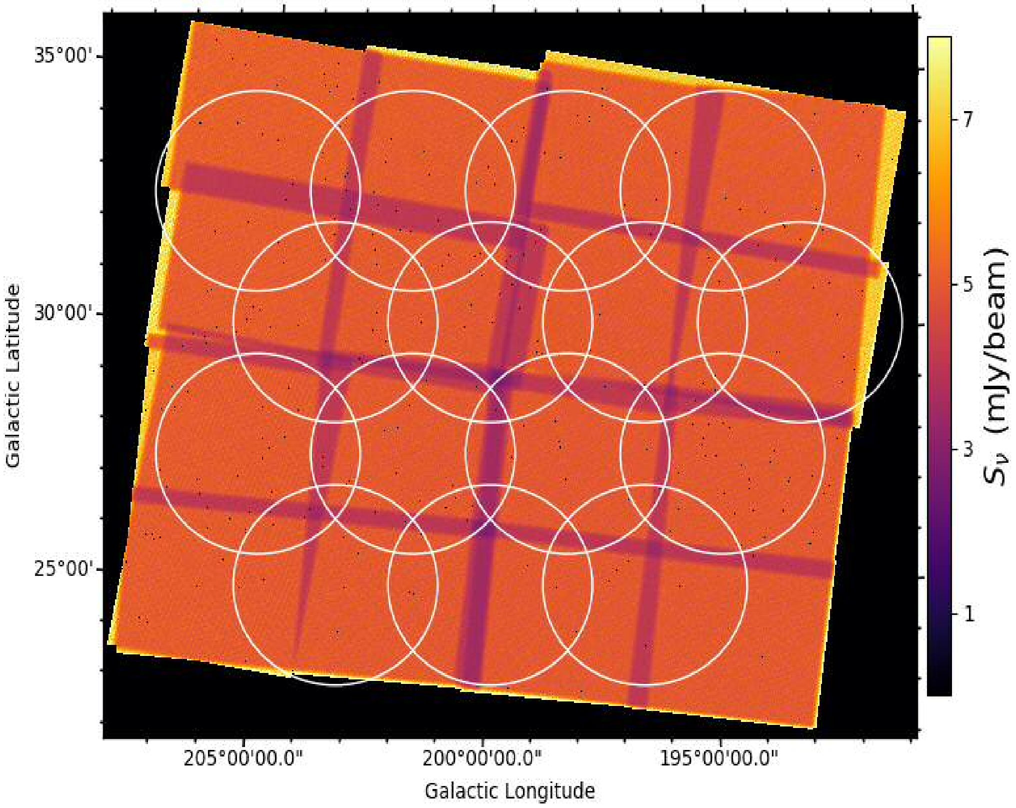

Figure 3.4: The filtered variance map of the *NGP* field. The circular areas correspond to the 15 individual sub-regions that the field is divided, in order to perform the "delete one jackknife" resampling method. The black holes in the map indicate the regions covered by extended sources that were masked out.

were circular (see Figure 3.4).

The random catalogues were then created by drawing 10 times more points, than in our real catalogue of sources, from a uniform distribution.

In practise, however, our noise maps are not completely uniform (as seen in Figure 3.4), due to overlapping scanned regions. It is important that these non-uniformities not be imprinted on the measured clustering signal. We consider a similar approach to that adopted by Maddox et al. (2010), where we incorporated the noise (instrumental + confusion) information, while making sure we conserve the number counts of our real catalogues. This was achieved as follows: (a) a flux was chosen randomly using the cumulative probability distribution of fluxes of our real sources, (b) a random position was generated on the image, (c) the local noise was estimated as the quadratic sum of the instrumental noise in that pixel and the confusion noise (see Table 3; Valiante et al., 2016, for the GAMA fields), (d) we kept the source if its flux, perturbed by a Gaussian deviate equal to the total local noise estimate, was greater than 4σ otherwise the process was repeated starting from (a). The measurement of the angular correlation function using random catalogues generated this way, however, shows no significant difference compared to the simple uniform random catalogues. This is due to the fact that we apply a cut in flux-density at 250μm, which ensures that the fluxes of these sources are not significantly boosted.

3.3.3 The real-space correlation length

The simplest way to interpret the clustering strength of a galaxy population is to estimate its correlation length, r_0. We will determine this value for our SMG population at different redshift slices. We assume that the spatial correlation function, $\xi(r)$, is described by a power-law,

$$\xi(r) = \left(\frac{r}{r_0}\right)^{-\gamma} \tag{3.8}$$

where r is the comoving distance between two points, r_0 is the correlation length and γ is the power-law index.

The angular correlation function, parametrised as power-law model, $w(\theta) = A_w\theta^{-\delta}$ (where A_w is the amplitude and δ is the slope of the power-law model), can be deprojected using the Limber approximation (Limber, 1954) to yield a measurement on the correlation length over different redshift bins. This conversion is performed as follows,

$$r_0^{\gamma}(z) = A_w \left\{ \frac{H_0 H_\gamma}{c} \frac{\int_{z_i}^{z_j} N^2(z)(1+z)^{\gamma-(3+\epsilon)}\chi^{1-\gamma}(z)E(z)dz}{\left(\int_{z_i}^{z_j} N(z)dz\right)^2} \right\}^{-1}, \tag{3.9}$$

where the value $\epsilon = \gamma - 3$ is assumed, which corresponds to a constant clustering in comoving coordinates. In addition,

$$H_\gamma = \Gamma\left(\frac{1}{2}\right)\Gamma\left(\frac{\gamma-1}{2}\right)/\Gamma\left(\frac{\gamma}{2}\right) \tag{3.10}$$

with $\Gamma(x)$ being the gamma function and $\chi(z)$ is the radial comoving distance which can be computed from,

$$\chi(z) = \frac{c}{H_0}\int_0^z \frac{dz'}{E(z')}. \tag{3.11}$$

where H_0 is the Hubble constant and $E^2(z) = \Omega_{m,0}(1+z)^3 + \Omega_{\Lambda,0}(1+z)^{3(1+w)}$, where $\Omega_{m,0}$ and $\Omega_{\Lambda,0}$ are the present-day matter and dark energy density parameters of the ΛCDM cosmological model and w is the equation of state parameter of the dark energy (not to be confused with $w(\theta)$ that refers to the angular correlation function. Finally, $N(z)$ is the number of sources per unit of redshift interval within a solid angle. The redshift distributions are determined differently for the analysis of our low- and high-redshift samples. For our high-redshift sample we follow the methodology outlined in section 3.2.2, while for the low-redshift sample we simply used the optical photometric redshift distributions trimming off the distribution at the limits of each redshift bin.

3.4 Results

In this section we present our results of the angular auto-correlation function, $w(\theta)$, for source samples selected with at least a 4σ detection at 250-μm (~30 mJy). This selection criteria ensures that there are no significant photometry issues with the sources used in our analysis.The measurements were performed for evenly spaced logarithmic bins of angular separation in the range $0.5' < \theta < 50'$, where the lower limit comes from the FWHM of the SPIRE instrument's PSF at 250μm ($0.3'$; Griffin et al., 2010).In addition, as discussed in Section 3.2, our sample of sources is comprised of different galaxy populations at low and high redshifts. Therefore, we will examine these two cases individually in the sections that follow.

3.4.1 Evolution of Clustering with redshift for $z < 0.3$ SMGs

The clustering evolution of sub-mm sources selected at 250μm, in the low redshift regime ($z < 0.3$), has previously been studied by van Kampen et al. (2012). In their study, the authors used a sample of sources selected from the H-ATLAS Science Demonstration Phase (SDP) field at a 5σ significance level accounting for both instrumental and confusion noise. This resulted in a flux-density cut of $S > 33$ mJy/beam at $250\mu m$. Additional selection criteria that were introduced in their study, specifically concerning the reliability of counterpart identification and the quality of optical spectroscopic redshifts, were identical to the ones introduced here.

Table 3.2: Results of Clustering Analysis for $z < 0.3$ SMGs

	$0.05 < z < 0.10$	$0.10 < z < 0.15$	$0.15 < z < 0.20$	$0.20 < z < 0.25$	$0.25 < z < 0.30$
N_{gal}	6225	8284	8385	7914	6744
A_w	$1.44^{+0.67}_{-0.50}$	$1.45^{+0.37}_{-0.30}$	$1.34^{+0.41}_{-0.36}$	$0.74^{+0.48}_{-0.32}$	$0.88^{+1.25}_{-0.57}$
δ	$0.83^{+0.14}_{-0.14}$	$0.77^{+0.08}_{-0.08}$	$0.85^{+0.09}_{-0.10}$	$0.75^{+0.18}_{-0.19}$	$1.24^{+0.43}_{-0.40}$
$r_0(h^{-1}Mpc)$	2.4 ± 0.1	3.3 ± 0.1	3.2 ± 0.2	2.7 ± 0.3	2.0 ± 0.5

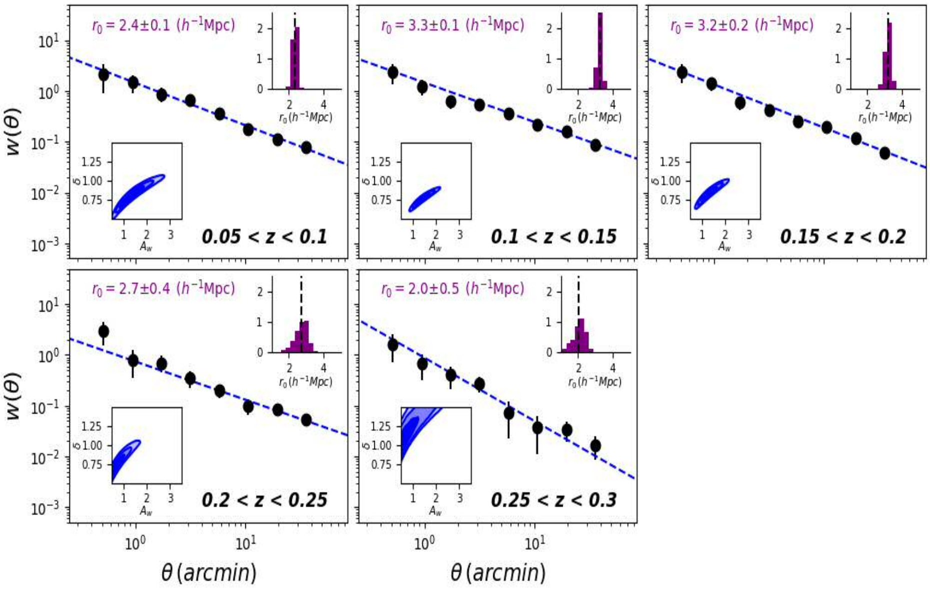

Figure 3.5: The angular correlation function of sub-mm galaxies for each redshift slice in the redshift range $z < 0.3$. The dashed lines show the best-fit two-parameter model, $w(\theta) = A_w\theta^{-\delta}$, where the best-fit values can be found in Table 3.2. The inset plot in the lower left corner in each panel corresponds to the 1, 1.5 and 2σ contours in the fitted (A_w, δ) parameter space. The inset plot in each panel shown the histogram of correlation length values which were derived from our bootstrap method. The black dashed vertical line in the inset plot of each panel, indicates the mean of the distribution which is also shown in the upper left corner in each panel.

In this section we repeat the analysis of van Kampen et al. (2012) for a sample of sources selected at $250\mu m$, from the *GAMA+NGP* fields of the H-ATLAS survey. The SGP field was not used in this analysis since the optical counterpart identification analysis has not been performed as yet for this field. Similarly to van Kampen et al. (2012) we start our analysis at redshift $z \sim 0.05$ where the redshift distribution starts to pick up (see Figure 3.2) and end at $z \sim 0.3$ where the completeness starts to drop sharply (see Bourne et al., 2016). We use a redshift bin width size of $\Delta z{\sim}0.05$, which results in five individual redshift bins.

Our clustering measurements are shown in Figure 3.5, where each panel corresponds to a different redshift bin indicated at the bottom right corner. The redshift distribution of sources for which this measurement corresponds, are shown as the grey histograms in each panel of Figure 3.2. One thing to note is that the clustering signal in the *NGP* field is slightly weaker compared to the *GAMA* fields, which is probably due to the lack of spectroscopic redshifts coverage.

In order to model the clustering signal we used a two-parameter power-law model, $w(\theta) = A_w \theta^{-\delta}$, and performed an MCMC fitting method using the *emcee* package (Foreman-Mackey et al., 2013). The 1, 1.5 and 2σ contours of the fitted (A_w, δ) parameter space are shown in the bottom left inset plot in each panel of Figure 3.5. The resulting best-fit values for the parameters of our model in each redshift bin are presented in Table 3.2. These correspond to predictions that are shown as blue dashed lines in each panel of Figure 3.5. The power-law slopes in all redshift bins are broadly consistent with that of normal star-forming galaxies, $\delta \sim 0.8$ (Zehavi et al., 2011). Although 20-30% of H-ATLAS galaxies have the red optical colours typical of traditional passive galaxies, Eales et al. (2018) show that these are still star-forming galaxies, although with a significant old stellar population. Therefore, it is not surprising that we find a clustering signal typical of star-forming galaxies.

The clustering length, r_0, in each redshift slice was calculated following a bootstrap method. We performed $N \sim 1000$ realisation where in each one we randomly drew, without replacement, a parameter value pair (A_w, δ) from the output MCMC chain of our fitting method. In this way we also account for the degeneracies in the parameters of our model. The resulting normalised histograms of r_0 values from our bootstrap method are shown in the upper right corner inset plot of each panel in Figure 3.5. The black vertical dashed line indicates the mean of the distribution, which was derived by fitting a Gaussian distribution to the histogram. This value corresponds to our measurement of the clustering length, r_0 which is shown in the upper left corner of each panel, where the 1σ uncertainty is taken as the standard deviation of the fitted Gaussian distribution. Our results are shown in the last column of Table 3.2 and seem to agree fairly well with van Kampen et al. (2012) measurements, even thought their uncertainties were considerable.

We need to note here that we find a significant difference in the measurement of the correlation length, r_0, in the redshift bin $0.15 < z < 0.2$ compared to van Kampen et al. (2012). The authors report in their study the existence of a structure around $z \sim 0.164$, which might be responsible for the excess clustering strength. Due to the small area used in their analysis, this structure dominates the clustering signal in this redshift bin. However, we are using a much larger area in our study and this signal gets diluted, which is what probably causes this difference in the measurement of the clustering length.

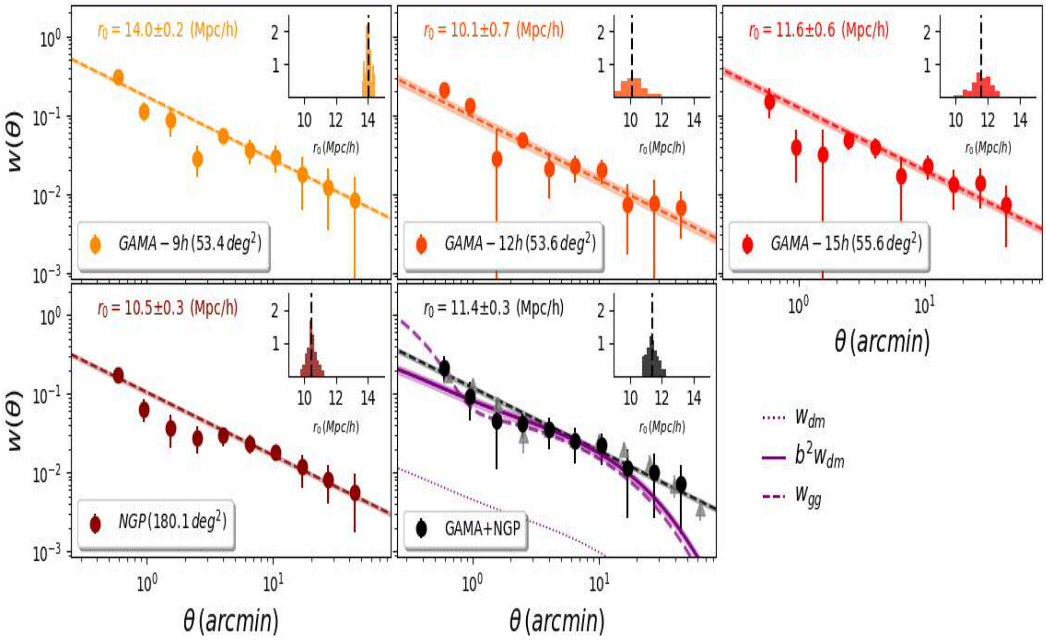

Figure 3.6: The angular correlation function of sub-mm sources identified in the four *H-ATLAS* fields: *GAMA-9h* (top-left), *GAMA-12h* (top-middle), *GAMA-15h* (top-right) and *NGP* (bottom-left). The error bars are derived using a 'delete one jackknife' resampling method . The bottom-middle panel shows the measured angular correlation function of the combined GAMA+NGP fields. The measurements were corrected by a factor of 1.25, as determined from our simulations in Appendix A, for the effect of filtering with a matched-filter.The dashed line show the best-fit one parameter power-law model with fixed slope, $w(\theta) = A\theta^{-0.8}$, where the 1σ uncertainty is shown as the shaded region. The inset plot in each panel shown the histogram of correlation length values which were derived from our bootstrap method. The black dashed vertical line in the inset plot of each panel, indicates the mean of the distribution which is also shown in the upper left corner in each panel. The purple dotted curve shows the dark matter angular correlation function, w_{dm}. This has been scaled by the best-fit value of the linear bias factor, b, which is shown as the solid purple curve, with the 1σ uncertainty shown as the shaded region. Finally, we show as the purple dashed curve the galaxy-galaxy angular correlation function, w_{gg}, that corresponds to the best-fit HOD model. In addition, we show the results from González-Nuevo et al. (2017) as grey triangles.

3.4.2 Clustering of $z > 1$ SMGs

Previous studies on the clustering of SMGs have focused on the broad redshift range $1 < z < 5$ (e.g. Webb et al., 2003; Blain et al., 2004; Webb et al., 2003; Weiß et al., 2009; Cooray et al., 2010; Maddox et al., 2010; Williams et al., 2011; Hickox et al., 2012; Mitchell-Wynne et al., 2012; Chen et al., 2016a,b; Wilkinson et al., 2017). As seen from the redshift distributions in Figure 3.2, the majority of our sources lie in that redshift range with the peak of the redshift distribution occurring around $z \sim 1.25$ (excluding the optically identified counterparts which typically reside at $z < 0.5$). Therefore, in order to make a direct comparison with previous clustering measurements, we first perform our clustering analysis for sources within this redshift range.

The measured angular correlation functions of sub-mm sources, for each of the *H-ATLAS* fields under investigation, are shown in Figure 3.6: top panels for the three equatorial GAMA fields and bottom-left for the *NGP* field. Our measurements were corrected by a factor of 1.25, as determined from our simulations in Appendix A, for the effect of filtering with a matched-filter to remove the background cirrus emission. The error bars were determined as $\sigma_i \sim \sqrt{C_{ii}}$, where C_{ii} is given by Eq. 3.5.

In the bottom-middle panel of the same figure we show the measured angular correlation function by combining the three equatorial GAMA fields with the *NGP* field. In the same panel, we overlay the measurement from González-Nuevo et al. (2017) which was obtained using 250μm-selected sources in the redshift range $z > 1.2$ from the GAMA fields as well as a small part of the *SGP* field. In this study the authors used sources selected with at least a 4σ detection at $250\mu m$, which results in a $S > 29\,$mJy cut in flux density, and a 3σ detection at $350\mu m$ in order to preferentially select high redshift sources. The two measurements seem to agree fairly well across all angular scales. We can also compare our results with Cooray et al. (2010), who used the two widest fields from the Herschel Multi-tiered Extragalactic Survey (HerMES; Oliver et al., 2010), Lockman-SWIRE and Spitzer First Look Survey (FLS). For this comparison there seems to be a large disagreement, with the authors of this paper reporting a stronger clustering signal across all angular scales. This disagreement, which was first realised by comparing the results from Maddox et al. (2010), is alarming and it is not fully understood. We will discuss this further in Appendix A.3, where we suggest that the removal of the background cirrus emission being one possibility for this difference.

As a first step towards modelling the clustering signal, we use a one-parameter power-law model, $w(\theta) = A_w \theta^{-0.8}$, with a fixed slope. We perform the fitting for each individual field, as well as for the combined *GAMA+NGP*. The resulting best-fit values for the parameter of our model are summarised in Table 3.3. These correspond to the dashed colored lines in each panel of Figure 3.6, where the 1σ uncertainty is shown as the shaded region.

The correlation length, r_0, was calculated following a bootstrap method in order to consider the uncertainty in the best-fit value of the power-law model. In each realisation we randomly sample the parameter A_w from a Gaussian distribution, centred at the best-fit value with a standard deviation equal to it's error, and use Equation 3.9 to calculate the correlation length. The resulting normalised histograms of r_0 values, from our bootstrap method, are shown in the upper right corner of each panel in Figure 3.6. The black vertical dashed line indicates the mean of the distribution, which was derived by fitting a Gaussian distribution to the histogram. This value corresponds to our measurement of the clustering length, r_0 which is shown in the upper left corner of each panel, where the 1σ uncertainty is taken as the standard deviation of the fitted Gaussian distribution. The results are summarized in Table 3.3. We need to note here that the redshift distribution that enters the calculation of the correlation length, r_0, has been corrected for the effect of random photometric redshift errors, as described in Section 3.2.2.

We estimate the correlation length for our whole sample of $z > 1$ sources (including the NGP+GAMA fields) to be $r_0 = 11.4 \pm 0.4\,h^{-1}$Mpc[3]. The error in the measurement is relatively small, which is due to the assumption of a power-law model with a fixed slope thus reducing the uncertainties from introducing additional parameters. The measurement of the correlation length is in general agreement with previous studies (Webb et al., 2003; Blain et al., 2004; Weiß et al., 2009; Williams et al., 2011; Hickox et al., 2012; Chen et al., 2016a,b). The measurement is also in agreement with Maddox et al. (2010), who used 250μm-selected sources from the *SDP* field of *H-ATLAS*, reporting a clustering length in the range $r_0 \sim 7 - 11\,h^{-1}$Mpc when considering additional colour cuts to preferentially select high-redshift sub-mm sources. However, comparing our results with Wilkinson et al. (2017) we seem to find a larger clustering strength, even when compared with their sample of SMGs with radio-identified counterparts which are typically comprised of more luminous SMGs. The reason for this is not very clear as there might be many different factors that can contribute to this disagreement (e.g. source extraction, counterpart identification, errors in the photometric redshifts,

---

[3] The value of r_0 from our full sample is in $< 2\sigma$ agreement with the measurements from the individual fields, all expect GAMA-9h. This is because the mean r_0 as well as it's error is computed using 4 individual sub-regions (see section 3.3.1), while for the full sample 27 are used which could be the reason for diluting the strong signal of the GAMA-9h field.

different properties of the source populations).

3.4.2.1 Halo Bias model

In order to convert the clustering strength to the inferred dark-matter halo mass, M_{halo}, we need to compute the galaxy bias, b. Galaxies are biased tracer of the underlying dark-matter density field, therefore this quantity can be inferred by scaling the dark-matter angular correlation function, $w_{dm}(\theta)$, according to the following relation:

$$w(\theta) = b^2 w_{dm}(\theta). \tag{3.12}$$

In the above expression the dark matter angular correlation function, $w_{dm}(\theta)$, can be computed using the Limber′s equation which is used in order to convert a 3D power spectrum, $P(k,z)$ into a projected angular correlation function from,

$$w_{dm}(\theta) = \frac{1}{c}\int \left(\frac{dN}{dz}\right)^2 H(z) \int \frac{k}{2\pi} P(k,z) J_0\left(\frac{k\theta}{\chi^{-1}(z)}\right) dk dz \tag{3.13}$$

where J_0 is the zero-th order Bessel function and dN/dz is the corrected redshift distribution as described in Section 3.2.2. In this case $P(k,z)$ is the non-linear dark matter power spectrum, $P_{NL}(k,z)$ which was computed using the HALOMOD package (Murray et al. in prep). This package implements the HaloFit code (Smith et al., 2003) with improved parametrisation provided by Takahashi et al. (2012).

Fitting our modelled angular correlation function, which is given by Equation 3.12, we determined the galaxy bias. Our theoretical prediction is shown as the purple curves in bottom-middle panel of Figure 3.6, where the 1σ uncertainty is shown as the shaded region. The best-fit value of the galaxy bias for the combined *GAMA+NGP* is $b = 4.26 \pm 0.27$ (see Table 3.3).

Finally, in order to infer the dark matter halo mass that corresponds to a specific value of the galaxy bias we need to assume a bias function, $b(M,z)$. The value of the halo mass, M_{halo}, will strongly depend on the assumed parametrisation of the bias function. We opted to use the function introduced by Tinker et al. (2010),

$$b(\nu) = 1 - \frac{\nu^{\alpha}}{\nu^{\alpha} + \delta_c^{\alpha}} + B\nu^{b} + C\nu^{c} \tag{3.14}$$

where $B = 0.183$, $b = 1.5$, $c = 2.4$, δ_c is the critical density for collapse and $\nu = \delta_c/\sigma(M,z)$ is the "peak height" in the linear density field, with $\sigma(M,z)$ being the linear matter variance which is given by,

$$\sigma^2 = \frac{1}{2\pi^2}\int P(k,z)\hat{W}^2(kR)k^2 dk\,, \tag{3.15}$$

which is smoothed on a scale of comoving radius $R = (3M/4\pi\bar{\rho}_{m,0})^{1/3}$, using the Fourier transform of the real-space top-hat filter,

$$\hat{W}(kR) = \frac{3\left[sin(kR) - (kR)cos(kR)\right]}{(kR)^3}\,. \tag{3.16}$$

In the above expression the parameters $\bar{\rho}_{m,0}$ is the mean matter density at the current epoch.

The inferred dark matter halo mass using the bias function, which was detailed above, is $\log(M_{\rm halo}) = 13.2 \pm 0.1$ (see Table 3.3) and was calculated at the median redshift $\langle z \rangle \sim 1.75$.

3.4.2.2 Halo Occupation Distribution (HOD) model

We can see for Figure 3.6 that our model adopting the halo bias formalism does not provide an accurate fit to the small angular scales. In an attempt to model this clustering signal we make use of the halo model power spectrum, $P(k)$, which is written as the sum of two terms. The 1-halo term arises from interactions between galaxies within a single dark matter halo and dominates on small scales, while the 2-halo term arises from interactions of galaxies that belong to different halos and dominates on large scales (see Cooray and Sheth, 2002). These terms are computed from,

$$P^{1h}_{gg}(k,z) = \int n(M,z)\frac{\langle N(N-1)|M\rangle}{\bar{N}^2_{gal}}y^2(k|M,z)dM \tag{3.17}$$

$$P^{2h}_{gg}(k,z) = P_{lin}(k,z)\left(\int n(M,z)b(M,z)\frac{\langle N|M\rangle}{\bar{N}_{gal}}y(k|M,z)dM\right)^2\,, \tag{3.18}$$

where $n(M,z)$ is the halo mass function (Tinker et al., 2008), $y(k|M,z)$ is the normalised Fourier transform of the halo density profile, $b(M,z)$ is the linear large-scale bias and $P_{lin}(k,z)$ is the linear matter power spectrum which is computed using the *CAMB* code (Lewis et al., 2000).

This formalism introduces the Halo Occupation Distribution (HOD) parametrisation to the clustering signal arising from galaxy populations. In this parameterisation, the mean numbers of central and satellite galaxies in a halo of mass M are given by,

$$\langle N_{cen}|M\rangle = \frac{1}{2}\left[1+\mathrm{erf}\left(\frac{\log M-\log M_{cen}}{\sigma_{\log M}}\right)\right], \tag{3.19}$$

$$\langle N_{sat}|M\rangle = \frac{1}{2}\left[1+\mathrm{erf}\left(\frac{\log M-\log M_{cen}}{\sigma_{\log M}}\right)\right]\left(\frac{M}{M_{sat}}\right)^{\alpha_{sat}}, \tag{3.20}$$

where *erf*(x) is the error function, M_{cen} is the minimum halo mass above which all halos host a central galaxy, σ_{logM} is the width of the central galaxy mean occupation, M_{sat} is the mass scale at which one satellite galaxy per halo is found, in addition to the central galaxy, and α_{sat} is the power-law slope of the satellite occupation number with halo mass.

The best-fit values of the parameters of our HOD model, which resulted from our MCMC analysis, are summarized in the first row of Table 3.3 for which we used flat priors for the parameters of our model within the range: $12 < \log(M_{cen}/h^{-1}M_{\odot}) < 14$, $10 < \log(M_{sat}/h^{-1}M_{\odot}) < 15$ with a fixed power-law slope for the satellite occupation number, $\alpha_{sat} = 1.0$, and width of the central galaxy mean occupation, $\sigma_{logM} = 0.3$. Our theoretical prediction is shown as the purple dashed curve in bottom-middle panel of Figure 3.8 and seems to provide a more accurate fit to the data.

In order to select which of our models is better at describing our data in a bayesian sense we use the Bayesian information criterion (BIC). Adding more parameters to our model might increase the likelihood, $\hat{L}$, ($\hat{L} \propto e^{-\chi^2}$), but in exchange that could result in over-fitting our data. The BIC introduces a penalty term given the number of free parameters in our model and in doing so it attempts to resolve this problem. Using the BIC, which is given by

$$\mathrm{BIC} = \ln(n)k - 2\ln(\hat{L}) \tag{3.21}$$

where n is the number of data points and k is the number of free parameters in our model, we find:

- $w(\theta) = A\theta^{-0.8}$: 6.00 (1 parameter)
- $w(\theta) = b^2 w_{dm}$: 6.32 (1 parameter)
- $w(\theta) = w_{gg}$: 7.71 (2 parameter)

The BIC seem to prefer a power-law model, $w(\theta) = A\theta^{-0.8}$, which provides a better fit to the largest scales. Although, if we were to exclude the last two data points, the BIC seem to prefer the $w(\theta) = w_{gg}$ model.

In addition, we would like to note that we considered using the HOD parametrisation of Geach et al. (2012), which is more appropriate for star-formation rate selected samples. However, this HOD model has a lot more free parameters which were impossible to constrain given the errors in our measurements and the fact that we do not probe scales in the non-linear regime. The only parameter that is well constrained using this alternative parametrisation is the minimum halo mass above which all halos host a central galaxy M_{cen}. This is the main parameter of interest for this work and its value was consistent between the two different parameterisations.

3.4.3 Evolution of Clustering with redshift for $z > 1$ SMGs

The large sample of high-z sub-mm sources ($z > 1$) in the combined *GAMA+NGP* fields allow us to investigate the redshift evolution of the clustering signal. To do that, we split our sample into three redshift bins, $1 < z < 2$, $2 < z < 3$ and $3 < z < 5$ similarly to Chen et al. (2016b). The redshift distributions, $p(z|W)$, after accounting for the effect of random photometric redshifts are shown in the bottom panel of Figure 3.7 for the different redshift bins. We restricted our analysis to three redshift bins in order to avoid excessive overlap between the corrected redshift distribution.

The resulting clustering measurements are shown in Figure 3.8 for each redshift bin. The measurements were corrected by a factor of 1.25 as determined from our simulations in Appendix A. In each panel, we also include the measurement from Chen et al. (2016b) as red triangles, which probe angular scales down to ~1". The two measurements agree fairly well in the angular scales probed by *Herschel*. However, in the highest redshift bin we find an excess signal in the lowest probed angular bin compared to Chen et al. (2016b).

We fit a one-parameter power-law model with a fixed slope, $w(\theta) = A_w\theta^{-0.8}$, in order to model the angular correlation functions in each redshift bin. The resulting best-fit value for the parameter of our model, in each redshift bin, are shown in Table 3.3. These corresponds to the black lines in each panel of Figure 3.8, where the 1σ uncertainty is shown as the grey-shaded region.

The correlation length, r_0, in each redshift slice was calculated following a bootstrap method, in order to consider the uncertainty in the best-fit value of the power-law model. In each realisation we randomly sample the parameter

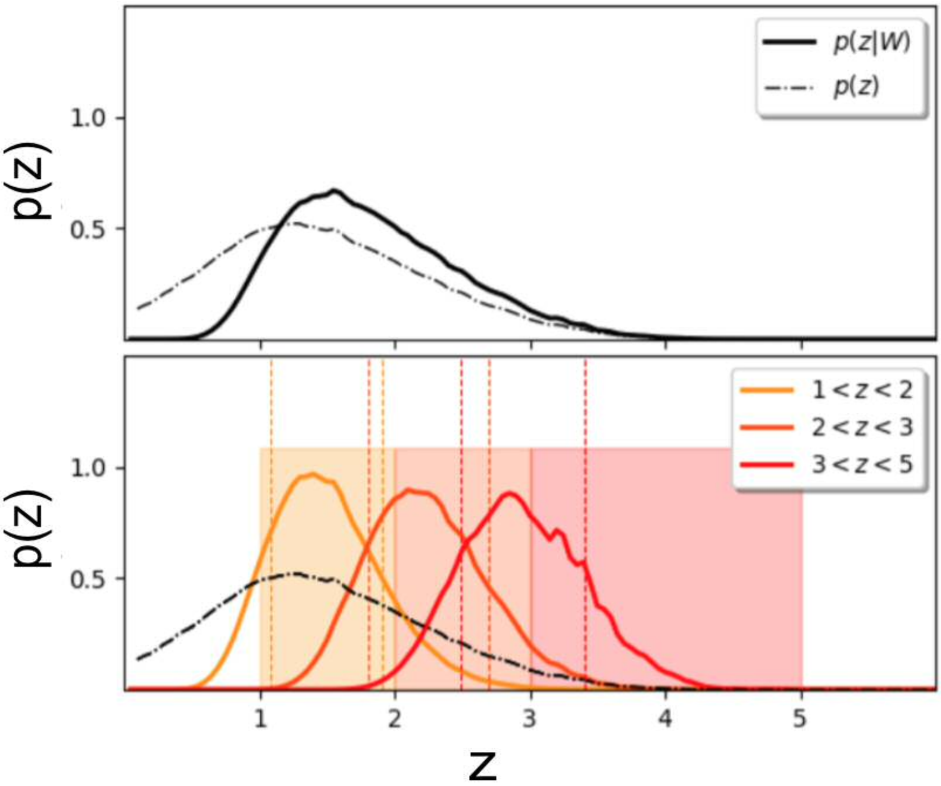

Figure 3.7: The estimated redshift distributions $p(z|W)$ taking into account the window functions, $W(z_{ph})$, and the photometric redshift error function, $p(z_{ph}|z)$. The black dot-dashed line shows the initial (i.e. the observed one; see main text) redshift distribution, $p(z)$ of our sources. The top panel shows the "corrected" redshift distribution for sources in the redshift range $1 < z < 5$, while similarly in the bottom panel for the different redshift bins indicated at the right upper corner. The vertical solid lines correspond to the 50th percentile of the distribution, while the vertical dashed lines left and right of it correspond to the 16th and 84th percentiles respectively. The shaded regions show the width of our window functions.

Table 3.3: Results of Clustering Analysis for $z > 1$ SMGs.

Sample	Field	$N_{\rm gal}$	$\langle z \rangle$	A_w	r_0 $(h^{-1}Mpc)$	b	$log\left(\frac{M_{halo}}{h^{-1}M_\odot}\right)$	$log\left(\frac{M_{cen}}{h^{-1}M_\odot}\right)$	$log\left(\frac{M_{sat}}{h^{-1}M_\odot}\right)$
$1<z<5$	*GAMA+NGP*	85319	$1.75^{+0.55}_{-0.70}$	0.13 ± 0.01	11.4 ± 0.4	4.3 ± 0.3	13.2 ± 0.1	$13.00^{+0.14}_{-0.22}$	$14.17^{+0.65}_{-0.75}$
$1<z<2$	*GAMA+NGP*	55749	$1.47^{+0.38}_{-0.46}$	0.09 ± 0.01	8.1 ± 0.5	3.2 ± 0.1	13.1 ± 0.1	$12.91^{+0.11}_{-0.14}$	$14.78^{+0.50}_{-0.64}$
$2<z<3$	*GAMA+NGP*	25108	$2.21^{+0.42}_{-0.49}$	0.11 ± 0.02	8.5 ± 0.8	4.5 ± 0.4	12.9 ± 0.1	$12.50^{+0.28}_{-0.21}$	$12.32^{+1.71}_{-1.29}$
$3<z<5$	*GAMA+NGP*	4462	$2.93^{+0.45}_{-0.48}$	0.31 ± 0.16	13.9 ± 3.9	9.0 ± 2.5	13.2 ± 0.2	$12.88^{+0.35}_{-0.41}$	$12.93^{+1.71}_{-1.64}$

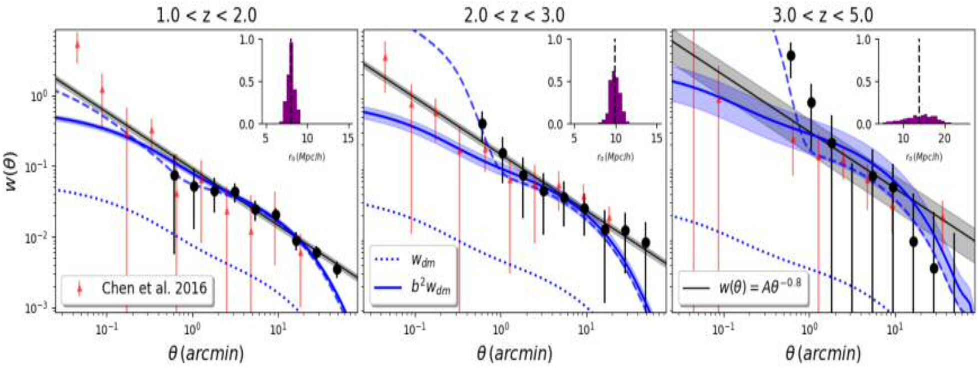

Figure 3.8: The angular correlation function of sub-mm galaxies for each redshift slice in the redshift range $1 < z < 5$ (black circles).The measurements were corrected by a factor of 1.25, as determined from our simulations in Appendix A.The black solid lines corresponds to our fitted power-law model with a fixed slope, $w(\theta) = A\theta^{-0.8}$, where the 1σ uncertainty is shown as the black shaded region. The inset plot in each panel show the histogram of correlation length values which were derived from our bootstrap method. The black dashed vertical line in the inset plot of each panel, indicates the mean of the distribution. The blue dotted curve shows the dark matter angular correlation function, w_{dm}. This has been scaled by the best-fit value of the linear bias factor, b, which is shown as the solid blue curve, with the 1σ uncertainty shown as the blue shaded region. Finally, we show as the blue dashed curve the galaxy-galaxy angular correlation function, w_{gg}, that corresponds to the best-fit HOD model. In addition, we also include the measurements from Chen et al. (2016b) shown as red triangles.

A_w from a Gaussian distribution, centred at the best-fit value with a standard deviation equal to its error, and use Equation 3.9 to calculate the correlation length. The resulting normalised histograms of r_0 values, from our bootstrap method, are shown in the upper right corner of each panel in Figure 3.8. The black vertical dashed line indicates the mean of the distribution, which was derived by fitting a Gaussian distribution to the histogram. This value corresponds to our measurement of the clustering length, r_0, where the 1σ uncertainty is taken as the standard deviation of the fitted Gaussian distribution. Our results are shown in Table 3.3 for each redshift slice.

Finally, we compute the bias parameters, b, for each redshift slice following the same methodology outlined in Section 3.4.2, using the corrected redshift distributions shown in Figure 3.7 in order to compute the projected the dark matter angular correlation functions, $w_{dm}(\theta)$. In Figure 3.8 we shown $w_{dm}(\theta)$ in each panel as the blue dashed lines. In the same Figure, the blue solid lines in each panel show the projected the dark matter angular correlation functions scaled by the best-fit value of the linear bias parameters, where the 1σ uncertainty is shown as the blue-shaded region. Our results are shown in Table 3.3 for each redshift slice along with the halo masses, M_{halo}, that correspond to these bias measurements according to Equation 3.14.

In the last two panels of Figure 3.8 we see that the scaled dark matter angular correlation functions does not provide a satisfactory fit to the data, indicating the need of using an HOD model, similar to the analysis in the previous section. The results from our MCMC analysis are shown in Table 3.3 for which we used flat priors for the parameters of our model within the range: $12 < \log(M_{cen}/h^{-1}M_{\odot}) < 14$ and $10 < \log(M_{sat}/h^{-1}M_{\odot}) < 15$ with a fixed power-law slope for the satellite occupation number, $\alpha_{sat} = 1.0$, and width of the central galaxy mean occupation, $\sigma_{logM} = 0.3$. We were not able to set good constrains on M_{sat}. The resulting errors depend strongly on the range of prior, we adopted for this parameter.

3.5 Discussion

Our findings are summarised in Figure 3.9 where we plot the evolution of the correlation length, r_0, as a function of redshift for our sample of 250μm-selected sources with flux densities $S > 30\,\mathrm{mJy}$. The green points correspond to measurements from Wilkinson et al. (2017), while the red points correspond to measurements from Chen et al. (2016b). The black lines are the theoretical predictions for the evolution of the correlation length with redshift for different halo masses, which were estimated using the formalism of Peebles (1980). According to that formalism the correlation length is related to the bias parameter, as

$$r_0 = 8\left(\frac{\Delta_8^2}{C_\gamma}\right)^{1/\gamma} = 8\left(\frac{b^2\sigma_8^2 D^2}{C_\gamma}\right)^{1/\gamma} \tag{3.22}$$

where Δ_8 is the clustering strength of haloes, more massive than the mass M at redshift z and is defined as $\Delta_8(M,z) = b(M,z)\sigma_8 D(z)$, with $D(z)$ being the growth factor of linear fluctuations in the dark matter distribution which is computed from,

$$D(z) = \frac{5\Omega_m E(z)}{2}\int_z^{\infty}\frac{1+y}{E^3(y)}dy\,. \tag{3.23}$$

The factor C_γ is computed from, $C_\gamma = 72/(3-\gamma)(4-\gamma)(6-\gamma)2^{\gamma}$, where γ is the slope of power-law model which parametrises the spatial correlation function and is taken to be $\gamma = 1.8$ (since we assume the same power-law slope when computing the correlation length, see Section 3.3.3). The inset plot in Figure 3.9 shows the

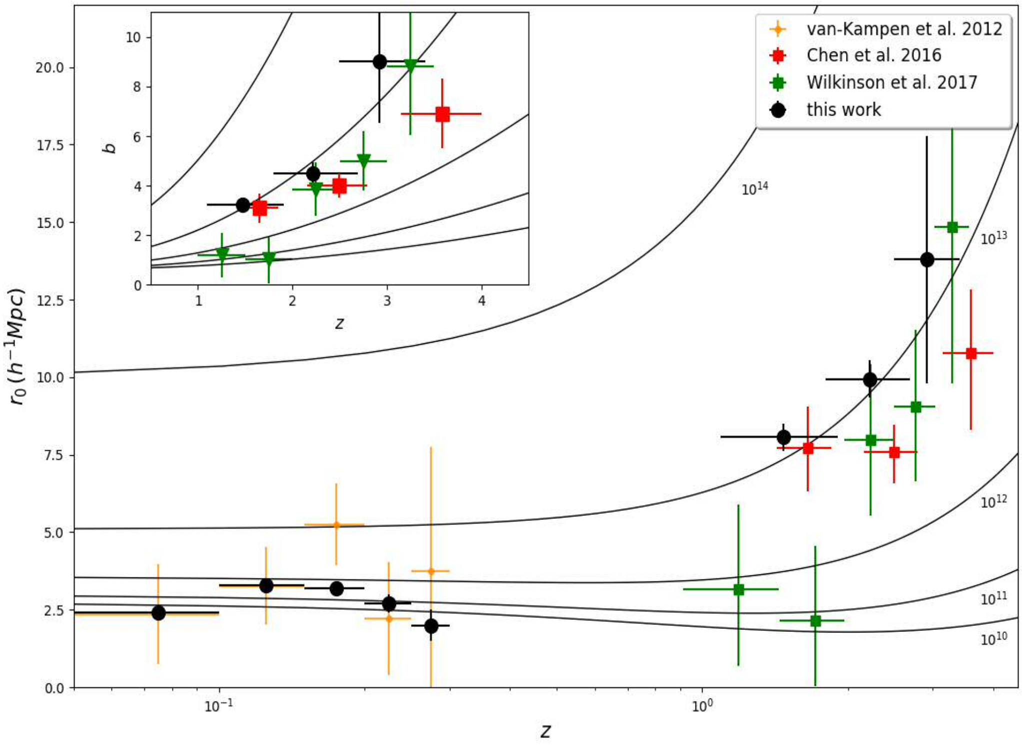

Figure 3.9: The evolution of the correlation length r_0 with redshift for our sample of 250μm-selected sources with flux densities $S > 30\,$mJy (black points). We also show the clustering results from previous studies: Herschel-ATLAS science demonstration phase (SDP) field 250μm-selected sources at 0.05 < z < 0.3 (van Kampen et al., 2012, yellow points), UKIRT Infrared Deep Sky Survey (UKIDSS) 850μm-selected SMGs at 1 < z < 5 (Chen et al., 2016b, red points), SCUBA-2 Cosmology Legacy Survey 850μm-selected SMG's at 1 < z < 3.5 (Wilkinson et al., 2017, green points). The black solid lines show the evolution of r_0 with redshift for dark matter halos of different masses (in units of $h^{-1}M_{\odot}$) using Equation 3.22. The inset plot of the top left corner shows the evolution of the galaxy bias as a function of redshift, where the black solid lines show the theoretical predictions using Equation 3.14 of the bias function from Tinker et al. (2010).

evolution of the bias parameter as a function of redshift, where the green and red points correspond to the values found in the aforementioned studies. The black solid lines correspond to theoretical predictions using Equation 3.14 of the bias function from Tinker et al. (2010).

At high redshifts our results are in general agreement with previous studies for the evolution of clustering of SMGs. Above redshift of about ~ 2, however, we find our population of bright SMGs selected at 250μm with flux densities $S_{250} > 30$mJy exhibit larger clustering strengths (2σ discrepancy) compared to Chen et al. (2016b) where the authors studied a sample of faint SMGs selected at 850μm with flux densities $S_{850} < 2$mJy. This indicates that brighter SMGs cluster more strongly than their faint counterparts even at high redshifts, which is also supported by the fact that our results are more in agreement with Wilkinson et al. (2017) where the authors studied bright SMGs selected at 850μm with flux densities $S_{850} > 2$mJy. On the other hand, we find that SMGs in the redshift range $1 < z < 2$ follow the same evolutionary track as those at higher redshifts, in contrast to the findings of Wilkinson et al. (2017) where the authors reported a downsizing effect (3σ discrepancy). However, this effect is not present in the analysis of Chen et al. (2016b). It is not straightforward to determine the cause for this difference, as there might be biases folded in the measurements associated with the selection of these SMGs.

The discrepancies of the aforementioned differences are at 2-3σ. If we also were to consider that the errors on our measurements are slightly underestimated as determined from our simulations in Appendix A, the agreement becomes even better. This suggest that we need to improve the accuracy of our measurements in order to confidently differentiate the clustering properties of faint and bright SMGs, as well as SMGs selected at different wavelengths. This improvement can come by obtaining more realistic photometric redshift measurements and potentially use ALMA to improve our counterpart identification techniques (Jin et al., 2018).

3.6 Conclusions

We measured the angular auto-correlation function of low- and high-redshift sub-mm sources identified in the GAMA+NGP fields of the H-ATLAS, which comprise the largest area extragalactic survey at sub-mm wavelengths. We selected a sample of sources detected at the 4σ significance level (~ 30 mJy) at 250-μm. Our main results are summarised as follows:

- We performed simulations of clustered sources and assessed our methodology of extracting sources from our 250μm H-ATLAS maps. We estimated the correction factor that needs to be applied to the measured angular correlation function due to the loss of clustering power from our method for removing Galactic cirrus emission. Our simulations and methodology for calculating this correction factor are described in Appendix A.

- First, we studied the evolution of clustering with redshift for our low redshift ($z < 0.3$) sample. We showed that SMGs in this redshift range exhibit clustering lengths of the order of $\sim 2-3h^{-1}$Mpc, similar to normal galaxies selected at optical wavelengths. Our results agree with the findings of van Kampen et al. (2012), albeit with much improved errors on the measurement due to our larger sample.

- We performed an auto-correlation analysis of SMG in the redshift range $1 < z < 5$, which is similar to the redshift range of many previous studies. We showed that SMGs are strongly clustered, finding a clustering length $r_0 = 11.4 \pm 0.4h^{-1}$Mpc. We modelled the clustering signal by scaling the dark matter angular correlation function by the linear bias factor, finding a value of $b = 4.26 \pm 0.27$ that corresponds to a dark matter halo mass of $\log(M_{halo}) = 13.2 \pm 0.1h^{-1}M_{\odot}$.

- In addition, we studied the evolution of clustering with redshift for our sample of high redshift ($z > 1$) sub-mm sources. We showed that SMGs occupy dark matter halos with masses of the order of $10^{12.9}$, $10^{12.5}$ and $10^{12.9}h^{-1}M_{\odot}$ at $z = 1-2$, $2-3$ and $3-5$, respectively. We did not find a downsizing effect for SMG below redshift of about ~ 2, as reported in Wilkinson et al. (2017).

- Finally, we point out that galaxies selected at 250μm at high and low redshifts are not the same population. The star formation activity seems to be shifting from high mass halos at $z > 1$ to less massive halos at $z < 1$, consistent with the downsizing effect reported in Magliocchetti et al. (2014).

CHAPTER 4

THE NATURE OF J091043.0−000322

ABSTRACT

We investigate the physical properties of the ISM in the strongly lensed $z_s = 1.7830 \pm 0.0002$ galaxy J091043.0−000322 (SDP.11) which was discovered in the $H-$ATLAS survey. We use a multi-wavelength suite of observations which were carried out in the near-infrared with the *Hubble Space Telescope* (HST), in the sub-millimeter with ALMA and the *Submillimeter Array* (SMA) and in the millimeter regime with *Plateau de Bure Interferometer* (PdBI). We build a robust model for the lens from the modelling, in the uv-plane, of the dust continuum emission in ALMA Band 9 which we use to reconstruct the lensed emission from all our observations. Our high resolution observations allow us to probe scales down to 300 − 700 pc at the redshift of the source, where the gas emission breaks into several clumps none of which is associated with the more compact dust emission. We use the reconstructed kinematics to investigate the nature of SDP.11, finding evidence that the source is undergoing a major-merging event. The content of this Chapter is currently in preparation for publication (Amvrosiadis et al. in prep.).

4.1 Introduction

As already discussed in chapter 1, the biggest challenge in studying high redshift DSFGs is the lack of sufficient angular resolution to probe the properties of their ISM down to sub-kpc scales (where ~ 100 pc is roughly the size of Giant Molecular Clouds; GMCs). However, strong gravitational lensing offers the unique ability to study the properties of stars, dust and gas at higher angular resolution and signal-to-noise ratio (SNR) by boosting the apparent flux of these sources, and magnifying their apparent solid angle.

Follow-up studies of strongly lensed SMGs, either spatially resolved (e.g. Bussmann et al., 2012, 2013; Hezaveh et al., 2013; Messias et al., 2014; Dye et al., 2015; Spilker et al., 2015, 2016; Oteo et al., 2017; Dye et al., 2018; Amvrosiadis et al., 2018; Enia et al., 2018; Marrone et al., 2018; Spilker et al., 2018; Leung et al., 2019; Litke et al., 2019; Dong et al., 2019; Yang et al., 2019) or un-resolved yet able to probe the global properties (e.g. Aravena et al., 2016; Yang et al., 2016, 2017; Wardlow et al., 2017, 2018; Andreani et al., 2018; Harrington et al., 2018; Zhang et al., 2018), have now become a common practise in order to characterize the stellar, dust and gas content in these objects.

In order to extract physical information from these strong lensing objects, many lens modelling techniques have been developed in the past decade. These mainly fall into two categories: parametric methods and semi-parametric methods, the former modelling both the lens and the source with analytical models (i.e. Singular Isothermal Ellipsoid for the lens, Sersic profiles for the source), the latter modelling the lens with an analytic model while describing the source with a grid of pixels, in which the intensity in each pixel is free to vary. The latter method makes no assumptions about the form of the source. Due to the clumpy and irregular nature of these kind of sources, in this work we use a semi-parametric approach, based on the Regularized Semilinear Inversion (Warren and Dye, 2003; Nightingale and Dye, 2015), extended to work directly with visibility datasets whenever used (see Dye et al., 2018; Enia et al., 2018).

One of the first five strongly lensed galaxies discovered in the *H*-ATLAS survey is J091043.0−000322 (SDP.11; Negrello et al., 2010) at redshift $z = 1.783$ (Lamarche et al., 2018). In this work we build a model for the lens from high-resolution ALMA Band 9 observations (Lamarche et al., 2018) and use this model to reconstruct the background lensed source at various wavelengths to study the stellar, dust and gas components of its interstellar medium (ISM) at sub-kpc resolution. In addition, we also study the kinematics of the background reconstructed source in order to understand the mechanism responsible for the extreme star-formation rate in this system (i.e. is it a merger-induced event or a clumpy rotating disk).

The outline of this Chapter is as follows. In Section 4.2 we will present the available datasets for SDP.11 and discuss the image plane properties of the source in Section 4.3. The strong lens modelling methodology is described in Section 4.4 followed by a discussion on the retrieved properties of our source in Section 4.5. In Section 4.6 we investigate the nature of SDP.11, specifically trying to distinguish between a rotating disk or a major-merger. Finally, a short summary of our finding is presented in Section 4.7 along with our conclusions. Throughout this work, we adopt a spatially-flat Λ-CDM cosmology with $H_0 = 67.8 \pm 0.9$ km s^{-1} Mpc^{-1} and $\Omega_M = 0.308 \pm 0.012$ (Planck Collaboration et al. 2016), with an angular-size scale of 8.65 kpc/″ at $z = 1.783$ (used to convert angular to physical scales in the source-plane).

4.2 Data

In this section, we present all the available data sets for SDP.11. This object was selected as a candidate strongly lensed galaxy from the *Herschel Astrophysical Terahertz Large Area Survey* (H-ATLAS; Eales et al., 2010) for having a flux density higher than 100 mJy at 500 μm (Negrello et al., 2007, 2010, 2017). The strong lensing nature of the source was subsequently confirmed with follow-up observations conducted with the HST Wide−Field Camera 3 (WFC3), taken in the F110W (1.150 μm) and F160W (1.545 μm) filters (Negrello et al., 2014), and with the SMA at 880μm (Bussmann et al., 2013). In addition, this object was observed with ALMA in Band 7 and Band 9 as well as with the Plateau de Bure Interferometer (PdBI).

In this work we will model all of these available archival data sets; as such, a brief description of the individual observations is given in the following subsections.

4.2.1 ALMA data

4.2.1.1 Band 7

The object SDP.11 was observed with ALMA in Cycle 4, on 2016 November 25 (Proposal Code: 2016.1.00282.S; PI: E. Falgarone) in the 873 μm atmospheric window (Band 7). The array was in the configuration C40-3, using 40 out of 54 of the 12m array antennas with baselines ranging from 15 meters to 704 meters. The total on-source integration time was ~ 27.4 minutes, with a total amount of time for additional overheads of ~ 29 minutes. The overheads include pointing, focusing, phase, flux density and bandpass calibrations. J0909+0121 was used as the phase calibrator, J0854+2006 as the bandpass calibrator and J0854+2006 as the flux calibrator. The weather conditions were excellent with precipitable water vapors (PWVs) ~1.35 mm.

The total bandwidth in Band 7 was divided into four spectral windows, where two of the spectral windows have 128 channels with a spectral width of 15.625 MHz and the other two have 240 channels with a spectral width of 7.8125 MHz, where both values correspond to the per channel width. The central frequencies of the spectral windows are 287.14 (SPW1; 286.15-288.13 GHz), 288.90 (SPW0; 287.91-289.89 GHz), 298.97 (SPW3; 298.03-299.90 GHz) and 300.57 (SPW2; 299.64-301.51 GHz).

The dust continuum image was produced using the Common Astronomy Software Applications (CASA; McMullin et al., 2007) task *clean* by combining

Table 4.1: Details of the ALMA observations of the strongly lensed $z_s = 1.7830$ galaxy SDP.11 in bands 7 and 9.

Band	Date		Calibrator		t_{source}	Baselines		SPW	Science Goal
		Bandpass	Flux	Phase	(min)	min (m)	max (m)		
7	25-Nov-2016	0854+2006	0854+2006	0909+0121	27.4	15	700	3	CH$^+$
								0-3	Continuum
9	16-Nov-2016	J0854+2006	J0522−3627	J0909+0121	13.0	15	920	0-1	C_{II}
								0-3	Continuum

Notes: The central observing coordinates (J2000) for SDP.11 are 09:10:43.10 (RA) and -00:03:21.00 (DEC) for both the Band 7 and Band 9 observations. SPW (spectral windows) cover the frequency range of 287.91-289.89 GHz (SPW0), 286.15-288.13 GHz (SPW1), 299.64-301.51 GHz (SPW2) and 298.03-299.90 GHz (SPW3) for Band 7 and 681.22-683.20 GHz (SPW0), 683.07-685.06 GHz (SPW1), 679.34-681.33 GHz (SPW2) and 677.45-679.43 GHz (SPW3) for Band 7, respectively. The CH$^+$ line is detected at the edge of SPW3 in Band 7 but is not used in this work.

all the line-free channels. In executing the CASA task *clean*[1], we apply natural weighting[2]. The full width at half maximum (FWHM) of the synthesized beam is $0.47'' \times 0.41''$ with a position angle of 77.2°. In order to assist with the cleaning convergence we used a circular mask which had a radius of ~1.5 arcsec. We used a cleaning threshold of 10^{-1} mJy and performed 5 cycles of 100 iterations/cycle. The root mean square (RMS) of the continuum reaches ~43 μJy beam^{-1}. The RMS was measured using CASA by averaging the RMS from regions of similar extent as the mask that was used for the cleaning, but did not contain any emission. The continuum emission was detected at a $\sim 150\sigma$ significance level at its peak.

4.2.1.2 Band 9

The object SDP.11 was observed with ALMA in Cycle 4 on 2016 November 16 (Proposal Code: 2015.1.01362.S; PI: G. Stacey; Lamarche et al., 2018) in the 450μm atmospheric window (Band 9). The array was in the configuration C40-4 using 36 out of 54 of the 12m array antennas with baselines ranging from 15 to 920 meters. The total on-source integration time was 13.0 minutes, with a total amount of time for additional overheads of ~ 34 minutes.The overheads include pointing, focusing, phase, flux density and bandpass calibrations. J0909+0121 was used as the phase calibrator, J0854+2006 as the bandpass calibrator and J0522−3627 as the flux calibrator. The weather conditions were excellent with precipitable water vapors (PWVs) ~ 0.3 mm.

The total bandwidth in Band 9 was divided into four spectral windows, where each spectral window has 128 channels with a spectral width of 15.625 MHz. The central frequencies of the spectral windows are 678.44 (SPW3; 677.45-679.43 GHz), 680.33 (SPW2; 679.34-681.33 GHz), 682.21 (SPW0; 681.22-683.20 GHz) and 684.07 (SPW1; 683.07-685.06 GHz), where the SPW0 and SPW1 were tuned for the C_{II} line ($\nu_{rest} = 1900.54$ GHz), which according to the source redshift, $z_s = 1.783 \pm 0.0002$, should be observed between $\nu_{obs} = 682.861 - 682.959$ GHz.

The visibility data were calibrated using the ALMA calibration pipeline. We perform the imaging of the calibrated visibility data using CASA. The dust continuum image was produced using the CASA task *clean* by combining all the line-free channels (i.e. excluding channels between 72 to 128 in SPW0 and between 0 to 34

---

[1] The CASA command *clean* has many functionalities, but at it's core it forms images from the observed visibilities.

[2] During deconvolution, which is performed by the command *clean*, CASA has different options for weighting the visibilities. The natural weighting means that low spatial frequencies are weighted up which results in the best possible signal-to-noise ratio that can be achieved, however, compromising the resolution of the final image that is produced.

in SPW1). In executing the CASA task clean, we apply both the natural and the *briggs* (robust=0.5) weighting. The full width at half maximum (FWHM) of the synthesized beams are $0.20'' \times 0.16''$ with a position angle of 55.8° and $0.17'' \times 0.14''$ with a position angle of 58.9°, respectively. We need to note that the different choice of weighting schemes is for demonstration purposes only since as we describe in Section 4.4 the modelling is carried out in the visibility space where a natural weighting is adopted. In order to assist with the cleaning convergence we used a circular mask which had a radius of ~1.9 arcsec. We used a cleaning threshold of 0.1 mJy and performed 5 cycles of 100 iterations/cycle. The root mean square (RMS) of the continuum reaches ~1.24 and ~1.21 mJy beam^{-1} for the natural and briggs weighting, respectively. The continuum emission was detected at a ~20σ significance level at its peak.

We use the CASA task *uvcontsub* to subtract the line emission from the continuum. We used a first-order polynomial to fit the continuum excluding channels that fully encompass the $C_{\rm II}$ emission line. The cube was produced using the CASA task *clean* using the same mask as in the continuum mode and a cleaning threshold of 10^{-2} mJy. We produce two separate cleaned cubes adopting a velocity resolution of ~29 km s^{-1} (which correspond to stacking 4 channels per cube slice) and ~55 km s^{-1} (which correspond to stacking 8 channels per cube slice), respectively, in order to increase the signal-to-noise ratio (SNR) of the $C_{\rm II}$ line emission in each slice. The cube with the higher spectral resolution is going to be used to produce the spectrum of the $C_{\rm II}$ line (see Section 4.3.3), while the lower resolution cube for the reconstruction of the lensed $C_{\rm II}$ line emission in each slice (see Section 4.5.2). In executing the CASA task clean, we only apply a natural weighting resulting in a FWHM of $0.20'' \times 0.15''$ with a position angle of 52.6°. The RMS of the cubes reaches ~6 and ~5 mJy beam^{-1} for the ~29 km s^{-1} and ~55 km s^{-1} resolution cubes, respectively.

4.2.2 HST data

The source SDP.11 was observed in the wide-J F110W (1.150 μm) and wide-H F160W (1.545 μm) filters the Wide Field Camera-3 (WFC3) on board of the HST. The observations were carried out on 2011 April as part of the cycle-18 proposal 12194 (PI: Negrello) and were presented in Negrello et al. (2014).

Two orbits were dedicated for the target, resulting in a total exposure time of 1412 and 3718 sec with the F110W and F160W filters, respectively. The data were reduced using the IRAF MultiDrizzle package, which resulted to a pixel scale of 0.064 arcsec and a point spread function (PSF) with full width at half-maximum

(FWHM) of ~ 0.13 and ~ 0.16 arcsec respectively for the 1.150 μm and 1.545 μm observations.

4.2.3 SMA data

The source SDP.11 was observed with the SubMillimeter Array (SMA) in 2011 and 2012, as a part of a large multi-semester program carried out to confirm the lensing nature of the fist sub-mm selected candidate lensed galaxies in the H-ATLAS and HerMES surveys (Bussmann et al., 2013).

The observations were performed in compact (COM), extended (EXT) and very extended (VEX) configuration over a period of two years[3]. The total integration time for this source is ~ 7 hours. The FWHM of the synthesized beam is $0.78'' \times 0.60''$ with a position angle of 84.0°. We refer the reader to Bussmann et al. (2013) for more details on the observations and data reduction.

4.2.4 PdBI data

Plateau de Bure Interferometer (PdBI) observations were carried out as part of the programs UAAA (SDP.9; PI: P. Cox) and UBAA (SDP.11; PI: R. J. Ivison). The data products were calibrated using GILDAS (for more details see Oteo et al., 2017) and then converted into CASA style format files for further analysis.

The full width at half maximum (FWHM) of the synthesized beam is $0.95'' \times 0.39''$ with a position angle of 112.1° using natural weighting. In order to assist with the cleaning convergence we used a circular mask which had a radius of ~2.5 arcsec. We used a cleaning threshold of 0.1 mJy and performed 50 cycles of 100 iterations/cycle. The root mean square (RMS) of the continuum reaches ~0.08 mJy beam^{-1}.

4.3 SDP.11 in the image-plane

Some useful information on the source properties are directly accessible from a careful analysis of the image plane alone. In this section we will discuss these image plane properties of SDP.11 at the different wavelengths of observation.

Table 4.2: Observed (i.e. not corrected for lensing magnification) near−IR stellar and dust continuum flux densities in units of mJy. The 1.150 and 1.545 μm flux densities are taken from Negrello et al. (2014) using the wide−J F110W and wide−H F1160W filters on board of HST. The 100 and 160 μm fluxes are taken from Zhang et al. (2018) using the PACS instrument on board of *Herschel*. The 250, 350 and 500 μm fluxes are taken from Negrello et al. (2017) using the SPIRE instrument on board of *Herschel*, however their uncertainties incorporate an additional 7% calibration error (Zhang et al., 2018). The 850 μm flux is taken from Bakx et al. (2018) using the SCUBA−2 instrument on JCMT. The 880 μm is taken from Enia et al. (2018) using the SMA, which differ from that reported in Bussmann et al. (2013). The 1.2 mm is taken from Negrello et al. (2014) using the MAMBO instrument on IRAM. The ALMA fluxes at 440 and 873 μm as well as the PdBI flux at 2.0 mm were computed as part of this work (see Section 4.2 for further details).

$S_{1.150\,\mu m}$	$S_{1.545\,\mu m}$	$S_{100\,\mu m}$	$S_{160\,\mu m}$	$S_{250\,\mu m}$	$S_{350\,\mu m}$	$S_{440\,\mu m}$	$S_{500\,\mu m}$	$S_{850\,\mu m}$	$S_{873\,\mu m}$	$S_{880\,\mu m}$	$S_{1.2\,mm}$	$S_{2.0\,mm}$
413 nm	555 nm	36 μm	58 μm	90 μm	126 μm	158 μm	180 μm	305 μm	313 μm	316 μm	412 μm	719 μm
23.8±4.3	47.7±6.9	161±10	363±20	421±30	371±26	240±5.0	221±17	52±1	22±1	24±2	12±2	0.66±0.07

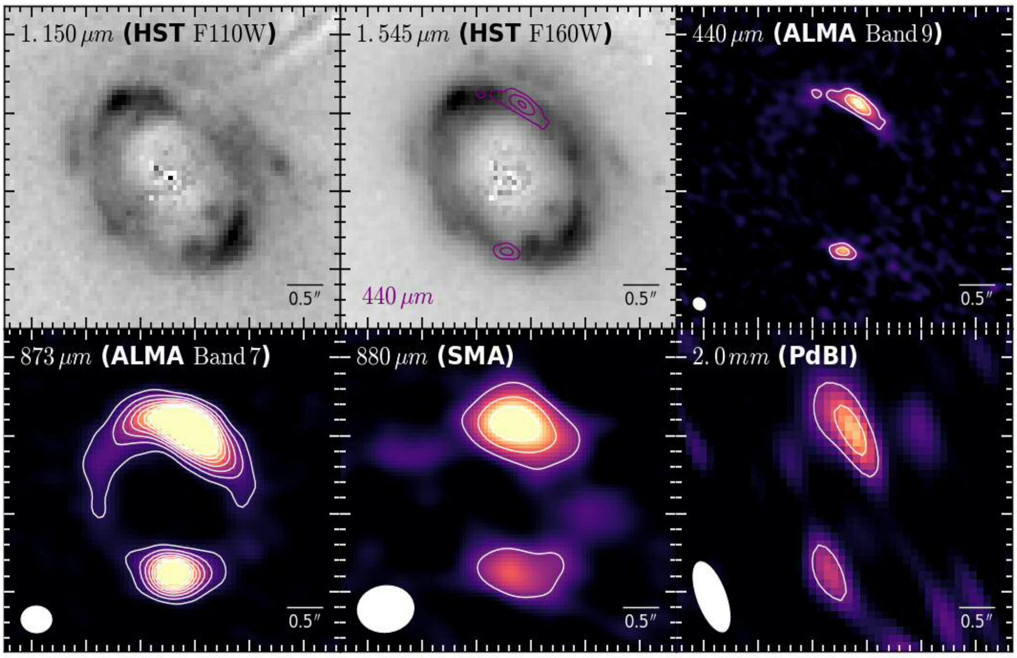

Figure 4.1: Images of the near-IR stellar and dust continuum emission for the strongly lensed galaxy *H*-ATLAS J085358.9+015537. *From Left to Right and Top to Bottom:* 1.150 μm (rest-frame ~ 413 nm) wide-J F110W HST image; 1.545 μm (rest-frame ~ 555 nm) wide-H F160W HST image; 440 μm (rest-frame ~ 158.1μm) band 9 ALMA dust continuum image with $0.17'' \times 0.14''$ resolution and with contours starting from $\pm 5\sigma$ in steps of $\pm 5\sigma$ ($\sigma \sim 1.3 \times 10^{-3}$Jy beam^{-1}); 873$\mu$m (rest-frame ~313.7 μm) band 7 ALMA dust continuum image with $0.42'' \times 0.34''$ resolution and with contours starting from $\pm 5\sigma$ in steps of $\pm 5\sigma$ ($\sigma \sim 4.6 \times 10^{-5}$ Jy beam^{-1}); 880 μm (rest-frame ~ 316.2 μm) SMA dust continuum image with $0.77'' \times 0.59''$ resolution and with contours starting from $\pm 5\sigma$ in steps of $\pm 5\sigma$ ($\sigma \sim 6.6 \times 10^{-4}$Jy beam^{-1}); 2.0 mm (rest-frame ~ 718.6μm) PdBI dust continuum image with $0.95'' \times 0.39''$ resolution and with contours starting from $\pm 3\sigma$ in steps of $\pm 3\sigma$ ($\sigma \sim 6.7 \times 10^{-5}$ Jy beam^{-1}).

4.3.1 Near-IR stellar and dust continuum emission images

In the first two panels in the top row of Figure 4.1 we show the near-IR stellar emission in the wide-J F110W (1.150 μm; rest-frame ~ 413 nm) and the wide-H F160W (1.545 μm; rest-frame ~ 555 nm) HST filters, where the emission from the lens has been subtracted using GALFIT (Peng et al., 2002). In addition, we also subtract from both panels the emission coming from the $z = 0.39 \pm 0.09$ spiral galaxy north-west (NW) of the lens. The details on the lens subtraction can be

---

[3] The SMA's antennae can be arranged in different configurations. Its most compact configuration, COM, configuration results in an angular resolution of ~ 5 arc-seconds, while its most extended configuration, VEX, the resolution is increased by ~20 times that of COM.

found in Negrello et al. (2014)

The rest of the panels from top to bottom and left to right of Figure 4.1 show the dust continuum emission at 440 μm (ALMA Band 9; rest-frame ~ 158 μm), 873 μm (ALMA Band 7; rest-frame ~ 313 μm), 880 μm (SMA; rest-frame ~ 316 μm) and 2.0 mm (PdBI; rest-frame ~ 719 μm). The peak of the emission is detected at 20σ, 150σ, 15σ and 10σ significance level, respectively. All of the above continuum images reveal quite a similar structure, with two major image components North and South of the lens, the former significantly brighter than the other. The 873 μm emission start to resolve (at >5σ significance) an almost complete Einstein ring of ~ $2.0''$ in diameter.

We have also superimposed the dust continuum at 440 μm on the 1.545 μm (second panel, top row of Figure 4.1). We can immediately see that there is a significant offset, ~ $0.5''$, between the peaks in the stellar and the dust continuum emission, which is something that has been observed many times in other SMGs at high redshift (e.g. Dye et al., 2015; Oteo et al., 2017; Massardi et al., 2018).

The dust continuum emission is detected in regions where the stellar emission is faint. One possible explanation for this is that the rest-frame UV stellar emission has been absorbed by dust in the region where it is faint. On the other hand, stellar emission is dominant in regions which are dust-poor and therefore less affected, if at all, by dust absorption. If this scenario is what we are witnessing then there are two components contributing to the total star formation rate (SFR) of the source: the un-obscured component traced by the rest-frame UV emission, and the dust obscured one traced by the rest-frame far-infrared (FIR) emission. In drawing the conclusion we are making the assumption that the ALMA Band 9 emission is tracing the bolometric dust emission (and therefore the dust-obscured star formation). This seems likely to be true but it is not necessarily so, since in the rest-frame of the galaxy ALMA Band 9 falls on the Rayleigh-Jeans tail (see later on in Section 4.5.1.1) and so is a better tracer of the column-density of dust rather than the bolometric dust emission.

We present the flux densities of the near-IR stellar and dust continuum emission in Table 4.2. The flux densities at 440 μm, 873 μm and 2.0 mm were computed as part of this work within a circular aperture of ~$4.0''$ in diameter using CASA's *imstat*. The rms noise of the image is given as the error for the flux density measurement (see Section 4.2 for details on the computation of the rms noise). The rest of the fluxes in Table 4.2 are taken from previous studies (Negrello et al., 2014; Enia et al., 2018; Bakx et al., 2018; Zhang et al., 2018).

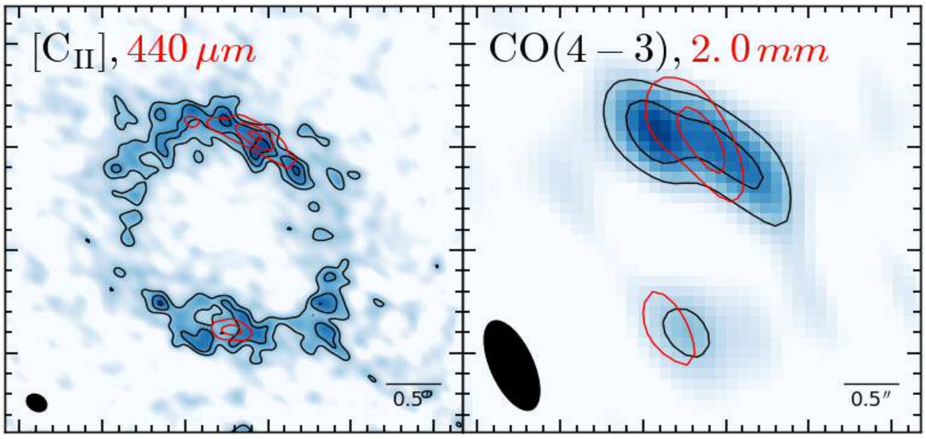

Figure 4.2: The 0^{th} moment (velocity-integrated intensity) color maps of the atomic $C_{\rm II}$ and molecular CO(4-3) lines observed with ALMA and PdBI, respectively. The red contours for the $C_{\rm II}$ start from $\pm 3\sigma$ with steps of $\pm 1\sigma$ ($\sigma \sim 1.5$ Jy beam^{-1} km s^{-1}) and for the CO(4-3) start from $\pm 3\sigma$ with steps of $\pm 3\sigma$ ($\sigma \sim 0.16$ Jy beam^{-1} km s^{-1}). We also show contours of the dust continuum at 440 μm (left panel) and 2.0 mm (right panel), where the contour levels are the same as in Figure 4.1.

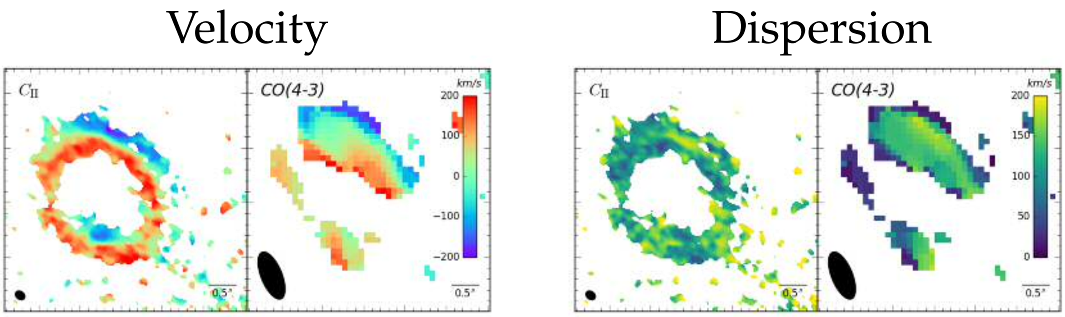

Figure 4.3: The 1^{st} moment (velocity; left two panels) and 2^{nd} moment (dispersion; right two panels) color maps of the C_{II} and CO(4-3) line. The velocity maps reveal the kinematics of the background source, which presents a significant velocity gradient. The C_{II} and CO(4-3) lines trace similar kinematic structure as shown by the close correspondence between their 1^{st} and 2^{nd} moment maps. In panel we indicate the size of the synthesised beam at the bottom left corner and the angular scale of the image at the bottom right corner.

4.3.2 Moments

As described in Sections 4.2.1.2 and 4.2.4 we have produced cubes with resolutions 27.4 and 28.3 km s^{-1} for the $C_{\rm II}$ and CO(4-3) emission lines, respectively. We use the CASA task *immoments* to compute the moments of these cubes, which we show in Figures 4.2 and 4.3. The channel range was selected to fully encompass the spectral range of both lines from the background source.

Figure 4.2 shows the 0^{th}-moment (velocity-integrated intensity) of the $C_{\rm II}$ and

CO(4-3) lines in the left and right panels, respectively. The $C_{\rm II}$ line emission displays a complete Einstein ring of ~ 2.0″ in diameter, while the CO(4-3) displays two major components. We have also superimposed (red contours) the continuum emission at 440 μm (left-panel) and 2.0 mm (right-panel) in the same figure. The dust continuum emission seem to be significantly less extended than the gas distribution as traced by both emission lines.

Figure 4.3 shows the 1^{st}-moment (left panels - velocity) and the 2^{nd}-moment (right panels - dispersion) moment maps of the $C_{\rm II}$ and CO(4-3) lines. Both the moment maps of the two emission lines show very similar structure in velocity and dispersion. The velocity map reveals the kinematics of the background source, showing a significant velocity gradient. Such velocity gradient can be reminiscent of a rotating disk or an early-stage major-merger as these system can also appear to have symmetric kinematics (only ~40-80% of merging systems show asymmetries in their kinematics; Hung et al. 2016). Both of these two scenarios will be explored later on.

4.3.3 Integrated Spectra and line fluxes

The continuum-subtracted spectra, integrated over the entire source is shown in Figure 4.4. We used an elliptical annulus to extract the flux density in each channel of the ALMA Band 9 cube with ~ 1.9″ × 1.4″ and ~ 0.50″ × 0.28″ outer and inner major/minor axis, respectively, and a position angle of 130°, measured East of North. The top panel shows the ALMA Band 9 spectra from the combination of SPW0 and SPW1, which covers the frequency range from 681.22 to 685.06 GHz (or equivalently 437.61 to 440.08 μm) while the bottom panel shows PdBI spectra. The emission lines $C_{\rm II}$ and CO(4-3) are clearly detected in the spectra with signal-to-noise (SNR) at their peak of ~ 15σ and ~ 5σ, respectively.

After extracting the spectra integrated over the elliptical apertures containing the entire spatial region of the sources, the $C_{\rm II}$ emission line was fitted with multiple Gaussian profiles. We first attempt to fit the spectra using two Gaussian profiles, which is shown as a yellow curve in the inset plot of the top panel in Figure 4.4. However, the two Gaussian profiles fit leads to significant residuals in both the blue and red part of the spectrum between −150 to 150 km s^{-1}. Therefore we tried to fit the spectrum using three Gaussian profiles, which resulted in a much better fit as shown in the top panel of Figure 4.4. The three components of the triple Gaussian fit are marked as "B" for the approaching (blue-shifted) component and "R_1" and "R_2" for the receding (red-shifted) components of the spectrum. The results that we obtain from the three Gaussian profiles fit (i.e. the line centroid

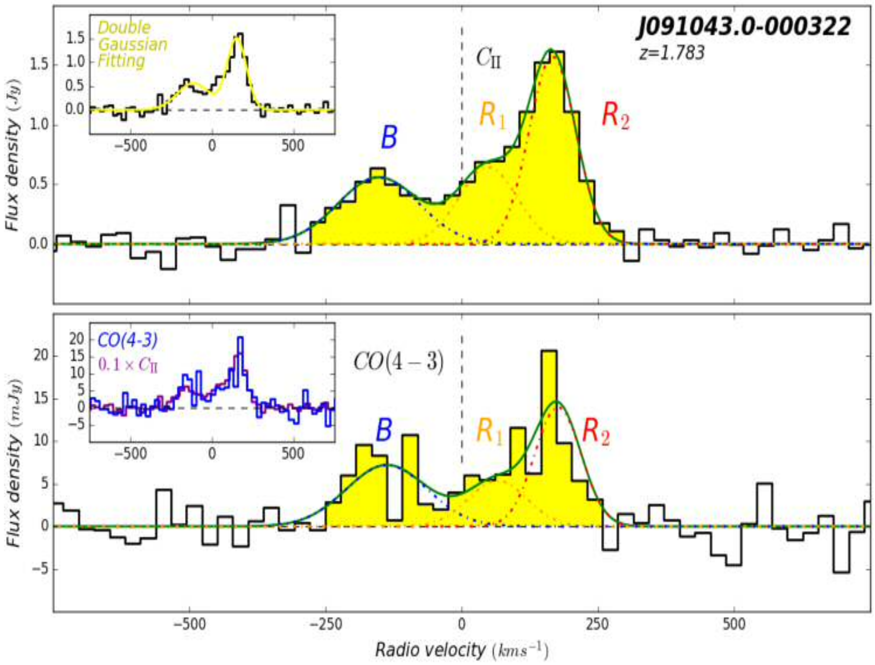

Figure 4.4: Spatially-integrated, continuum-subtracted spectra for SDP.11. *(Top row):* 440 μm ALMA Band 9 spectra of the $C_{\rm II}$ emission line with a spectral resolution of 27.4 km s^{-1} (4 channels per velocity slice were binned to generate this cube from the SPW0 and SPW1). *(Bottom row):* 2.0 mm PdBI spectra of the CO(4-3) emission line with spectral resolution of 28.9 km s^{-1}. In each panel, the yellow-filled part of the histogram corresponds to the full with at zero intensity (FHZI; i.e where the intensity drops bellow zero going from the centre of the line and outwards). The vertical dashed line represents the expected central position of the two emission lines (corresponding to $v = 0$ km s^{-1}) The dot-dashed lines represent the corresponding Gaussian decomposition: blue represents the approaching gas component (marked as "B") while orange and red represents the receding gas component (marked as "R_1" and "R_2", respectively), with the green line being the sum of the three components. The top left inset plot in the top panel shows the fit of the spectrum using a double Gaussian profile, which does not seem to capture the total line emission, while the bottom one shows the comparison of the two spectra, where the $C_{\rm II}$ spectra has been scaled for visualization purposes. The profiles of the two line emissions seem to agree remarkably well, indicating that the two components are co-spatial.

Table 4.3: Molecular line properties of SDP.11 derived from their spatially-integrated continuum subtracted spectra. We also show the corresponding properties for mid to high-J CO lines where CO(4-3) is taken from (Oteo et al., 2017) and CO(5-4), CO(6-5) and CO(7-6) which are taken from Lupu et al. (2012).

Line	ν_{rest} (GHz)	Components	u_{center} (km s^{-1})	FWHM (km s^{-1})	I_{line} (Jy km s^{-1})	$I_{comp.}/I_{tot}$	$\mu L_{line}/10^9$ ($L_{\odot}$)	$\mu L^{'}_{line}/10^{10}$ (K km s^{-1} pc^2)
[-2.0mm]		B	-137.5 ± 13.3	115.5 ± 21.1	87.1 ± 21.8	0.28 ± 0.07	11.3 ± 2.8	5.1 ± 1.3
$C_{\rm II}$	682.86	R$_1$	42.5 ± 19.2	83.0 ± 32.7	44.5 ± 18.6	0.14 ± 0.06	5.8 ± 2.4	2.6 ± 1.1
		R$_2$	163.5 ± 8.1	66.1 ± 7.1	183.1 ± 17.7	0.58 ± 0.08	23.7 ± 2.3	10.8 ± 1.0
		Total			314.7 ± 29.0		40.7 ± 3.6	18.5 ± 1.7
CO(4-3)	165.65	Total			8.9 ± 1.0		0.28 ± 0.03	8.9 ± 0.1
CO(5-4)	207.07	Total			23.0 ± 8.0		0.9 ± 0.3	14.7 ± 5.1
CO(5-6)	248.46	Total			29.0 ± 10.0		1.4 ± 0.5	12.9 ± 4.4
CO(7-6)	289.85	Total			18.0 ± 14.0		1.0 ± 0.8	5.9 ± 4.6

Notes: ν_{obs} is the observed frequency of the line, $\nu_{obs} = \nu_{rest}/(1+z)$, according to the source redshift, $z_s = 1783$. v_{center} and FWHM is the central velocity and the Full Width at Half Maximum of the Gaussian profile that resulted from our fitting procedure to the spectra. The line widths that were used to fit the CO(4-3) were assumed to be the same as those that were derived from fitting the high resolution $C_{\rm II}$ spectra. The errors for the velocity-integrated line fluxes were computed by randomly sampling (N~10000 realisations) the parameters of the Gaussian component fits.

positions and line widths, both in units of km s^{-1}) are given in Table 4.3.

We used the same three Gaussian profiles to fit the CO(4-3) spectra, fixing the line widths to the ones obtained from the $C_{\rm II}$ spectral line fit. This is because the spectra of the $C_{\rm II}$ and CO(4-3) lines have very similar profiles, as seen from their comparison in the inset plot of the bottom panel in Figure 4.4. This similarity between the spectra of two different ISM tracers is an indication that the emitting regions overlap.

In order to measure the line fluxes of each individual component we integrate the Gaussian profiles between -250 to 250 km s^{-1}. The total flux density of the line is computed by summing up the contribution from all individual components. We measure a total $C_{\rm II}$ flux density of 314.7 ± 29.0 Jy km s^{-1}, where the error comes from the uncertainty in the Gaussian profile fit. The $C_{\rm II}$ flux density that we measure is significantly higher to the one reported in (Lamarche et al., 2018). We attribute this difference to the different method of measuring the flux density. The flux density for the $C_{\rm II}$ line is given in Table 4.3 along with the flux densities of the various CO lines. The flux densities of the CO lines are not computed as part of this work, instead they are taken from Oteo et al. (2017) for the CO(4-3) and from Lupu et al. (2012) for the CO(5-4), CO(6-5) and CO(7-6) lines.

We derive the apparent (i.e. not corrected for magnification) line emission luminosities μL_{line} (in units of L$_\odot$) and $\mu L^{'}_{line}$ (in units of K km s^{-1} pc^2) according to the expressions in Solomon and Vanden Bout (2005):

$$L_{line} = 1.04 \times 10^{-3} S_{line} \Delta_v \frac{v_{rest} D_L^2(z)}{z+1}, \tag{4.1a}$$

$$L^{'}_{line} = 3.25 \times 10^{7} S_{line} \Delta_v \frac{D_L^2(z)}{v_{obs}^2 (z+1)^3}, \tag{4.1b}$$

where $S_{line}\Delta_v$ is the observed line flux density (in units of Jy km s^{-1}), v_{rest} and v_{obs} are the rest-frame and observed frequencies (in unit of GHz), and D_L is the luminosity distance (in units of Mpc). The apparent line luminosity for the $C_{\rm II}$ is $(40.7 \pm 3.6) \times 10^9$ L$_\odot$ or $(18.5 \pm 2.7) \times 10^{10}$ K km s^{-1} pc^2. The apparent luminosities are given in Table 4.3, along with the apparent luminosities of their individual components "B", "R_1" and "R_2". In the same table we also show the apparent luminosities of the various CO lines.

4.4 Strong Lens Modelling

We have applied the Warren and Dye (2003) semi-linear inversion (SLI) lens modelling methodology, which has been modified to work directly on the visibility data in the interferometric *uv-plane* (Rybak et al., 2015a; Hezaveh et al., 2016; Dye et al., 2018; Enia et al., 2018; Litke et al., 2019, Negrello et al. in prep). The method reconstructs the intrinsic source surface brightness distribution on a grid of pixels, adapting to the lens magnification pattern, plotted on Voronoi tesserae[4]. In addition, a regularisation term is introduced in order to monitor the level of smoothness of the reconstructed source and serves as a penalty term in the computation of the likelihood function (Suyu et al., 2006). The SLI method has been thoroughly described in many previous works (e.g. Warren and Dye, 2003; Dye and Warren, 2005; Suyu et al., 2006; Vegetti and Koopmans, 2009; Dye et al., 2014; Nightingale and Dye, 2015; Nightingale et al., 2018) and so we choose not to discuss the details of the method.

We model the mass distribution of the lens galaxy assuming a power-law, $\rho \propto r^{-2}$, density profile, commonly referred to as the Singular Isothermal Ellipsoid (SIE; Kormann et al., 1994), where r is the elliptical radius ($r^2 = x^2 + q^2y^2$). This model is described by five parameters: the lens Einstein radius θ_E (in units of arcsec), the orientation of the lens semi-major axis θ measured East of North and the minor-to-major axis ratio q, the displacement of the lens center Δx_{cen} and Δy_{cen}. We also introduced an external shear with two additional parameters, the shear strength γ and the shear angle θ_γ, also measured East to North. The external shear is mandatory in order to obtain a satisfactory fit to the data, and its use is justified by the presence of a spiral galaxy NE of the lensed image for SDP.11 as clearly seen form the HST image with F110W and F160W filters (Negrello et al., 2014).

As mentioned before, we performed the modelling in the uv-plane in order to overcome the caveats related to side-lobes and correlated noise from interferometric data. The number of visibilities that resulted from our observations was of the order of $\sim 10^8$ which would require many hours of computing time to process. In order to ease the computational cost, we performed some averaging reducing the size of our data (see Section 4.4.1 for more details on our treatment of the visibilities). For the non-linear parameter search we use the *emcee* python package, which implements the Goodman and Weare's Affine Invari-

---

[4] Given a set of N points on a 2D-plane, the voronoi tessalisation split this 2D-plane into N individual region. Each region corresponds to one point and is construct such as its edges are closer to this point than any other point in the same plane.

ant MCMC sampler. We used flat priors for the lens model where the values of the parameters range: $0.7\,\mathrm{arcsec} < \theta_E < 1.2\,\mathrm{arcsec}$, $0° < \theta < 180°$, $0.25 < q < 0.75$, $-0.15\,\mathrm{arcsec} < \Delta x_{cen} < 0.15\,\mathrm{arcsec}$, $-0.55\,\mathrm{arcsec} < \Delta y_{cen} < 0.15\,\mathrm{arcsec}$, $0 < \gamma < 0.25$ and $0° < \theta_\gamma < 180°$. Another factor that helps us speed up the search is the use of an elliptical annulus mask that contains the lensed emission and as little of the background sky as possible.

After determining the best-fit lens model parameters, we use them to finally reconstruct the original source morphology, and retrieve its physical properties, starting from the estimation of the magnification factor, μ. This is computed as the ratio between the total flux density of the source as measured in the source-plane (SP) and image-plane (IP), $\mu = F^{SP}/F^{IP}$, respectively. Essentially, we interpolate the Voronoi tesserae on to a regular grid and then we forward-lens this plane. We estimate the magnification by selecting only pixels in the SP with SNR > 3 ($\mu_{3\sigma}$) and SNR > 5 ($\mu_{5\sigma}$). In order to estimate the uncertainties for these quantities we perform ~ 600 realizations, each time perturbing the lens model parameters (we randomly draw each parameter from a gaussian distribution centered at the best-fit value with a standard deviation equal to each error). The final magnifications are computed as the median of the resulting distribution with errors given by the 16th and 84th percentile of the same distribution. In addition we estimate an effective radius for the reconstructed sources, which is computed as the radius of a circle with area equal to the regions with $SNR > 3$ ($r_{eff,3\sigma}$) and $SNR > 5$ ($r_{eff,5\sigma}$). The errors are computed in the same manner as for the magnification factor uncertainties. This apparently unconventional method of estimating sizes was introduced by Enia et al. (2018) to measure sizes for a sample of lensed *H*-ATLAS galaxies from observations of the dust continuum emission with SMA. This method was shown to provide a more accurate estimate of the size when compared to the results coming from the same sample (Bussmann et al., 2013) where a parametric source was used for the modelling.

4.4.1 Preliminary treatment of the visibilities

As mentioned before, it is essential to properly reduce size of our observed visibilities in order to speed up the non-linear parameter search (using the emcee package), but without loosing too much information contained in the data. The ALMA on-source observing time was not conducted continuously, but rather in steps of ~ 3 to 4 mins. As such, the visibility data reduction procedure described below was performed in each individual observing block, and for each individual spectral window. The visibilities were then concatenated together, in order to be fed to our lens modelling code and perform the non-linear search.

As a first step, we remove visibilities corresponding to "bad" channels (i.e. those with negative weights as determined from the CASA calibration pipeline). "Bad" channels are usually found at the edges of each spectral window (~4 channels at the beginning and end for each spectral windows). After the removal of those channels we performed an average over the remaining channels.

Then, we evaluate the absolute errors associated with the visibilities which is a mandatory step in order to perform proper lens modelling in the uv-plane, as the standard CASA calibration pipeline only provide relative weights (weights are the inverse of the errors). This is performed grouping together visibilities corresponding to the same baseline. We compute the rms scatter of the real and imaginary parts of the visibilities in each group, and from that we use the following expression to calculate the visibility error:

$$\sigma_V^2 = \frac{V_{\mathbb{R}}^2 \sigma_{\mathbb{R}}^2 + V_{\mathbb{I}}^2 \sigma_{\mathbb{I}}^2}{V_{\mathbb{R}}^2 + V_{\mathbb{I}}^2}, \tag{4.2}$$

where $V^2 = V_{\mathbb{R}}^2 + V_{\mathbb{I}}^2$ is the sum of the real and imaginary parts of each complex visibility. Note that the same error is assigned to each visibility corresponding to the same baseline in each observing block. At this stage each visibility has two polarisations. However, our source is not polarised and so we can perform a weighted average over this property. At this stage, all visibilities corresponding to the same baseline are assigned with the same error. We thus perform a baseline averaging, resulting to a single visibility point for each baseline grouping.

4.4.2 Lens modelling results

In order to infer our best-fit lens model we perform our non-linear search using the 440 μm ALMA Band 9 dust continuum visibility data that correspond to SPW2 and SPW3, since they do not contain any molecular line emission. Following the procedure outlined at the beginning of this section, we determine our best-fit lens model parameters which are given in Table 4.4, where the 1σ errors were computed by taking the 24th, 50th and 86th percentiles of the marginalized distributions.

We find that the lens galaxy at redshift $z = 0.7932 \pm 0.0012$ has a highly elliptical mass distribution, with a minor-to-major axis ratio of $q \sim 0.5$, and is orientated parallel to the light distribution (see Negrello et al., 2014, for details on the lens light subtraction). Our lens modelling favours a significant external shear, γ, with a strength of $\gamma \sim 0.16$, which is expected given the presence of a spiral $z = 0.39 \pm 0.09$

Table 4.4: The best-fit lens model parameters obtained from the modelling, in the *uv-plane*, of the lensed dust continuum emission in the ALMA Band 9 (440 μm). Lens model parameters are: Einstein radius θ_E (in units of arcsec), the minor-to-major axis ratio q, the orientation of the lens semi-major axis θ measured counterclockwise from West to North (in units of degrees), the displacement of the lens center Δx_{cen} and Δy_{cen} both measured with respect to the centre of the image (in units of arcsec), the shear strength γ and the shear angle θ_γ measured counterclockwise from West to North (in units of degrees). Note that the lens centre is defined with respect to the centre of the image cutout that was used for the modelling.

	model	θ_E (arcsec)	q	θ (deg)	γ	θ_γ (deg)	x_{cen} (arcsec)	y_{cen} (arcsec)
continuum ALMA (Band 9)	SIE+shear	$1.01^{+0.02}_{-0.02}$	$0.50^{+0.03}_{-0.04}$	$121.1^{+4.9}_{-4.8}$	$0.16^{+0.02}_{-0.02}$	$36.4^{+6.6}_{-6.9}$	$-0.06^{+0.03}_{-0.02}$	$-0.34^{+0.03}_{-0.03}$

galaxy ~4.5 arcsec north-west of the lens.

Our best-fit lens model parameters are significantly different from the ones reported in Enia et al. (2018), which were obtained from modelling the 880 μm SMA data[5]. This is not surprising given the better quality of our ALMA data, which allow us to determine a much more reliable lens model. A direct comparison with the best-fit model parameters found by Dye et al. (2014) from the modelling of the HST data (which are of similar quality to our ALMA data) is less intuitive as the authors use a power-law model with a slope of 1.8 instead of 2.0 (SIS). We find differences for the axis ratio, q, and the strength of the external shear, γ, which is not surprising given the degeneracy between these two parameters. Note that in Dye et al. (2014) the authors use a different definition for the position angle, θ, which brings our results and theirs in agreement. Considering all the above, we are confident that our results are very robust.

Once the best-fit parameters of our lens model are determined, we use them to reconstruct the lensed emission in all the other wavebands. Our results from the modelling are shown in Figure 4.5, where in all cases the residuals are below the noise level. It is important to note that before reconstructing the lensed emission in the other bands, we first perform a non-linear search for the lens center (keeping all other parameters fixed to the ones reported in Table 4.4), defined with respect to the centre of the image cutout, in order to overcome eventual alignment errors in the astrometry of different datasets. This will potentially correct any systematic astrometric shift between the HST and ALMA data.

We also performed the modelling in the image-plane, as a consistency check, using the publicly available lens modelling software PyAutoLens (Nightingale et al., 2018). We used the synthesized beam as our PSF and a uniform noise map. The results we obtain from the modelling in the image-plane are in good agreement with our *uv*-plane modelling results. This is also in line with Dye et al. (2018) findings, who showed that image- and *uv*-plane model fitting can yield highly consistent results with ALMA data if sufficiently high *uv*-plane coverage is achieved, and thus small "dirty" beam side-lobes (which is the case with our ALMA observations).

---

[5] Strong gravitational lens modelling suffers from degeneracies between its model parameters (e.g. Einstein radius, axis ratio and magnitude of the external shear). However, a more complex background source allows for better, more precise, determination of these parameters while simultaneously allowing for some of these degeneracies to be alleviated. In this case observations conducted at different resolution where one shows significantly more structure than the other, can lead to significantly different best-fit parameters.

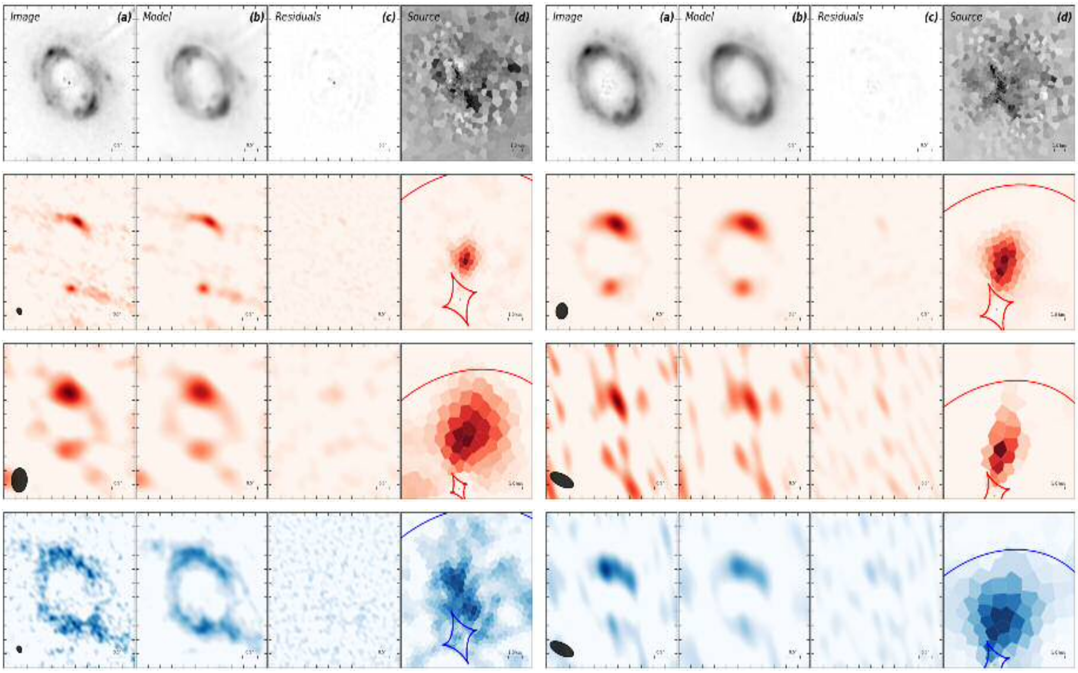

Figure 4.5: Lens modelling results for the source SDP.11. *Top row:* The 1.150 μm (F110W filter; left-panel) and 1.545 μm (F160W filter; right-panel) HST near-IR images, where the emission from the lens has been subtracted using (GALFIT Peng et al., 2002). *Top-Middle row:* The 440 μm (Band 9; left panel) and the 873 μm (Band 7; right panel) ALMA dust continuum image. *Bottom-Middle row:* The 880 μm (SMA; left panel) and 2.0 mm (PdBI; right panel) dust continuum images. *Bottom row:* The CO(4-3) and $C_{\rm II}$ line emission images. In both columns the panels, from left to right, correspond to: (a) the observed image, (b) the reconstructed image, (c) the residuals (data-model) and (d) the reconstructed source. The caustics are shown on the last panel of each sub-figure while the size of the synthesized beam is shown in the first panel of each figure as a black ellipse. We also indicate the angular scale of the images in the right bottom corner of each panel (0.5″ in the image-plane and 1 kpc in the source-plane).

4.5 SDP.11 in the source-plane

For illustrative purposes we show in Figure 4.6 the reconstructed source (showing only $> 3\sigma$ tessels) at each different observed wavelength. Each of the panels in this figure correspond to the last panel of each subplot in Figure 4.5, although shifted so that the critical curves in each panel are aligned. The necessity of shifting the axes is a consequence of modelling the centre of the lens with respect to the centre of the image cutout that was used. The basic quantities that we derive from the modelling of the lensed emission for each of the aforementioned images (i.e. sizes and magnifications) are given in Table 4.5.

Table 4.5: Properties of the reconstructed sources in the various wavelengths that we modelled the lensed emission. The quantities $\mu_{3\sigma}$ and $\mu_{5\sigma}$ correspond to the magnifications that the regions with $SNR > 3$ and $SNR > 5$ experience, while the quantities $r_{eff,3\sigma}$ and $r_{eff,5\sigma}$ (in units of kpc) correspond to the radius of a circle with area equal to the areas $A_{3\sigma}$ and $A_{5\sigma}$ of the regions with $SNR > 3$ and $SNR > 5$, respectively.

Property	Unit	ALMA 440 μm	ALMA 873 μm	SMA 880 μm	PdBI 2.0 mm	C_{II} 1900.54 GHz	CO(4-3) 461.041 GHz
$\mu_{3\sigma}$		7.1±1.6	6.2±1.2	5.4±0.7	7.1±1.3	8.3±0.8	7.5±1.4
$\mu_{5\sigma}$		6.8±1.6	5.8±1.2	5.4±1.0	7.2±2.0	9.7±1.4	7.0±1.8
$A_{3\sigma}$	kpc^2	6.2±1.8	13.9±2.6	22.9±3.4	16.6±4.3	36.3±4.3	22.9±3.4
$A_{5\sigma}$	kpc^2	3.8±1.4	9.1±2.1	12.6±2.5	7.1±1.9	15.2±1.4	12.6±2.5
$r_{eff,3\sigma}$	kpc	1.4±0.2	2.1±0.2	2.7±0.2	2.3±0.3	3.4±0.2	2.7±0.2
$r_{eff,5\sigma}$	kpc	1.1±0.2	1.7±0.2	2.0±0.2	1.5±0.2	2.2±0.1	2.0±0.2

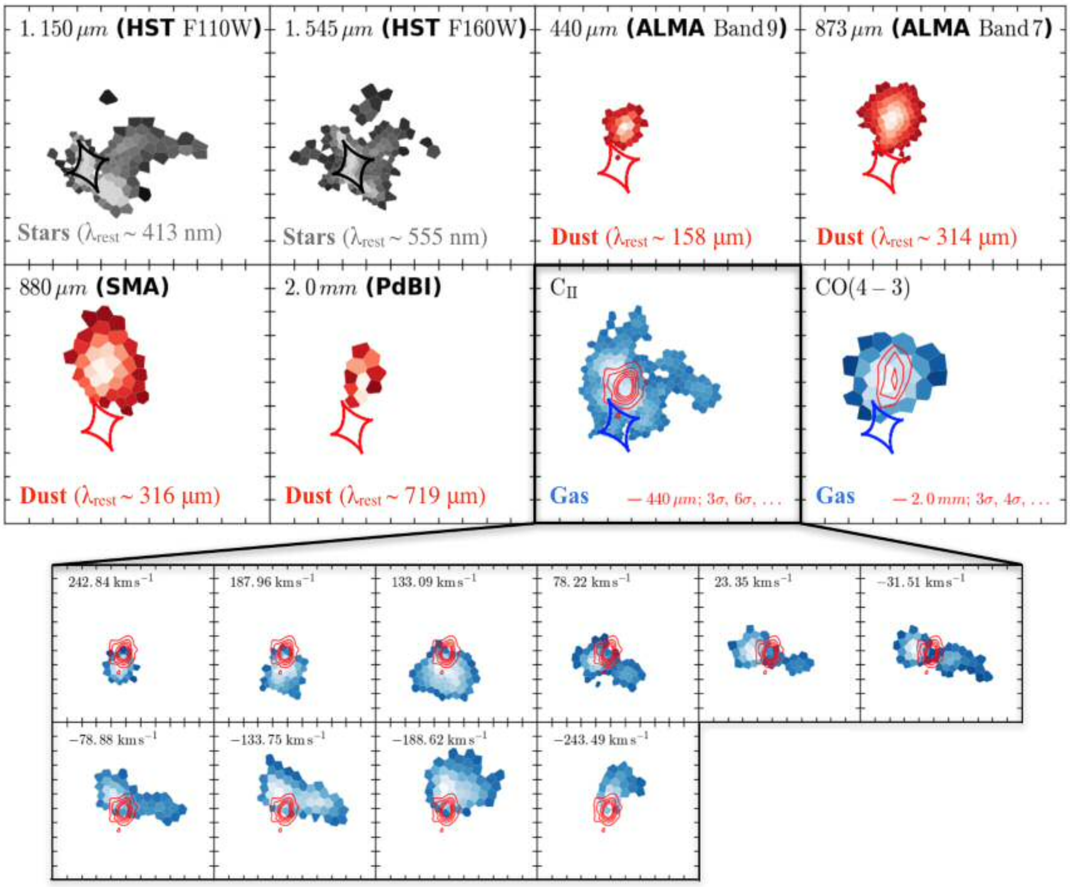

Figure 4.6: The reconstructed source (showing only $> 3\sigma$ tassels) at each different observed wavelength: *From Left to Right and Top to Bottom*: 1.150 μm (HST F110W), 1.545 μm (HST F160W), 440 μm (ALMA Band 9), 873 μm (ALMA Band 7), 880 μm (SMA), 2.0 mm (PdBI), $C_{\rm II}$ and CO(4-3). *(Bottom panels):* The reconstructed $C_{\rm II}$ line emission in each velocity slice (which is indicated at the top left corner in each panel). In each panel we show the contours of the reconstructed dust continuum emission at 440 μm (ALMA Band 9) where the contours start from $\pm 3\sigma$ with steps of $\pm 3\sigma$. The colored curve is each panel corresponds to the radial caustic curve.

4.5.1 Dust

The reconstructed dust continuum emission is shown in the last and first two panels of the top and bottom rows of Figure 4.6, respectively, where the corresponding wavelength is indicated at the top left corner of each panel. The overall morphology of the dust continuum emission is similar between the different bands, showing a compact distribution with a single well defined peak. We note that the apparent difference in spatial extent of dust continuum emission in the different bands is not intrinsic but rather a consequence of the difference in sensitivity of the various observations (see Appendix B).

We estimate that the spatial extent of the dust continuum emission at 440

μm is $A_{3\sigma} = 6.2 \pm 1.8$ kpc^2 at a $>3\sigma$ level, corresponding to an effective radius of $r_{eff,3\sigma} = 1.4 \pm 0.2$ kpc (see Table 4.5). However, in order to compare our finding with those in the literature we follow the standard approach of fitting a Gaussian profile to the reconstructed dust continuum emission. We use the python package *scipy.curve_fit* to perform the fit (see Figure B.2 in Appendix B), finding a FWHM of ~0.6 and ~0.7 kpc for the minor and major axis, respectively, where the latter forms an angle of ~70 degrees with the x-axis. The measured size of the dust continuum emission is consistent with other studies of SMG (Bussmann et al., 2012; Hezaveh et al., 2013; Simpson et al., 2015; Spilker et al., 2016; Hodge et al., 2016, 2018; Dye et al., 2018; Enia et al., 2018; Gullberg et al., 2018; Rujopakarn et al., 2019), albeit closer to the lower end side of the distribution of sizes.

We estimate a magnification factor of $\mu_{3\sigma} = 7.1 \pm 1.6$ from the modelling of the dust continuum emission at 440 μm. Accounting for the boost in angular resolution offered by strong lensing, where the average scale magnification is computed as $\sqrt{\mu}$, we can probe scale down to ~500 − 600 pc. At these scales, the distribution of dust appears to be very smooth with no evidence for clumps, which have been reported in other studies of SMGs (e.g. Hodge et al., 2012, 2015; Swinbank et al., 2015; Dye et al., 2015; Hodge et al., 2018; Rujopakarn et al., 2019)

4.5.1.1 Spectral Energy Distribution (SED) Modelling

We model the SED of SDP.11 using the de-magnified (assuming a magnification factor of $\mu = 7.1 \pm 1.6$ to de-magnify the PACS and SPIRE flux densities) rest-frame fluxes densities from FIR (~36 μm) to sub-mm (~719 μm) wavelengths. We adopt as our SED template a modified blackbody spectral energy distribution, consisting of two dust components with different temperatures, whose functional form is given by Eq. 1.1.

The fitting of our SED template to our observed data points is performed using the *emcee* package (Foreman-Mackey et al., 2013). During the fitting process we fix the emissivity index ($\beta = 2$; Pearson et al., 2013), and we use the redshift of the source ($z_s = 1.783$) to convert to rest-frame wavelengths (see Eq. 3.2.1). We show the best-fit SED model for SDP.11 in Figure 4.7 as the purple solid line, where the green and blue dashed lines correspond the hot and cold dust components, respectively. We find $T_h = 50.3 \pm 4.3$ K, $T_c = 25.3 \pm 1.2$ K and $\alpha = 32.4 \pm 9.4$ as our best-fit parameters of our SED model. The error in the redshift measurement is negligible and so is not taken into account when computing errors for the best-fit parameters of the our SED template.

We estimate the total magnification-corrected far-IR (FIR) luminosity, L_{IR},

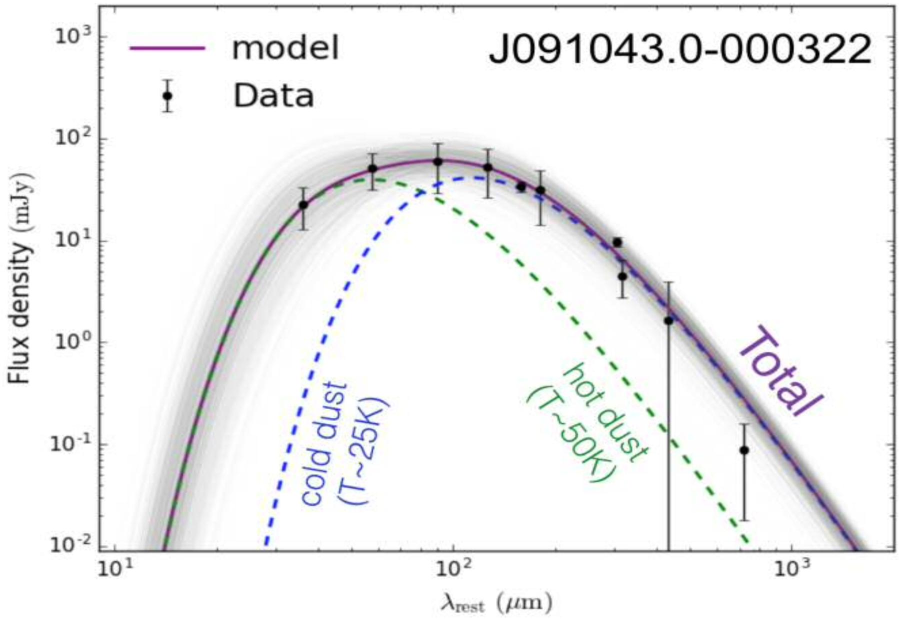

Figure 4.7: The best-fit SED model of SDP.11. The fluxes that were used for the fitting are given in Table 4.2. The red and blue dashed lines show the decomposition of the SED into the hot (~ 50K) and the cold (~ 25K) components, respectively, where the purple line is the sum of the different temperature components. The grey lines were produced by perturbing the parameters of the SED model 1σ around the best-fit values.

for SDP.11 (in units of L$_\odot$) by integrating our best-fit SED model, S_ν, between 8-1000 μm in the rest-frame, using Eq. 1.3. The total FIR luminosity and its error, $L_{IR} = (7.2^{+2.5}_{-1.8}) \times 10^{12}$ L$_\odot$, are computed from the percentiles of the distribution that results from $N \sim 10000$ realisations, where we randomly sample the posteriors of our SED model parameters. In the same manner we compute the total IR luminosities of the hot and cold dust components finding $L_{IR,h} = (4.6 \pm 2.8) \times 10^{12}$ L$_\odot$ and $L_{IR,c} = (2.5 \pm 2.8) \times 10^{12}$ L$_\odot$, respectively. The value of the total L_{IR} is in good agreement with the one reported in Enia et al. (2018), where the authors used a single temperature backbody SED model to fit the sum-mm fluxes.

We estimate the star formation rate (SFR) for SDP.11 (in units of M$_\odot$ yr^{-1}) from the magnification-corrected FIR luminosity, L_{IR}, using Eq. 1.4. We compute a star formation rate of $SFR = 936^{+325}_{-234}$ M$_\odot$ yr^{-1}, however we note that this value might be overestimated due to the presence of an AGN in SDP.11 (Massardi et al., 2018). In adittion, we can estimate the star formation rate density, Σ_{SFR}, using the area of the reconstructed source corresponding to $> 3\sigma$ pixels, $A_{3\sigma} = 6.2 \pm 1.8\, kpc^2$. The value we obtain for the star formation rate density, $\Sigma_{SFR} = 151 \pm 36\, M_\odot yr^{-1} kpc^{-2}$, is consistent with the average Σ_{SFR} found in the most luminous starburst galaxies that have been observed at high redshift ($\sim 80 - 1000\, M_\odot yr^{-1} kpc^{-2}$; Tacconi et al., 2006; Iono et al., 2016).

4.5.1.2 Dust Mass

We can also compute the dust mass for SDP.11, following Dunne et al. (2011), from

$$M_d = \frac{S_{850} D_L^2 K}{(1+z)\kappa_{850} B(\nu_{850}, T)}, \tag{4.3}$$

where T is the dust temperature of the hot dust component, K is the K-correction factor (given by Eq. 2 in Dunne et al., 2011) and κ_{850} is the dust mass absorption coefficient which we take to be equal to 0.077 $\mathrm{m}^2\ \mathrm{kg}^{-1}$ (James et al., 2002; da Cunha et al., 2008; Dunne et al., 2011) for a dust emissivity index of $\beta = 2$. Substituting the magnification-corrected flux density at 850 μm, $S_{850} = 7.3 \pm 1.7$ mJy, along with all other values in the above equation we estimate a dust mass of $M_d = (4.3 \pm 1.2) \times 10^8$ $\mathrm{M}_\odot$.

Our estimate of the dust mass together with the SFR puts SDP.11 at an offset from the empirical relationship between the two properties which was determined by (Rowlands et al., 2014) for a sample of high redshift SMGs and local ULIRGs. Dye et al. (2018) suggests that a potential explanation for this offset is the presence of an AGN. In fact recent X-rays observations with Chandra (Massardi et al., 2018) verify the presence of an AGN in SDP.11, which was already suggested by Negrello et al. (2014), finding it to be co-spatial with the peak of the dust continuum emission and potentially contributing to the total FIR luminosity.

4.5.2 Gas

The distribution of molecular and atomic gas is resolved in SDP.11 using the CO(4-3) and C_{II} emission lines. C_{II} originates from photodissociation regions (PDRs) found at the surfaces of molecular clouds, which are exposed to ionizing UV radiation from young stars. The reconstructed emission of these two lines is shown in the last and second to last panels of Figure 4.6, respectively. In the same two panels, we also show contours of the dust continuum emission at 2.0 mm and 440 μm, respectively, where contour levels start at 3σ and increase in steps of 3σ. In both cases the dust continuum emission is significantly less extended than the corresponding line emission in the same band. Specifically, the atomic C_{II} line is ~2.5 times more extended, at the $> 3\sigma$ level, than the dust continuum emission at 440 μm. This is consistent with previous studies of high redshift SMGs (Swinbank et al., 2012; Nesvadba et al., 2016; Gullberg et al., 2018; Litke et al., 2019; Rybak et al., 2019).

The lower resolution PdBI observations, ~ 0.9 arcsec translating to ~ 2.8 kpc in the source-plane, seem to suggest that the dust and molecular gas are co-spatial, with the latter being slightly more extended. However, our higher resolution ALMA Band 9 data reveal that the gas distribution, as traced by the atomic C_{II} line, breaks into smaller clumps (~ $2-3$ clumps can be identified above 10σ). More surprising is that none of the clumps is associated with the peak of the dust continuum emission. Unfortunately, comparing the reconstructed emission of the C_{II} with the CO(4-3) line in terms of spatial extent is not straightforward, as the two observations have significantly different resolutions and sensitivities. Tapering the ALMA visibilities, in order to achieve the same resolution as with the PdBI observations, leads to a very small number of visibilities to perform the reconstruction which in this case might not even be reliable. Higher resolution observations of the CO molecular line are required for a more robust comparison. However, as a general remark we see that the reconstructed emission from both lines is broadly co-spatial.

4.5.2.1 Spectrum

In the bottom panels of Figure 4.6 we show the reconstructed C_{II} line emission in each velocity slice of ~ 54 km s^{-1} resolution cube. We can clearly see that the position of the reconstructed source changes significantly with respect to the caustic as a function of velocity. We, therefore, expect that different parts of the source to experience different magnification factors, an effect known as differential magnification. This differential magnification effect needs to be accounted for as it will affect the inferred intrinsic shape of the spectrum. We compute the magnification factors $\mu_{3\sigma}$ and $\mu_{5\sigma}$ in each velocity slice, which we show in the top panel of Figure 4.8 as yellow and purple, respectively, where the shaded regions represent the error for each measurement. We see a continuous increase of the magnification factor as we move towards higher velocities. This is because the regions of the gas associated with the red-shifted component are located closer to the caustic and hence experience significantly higher magnifications (ranging from ~ 6 to 16) compared to the blue-shifted component (~ 3.5 to 6). In addition, we also compute the effective radii $r_{eff,3\sigma}$ and $r_{eff,5\sigma}$ as a function of velocity, which are shown in the inset plot of the top panel in the same Figure. Considering only the effective radii computed using $> 3\sigma$ pixels, we find that the red-shifted component is slightly more compact compared to the blue-shifted component.

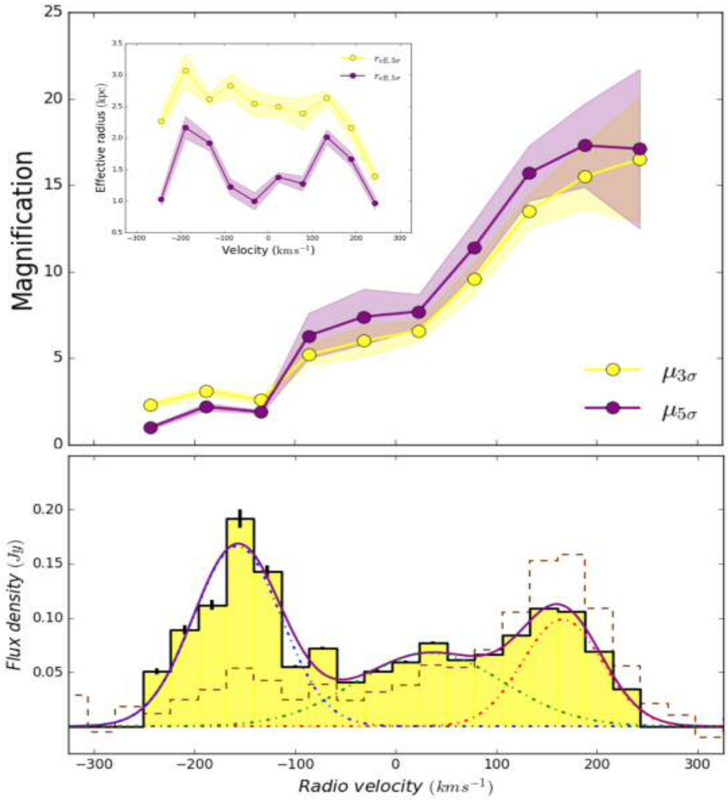

Figure 4.8: *(Top panel):* The magnification, μ, as a function of velocity for the $C_{\rm II}$ line emission cube. The yellow and purple curves correspond to regions in the source-plane with SNR>3 and SNR>5 experiencing there properties. The inset plot show the same but for the effective radius (r_{eff}). *(Bottom panel):* The intrinsic spectrum (i.e. corrected for differential lensing magnification according to the top panel of the same figure) of the $C_{\rm II}$ line emission. The purple curve shows the sum of the three Gaussian components that were used for the fitting: the blue curve represents the "B" blue-shifted, the green "G" and red "R" represents the red-shifted component ("G" and "R" correspond to the "R_1" and "R_2" components from Figure 4.4). The brown dashed histogram shows the scaled spectrum before magnification correction was applied.

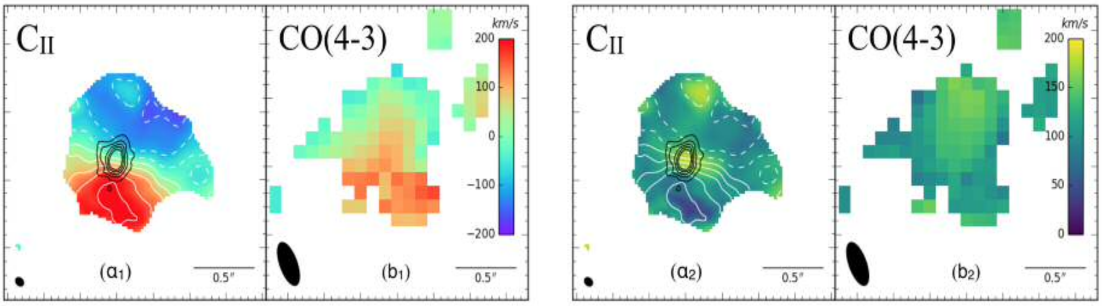

Figure 4.9: The 1^{st} moment (velocity; left two panels) and 2^{nd} moment (dispersion; right two panels) color maps of the reconstructed C_{II} and CO(6-5) line. The velocity maps reveal the kinematics of the background lensed galaxy SDP.11 which shows a significant velocity gradient. The white contours in panels (α_1) and (α_2) correspond to velocities starting from -200 km/s and increasing in steps of 100 km/s. The C_{II} and CO(6-5) lines trace similar kinematic structure as shown by the close correspondence between their 1^{st} and 2^{nd} moment maps. In each panel we indicate the size of the synthesised beam in the source plane (accounting for the increase in angular resolution by a factor of $\sim \sqrt{\mu}$) at the bottom left corner and the angular scale of the image at the bottom right corner.

We correct the observed spectrum of the $C_{\rm II}$ line for the effect of differential magnification using the computed magnification as a function of velocity. The de-magnified spectrum is shown in the bottom panel of Figure 4.8 as the yellow filled histogram, while the original un-corrected spectrum is shown as the brown dashed histogram, which has been scaled for visualization purposes. Even after correcting for the effect of differential magnification, it appears that the intrinsic $C_{\rm II}$ emission line spectrum is also asymmetric. We are going to discuss a potential reason for the assymetry of the spectrum in Section 4.6.

We fit the de-magnified spectrum using three Gaussian profiles, following the same procedure outlined in Sec. 4.3.3. The resulting fluxes are reported in Table 4.6 for each of the individual "B","G" and "R" components. Comparing the individual linewidths we see that the "B" and "R" components have very similar linewidths, which are consistent within the errors, while the "G" component is as twice as large as the other two. Most of the $C_{\rm II}$ line flux is coming from the "B" component (~ 45%), while the "G" and "R" components have almost similar contribution to the total flux.

4.5.2.2 Moments

Finally we compute the moment maps of the reconstructed cube following the same procedure outlined in Section 4.3.2. These are shown in the panels (α_1) and (α_2) of Figure 4.9 for the velocity and dispersion maps, respectively. In these panels

Table 4.6: Molecular line properties of SDP.11, which were derived from their spatially-integrated continuum subtracted spectra in the source plane.

Line	ν_{obs} (GHz)	Components	v_{center} (km s^{-1})	FWHM (km s^{-1})	I_{line} (Jy km s^{-1})	$I_{comp.}/I_{tot}$	$L_{line}/10^9$ ($L_\odot$)	$L^{'}_{line}/10^{10}$ (K km s^{-1} pc^2)
$C_{\rm II}$		B	-157.5 ± 2.9	43.8 ± 2.6	18.3 ± 1.3	0.45 ± 0.05	2.37 ± 0.17	1.08 ± 0.08
		G	33.6 ± 17.3	72.8 ± 23.3	12.3 ± 4.0	0.30 ± 0.10	1.59 ± 0.52	0.72 ± 0.24
		R	165.5 ± 6.2	39.6 ± 5.5	9.8 ± 2.3	0.24 ± 0.06	1.27 ± 0.30	0.58 ± 0.14
		Total			40.5 ± 4.8		5.23 ± 0.62	2.38 ± 0.29

we also show contours of the dust continuum emission at 440 μm, where contours levels are the same as in Figure 4.6. On the other hand, panels (b_1) and (b_2) in the same figure show the corresponding moment maps which were computed using the reconstructed cube of the CO(4-3) line. The kinematical morphology of the CO(4-3) line is consistent with that of the $C_{\rm II}$ line, suggesting that the molecular gas feels the same gravitational potential as the photodissociation regions (PDRs).

To first order, the velocity map of SDP.11 suggests that this system is consistent with a rotating disk showing a smooth gradient along the NW to SE direction with no obvious asymmetries. On the other hand, that is less obvious when looking at the dispersion map instead, which shows clear sings of assymetries in the most northern and southern parts of the source. We need to note that based on the kinematics of the system alone, it is not straightforward to derive a definitive conclusion about the nature of this system, as it has been shown that ~40-80% of merging systems show asymmetries in their kinematical structure (Hung et al., 2016). In Section 4.6 we will explore these two cases individually in order to try and understand the nature of our source.

4.5.2.3 Gas masses

Molecular gas provides the fuel for the formation of new stars (see review by Carilli and Walter, 2013). The typical approach to estimating molecular gas masses is to use the CO(1-0) line luminosity, $L^{'}_{CO(1-0)}$ and substitute it in the linear relation,

$$M_{gas} = \alpha_{CO} L^{'}_{CO(1-0)}, \tag{4.4}$$

where α_{CO} is the CO-to-H$_2$ conversion factor (see Bolatto et al., 2013, for a review). Since we do not have an estimate of the CO(1-0) line luminosity we approximate it using the CO(4-3) line luminosity together with the conversion factor, r_{43}, which for SMGs is ~0.46 (Carilli and Walter, 2013, where r_{43} is the ratio between the CO(1-0) and CO(4-3) line luminosities.). We assume a CO-to-H$_2$ conversion factor of $\alpha_{CO} \sim 0.8\ M_{\odot}/(Kkms^{-1}pc^{2})$ for consistency with previous studies of this object (e.g. Lupu et al., 2012; Massardi et al., 2018), which is typical for local ULIRGs. However, we need to note that more recent studies of high redshift ($z > 1.5$) starburst galaxies (e.g. Aravena et al., 2016; Béthermin et al., 2016; Popping et al., 2017) indicate that this value ranges between $0.8 < \alpha_{CO} < 1.5$ and so our estimate of the molecular gas mass from measurements of the CO(4-3) line should be taken as a lower limit. Following this approach we estimate a molecular gas mass of $M_{gas} \sim (2.1 \pm 0.5) \times 10^{10} M_{\odot}$. The only sources of uncertainty in this measurement come from the error in our estimate of the magnification factor derived from the modelling of the CO(4-3) line emission and the error in the estimate of the CO(4-3) line flux. Considering that the conversion factors α_{CO} and r_{43} are very uncertain our error estimate should be taken as a lower limit. In addition, we also find a similar value for the gas mass, $M_{gas} \sim (6.5 \pm 0.4) \times 10^{10} M_{\odot}$, by scaling the dust mass (see Section 4.5.1.2) assuming a typical dust-to-gas ratio of 150 (Dunne et al., 2000; Sandstrom et al., 2013; Swinbank et al., 2014). An alternative approach would be to use the $C_{\rm II}$ apparent luminosity, $L^{'}_{C_{\rm II}}$, and substitute in the linear relation, $M_{gas} = \alpha_{C_{\rm II}} L_{C_{\rm II}}$, where $\alpha_{C_{\rm II}}$ is the $C_{\rm II}$-to-H_2 conversion factor. This factor was constrained to $\alpha_{C_{\rm II}} \sim 10 \pm 2$ M$_{\odot}$/L$_{\odot}$ (Swinbank et al., 2012). Following this approach we estimate a gas mass of $M_{gas} \sim (5.2 \pm 0.2) \times 10^{10} M_{\odot}$.

Recently, Scoville et al. (2016, 2017) combined measurements of molecular gas masses inferred from CO detections and dust continuum measurements in order to calibrate an empirical relation between the two properties. Here we use this relation by Scoville et al. (2016, 2017) which is given by,

$$\begin{aligned} \frac{M_{gas}}{10^{10} M_{\odot}} =& 1.78 \left(\frac{S_{\nu_{obs}}}{mJy}\right) (1+z)^{-4.8} \left(\frac{\nu_{850\mu m}}{\nu_{obs}}\right)^{3.8} \left(\frac{D_L}{Gpc}\right)^{2} \\ & \times \left\{\frac{6.7 \times 10^{19}}{\alpha_{850}}\right\} \frac{\Gamma_0}{\Gamma_{RJ}} \quad for\ \lambda_{rest} \geq 250\,\mu m \end{aligned} \tag{4.5}$$

where α_{850} is an empirical constant given by the ratio $\alpha_{850} = L_{\nu_{850}}/M_{gas}$ and it's value is taken to be $\alpha_{850} = (8.4 \pm 1.7) \times 10^{19}$ erg s^{-1} Hz^{-1} M$_{\odot}^{-1}$, which was calibrated using a sample of SMGs at redshift z~2 (Scoville et al., 2017). The correction factor, Γ_{RJ}, in Eq. 4.5 is given by

$$\Gamma_{RJ}(T_d, \nu_{obs}, z) = \frac{h\nu_{obs}(1+z)/kT_d}{e^{h\nu_{obs}(1+z)/kT_d} - 1} \tag{4.6}$$

where T_d is the temperature of the cold dust component, T_d = 25 K, and $\Gamma_0 = \Gamma_{RJ}(T_d, \nu_{obs}, z = 0)$ (see Appendix A in Scoville et al. (2016) for more details on the derivation of this expression). Using the magnification-corrected flux density measured at 850 μm, $S_{850\mu m} = 7.3 \pm 1.7$ mJy, and substituting all quantities in Eq. 4.5 we estimate a gas mass of $M_{gas} = (16.6 \pm 3.9) \times 10^{10}$ M$_{\odot}$, which is significantly higher than the measured value from the other two methods. This discrepancy is explained by the fact that Scoville et al. (2016, 2017) used a CO-to-H_2 conversion factor of $\alpha_{CO} \sim 6.5\ M_{\odot}/(Kkms^{-1}pc^2)$. If we instead use this factor to derive the gas mass from our CO measurement we find $M_{gas} \sim (17.4 \pm 4.2) \times 10^{10} M_{\odot}$, bringing the values derived from the two methods in total agreement.

Regardless of the method we use, however, the measured molecular gas mass of SDP.11 is still in line with other previous studies targeting high redshifts SMGs, where values range between $(1-30) \times 10^{10}$ $M_{\odot}$ (e.g Bothwell et al., 2013; Aravena et al., 2016; Yang et al., 2017; Huynh et al., 2017; Harrington et al., 2018).

4.6 The Nature of SDP.11

Previous studies of the nature of high redshift SMGs separate them into two different categories where a system is interpreted either as a smooth/clumpy rotating disk typically in the process of collapse (e.g. Hodge et al., 2012; Dye et al., 2015; Rivera et al., 2018; Tadaki et al., 2018; Calistro Rivera et al., 2018) or as if it is undergoing a major-merger event (e.g. Engel et al., 2010; Spilker et al., 2015; Litke et al., 2019; Yang et al., 2019). In the following sub-sections we are going to employ different strategies that have been used in the literature in order to investigate the nature of SDP.11 and decide to which of these two categories this system belongs.

4.6.1 The case for a major-merger

We first investigate the possibility that SDP.11 is undergoing a major-merger event. In order to do that we reconstruct the lensed $C_{\rm II}$ emission using visibilities corresponding to channels with velocities between -250 to 0 km/s ("B" component) and between 0 to +250 km/s ("R" component). These are shown in the left top and bottom panels of Figure 4.10, where blue and red contours show the 3σ and 5σ levels of their spatial extent.

We fit a double Gaussian profile separately to the reconstructed emission of the two components, following the same procedure outlined in Sections 4.5.1 and 4.5.2. The best-fit models are show in the middle panel of Figure 4.10, with blue and red for the "B" and "R" components, respectively. The FWHM of the major and minor axis of the main component of our model for each component are shown in the upper left corner in the same panel. The peaks of the two components are separated by a projected distance of ~ 2.2 kpc and their difference in velocities are ~ 300 km/s. These observed offsets between the two components can be used to argue that SDP.11 is actually comprised of two galaxies undergoing a major-merging event (e.g. Neri et al., 2014; Spilker et al., 2015; Litke et al., 2019). In the same panel we also show contours of the reconstructed dust continuum emission at 440 μm, where contours levels are the same as in Figure 4.6. We can clearly see that the dust continuum emission originates from a region between the two components. According to our SED modelling the emission in this band falls in the region of the RJ tail, which traces the bulk of the dust mass but not

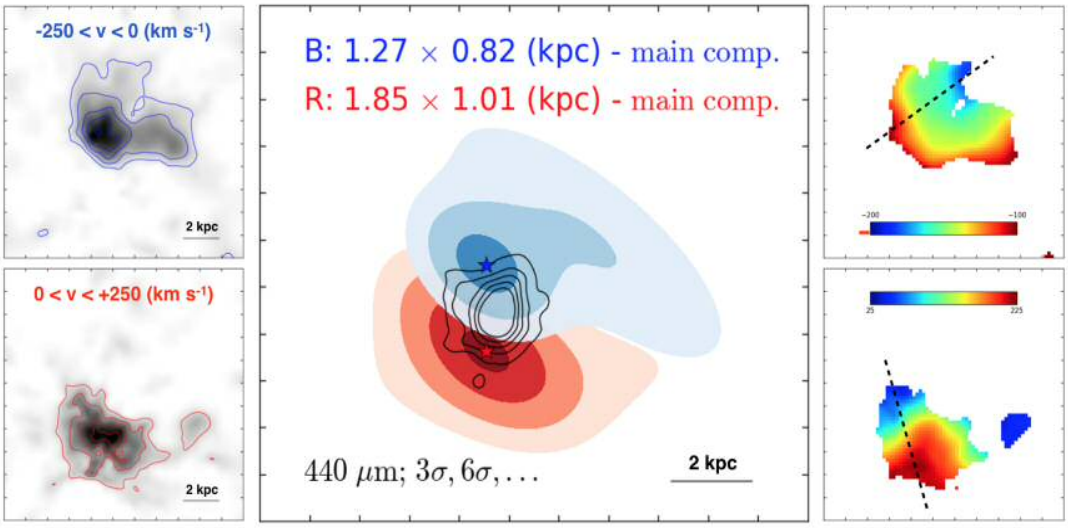

Figure 4.10: *(Left panels):* The reconstructed $C_{\rm II}$ line emission using channels corresponding to velocities in the range between -250 to 0 km/s ("B" component; top panel) and 0 to +250 km/s ("R" component; bottom panel). The scale of the images is indicated at the bottom right corner. *(Middle panel):* The best-fit double Gaussian profile models for the "B" (blue) and "R" (red) components, where the FHWM of the major and minor axis of the main Gaussian component of our model is indicated at the top left corner. The peak flux of each component is indicated with star, where the spatial offset between the two is ~2.2 kpc. *(Right panels):* The velocity (1^{st} moment) maps of the "B" (top) and "R" (bottom) components of the $C_{\rm II}$ emission. The dashed lines have been drawn by eye to indicate the position angle of the kinematical rotation axis.

necessarily the obscured star formation activity. If we make the assumption that the distribution of the FIR emission from PACS and SPIRE follow the ALMA dust continuum emission then that would further supports the merger scenario where we have a burst of star formation in the region between the interacting galaxies (e.g. Antennae Galaxies; Mirabel et al., 1998).

The merger scenario is further supported by the fact that the two distinct components ("B" and "R") show independently signs of rotation. This can be seen from the velocity maps of the two components which are shown in the right top and bottom panels of Figure 4.10 for the "B" and "R" components, respectively. These were computed following the same procedure as in Section 4.3.2, but only collapsing channels corresponding to the velocity range that was used to reconstruct the $C_{\rm II}$ line emission of each component. The velocity maps are masked at the 3σ level of the reconstructed emission of the corresponding component. The dashed lines in these panels have been drawn by eye to represent the kinematical rotational axis.

Another indication for the merger scenario comes from the de-magnified (i.e.

intrinsic) spectrum of the C_{II} line (see bottom panel of Figure 4.8). We can clearly see an asymmetry between the "B" and "R" components of the spectrum with a significant decrease in emission for velocities between these two components. Furthermore, obvious asymmetries are observed in the reconstructed dispersion map (see right panels in Figure 4.9), where the observed asymmetries are co-spatial with the reconstructed "B" and "R" components.

Finally, as discussed in Section 4.5.1, SDP.11 harbours an AGN whose peak flux position is co-spatial with the peak in the dust continuum emission (see Figure 1 in Massardi et al., 2018). It has been shown that mergers can trigger the onset of an AGN (e.g. Wang et al., 2013) and in fact this has been observed in local ULIRGs undergoing a major-merger event (e.g. Sanders and Mirabel, 1996) as well as in high redshift SMGs (e.g. Rawle et al., 2014).

4.6.2 The case for a clumpy rotating disk

We are now going to investigate if the system is consistent with being a clumpy rotating disk rather than a major merger. We have already reconstructed the C_{II} line emission in each velocity slice of the ~54 km s^{-1} resolution cube (see Figure 4.6) and produced it's moment maps (see Figure 4.9). As discussed before, the reconstructed velocity map ressembles typical signatures of a rotating disk (e.g. Hodge et al., 2012, 2016; Dye et al., 2015; Swinbank et al., 2015).

We start by adopting a simple circular rotating thin disk model for SDP.11, where the disk motion is totally determined by the gravitational potential of the disk. We assume that the potential of the disk can be described by an exponential profile, so that the surface mass density can be written as,

$$\Sigma(R) = \Sigma_0 e^{-R/R_d} \tag{4.7}$$

where Σ_0 is the disk's surface density and R_d is it's radius. Following the prescription by Freeman (1970) the radial velocity profile can be written as

$$V^2(R) = 4\pi G \Sigma_0 R_d y^2 \left[I_0(y)K_0(y) - I_1(y)K_1(y)\right] \tag{4.8}$$

where $y = R/2R_d$, G is the gravitational constant, I_n and K_n are the Bessel function of the first and second kind. In order to fit the kinematics, we take a slice of the velocity map along the axis indicated by the black dashed line in the inset plot of Figure 4.11 which passes through the peak of the dust continuum emission (see Figure 4.9). We fit our model (given by Eq. 4.8) to the data (black points in

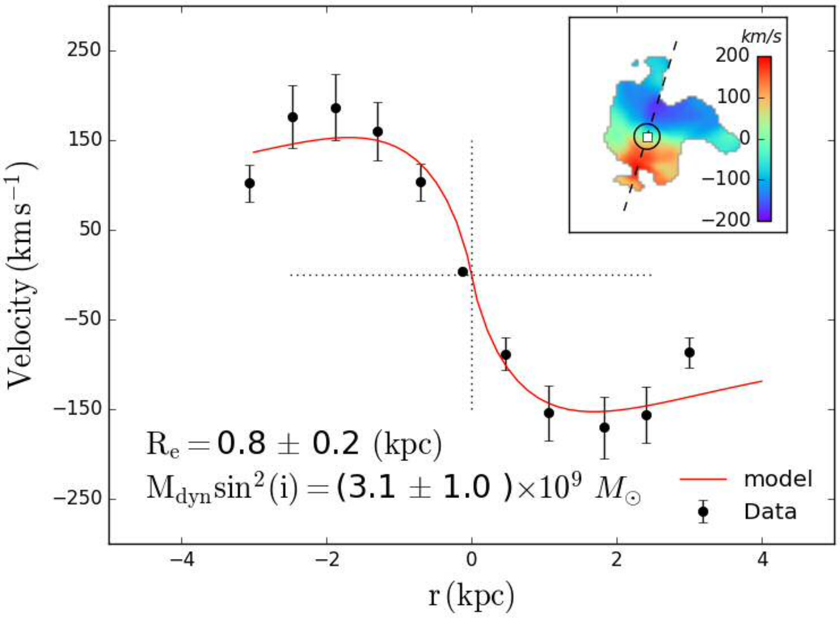

Figure 4.11: Results from the 1D kinematical modelling following the prescriptions of Freeman (1970). The observed data points have been extracted from a slice in the velocity field (inset plot) along the major axis (black dashed line). The best-fit model is shown in red which correspond to a disk radius of $R_d = 0.8 \pm 0.2$ kpc which is also shown as a black circle in the inset plot.

Figure 4.11) using the python package *scipy.curve_fit*, where error are taken as 10% of our measurement.

The best-fit model (red curve of Figure 4.11) to our data gives a disk radius of $R_d = 0.8 \pm 0.2$ kpc, which is indicated as black circle in the inset plot of Figure 4.11. This value of the disk radius is significantly smaller that we would expect from the data and is unable to explain the observed offset between the "B" and "R" components. In addition, the dynamical mass that we measure from these results is significantly lower that our estimates of the molecular gas mass (even accounting for the inclination). Based on these results alone we would reject the hypothesis that SDP.11 is consistent with a rotating disk. However, it is possible that this simple model is not sufficient to describe our data, so we are going to use a more sophisticated approach to model the kinematics.

We model the kinematics of the the $C_{\rm II}$ emission line, using the publicly available software GALPAK3D (Bouché et al., 2015). GALPAK3D uses a Bayesian parametric Markov Chain Monte Carlo approach to extract the kinematical and morphological parameters from three-dimensional image cubes while simultaneously trying to disentangle the galaxy kinematics from the resolution effects. The software accounts for both the spatial and spectral response of the observing

Table 4.7: The best-fit parameters of our exponential thick disk model with an arctan velocity profile that results from fitting the reconstructed $C_{\rm II}$ line emission cube of SDP.11 with GalPAK3D.

r (kpc)	i (deg)	PA (deg)	V_{max} (km s^{-1})	σ (km s^{-1})
2.7 ± 0.3	36.0 ± 3.6	162 ± 1	346 ± 80	0.7 ± 0.7

instrument and assumes a parametric model for a rotating disc. Starting from a set of uniform priors on the disk parameters, a 3D disk galaxy model is produced and compared to the data to compute a reduced χ^2 value, which is then minimized during the sampling process.

We adopt a circularly rotating thick disk model for SDP.11 in order to test whether this would provide an adequate fit to our source plane $C_{\rm II}$ data cube. We describe the emission in each slice of the reconstructed cube using an exponential disk so that the radial flux profile can be written as

$$I(r) = I_e \exp\left\{-b_n \left[\left(\frac{r}{r_e}\right)^{1/n} - 1\right]\right\} \tag{4.9}$$

where r_e is the effective radius of the disk, I_e is the surface brightness of the disk at r_e and b_n is a constant which given by $b_n \approx 1.9992n - 0.3271$ where n is the Sersic index which is set to $n = 1$ for an exponential profile. For our velocity profile we use an arctan model which is given by

$$V(r) = \frac{2V_{max}}{\pi} \arctan\left(\frac{r}{r_t}\right) \tag{4.10}$$

where r_t is the turnover radius and V_{max} is the maximum circular velocity. Finally we assume a Gaussian flux profile perpendicular to the disc, $I(z) \propto \exp(-|z|/h_z)$, to account for the disk thickness. In total, our model is comprised of 10 free parameters: the x, y and z positions of the source centre in the cube, a scaling factor for the flux, radius, inclination, position angle (measured clockwise from East to North), turnover radius, maximum velocity (de-projected according to the inclination) and dispersion. We assume wide flat priors for these parameters and allow the MCMC to run for N~10000 iterations. The best-fit model parameters that we derive from the fitting process are given in Table 4.7 along with 1σ error.

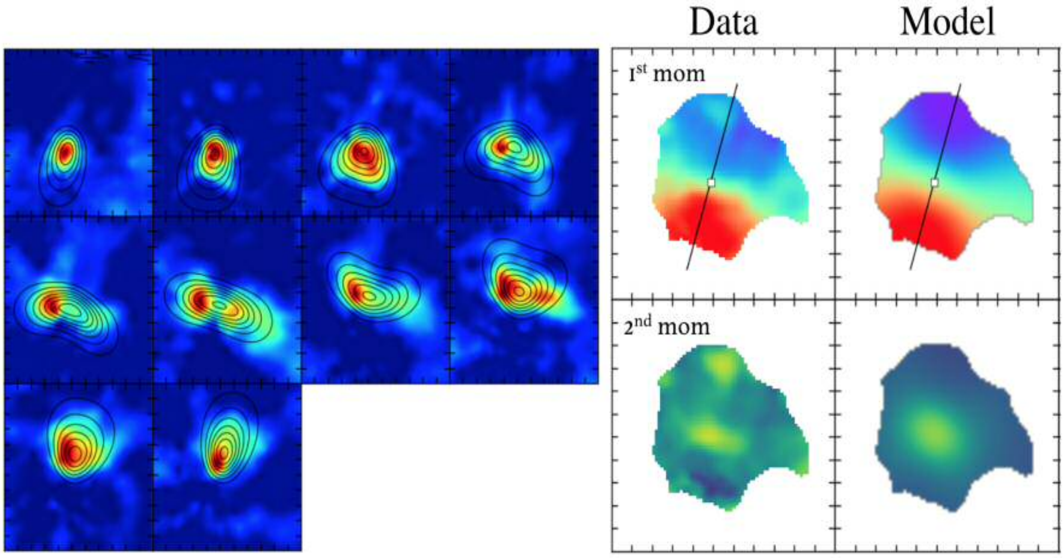

Figure 4.12: Results from our 3D dynamical modelling of SDP.11 using the GALPAK3D package. *(Left panels):* The color-scale map corresponds to the reconstructed $C_{\rm II}$ line emission in the source-plane averaged over ~55 km s^{-1} wide channels where velocities range between -250 to 250 km s^{-1}. Contours show the corresponding emission in our model cube. *(Right panels):* The velocity (1^{st} moment; top row) and dispersion (2^{nd} moment; bottom row) maps from our observed (left column) and model (right column), respectively. The white square in the top panels indicates the dynamical centre and the black straight line show the position angle of the kinematical rotation axis.

In the left panels of Figure 4.12 we compare the reconstructed $C_{\rm II}$ emission, in each velocity slice of our cube, with our best-fit model. In the top and bottom rows of the right panels of the same figure we show the velocity and dispersion maps, which were produced from our observed (left column) and model (right column) cubes, respectively. To first order, the model seem to reproduce the observed $C_{\rm II}$ emission in each slice of the cube. The overall model velocity field seem to be consistent with the observed one, although there seem to be some significant residuals in the northern part of the source where the model overestimates the observed velocity at radii > 2 kpc from the dynamical centre. In addition, the best-fit disk radius of our model is somewhat consistent with the offset between the "B" and "R" components of the reconstructed $C_{\rm II}$ line emission (see Section 4.6.1). On the other hand, the model velocity dispersion map does not look consistent with the data, which is to be expected since the observed dispersion map shows assymetries in both the northern and southern part of the source.

We also need to note that there is a misalignment between the position angle of the velocity-integrated flux density map and the kinematical rotation axis. This would suggest that the gas in the disk is not in equilibrium, which would also explain the asymmetries in the dispersion map. However, this doesn't have to mean that the kinematics are disturbed (e.g. due to a merging event). It is not surprising that this simple flux profile model is not suffiecient to fully characterize the observed flux distribution. As discussed in Section 4.5.2 we see multiple clumps in the distribution of the line flux, indicative of the need of multiple components for the flux profile model. This is beyond the scope of this work, but we intend to use the publicly available *KINematic Molecular Simulation* (KinMS; Davis et al., 2013) software in the future which allows for the use of arbitrary flux distributions.

Having determined the best-fit parameters of our model we can estimate the dynamical mass of the system, which is an estimate of the total matter (baryonic+dark matter) of the system, and is given by

$$\left(\frac{M_{dyn}}{M_{\odot}}\right) = 2.32 \times 10^5 \left(\frac{v_{cir}}{km\,s^{-1}}\right)^2 \left(\frac{r}{kpc}\right) \tag{4.11}$$

where r is the radius and v_{cir} is the de-projected (accounting for the inclination, i) circular velocity of the disk. Substituting the values found in Table 4.7 to the above equation we estimate a dynamical mass of $M_{dyn} = (8.0 \pm 3.6) \times 10^{10}$ $\mathrm{M}_{\odot}$ which is consistent with our estimate of the molecular gas mass from the molecular CO(4-3) and the atomic C_{II} lines, but not with the one estimated from the dust continuum emission (see Section 4.5.2.3). In the first case, using the gas mass estimates from either the molecular or the atomic lines we estimate a molecular gas mass fraction of $M_{gas}/M_{dyn} \sim 30-80\%$, which spans the whole range of values found for other SMGs (e.g. Aravena et al., 2016).

4.7 Summary & Conclusions

In this Chapter we presented a robust model for the strongly lensed $z_s = 1.7830 \pm 0.0002$ galaxy SDP.11. The best-fit lens model was determined from the modelling, in the *uv-plane*, of the dust continuum emission at 440 μm (ALMA Band 9), which has resolution of $0.17'' \times 0.14''$ comparable to the HST images and is unaffected from contamination from the lens light. We then used our derived model to reconstruct the source-plane images of SDP.11 in stellar and dust continuum emission as well as all the molecular and atomic emission lines of CO(4-3) and C_{II}, respectively, providing the most complete picture of the ISM in a high redshift SMG.

With magnifications of $\mu \sim 7$ for the dust continuum and $\mu \sim 4-16$ for the C_{II}

line emission across different velocity channels, we probe spatial scales down to $360-720$ pc. At the scales the atomic gas breaks into several (~2-3) clumps, of ~500 pc in size, none of which is associated with the smooth dust continuum emission. The bulk of the stellar emission is offset from the dust/gas by > 1 kpc and also appears to break down into several clumps, the size of which is comparable to the clumps seen in the reconstructed $C_{\rm II}$ emission.

We investigate the two possible scenarios for the nature of SDP.11, specifically whether we are witnessing a clumpy rotating disk in the process of collapse or a major-merger event. We present evidence for both scenarios and discuss potential reasons for some of the inconsistencies each of these scenarios faces. Although we can not definitively say which of the two cases is correct, at this stage most of the evidence seem to suggest that SDP.11 is undergoing a merging. Higher resolution ($< 0.05''$) and better sensitivity ($> 15\sigma$) observations of molecular or atomic lines in SDP.11 with ALMA are required in order to resolve scales down to tens of pc which are typical of GMC in local star forming galaxies.

Chapter 5

ALMA observations of lensed Herschel sources : Testing the dark-matter halo paradigm

ABSTRACT

With the advent of wide-area submillimeter surveys, a large number of high-redshift gravitationally lensed dusty star-forming galaxies (DSFGs) has been revealed. Due to the simplicity of the selection criteria for candidate lensed sources in such surveys, identified as those with $S_{500\mu m} > 100$ mJy, uncertainties associated with the modelling of the selection function are expunged. The combination of these attributes makes submillimeter surveys ideal for the study of strong lens statistics. We carried out a pilot study of the lensing statistics of submillimetre-selected sources by making observations with ALMA of a sample of strongly-lensed sources selected from surveys carried out with the Herschel Space Observatory. We attempted to reproduce the distribution of image separations for the lensed sources using a halo mass function taken from a numerical simulation which contains both dark matter and baryons. We used three different density distributions, one based on analytical fits to the halos formed in the EAGLE simulation and two density distributions (Singular Isothermal Sphere (SIS) and SISSA) that have been used before in lensing studies. We found that we could reproduce the observed distribution with all three density distributions, as long as we imposed an upper mass transition of $\sim 10^{13}\mathrm{M}_{\odot}$ for the SIS and SISSA models, above which we assumed that the density distribution could be represented by an NFW profile. We show that we would need a sample of ~500 lensed sources to distinguish between the density distributions, which is practical given the predicted number of lensed sources in the Herschel surveys. The content of this Chapter was published in Amvrosiadis et al. (2018).

5.1 Introduction

The statistics of angular separations, for a sample of strongly lensed sources, depend mainly on four factors: (a) the luminosity function of the source population (More et al., 2012); (b) the number density of dark-matter halos as a function of halo mass and redshift (Eales, 2015); (c) the mass density distributions within the halos (Takahashi and Chiba, 2001; Kochanek and White, 2001; Oguri, 2002, 2006); (d) the cosmological model (Li and Ostriker, 2002, 2003; Chae, 2003; Oguri et al., 2008, 2012). In principle, therefore, the statistics of image separations for a suitable sample of lensed sources is a powerful way of examining the mass density distribution of the total matter in the halo and halo mass functions predicted by simulations.

The two alternative methods for producing samples of strong lenses for statistical purposes are to start from either a population of objects that potentially act as lenses or from a population of potentially lensed sources. Follow-up observations are necessary in both cases to confirm the strong lensing nature. Examples of the first method are the Sloan Lens ACS (SLACS) Survey (Bolton et al., 2006) and the BOSS Emission-Line Lens Survey (BELLS) (Brownstein et al., 2012), in both of which the potential lensed systems were found by looking for galaxies with a spectrum which shows two redshifts - with confirmation of the lensing provided by imaging with the Hubble Space Telescope. For our purpose of investigating the properties of halos, the disadvantage of this approach is that it is prone to selection effects.

Examples of the second method were the Cosmic Lens All-Sky Survey (CLASS) (Myers et al., 2003; Browne et al., 2003) and the Sloan Digital Sky Surveys Quasar Lens Search (SQLS) (Oguri et al., 2006). CLASS was the the largest survey of strongly lensed quasars conducted at radio wavelengths. Starting from a well-defined statistical sample of ~ 9000 flat-spectrum radio sources, the CLASS team used high-resolution radio observations to produce a statistically well-defined sample of 13 lensed sources (Browne et al., 2003). The SQLS selected potential lens candidates from the Sloan Digital Sky Survey (Oguri et al., 2006), producing a final catalogue (Inada et al., 2012) of 26 lensed quasars from an initial catalogue of ~ 50000 quasars. It is worth pointing out that both optical and radio surveys require huge parent samples in order to identify a few strong lenses, as the candidate selection efficiency is very low.

With the advent of wide-area extragalactic surveys undertaken with *Herschel Space Observatory* at submillimeter wavelengths on the other hand, a new method for discovering high-redshift gravitationally lensed DSFGs has been made possible with an almost 100 per cent efficiency (see Chapter 2 for details of this methos). As already discussed in Chapter 2, exploiting the whole ~ 600 deg^2 area covered by H-ATLAS, Negrello et al. (2017) have identified a sample of 80 candidate strongly lensed SMGs using the same selection criteria. Follow-up observations with submillimetre interferometers or with the *Hubble Space Telescope* and *W. M. Keck Observatory* have confirmed so far that 20 of these extragalactic sources show a strong lensing morphology. Complementary samples of lensed sources have been produced using the same method from other *Herschel* surveys (see Chapter 2).

In a previous work, (Bussmann et al., 2013, B13) presented 880 μm observations with SMA of a sample of 30 candidates strong gravitational lenses identified from the two widest *Herschel* extragalactic surveys, H-ATLAS & HerMES. Using the sample of B13, Eales (2015) investigated whether the standard dark-matter halo paradigm could explain the distribution of Einstein radii measured from the SMA observations. We tried three halo mass functions, all estimated from numerical simulations that only included dark matter, and two different methods for calculating the lensing magnification produced by each dark-matter halo. In all cases we found that the model predicted a larger number of sources with large Einstein radii than we observed. In this Chapter, we have extended and improved the study of Eales (2015) in several ways. First, the SMA results we used in our previous paper had limited angular resolution and sensitivity, and we were concerned that we might have missed arcs of large angular size with low surface brightness, causing us to underestimate the number of sources with large image separations. For this reason, we started a project to map the lensed Herschel sources with ALMA, and in this Chapter we present the first results from this ALMA project. We compare the distributions of image separations measured from the ALMA images with the predictions of our models. Our second improvement is to use a halo mass function and density distributions from the halos derived from a numerical simulation that include baryons as well as dark matter.

The layout of this Chapter is as follows. In Section 2, we present the first results from our ALMA project. In Section 3 we describe the halo models and lay down the theoretical background for computing the lensing properties of the halos. Section 4 describes the comparison between the observed and predicted Einstein radii. We discuss our results in Section 5. Throughout this paper, we assume a flat ΛCDM model with the best-fit parameters derived from the results from the *Planck Observatory* (Planck Collaboration et al., 2016), which are $\Omega_m = 0.307$ and $h = 0.693$.

5.2 The Pilot Sample and the ALMA Observations

ALMA has much better angular resolution and surface-brightness sensitivity than the SMA, making it a much better instrument for mapping a strongly-lensed submillimetre source. In our previous SMA study of the lensing statistics of strongly-lensed Herschel sources (B13), the limited angular resolution of the SMA meant that it was often not clear whether the structure seen on the maps was actually due to lensing. There is also the possibility that large arcs were missed by their falling below the surface-brightness limit of the SMA. Since the new ALMA observations would be so much better than the SMA observations, we defined a new sample of sources for our ALMA programme.

As an initial sample for our ALMA programme, we selected 42 sources from the H-ATLAS and HELMS surveys with the highest 500-μm flux densities and with spectroscopic redshifts > 1. We checked that none of our candidates is a radio-loud AGN. In almost all cases, the 500-μm flux densities of the sources are >100 mJy, the flux limit used by Negrello et al. (2010). The lower redshift limit, of course, removes any nearby galaxies, and so we expect virtually all of the sources to be strongly lensed. For the reasons described above, the requirement that the sources have spectroscopic redshifts has probably introduced a slight bias towards certain redshift ranges, but the conditional probability statistics we use in this Chapter (see Section 5.4) ensure that our results will not be affected by this bias. Of the 42 sources, only 16 were finally observed by ALMA before the end of Cycle 2, but this should not introduce any bias because we did not rank the sources in priority. Table 5.1 lists the sample of 16 sources.

We observed each source for approximately 2-4 minutes with ALMA at 873 μm with a maximum baseline of 1km, which gives an angular resolution of 0.12 arcsec. The final image products were produced by the standard ALMA pipeline. The lensed sources are shown in Figure 5.1, all exept HATLAS J083344.9+000109. The source HATLAS J083344.9+000109 is barely detected in the ALMA image and is the faintest 500-μm source in the sample. There are no obvious signs of lensing features, either on the ALMA image or on the optical image from the Sloan Digital Sky Survey[1]. This source is coincident with a QSO. In addition, the source HATLAS J141351.9-000026 does not seem to have any lensing structure. However, in Figure 3 of Negrello et al. (2017) which shows a Keck (K_s-band) image of this object, we can clearly see that there is a large faint arc associated with a group of galaxies. In the same plot we can see that submm imaging with SMA captures a small part of this faint extended arc. As the ALMA emission coincides with the SMA emission we can conclude that the same part of the arc is captured by ALMA.

For the remaining sources in the sample, there is clear evidence of strong lensing features in the ALMA images. Modelling of the submillimetre emission, by constructing detailed lensing models, will be presented in two published/upcoming papers (Dye et al., 2018, Negrello et al. in prep.). The Einstein radii were measured

---

[1] The sample of sources for ALMA follow-up observations was selected prior to the final release of our H-ATLAS source catalgue. In this final and improved version of this catalogue the source HATLAS J083344.9+000109 has a flux density <100 mJy, and so it does not qualify as a candidate strongly lensed candidate.

Table 5.1: The ALMA sample

IAU Name	Other name	500-μm flux density [mJy]	z_l	z_s	$\theta_E\,['']$	Ref.
HeLMS J001615.8+032435	HeLMS13	149±7	0.663	2.765	5.22 ± 0.05	N16
HeLMS J001626.2+042612	HeLMS22	127±7	0.2154	2.509	0.98 ± 0.05	M17, N16
HeLMS J004714.2+032453	HeLMS8	168±8	0.478	1.195	0.58 ± 0.05	N16
HeLMS J004723.5+015750	HeLMS9	164±8	0.3650	1.441	2.66 ± 0.05	M17, N16
HeLMS J005159.4+062240	HeLMS18	135±7	-	2.392	6.54 ± 0.05	N16
H-ATLAS J083051.0+013225	G09v1.97	269±9	0.626	3.634	0.85 ± 0.04	B13, MN17
H-ATLAS J083344.9+000109	-	96±9	-	2.530	-	M17
H-ATLAS J085358.9+015537	G09v1.40	228±9	-	2.089	0.55±0.04	B13, MN16, M17
H-ATLAS J141351.9-000026	G15v2.235	176±9	0.547	2.478	-	B13, H12, MN17
H-ATLAS J142413.9+022303	G15v2.779	193±9	0.595	4.243	1.02 ± 0.04	C11, B13, MN17
H-ATLAS J142935.3-002836	G15v2.19	200±8	0.218	1.027	0.71 ± 0.04	C14, M14, MN17
HeLMS J232439.5-043935	HeLMS7	172±9	-	2.473	0.65 ± 0.05	N16
HeLMS J233255.4-031134	HeLMS2	263±8	0.426	2.689	0.93 ± 0.05	N16
HeLMS J233255.6-053426	HeLMS15	147±9	0.976	2.402	0.98 ± 0.05	N16
HeLMS J234051.5-041938	HeLMS5	205±8	-	3.503	0.54 ± 0.05	N16
HeLMS J235331.9+031718	HeLMS40	111±7	0.821	-	0.26 ± 0.05	N16

Notes: Column θ_E corresponds to the Einstein radius, which is half the image separation. The references, from which the lens and source redshift were obtained, are as follows: C11 = (Cox et al., 2011); B13 = (Bussmann et al., 2013); C14 = (Calanog et al., 2014); N16 = (Nayyeri et al., 2016); MN17 = (Negrello et al., 2017); M17 = Marchetti et al. in prep.

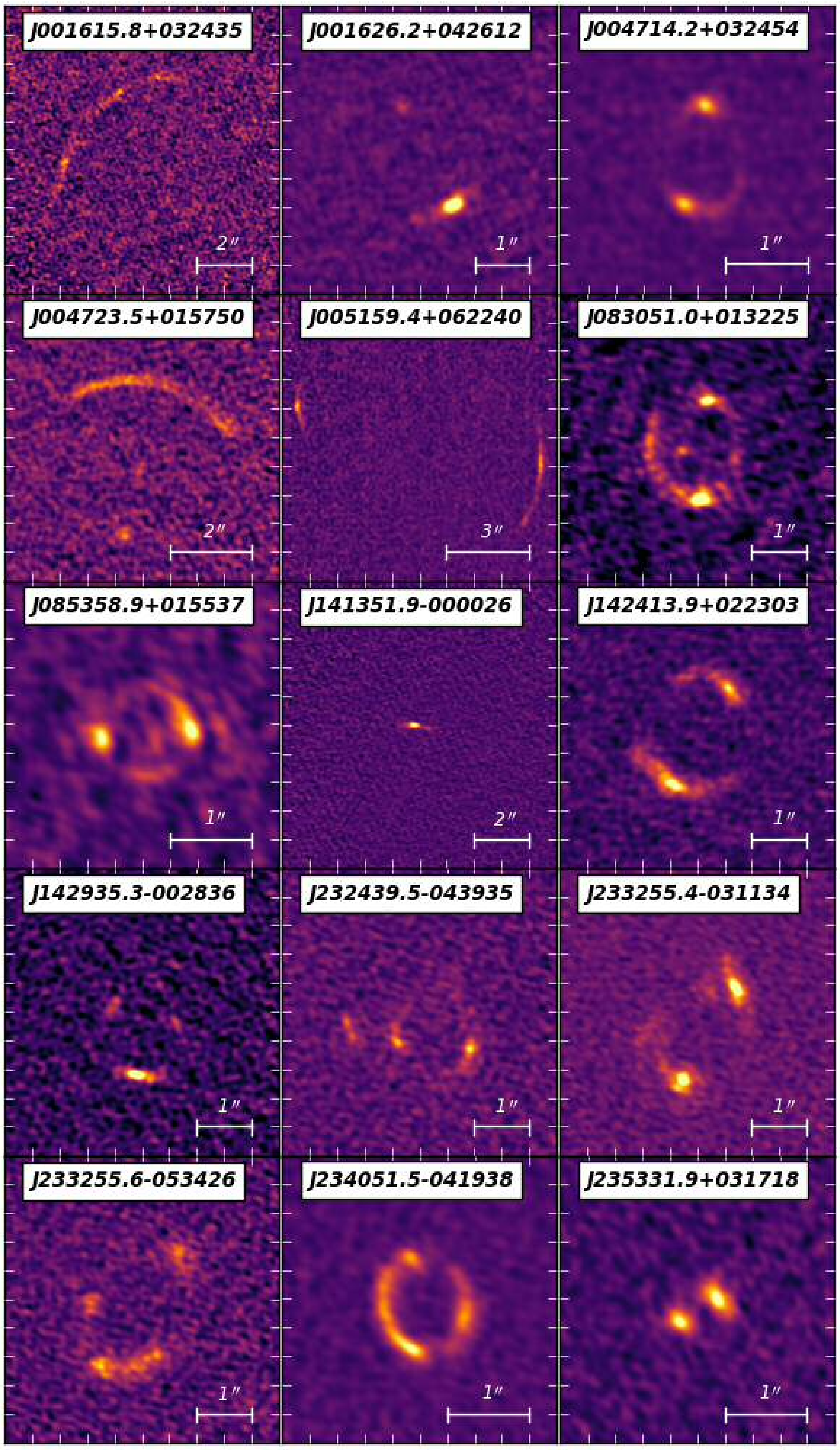

Figure 5.1: The 873-μm continuum emission images of the 15 sources we observed with ALMA. The source HATLAS J083344.9+000109, which was part of the observing run, has been neglected because it doesn't reveal any lensing features. The flux axes are not shown on the same scale for all the lens systems, as the large arcs would appear very faint. North is up and East is left.

directly from the images (as half the separation between the multiple images) and subsequently compared with the respective values that arise from preliminary lensing models of these systems, where upon an agreement was confirmed. In cases where only an arc is visible (e.g HeLMS J001615.8+032435) a rough estimate of the Einstein radius was performed by fitting a circle to the peaks of the emission ($> 4\sigma$). A uniform weighting was applied to these pixels, alleviating any dependence on their fluxes and taking into account only their positions.

For three sources (H-ATLAS J083051.0+013225, H-ATLAS J085358.9+015537, H-ATLAS J142413.9+022303) there are also measurements of the Einstein radius from SMA observations (see Table 5.2). For these sources, the pairs of measurements, with the SMA measurement first are: 0.82 ± 0.03 ($0.39 \pm 0.02/0.43 \pm 0.02$) and 0.85 ± 0.04 arcsec; 0.55 ± 0.04 and 0.55 ± 0.04 arcsec; 0.97 ± 0.01 ($0.57 \pm 0.01/0.40 \pm 0.01$) and 1.02 ± 0.04 arcsec[2]. This disagreement in the inferred values of the Einstein radii can be attributed to the complex structure of the submillimeter emission which can not be fully resolved with the SMA observations, as well as the complexity of the foreground mass distribution (Bussmann et al., 2013).

5.3 Methodology

In this section we describe the methodology for predicting the distribution of image separations. In section 5.3.1 we discuss the different density profiles that were considered in this work. In section 5.3.2 we present the halo mass function model. In section 5.3.3 we describe the standard approach for computing lensing properties assuming spherical symmetry and finally in section 5.3.4 we lay down the formalism for computing strong lensing statistics.

5.3.1 The Halo Density Profiles

In the dark-matter halo paradigm, galaxies are forming in an evolving population of dark-matter haloes. High-resolution pure dark-matter N-body simulations have been used extensively to study this dark component of the universe. These studies suggest that the spatial mass density distribution of dark matter, inside the halos identified in simulations, is well fitted by a single profile across a wide range of halo masses, the NFW profile (Navarro et al., 1996, 1997). The NFW density profile

---

[2] For two of these sources we have two individual measurements for the Einstein radius because two lenses were used for the modelling of the SMA data. In this case the final Einstein radius is given as the sum of the two

Table 5.2: The SMA sample

IAU Name	Name	z_l	z_s	$\theta_E\,['']$	Ref.
H-ATLAS J083051.0+013225	G09v1.97	0.6260	3.6340	0.39 ± 0.02	B13
H-ATLAS J085358.9+015537	G09v1.40	-	2.0894	0.55 ± 0.04	B13, M17
H-ATLAS J090302.9-014127	SDP17	0.9435	2.3049	0.33 ± 0.02	N10, B13
H-ATLAS J090311.6+003906	SDP81	0.2999	3.0420	1.52 ± 0.03	N10, B13
H-ATLAS J090740.0-004200	SDP9	0.6129	1.5770	0.59 ± 0.04	N10, B13
H-ATLAS J091043.1-000321	SDP11	0.7930	1.7860	0.95 ± 0.02	N10, B13
H-ATLAS J091305.0-005343	SDP130	0.2201	2.6260	0.43 ± 0.07	N10, B13
H-ATLAS J114637.9-001132	G12v2.30	1.2247	3.2590	0.65 ± 0.02	B13, O13
H-ATLAS J125135.4+261457	NCv1.268	-	3.6750	1.02 ± 0.03	B13
H-ATLAS J125632.7+233625	NCv1.143	0.2551	3.5650	0.68 ± 0.01	B13
H-ATLAS J132427.0+284449	NBv1.43	0.9970	1.6760	-	G05, G13
H-ATLAS J132630.1+334410	NAv1.195	0.7856	2.9510	1.80 ± 0.02	B13
H-ATLAS J133649.9+291801	NAv1.144	-	2.2024	0.40 ± 0.03	B13, O13
H-ATLAS J133542.9+300401	-	0.980	2.6850	-	S14, R17
H-ATLAS J133846.5+255054	-	0.420	2.4900	-	N17
H-ATLAS J134429.4+303036	NAv1.56	0.6721	2.3010	0.92 ± 0.02	H12, B13
H-ATLAS J142413.9+022303	G15v2.779	0.5950	4.243	0.57 ± 0.01	B13
HERMES J021830.5-053124	HXMM02	1.350	3.3950	0.44 ± 0.02	B13, W13
HERMES J105712.2+565457	HLock03	-	2.7710	-	W13
HERMES J105750.9+573026	HLock01	0.600	2.9560	3.86 ± 0.01	B13, W13
HERMES J110016.3+571736	HLock12	0.630	1.6510	1.14 ± 0.04	C14
HERMES J142825.5+345547	HBootes02	0.414	2.8040	0.77 ± 0.03	B13, W13

Note: Column θ_E corresponds to the Einstein radius, which is half the image separation. The references, from which the lens and source redshift were obtained as well as the estimates for the Einstein radii, are as follows: G05 = (Gladders and Yee, 2005); N10 = (Negrello et al., 2010); H12 = (Harris et al., 2012); B13 = (Bussmann et al., 2013); G13 = (George et al., 2013); O13 = (Omont et al., 2013); W13 = (Wardlow et al., 2013); C14 = (Calanog et al., 2014); D14 = (Dye et al., 2014); M14 = (Messias et al., 2014); S14 = (Stanford et al., 2014); N16 = (Nayyeri et al., 2016); M17 = Marchetti et al. in prep.; R17 = Riechers et al. in prep.

is given by

$$\rho(r) = \frac{\rho_s}{(r/r_s)(1+r/r_s)^2} \tag{5.1}$$

where $r_s = r_{vir}/c$ is the scale radius with c being the concentration parameter which is approximated by the formula

$$c(M,z) = 5\left(\frac{M_h}{10^{13}M_\odot}\right)^{-0.074}\left(\frac{1+z}{1.7}\right)^{-1} \tag{5.2}$$

and is derived from numerical simulations of Prada et al. (2012).

However, the objects that we observe in the real universe are comprised of both dark and baryonic matter. The difficulty is in producing density profiles for halos that also include baryons, because the physics of how baryons accrete into the centre of the halo and the astrophysical processes that take place in these central regions are complex and poorly understood. Two different analytic approaches are considered in this study, in an attempt to describe the total mass density distribution in early-type galaxies.

The simplest approach, which is frequently used in the literature is the Singular Isothermal Sphere (SIS) model. The SIS density profile is given by

$$\rho(r) = \frac{\sigma_v^2}{2\pi G r^2}\,, \tag{5.3}$$

where G is the gravitational constant and σ_v is the velocity dispersion of the halo. For a given halo mass, M_h, the latter can be determined from the circular velocity of the halo, $V^2 = GM_h/r_{vir}$, following the commonly used assumption that $\sigma_v \approx V/\sqrt{2}$ (see below how the r_{vir} is computed).There are strong observational evidences that this power law model provides a good description of the total mass distribution in field early-type galaxies. Joint gravitational lensing and stellar-dynamical analysis of a sample of strong lenses from the SLACS survey, does indeed confirm that the average logarithmic slope for the total mass density is $\langle\gamma\rangle \simeq 2.0$ with some intrinsic scatter (Koopmans et al., 2006, 2009). Similar analysis was performed for the first five strong gravitational lens systems discovered in H-ATLAS (Dye et al., 2014), where the results found were in agreement with previous studies.

Recently, Lapi et al. (2012) adopted a rather theoretical approach by considering the contribution from baryons and dark matter, separately. They used an NFW profile to represent the mass density distribution for the dark matter component and a Sersic profile for the stellar component. The three-dimensional functional form of the Sersic profile (Prugniel and Simien, 1997) is given by,

$$\rho(r) = \frac{M_\star}{4\pi R_e^3} \frac{b_n^{2n}}{n\Gamma(2n)} \left(\frac{r}{R_e}\right)^{-\alpha_n} exp\left[-b_n\left(\frac{r}{R_e}\right)^{1/n}\right], \tag{5.4}$$

where n is the Sersic index, R_e is the effective radius, $b_n = 2n - 1/3 + 0.009876/n$, $a_n = 1 - 1.188/2n + 0.22/4n^2$ and $M_\star$ is the stellar mass. The stellar mass can be determined by assuming a fixed ratio between the halo and stellar mass $M_h/M_\star$.

Lapi et al. (2012) showed that for galaxy-scale lenses this model, hereafter referred to as the SISSA model, yields very similar results to the SIS model under the assumption of reasonable parameters. However, this model has two additional free parameters that are affected by a large scatter. The first parameter is the ratio of halo to stellar mass, which for early-type galaxies is expected to lie in the range of $10-70$. The second parameter is the concentration parameter, c, which is expected to have a 20% scatter. In our analysis we will omit the scatter in the c-M relation and adopt a constant ratio of halo to stellar mass of 30. However, we show in Appendix C how these parameters can affect our results.

An additional parameter that is introduced in the above mentioned models is the virialization redshift $z_{l,v}$. This parameter is used to determine the virial radius of the halo r_{vir}

$$r_{vir} = \left(\frac{3M_h}{4\pi\Delta_c\rho_{crit}}\right)^{1/3}, \tag{5.5}$$

where $\rho_{crit}(z) = \rho_{crit,0}E^2(z)$ is the critical density of the universe at redshift z, with $\rho_{crit,0}$ being its value at redshift zero and $E(z)$ is the scaled Hubble parameter,

$$E^2(z) = \frac{H^2(z)}{H_0^2} = \Omega_{m,0}(1+z)^3 + \Omega_{\Lambda,0}(1+z)^{3(1+w)}. \tag{5.6}$$

Assuming a flat cosmology ($\Omega_m + \Omega_\Lambda = 1$) we can use an approximate expression for Δ_c, which was derived from a fit to simulations of Bryan and Norman (1998),

$$\Delta_c = 18\pi^2 + 82x - 39x^2, \tag{5.7}$$

where $x = \Omega_m(z) - 1$ and the redshift evolution of the cosmological parameter of matter is

$$\Omega_m(z) = \frac{\rho_m}{\rho_{crit}} = \Omega_{m,0}(1+z)^3/E^2(z). \tag{5.8}$$

Lapi et al. (2012) suggested that the frequently made approximation, that the observed redshift of a galaxy is equal to the virialization redshift $z_l \approx z_{l,v}$, leads to an overestimation of the halo size. Alternatively they propose a virialization redshift in the range $z_{l,v} \sim 1.5 - 3.5$, which is much more in line with the ages of the stellar populations found in early-type galaxies.

Besides the analytic models presented above, we also now have results from cosmological hydrodynamic simulations which provide the means to examine how baryonic effects modify the structure of dark-matter halos in a more rigorous way (i.e. adiabatic effects of dark-matter, radiative transfer models, feedback, etc). In recent studies, Schaller et al. (2015a,b) investigated the internal structure of halos produced in the EAGLE simulations, which include both baryons and dark matter (Schaye et al., 2015). Some of the baryonic effects that are included in these simulation runs are feedback processed from massive stars and active galactic nuclei (AGN), radiative cooling, and contraction of the dark matter in the central halo regions due to the presence of baryons. The authors demonstrated that the following formula,

$$\frac{\rho(r)}{\rho_{crit}} = \frac{\delta_s}{(r/r_s)(1 + r/r_s)^2} + \frac{\delta_i}{(r/r_i)\left(1 + (r/r_i)^2\right)}, \tag{5.9}$$

provides a good fit to the data. From the above functional form we clearly see that the first term is the NFW profile which provides a fairly good description of the outer part of the halo. The second term is an NFW-like profile with a steeper slope to account for the concentration of baryons in the central region of the halo. The parameters of this model as a function of mass, namely δ_s, r_s, δ_i and r_i, are determined by fitting 3rd-order polynomials to the values found in Table 2 of Schaller et al. (2015a). The halo mass range probed in this study ranges from $M_h = 10^{10} - 10^{14} M_\odot$.

5.3.2 Halo Mass Function

The halo mass function describes the comoving number density of dark matter halos as a function of redshift and per comoving mass interval. In our earlier paper (Eales, 2015), we used analytic functions, obtained by fitting to the results of numerical simulations of the evolution of dark matter, of Sheth and Tormen (1999) and Tinker et al. (2008). We found very little difference between the results predicted from the two halo mass functions. Both these analytic functions were based on numerical simulations containing only dark matter. In this Chapter, we use the analytic function for the halo mass function that was derived by Bocquet et al. (2016) by fitting to the results of a numerical simulation that contains both baryons and dark matter, using the same formalism as T08. The comoving number density of haloes of mass M is given by

$$\frac{dn}{dM} = f(\sigma)\frac{\bar{\rho}_m}{M}\frac{dln\sigma^{-1}}{dM}. \tag{5.10}$$

The function $f(\sigma)$ is parametrized as

$$f(\sigma) = A\left[\left(\frac{\sigma}{b}\right)^{-\alpha} + 1\right]e^{-c/\sigma^2} \tag{5.11}$$

where the parameters A, α, b and c are all expressed as functions of redshift $A(z) = A_0(1+z)^{A_z}$, $\alpha(z) = \alpha_0(1+z)^{\alpha_z}$, $b(z) = b_0(1+z)^{b_z}$ and $c(z) = c_0(1+z)^{c_z}$ and σ is the variance of the mass-density field which is given by Eq. 3.15. The best fit values of these parameters are obtained from Table 2 of Bocquet et al. (2016) for the Hydro simulation.

5.3.3 Lensing Properties

In our analysis we consider the typical lensing configuration which is comprised of a point-like source located at redshift z_s, an object acting as a lens located at redshift z_l and an observer, in order to derive the lensing properties (Schneider et al., 1992). We always assume that the lens is spherically symmetric, since ellipticity does not significantly affect the statistics of image separations (Huterer et al., 2005).

5.3.3.1 Surface Density

The surface density Σ can be computed by integrating the 3D density profile of the halo $\rho(r)$ over the parallel coordinate along the line-of-sight, and expressed as a function of the perpendicular coordinate in the lens plane (thin lens approximation)

$$\Sigma(R) = 2\int_R^\infty dr\frac{r}{\sqrt{r^2-R^2}}\rho(r). \tag{5.12}$$

The condition for strong lensing to occur (i.e. the formation of multiple images) is that the surface mass density exceeds the critical threshold (critical surface density)

$$\Sigma_c = \frac{c^2}{4\pi G}\frac{D_s}{D_{ls}D_l}, \tag{5.13}$$

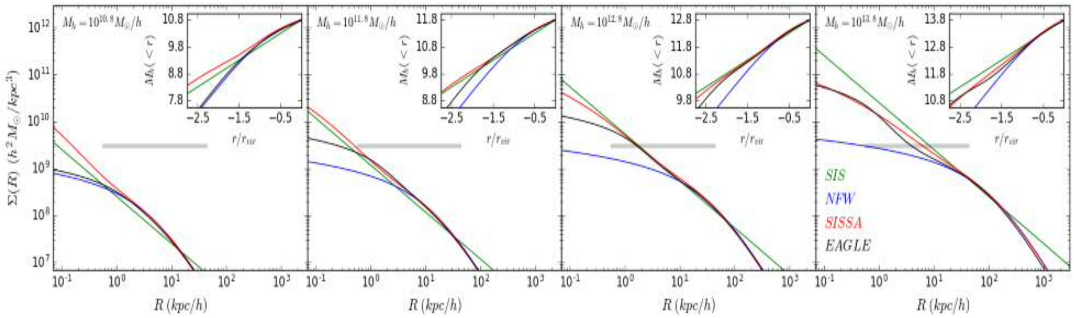

Figure 5.2: Surface mass density as a function of the radial distance in the lens plane for the different lens models: **SIS** (green line), **NFW** (blue line), **SISSA** (red line) and a halo profile derived from the **EAGLE** simulation (black line). The grey solid line corresponds to the critical surface density Σ_c for $z_l = 0.5$ and $z_s = 2.0$. The figure insets show the mass enclosed within radius r, where the x-axis is scaled by the virial radius r_{vir}.

which solely depends on the angular diameter distances from the observer to the lens and source plane, corresponding to D_l and D_s respectively, as well as the angular distance between lens and source plane D_{ls}. The angular diameter distance is given by

$$D_i = \frac{1}{(1+z_i)} \int_0^{z_i} \frac{c dz}{H(z)} \tag{5.14}$$

This expression holds in the case where a flat cosmology is assumed.

Figure 5.2 shows the radial dependence of the surface mass density for the various halo density profiles that were considered in this work. The critical surface density, when the source is at redshift $z_s = 2.0$ and the lens at $z_l = 0.5$, is also shown in the figure as the grey solid line. The different panels of the figure correspond to different halo masses (shown in their upper left corner). Note that the maximum resolution of the EAGLE simulation is ~ 1kpc, below which there is no guarantee their fit is realistic and should not be taken into consideration. Each panel has an inset plot showing the mass enclosed within a certain radius.

In low mass halos ($M_h < 10^{11.5} M_\odot$) the predictions from the EAGLE simulation agrees very well with the NFW profile. This range of halo masses corresponds to dwarf galaxies, where the baryon fraction of stellar to halo mass is very low and the dark matter dominates the mass budget. The critical surface density indicates that halos in this range are very inefficient lenses, not being able to produce multiple images. The SISSA model still predicts that there are baryons in these halos, but concentrated in lower radial scales beyond the probed range of the EAGLE simulation.

In intermediate mass halos $10^{11.5} M_\odot < M_h < 10^{13.5} M_\odot$ the EAGLE density profile gradually departs from the NFW model as baryons start to play an important role. This range of halo masses corresponds to typical early-type galaxies, where the baryon fraction peaks causing baryonic effects to be more prominent. The dense central regions in these objects, which result from the contribution of baryons, makes them very efficient lenses. There is a fairly good agreement between the EAGLE model and both SIS and SISSA models in this range.

In high mass halos $M_h > 10^{13.5} M_\odot$ the EAGLE model agrees fairly well with the NFW model for radii larger than about ~ 10 kpc, while their central regions are still dominated by the presence of baryons. This range of halo masses corresponds to groups/clusters of galaxies, where the baryon fraction gradually decreases until it reaches the universal mean value $f_b = \Omega_b/\Omega_m$. The SISSA model in this range produce denser central regions as expected (radial range between ~1 kpc to ~10 kpc), since it is not intended for the description of groups/clusters of galaxies (does not account for the increase in the ratio of halo to stellar mass as the halo increases in mass).

5.3.3.2 Image Separation

The definitions for the various lensing quantities that are going to be used this Chapter were already given in Chapter 1, however, we will express them here in terms of angular positions in the image and source planes. Assuming that light rays are coming from a distant point-like source and crossing the lens plane at an angular position θ, they will get deflected by an angle $\alpha(\theta)$ which is given by

$$\alpha(\theta|z_l, z_s, M_h) = \frac{2}{\theta}\int_0^\theta \theta d\theta \frac{\Sigma(D_l\theta|z_l, M_h)}{\Sigma_c(z_l, z_s)}. \tag{5.15}$$

This property strongly depends on the mass enclosed within the radius $R \equiv D_l\theta$. The true and observed positions of the source in the sky are related through the simple transformation from the lens to the source plane,

$$\beta(\theta) = \theta - \frac{\theta}{|\theta|}\alpha(|\theta|) \tag{5.16}$$

referred to as the lens equation. The solutions of the lens equation θ_i, given the position of the source β in the source plane, will give the positions of the lensed images in the lens plane. The magnification of individual images can then be

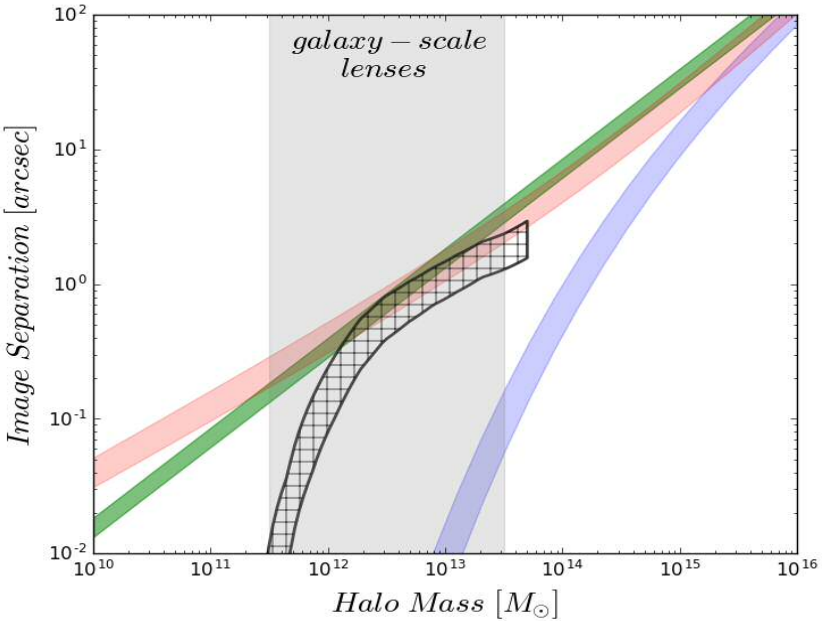

Figure 5.3: The image separation θ, as a function of the halo mass for the different lens models: **SIS** (green), **NFW** (blue), **SISSA** (red) and **EAGLE** (black hatched). The width of the stripes correspond to a lens redshift range $z_l = 0.5 - 1.0$, while the redshift of the source is kept fixed to $z_s = 2.0$. The virialization redshift is assumed to be equal to the redshift of the lens $z_{l,v} = z_l$ in this case.

computed from

$$\mu(\theta_i | z_l, z_s, M_h) = \frac{1}{\lambda_r \lambda_t}, \tag{5.17}$$

with

$$\lambda_{r,t} = 1 - \kappa(\theta_i) \pm \gamma(\theta_i), \tag{5.18}$$

where the quantities $\kappa(\theta) = \Sigma(\theta)/\Sigma_c$ and $\gamma(\theta) = \alpha(\theta)/\theta - \kappa(\theta)$ are the convergence and shear, respectively, given as a function of the angular position in the lens plane. Therefore, the total magnification of the source, at position β in the source plane, is computed by summing up the absolute values of the magnifications of the individual images μ_i that are formed.

The quantities $\lambda_{r,t}$ in the denominator of Eq. 5.17 define the radial and tangential critical curves in the lens plane, where the magnification diverges (when $\lambda_{r,t}$ become zero). The Einstein radius for a specific halo density profile corresponds to the radius of the tangential critical curve, from which we compute the image separation for a set of lens and source parameters as twice its value. Figure 5.3

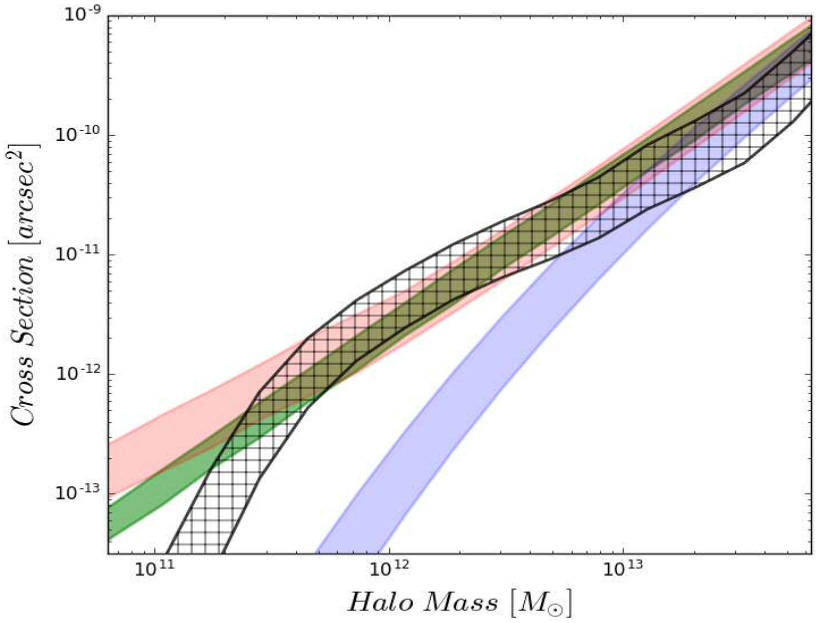

Figure 5.4: The cross section $\sigma(\mu > 2)$, as a function of the halo mass for the different lens models: **SIS** (green), **NFW** (blue), **SISSA** (red) and **EAGLE** (black hatched). The width of the stripes correspond to a lens redshift range $z_l = 0.5 - 1.0$, while the redshift of the source is kept fixed to $z_s = 2.0$. The virialization redshift is assumed to be equal to the redshift of the lens $z_{l,v} = z_l$ in this case. The range of halo mass corresponds to the grey highlighted area in Figure 5.3 of galaxy-scale lenses.

shows how the image separation changes as a function of the halo mass for the different halo models. We can see that EAGLE predicts far smaller image separations for lenses with a mass $10^{11.5} M_\odot < M_h < 10^{12.5} M_\odot$ compared to the SIS and SISSA models while in the range $10^{12.5} M_\odot < M_h < 10^{13.5} M_\odot$ there is a good agreement.

5.3.3.3 Cross-Section

The most important quantity for studies of strong lens statistics is the cross section. This is defined as the area in the source plane where the source has to lie in order to have a total magnification of $> \mu$. For a spherically symmetric mass distribution the cross section can be easily computed by

$$\sigma(\geq \mu, z_l, z_s, M_h) = \pi \beta^2(\mu), \tag{5.19}$$

where $\beta(\mu)$ is the radius in the source plane corresponding to a magnification μ.

We calculated the cross section using a minimum magnification factor of $\mu_{min} = 2$. For the SIS model, this corresponds to the strong-lensing regime in which multiple images are produced. We used the same minimum magnification factor

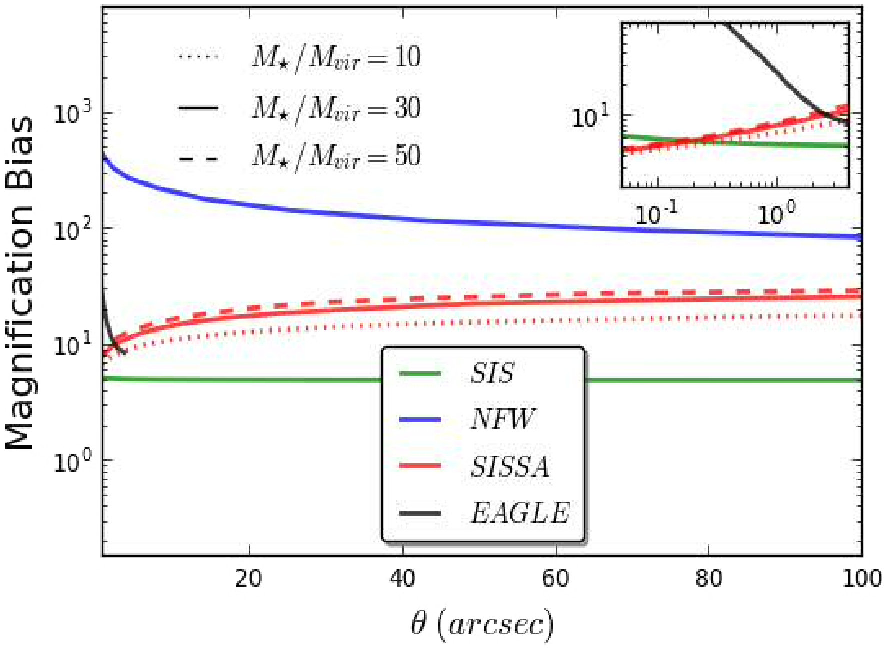

Figure 5.5: The magnification bias as a function of the image separation, computed for a luminosity function $\Phi(L) \propto L^{-2.1}$. The calculation is performed for different lens model : **SIS** (green), **NFW** (blue), **SISSA** (red) and **EAGLE** (black). The various red lines correspond to the SISSA model adopting different choices for the ration of stellar to halo-mass. The inset plot show a zoom in to the smaller angular scales. The EAGLE model is cropped at around a few arc-seconds cause halos of $<10^{14}$ $M_\odot$ (which are the most massive halos in EAGLE) can only multiple images that are separated by a few arc-seconds.

for the other density profiles, even though this is not the magnification at which multiple images start to be seen. This was partly for consistency but also because we did not originally select our sample of lensed sources because they had multiple images but because their flux densities were amplified enough to be detected in a sample of bright 500-μm sources.

Figure 5.4 shows the behaviour of the cross section as a function of the halo mass for the different halo models, only for the range of galaxy-scale lenses. As illustrated in the figure, for the range of masses relevant to galaxy-scale lenses $10^{11.5}M_\odot < M_h < 10^{13.0}M_\odot$, there is an agreement between the SIS, SISSA and EAGLE models. As the halo mass increases above $10^{13.0}M_\odot$ the EAGLE's cross section behavior starts to divert from these and becomes more similar to that of the NFW model.

5.3.3.4 Magnification Bias

′Magnification bias′ leads to lensed systems being over-represented in a flux-limited or magnitude-limited sample because there are more low luminosity sources in the universe, which lensing can boost over the flux limit, than high-luminosity sources (e.g. Mason et al., 2015; Eales, 2015). If "magnification bias" is not accounted for when studying the statistics of strongly lensed system that would lead to predictions being significantly lower than the observed distributions. In addition, shallower density distributions produce larger magnifications, and therefore if magnification bias is not accounted for when combining different density profiles that could potentially lead to inconsistent predictions of the distributions of Einstein radii. The magnifications bias can be modeled in the following way.

As mentioned before, the magnification bias causes sources that are fainter than the limiting magnitude of the survey to be detected in the sample. We define this bias factor as

$$B(L|z_s) = \frac{2}{\beta_r^2}\int_0^{\beta_r} \beta \frac{\Phi(L/\mu(\beta)|z_s)}{\Phi(L|z_s)}\frac{d\beta}{\mu(\beta)} \tag{5.20}$$

where $\Phi(L|z_s)$ is the luminosity function. We calculate how the bias factor depends on image separation for the different density distributions. We assume that the luminosity function follows a power-law with the form $\Phi(L|z_s) \propto L^{-2.1}$, which is a good approximation to the form of the submillimetre luminosity function at high luminosities (Gruppioni et al., 2013), and we assume this is the same for all source redshifts.

Figure 5.5 shows the computed magnification bias as a function of the image separation for the different lens models. Although, in principle, we could use our models to correct for this effect, we have decided not to do this because the luminosity function for submm sources is still very poorly constrained, and so the model is very uncertain. Figure 5 shows that there will be no effect for the SIS model, because the magnification bias is independent of angular image separation, but the effect for the other density profiles may be significant.

5.3.4 Formalism of Strong Lens Statistics

We adopt the standard formalism for computing lensing statistics (Turner et al., 1984), where we consider a population of dark-matter halos that act as deflectors located at redshift z_l and can be characterised by their mass M_h. The differential probability that a source at redshift z_s is strongly lensed with total magnification $\geq \mu$ by that population of deflectors is given by

$$\frac{dP}{dz_l dM_h} = \frac{d^2N}{dM_h dV} \frac{d^2V}{dz_l d\Omega} \sigma(\geq \mu, z_l, z_s, M_h), \tag{5.21}$$

where

$$\frac{d^2V}{dz_l d\Omega} = \frac{c}{H_0} \frac{(1+z_l)^2 D_A^2(z_l)}{E(z_l)} \tag{5.22}$$

is the comoving volume element per unit of z_l-interval and solid angle, while $d^2N/dM_h dV$ is the number density of deflectors per units of M_h-interval at different redshifts

The total lensing probability $P(z_s, \geq \mu)$ can be computed by integrating Eq. 5.21 over the lens redshift and halo mass ranges. To calculate the probability distribution of image separations we insert a selection function in the integral in order to select only the combination of parameters that produce image separations in the interval $\theta \pm d\theta$. The probability distribution as a function of the image separation then becomes

$$P(\theta \,|\, z_s, \geq \mu) = \int_0^{z_s} dz_l \int_0^{\infty} dM_h \frac{dP}{dz_l dM_h} \delta[\theta - \tilde{\theta}(z_l, z_s, M_h)], \tag{5.23}$$

where $\tilde{\theta}(z_l, z_s, M_h)$ is calculated for each model as twice the Einstein radius (tangential critical curve) and the Dirac δ-function is unity if the combination of parameters corresponds to image separation $\tilde{\theta}$ in the interval $(\theta - d\theta, \theta + d\theta)$.

The amplitude of the image separation distribution in Eq. 5.23 increases with increasing source redshift independently of the angular scale, since we sample a larger volume of the universe. The normalised image separation distribution on the other hand,

$$p(\theta \,|\, z_s, \geq \mu) = \frac{P(\theta \,|\, z_s, \geq \mu)}{\int_0^{\infty} d\theta P(\theta \,|\, z_s, \geq \mu)}, \tag{5.24}$$

is quite insensitive to the source population as well as the cosmological parameters (Oguri, 2002).Comparing the predicted normalised distribution with the observed one, we therefore probe the combination of the halo mass function and density profiles of halos which affect the shape of the distribution.

In our analysis we assume a two-transition mass model, following the methodology adopted in previous studies (Porciani and Madau, 2000; Kochanek and White, 2001; Oguri, 2002; Kuhlen et al., 2004). This approach was introduced in order to account for baryons, which probably affect the shape of halo's density profile by means of adiabatic contraction (Blumenthal et al., 1986) and cooling (White and Rees, 1978) when the baryon fraction is relatively high. In our model, halos below the mass M_{min} (corresponding to dwarf galaxies) and above M_{max} (corresponding to clusters of galaxies), are described by the NFW profile to account for the expected low baryon fraction.In the intermediate mass range (corresponding to early-type galaxies) halos are described by either the SIS or SISSA model, where the baryon fraction is expected to reach the peak.

Another quantity that was introduced in the analytic description of the SIS and SISSA models in Lapi et al. (2012), is the virialization redshift of the lens $z_{l,v}$. According to their study, the frequently-made approximation $z_{l,v} \approx z_l$ leads to an underestimate of the lensing probability. This is because a lower value of the virialization redshift leads to an overestimation of the halo size and therefore to an underestimation of the halo's density. As a result, a higher upper-transition mass would be necessary in order to match the observed distribution of image separations [3]. We examine the effect of the virialization redshift on the transition-masses of our model by considering both a $z_{l,v} = z_l$ and $z_{l,v} = 2.5$ (see Lapi et al., 2012, for details) when computing the theoretical distribution of image separations.

5.4 Results

In this section we follow the methodology described in Section 5.3, to derive the theoretical distributions of image separations. We then compare our model predictions with the normalised histogram of the observed image separations for two samples of Herschel selected lensed sources. We emphasize that the use of the conditional probability distribution means that our analysis is independent of the properties of the source population as its only sensitive to the shape of the distribution and not so much on its overall normalization, where the latter depends on the redshift of the source[4]. We carry out the analysis separately for the sample of sources observed with ALMA and SMA.

Table 5.3: Best-fit value of the two transition masses that were used in our analytic model, adopting either the SIS or SISSA model for the description of galaxy-scale lenses. These values were derived assuming a virialization redshift $z_{l,v} = z_l$ for the first two rows and $z_{l,v} = 2.5$ for the last two.

	$\log(M_{min})_{SIS}$	$\log(M_{max})_{SIS}$	$\log(M_{min})_{SISSA}$	$\log(M_{max})_{SISSA}$
ALMA$_{z_{vir}=z_l}$	≤ 12.4	13.25 ± 0.10	≤ 12.3	13.20 ± 0.11
SMA $_{z_{vir}=z_l}$	≤ 12.2	13.19 ± 0.07	≤ 12.0	13.20 ± 0.06
ALMA$_{z_{vir}=2.5}$	≤ 12.1	12.56 ± 0.13	≤ 12.1	12.48 ± 0.10
SMA$_{z_{vir}=2.5}$	≤ 11.9	12.54 ± 0.07	≤ 11.9	12.42 ± 0.10

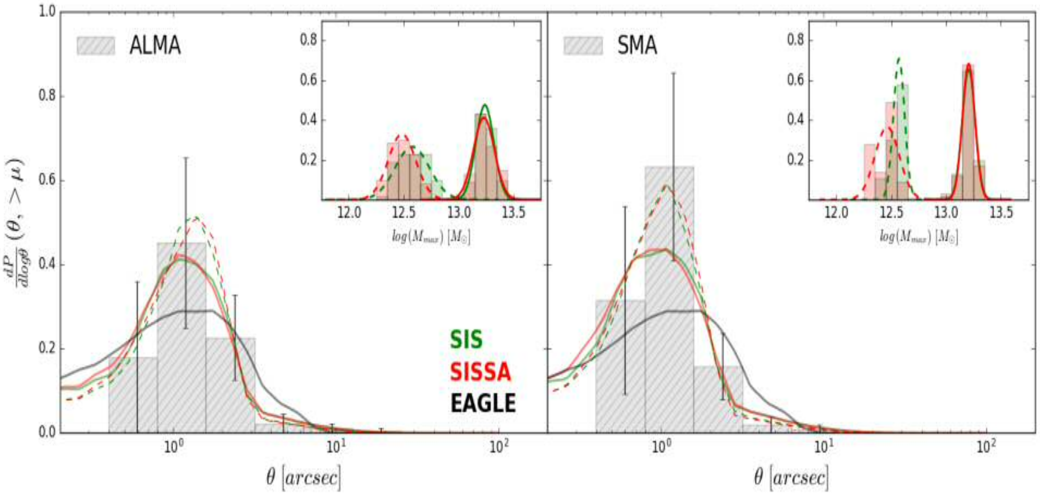

Figure 5.6: The predicted distribution of image separations adopting either the SIS (green) or SISSA (red) profiles for galaxy-scale lenses and following the procedure described in Section 5.4.1. The predicted distribution of image separation, which was derived assuming a halo model calibrated from the EAGLE simulation results, is shown with black dashed lines. Left and right panels correspond to the fits with the two samples of lenses followed-up with ALMA and SMA, respectively. The gray-scale histograms are the observed distributions of our samples. The figure insets show the distribution of the upper mass-transition parameter after performing ~100 realisations (see main text for details on the resampling method we use to estimate the errors of our model parameters). The predictions adopting a virialization redshift $z_{l,v} = z_l$ are shown as straight lines while the ones with a virialization redshift $z_{l,v} = 2.5$ are shown as dashed lines.

5.4.1 Comparison with Observations

We derive the values of our two transition-mass models, described in Section 5.3.4, by performing a standard χ^2 minimisation method

$$\chi^2 = \sum_i \frac{(P(\theta_i| \geq \mu) - P^{'}(\theta_i| \geq \mu))^2}{\sigma^2(\theta_i)}, \tag{5.25}$$

where $P(\theta)$ and $P^{'}(\theta)$ are the observed and theoretical normalised image separation distributions respectively. The quantity $\sigma(\theta)$ is the standard deviation of each bin of the observed histogram of image separations, which is derived from poisson statistics.

---

[3] Parameters associated with the NFW model (e.g. concentration, $c_{\rm vir}$) affect mainly the amplitude of the distribution, but not its shape and so their effects can be disentangled from that of the transition-mass.

[4] Intuitively, the higher the redshift of the background source, the higher is the chance that there is an object along its line-of-sight that is massive enough to cause a strong lensing event.

Figure 5.6 show a comparisons of the observed and predicted distributions of image separations. The black solid line shows the predicted distribution using the analytic mass density distribution obtained from the EAGLE simulation (Eq. 5.9). This agrees fairly well with the observations, and does not require the imposition of transition masses. The other lines show the predictions of our analytic models with two transition masses. The graphs show our predictions adopting a virialization redshift $z_{l,v} = z_l$ and $z_{l,v} = 2.5$ as straight and dashed lines, respectively.

The grey histograms in each graph correspond to the observed distributions for the sample of sources observed with ALMA on the left-hand side and with the sample of sources observed with SMA that was used in our previous study (Eales, 2015), on the right-hand side. The best-fit values of the two transition-masses are shown in Tables 5.3 for the two different choice of virialization redshift along with the different choices of halo density profiles and observed sample. In order to account for the uncertainty on the measured image separations, we perform 100 simulations for each measurement by resampling each value at random from a Gaussian distribution with a standard deviation equal to the value's error. For each realisation of the observed distribution we perform the above fitting procedure and we end up with a distribution for the upper transition-mass from which we derive its errors.

In our analysis we decided to exclude the object J141351.9-000026, which as discussed in Section 5.2 has a very large Einstein radius as a result of lensing by a galaxy cluster. If we were to include this object in the analysis there wouldn't be any significant difference in the constrained value of the Maximum transition masses. This is because the constraint is more sensitive to the contribution from the galaxy scale lenses. Increasing the Maximum transition mass will shift the kink of the distribution to larger scales and the lack of objects in that range constrains its value. Including an object with significantly larger Einstein radius than where the kink is observed will not significantly contribute to the fitting method. Furthermore, no proper modelling has been performed for this object to extract the value of its Einstein radius.

Predictions adopting either of the analytic profiles, SIS and SISSA, as well as the density profile derived from the EAGLE simulation, seem to be in good agreement with observations. Furthermore, comparing the fitted values of the upper transition mass that were obtained for the different samples of lenses, we find a slight difference that is not significant (i.e. $< 1\sigma$). As mentioned in Section 5.2, the observed distribution of image separations, for the SMA sample, is biased towards lower angular separations, which leads to an underestimate of the upper transition-mass. Concerning the lower transition-mass, we are still not in a position to set good constraints because our fitting method cannot distinguish models with $M_{min} \lesssim 10^{12.5} M_{\odot}$. Finally, the virialization redshift strongly affects the resulting transition masses, pushing them to lower values. However, there is still no evidence to support such a low-transition mass between galaxies and clusters.

5.5 Discussion & Conclusions

Wide-area extragalactic surveys conducted at submillimeter wavelengths has allowed us to discover a new population of strongly lensed galaxies (Negrello et al., 2010, 2017; Nayyeri et al., 2016). Their potential to produce very large samples of strong lenses (González-Nuevo et al., 2012) and the simplicity of the selection function (Blain, 1996; Perrotta et al., 2002, 2003; Negrello et al., 2007), will greatly benefit the study of strong lens statistics, a subject which has previously been studied by optical (Bolton et al., 2006; More et al., 2012) and radio surveys (Browne et al., 2003; Oguri et al., 2006). Extragalactic surveys undertaken with Herschel Space Observatory have demonstrated the potential of this method by producing large samples of candidate strong lenses (Wardlow et al., 2013; Nayyeri et al., 2016; Negrello et al., 2017). We carried out follow-up observations with ALMA of 16 candidate strongly lensed Herschel sources, selected from the H-ATLAS and HeLMS surveys, expecting that based on their bright 500-μm flux densities that they should be lensed. Out of these sources, 15 show clear evidence of lensing features.

In this study we predict the distribution of image separations of strongly lensed systems produced by a population of dark matter halos parametrised by the halo mass function derived from hydrodynamical cosmological simulations (Bocquet et al., 2016). The largest uncertainty that enters the calculation of the theoretical image separation distribution is the total mass distribution of these halos, which is the primary focus of this study. For the first time we used a halo density profile that was derived from the EAGLE simulation (Schaller et al., 2015a,a), which is calibrated so that it provides a good fit across a wide range of halo masses. We showed that the combination of mass density distributions and the halo mass function predicted by cosmological numerical simulations can reproduce the observed distribution of image separation of strong lenses found in submillimeter surveys.

We also consider a different approach adopting analytical recipes for the description of the total mass distribution in dark-matter halos. Since there is not a single analytic model to describe halo density profiles across the whole range of halo masses we introduce two transition masses between dwarf to early-type galaxies and early-type to cluster of galaxies, respectively. For the description of early-type galaxy halos we consider two approaches, the SIS and SISSA models, while for dwarfs and cluster of galaxies we adopt the NFW model. We utilise our samples of strong lenses from which we derive the observed distribution of image separation, in order to constrain the values of the transition masses. We were able to set good constraints on the maximum transition-mass (see Table 5.3). Our results agree with previous studies of strong lens statistics using the CLASS (Myers et al., 2003; Browne et al., 2003) sample of strong lenses, where they place the value of the upper transition-mass at $\sim 10^{13} M_{\odot}$ (Porciani and Madau, 2000; Kochanek and White, 2001; Oguri, 2002; Li and Ostriker, 2002; Kuhlen et al., 2004). A complementary approach was adopted by Oguri (2006) in which the author used a two-component halo density profile, comprised of an NFW dark matter halo and a Hernquist model for the central galaxy, that also considers the effect of adiabatic contraction of dark matter. This profile has a smooth transition between galaxy and cluster scale lenses and does not require the assumption of a transition mass and has the potential to better account for the contribution from group-scale lenses. This profile seem to provide a relatively good fit to radio (Oguri, 2006) and optical data (More et al., 2012). However, as our sample is still limited in numbers to make such distinctions between models, we have not considered this approach.

A larger sample is also required in order to distinguish between models with a minimum transition mass $< 10^{12} M_{\odot}$ (Ma, 2003). However, our candidate sample selection does not have any completeness issues at low angular resolutions as optical surveys do (More et al., 2016). This is because our selection is purely flux based and does not require the identification of individual multiply lensed images. Since our sample has no biases at small angular separation, follow up observations with ALMA can in fact probe the subarcsec scale of the image separation distribution (see e.g HeLMS J235331.9+031718).

We also examined the effect of varying the virialization redshift of the lens $z_{l,v}$, which is one of the parameters of our analytic models. Previous studies of strong lens statistics have ignored its effect and always assumed that it coincides with the actual redshift of the halo $z_{l,v} = z_l$. Lapi et al. (2012) argue that this approximation leads to an overestimate of the halo's size and, subsequently, to an underestimate of the lensing probability. We showed that adopting the value suggested by Lapi et al. (2012), $z_{l,v} = 2.5$, the constrained value of the maximum transition mass significantly decreases (see Table 5.3).

This approach of predicting the distribution of image separation based on the population of dark-matter halos selected on the basis of their halo mass, provides a confirmation of the standard cold dark-matter paradigm. However, the current samples of strong lenses are still not large enough in order to be able to distinguish between the different models that attempt to describe the internal structure of these halos. Scaling from the errors in Figure 5.6 we estimate that a sample of ~ 500 would be required for this distinction to be made possible.

Is it practical to produce such a large sample of lensed sources? González-Nuevo et al. (2012) have proposed a method for finding at least 1000 lensed sources from the Herschel surveys. However, their method is based on finding galaxies that lie close to the position of a Herschel source, and therefore have a high probability of being associated with it, but which have much lower estimated redshifts than the Herschel source. This method will therefore be biased towards lensing systems with small image separations and so is not suitable for our purpose.

The most promising method is a variant of the method used by Negrello et al. (2010). There are only $\simeq$150 probable lensed sources with the 500-μm flux densities >100 mJy (Nayyeri et al., 2016; Negrello et al., 2017), the cutoff used by Negrello et al. (2010). However, Negrello et al. (2010) estimate that the fraction of high-redshift Herschel sources that are strongly lensed is >50% down to a 500-μm flux density of $\simeq$50 mJy. We have shown in this Chapter that observations with ALMA with exposure times of only a few minutes are enough to show that a bright Herschel source is lensed. Therefore, a programme to obtain short ALMA continuum observations of 500-1000 bright Herschel sources seems a practical way of assembling the required sample of 500 lensed systems. The more challenging part of the programme would be to obtain redshifts for the sources. However,15-minute ALMA observations are often enough to obtain a redshift for a bright Herschel source. Therefore, even this part of the project seems practical in an ALMA Large Programme. In the slightly longer term, continuum surveys with the Square Kilometre Array will contain tens of thousands of lensed sources (Mancuso et al., 2015).

CHAPTER 6

SUMMARY AND FUTURE PROSPECTS

6.1 Summary

The discovery of the population of high redshift SMGs - intense star forming objects highly obscured by dust - has revolutionized our understanding of galaxy formation and evolution. Spanning a redshift range between $z \sim 1-6$ (e.g. Chapman et al., 2005; Wardlow et al., 2013; Simpson et al., 2014; Strandet et al., 2016; Negrello et al., 2017) not only do they probe the peak of cosmic star formation activity ($z \sim 2-3$; Madau and Dickinson, 2014) but also the earliest epoch of galaxy formation (Vieira et al., 2013). The extreme environments in these objects has put models of galaxy formation and evolution to the test, so much so that the debate on their nature is more lively than ever. This is because none of the existing scenarios, which were discussed in Section 1.4, can fully explain all the observational evidence but individually all can be found applicable to different situations (see Casey et al. (2014) for a review on the topic).

Less than 10 years ago, the number of known SMGs was only a handful due to the limited capabilities of instruments in the sub-mm regime. However, the advent of wide area extra-galactic surveys undertaken with Herschel at sub-mm wavelengths (e.g. H-ATLAS; Eales et al., 2010) has increased the number of known SMGs to hundreads of thousands (e.g. Valiante et al., 2016; Maddox et al., 2018). These huge samples of SMGs allow the statistical investigation of their properties to an accuracy that was not possible before. One such property is their clustering strength, which has been predicted to yield quite different results when examining the different models of their formation and evolution (i.e. galaxy-mergers or isolated disks; Xia et al., 2012). In Chapter 3 I measure the clustering strength for a sample 250 μm selected SMGs from the H-ATLAS survey. My findings suggest that $z > 1$ SMGs are consistent with being the progenitors of massive elliptical galaxies in the local Universe. These results are in line with predictions from the self-regulated galaxy evolution model of Granato et al. (2004) but not consistent with predictions assuming galaxy-mergers as the driving mechanics for their evolution (Almeida et al., 2011).

Although the number of known SMGs has drastically increased over the last few years, very few of them have been analyzed to a degree that we can definitively decipher the mysteries around their nature. This is partly due to the lack of counterpart for these high redshift objects, which would offer a multi-wavelength view of their ISM, but also due to the limited capabilities of instruments which are unable to resolve scales down to GMCs ($\sim 10 - 100$ pc). Both of these restrictions can be overcome by the magnifying power of strong gravitational lensing, which not only boosts the apparent flux density of the lensed object but also increases the spatial resolution by a factors of $\sim \sqrt{\mu}$. Especially at sub-mm wavelengths, the method of selecting candidate lensed galaxies is not only simple but also $\sim 100\%$ efficient (see Section 2). The enhanced resolution offered by strong lensing, coupled with the power of ALMA allow us to study these objects in unrepresented detail (e.g Dye et al., 2015). In Chapter 5, I study one of the strong lens discovered in the H-ATLAS survey using a multiwavelength suite of observations from rest-frame optical to sub-mm wavelengths, including various emission lines (CO, C_{II}). I explore the nature of this system and after a careful evaluation of both scenarios (i.e. merger or clumpy rotating disk) I conclude that most evidence seem to suggest that this object is undergoing a merger event. It is not surprising that the debate on the nature of these systems is still intense when two different techniques presented in this Thesis (i.e. clustering and morhological/kinematical analysis) support different interpretations. We need to note that the above statement does not imply that the whole population of SMGs is described by a single scenario. The most likely interpretation is that the SMG population is a mix of clumpy rotating disks and major mergers with the former describing the bulk of the population while the latter the most luminous of these objects.

Finally, besides offering a magnified view of the distant universe, gravitational lensing help us understand the density profiles of objects acting as lenses. The simplicity of our candidate selection (see Chapter 2) in the sub-mm regime allow us to build unbiased samples (in contrast to optical and radio selected samples; e.g. SLACS and SQLS) which will potentially allow us to answer various questions

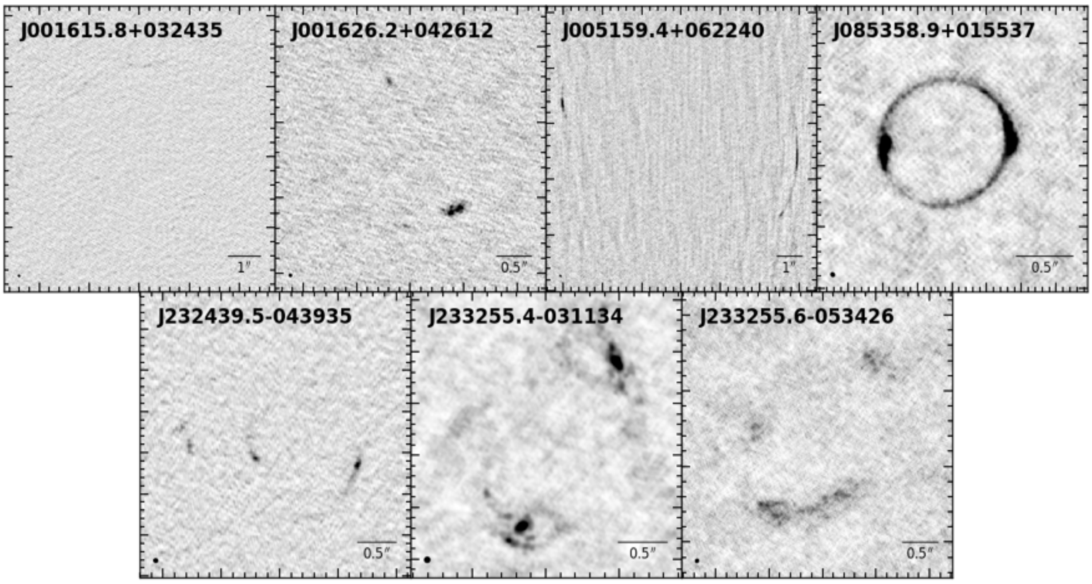

Figure 6.1: Band 9 (~ 1.3 mm) ALMA follow-up dust continuum emission images for seven strongly lensed galaxies in the Amvrosiadis et al. (2018) sample. The size of the synthesized beam is indicated at the bottom left corner of each panel (~ 35 – 37 mas).

regarding their internal structure. I demonstrate the potential of this method in Chapter 4 and show that with a sample of ~ 200 lenses, which is achievable given the predicted number of lensed sources in the Herschel surveys, we will be able to distinguish between the various density profiles that have been used in the literature (analytic or from simulations).

6.2 Ongoing and future work

The future of this field is very promising and more active than ever before. It is clear that the Herschel era has opened the way for current facilities (e.g. SMA, PdBI/NOEMA, ALMA) to further advance our understanding of this population by providing high-resolution follow-up observations for these objects. The list of recent studies on this field is extensive; whether it has to do with the morphology of these objects (e.g. Gullberg et al., 2018; Hodge et al., 2018; Rujopakarn et al., 2019), the nature of these systems based on kinematical studies (e.g. Litke et al., 2019; Tadaki et al., 2018; Yang et al., 2019) or the properties and conditions of their ISM (e.g. Yang et al., 2017; Scoville et al., 2017; Tacconi et al., 2018; Tadaki et al., 2019; Leung et al., 2019; Dong et al., 2019).

We recently obtained high-resolution (~ 35 – 37 mas) follow-up observations with ALMA (see Figure 6.1), both in line and continuum mode, for seven strongly

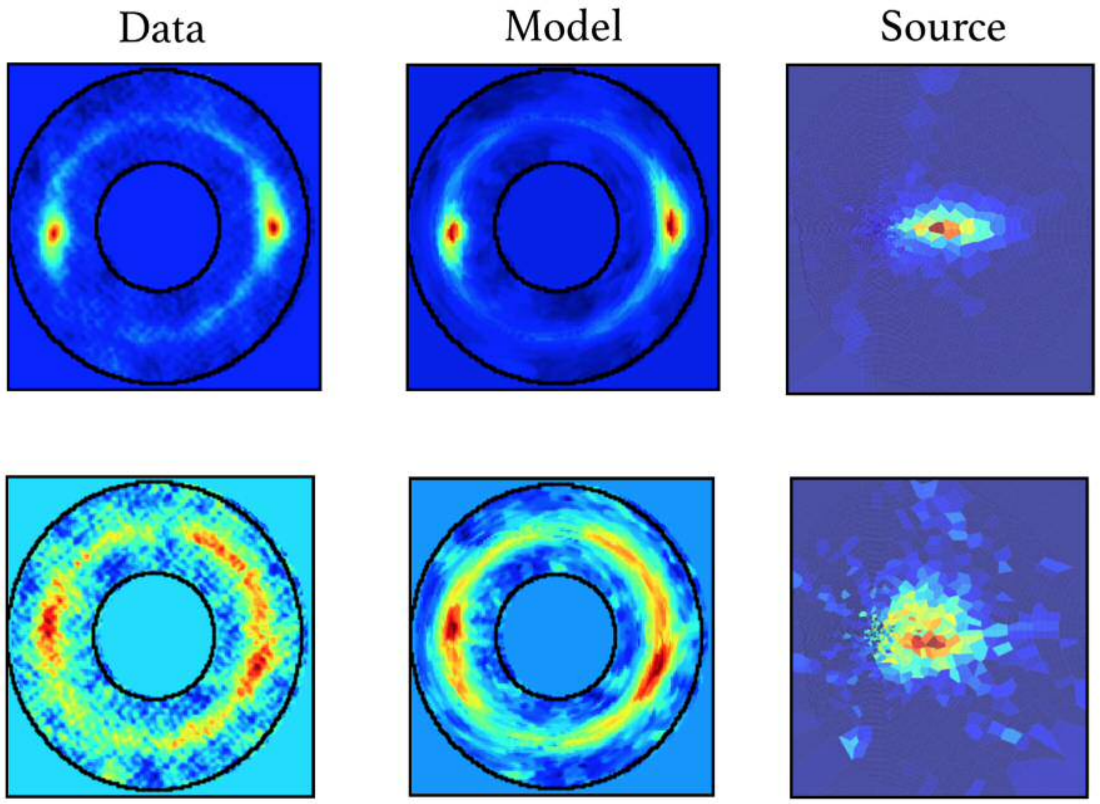

Figure 6.2: Modelling of the dust continuum (top row) and CO(6-5) line emission (bottom row) for the strongly lensed galaxy J085358.9+015537 (Amvrosiadis et al., in prep.). From left to right, the different columns correspond to the observed "dirty" image, the model image and the reconstructed source.

lensed galaxies from the sample presented in Amvrosiadis et al. (2018). We can already see from these images that in some cases (e.g. J001626.2+042612, J233255.6−053426) the background source appears to be breaking into multiple clumps in comparison to the $\sim 0.1''$ images of Amvrosiadis et al. (2018). In the case of J001615.8+032435 we barely detect the lensed emission from the giant arc, due to insufficient on-source integration time, but it's clearly detected in our lower resolution $\sim 0.1''$ images (Amvrosiadis et al., 2018).

Now, considering that these galaxies lie in the redshift range $z \sim 2-3$ means that we can probe scales down to ~ 100 pc (assuming a typical magnification factor of $\mu \sim 10$) which is typical of the largest GMCs seen in local ULIRGs.

This sample will complement the earlier work done by (Dye et al., 2015) on SDP.81 and potentially allow us to answer some fundamental questions about the nature of SMGs. More precisely whether SDP.81 is representative case of a galaxy building starburst or we are just probing one phase of the galaxy formation process. Some preliminary modeling results are shown in Figure 6.2 for one of the objects in this sample, where in this case the modeling was performed in the image-plane using the publicly available software AutoLens (Nightingale et al., 2018). In contrast to SDP.81 the dust continuum emission in this object appears to be very compact and smooth with no evidence of clumps. A similar morphology is found for the reconstructed CO(6-5) line emission, which however is more extended than the dust continuum emission. Once the whole sample is analysed and the kinematics of the background SMGs are reconstructed (Amvrosiadis et al., in prep.), we expect to have a much clearer view for the nature of these objects.

BIBLIOGRAPHY

Abazajian, K. N., Adelman-McCarthy, J. K., Agüeros, M. A., et al. The Seventh Data Release of the Sloan Digital Sky Survey. *{ApJS*, 182:543–558, June 2009.

Adelberger, K. L., Steidel, C. C., Pettini, M., et al. The Spatial Clustering of Star-forming Galaxies at Redshifts $1.4 < z < 3.5$. *ApJ*, 619:697–713, February 2005.

ALMA Partnership, Vlahakis, C., Hunter, T. R., et al. The 2014 ALMA Long Baseline Campaign: Observations of the Strongly Lensed Submillimeter Galaxy HATLAS J090311.6+003906 at z = 3.042. *ApJ*, 808:L4, July 2015.

Almeida, C., Baugh, C. M., and Lacey, C. G. Modelling the dusty universe - II. The clustering of submillimetre-selected galaxies. *MNRAS*, 417:2057–2071, November 2011.

Amblard, A., Cooray, A., Serra, P., et al. Submillimetre galaxies reside in dark matter haloes with masses greater than 3×10^{11} solar masses. *Nature*, 470:510–512, February 2011.

Amvrosiadis, A., Eales, S. A., Negrello, M., et al. ALMA observations of lensed Herschel sources: testing the dark matter halo paradigm. *MNRAS*, 475:4939–4952, April 2018.

Amvrosiadis, A., Valiante, E., Gonzalez-Nuevo, J., et al. Herschel-ATLAS : the spatial clustering of low- and high-redshift submillimetre galaxies. *MNRAS*, 483:4649–4664, March 2019.

Andreani, P., Retana-Montenegro, E., Zhang, Z.-Y., et al. Extreme conditions in the molecular gas of lensed star-forming galaxies at z 3. *A&A*, 615:A142, July 2018.

Aravena, M., Spilker, J. S., Bethermin, M., et al. A survey of the cold molecular gas in gravitationally lensed star-forming galaxies at z > 2. *MNRAS*, 457:4406–4420, April 2016.

Astropy Collaboration, Robitaille, T. P., Tollerud, E. J., et al. Astropy: A community Python package for astronomy. *A&A*, 558:A33, October 2013.

Auger, M. W., Treu, T., Bolton, A. S., et al. The Sloan Lens ACS Survey. X. Stellar, Dynamical, and Total Mass Correlations of Massive Early-type Galaxies. *ApJ*, 724:511–525, November 2010.

Baes, M., Fritz, J., Gadotti, D. A., et al. Herschel-ATLAS: The dust energy balance in the edge-on spiral galaxy UGC 4754. *A&A*, 518:L39, July 2010.

Bakx, T. J. L. C., Eales, S. A., Negrello, M., et al. The Herschel Bright Sources (HerBS): sample definition and SCUBA-2 observations. *MNRAS*, 473:1751–1773, January 2018.

Barger, A. J., Cowie, L. L., Sanders, D. B., et al. Submillimetre-wavelength detection of dusty star-forming galaxies at high redshift. *Nature*, 394:248–251, July 1998.

Bartelmann, M. and Schneider, P. Weak gravitational lensing. *Phys. Rep.*, 340: 291–472, January 2001.

Baugh, C. M., Lacey, C. G., Frenk, C. S., et al. Can the faint submillimetre galaxies be explained in the Λ cold dark matter model? *MNRAS*, 356:1191–1200, January 2005.

Béthermin, M., Daddi, E., Magdis, G., et al. A Unified Empirical Model for Infrared Galaxy Counts Based on the Observed Physical Evolution of Distant Galaxies. *ApJ*, 757:L23, October 2012.

Béthermin, M., De Breuck, C., Gullberg, B., et al. An ALMA view of the interstellar medium of the z = 4.77 lensed starburst SPT-S J213242-5802.9. *A&A*, 586:L7, February 2016.

Blain, A. W. Galaxy-galaxy gravitational lensing in the millimetre/submillimetre waveband. *MNRAS*, 283:1340–1348, December 1996.

Blain, A. W., Smail, I., Ivison, R. J., Kneib, J.-P., and Frayer, D. T. Submillimeter galaxies. *Phys. Rep.*, 369:111–176, October 2002.

Blain, A. W., Chapman, S. C., Smail, I., and Ivison, R. Clustering of Submillimeter-selected Galaxies. *ApJ*, 611:725–731, August 2004.

Blumenthal, G. R., Faber, S. M., Flores, R., and Primack, J. R. Contraction of dark matter galactic halos due to baryonic infall. *ApJ*, 301:27–34, February 1986.

Bocquet, S., Saro, A., Dolag, K., and Mohr, J. J. Halo mass function: baryon impact, fitting formulae, and implications for cluster cosmology. *MNRAS*, 456: 2361–2373, March 2016.

Bolatto, A. D., Wolfire, M., and Leroy, A. K. The CO-to-H_2 Conversion Factor. *ARA&A*, 51:207–268, August 2013.

Bolton, A. S., Burles, S., Koopmans, L. V. E., Treu, T., and Moustakas, L. A. The Sloan Lens ACS Survey. I. A Large Spectroscopically Selected Sample of Massive Early-Type Lens Galaxies. *ApJ*, 638:703–724, February 2006.

Bolton, A. S., Brownstein, J. R., Kochanek, C. S., et al. The BOSS Emission-Line Lens Survey. II. Investigating Mass-density Profile Evolution in the SLACS+BELLS Strong Gravitational Lens Sample. *ApJ*, 757:82, September 2012.

Bothwell, M. S., Smail, I., Chapman, S. C., et al. A survey of molecular gas in luminous sub-millimetre galaxies. *MNRAS*, 429:3047–3067, March 2013.

Bouché, N., Carfantan, H., Schroetter, I., Michel-Dansac, L., and Contini, T. GalPak^{3D}: A Bayesian Parametric Tool for Extracting Morphokinematics of Galaxies from 3D Data. *AJ*, 150:92, September 2015.

Bourne, N., Maddox, S. J., Dunne, L., et al. Colour matters: the effects of lensing on the positional offsets between optical and submillimetre galaxies in Herschel-ATLAS. *MNRAS*, 444:1884–1892, October 2014.

Bourne, N., Dunne, L., Maddox, S. J., et al. The Herschel-ATLAS Data Release 1 - II. Multi-wavelength counterparts to submillimetre sources. *MNRAS*, 462: 1714–1734, October 2016.

Browne, I. W. A., Wilkinson, P. N., Jackson, N. J. F., et al. The Cosmic Lens All-Sky Survey - II. Gravitational lens candidate selection and follow-up. *MNRAS*, 341: 13–32, May 2003.

Brownstein, J. R., Bolton, A. S., Schlegel, D. J., et al. The BOSS Emission-Line Lens Survey (BELLS). I. A Large Spectroscopically Selected Sample of Lens Galaxies at Redshift ˜0.5. *ApJ*, 744:41, January 2012.

Bryan, G. L. and Norman, M. L. Statistical Properties of X-Ray Clusters: Analytic and Numerical Comparisons. *ApJ*, 495:80–99, March 1998.

Budavári, T., Connolly, A. J., Szalay, A. S., et al. Angular Clustering with Photometric Redshifts in the Sloan Digital Sky Survey: Bimodality in the Clustering Properties of Galaxies. *ApJ*, 595:59–70, September 2003.

Bussmann, R. S., Gurwell, M. A., Fu, H., et al. A Detailed Gravitational Lens Model Based on Submillimeter Array and Keck Adaptive Optics Imaging of a

Herschel-ATLAS Submillimeter Galaxy at z = 4.243. *ApJ*, 756:134, September 2012.

Bussmann, R. S., Pérez-Fournon, I., Amber, S., et al. Gravitational Lens Models Based on Submillimeter Array Imaging of Herschel-selected Strongly Lensed Sub-millimeter Galaxies at z > 1.5. *ApJ*, 779:25, December 2013.

Bussmann, R. S., Riechers, D., Fialkov, A., et al. HerMES: ALMA Imaging of Herschel-selected Dusty Star-forming Galaxies. *ApJ*, 812:43, October 2015.

Cañameras, R., Nesvadba, N. P. H., Guery, D., et al. Planck's dusty GEMS: The brightest gravitationally lensed galaxies discovered with the Planck all-sky survey. *A&A*, 581:A105, September 2015.

Cai, Z.-Y., Lapi, A., Xia, J.-Q., et al. A Hybrid Model for the Evolution of Galaxies and Active Galactic Nuclei in the Infrared. *ApJ*, 768:21, May 2013.

Calanog, J. A., Fu, H., Cooray, A., et al. Lens Models of Herschel-selected Galaxies from High-resolution Near-IR Observations. *ApJ*, 797:138, December 2014.

Calistro Rivera, G., Hodge, J. A., Smail, I., et al. Resolving the ISM at the Peak of Cosmic Star Formation with ALMA: The Distribution of CO and Dust Continuum in z ~ 2.5 Submillimeter Galaxies. *ApJ*, 863:56, August 2018.

Carilli, C. L. and Walter, F. Cool Gas in High-Redshift Galaxies. *ARA&A*, 51: 105–161, August 2013.

Carlstrom, J. E., Ade, P. A. R., Aird, K. A., et al. The 10 Meter South Pole Telescope. *PASP*, 123:568, May 2011.

Casey, C. M. Far-infrared spectral energy distribution fitting for galaxies near and far. *MNRAS*, 425:3094–3103, October 2012.

Casey, C. M., Narayanan, D., and Cooray, A. Dusty star-forming galaxies at high redshift. *Phys. Rep.*, 541:45–161, August 2014.

Chae, K.-H. The Cosmic Lens All-Sky Survey: statistical strong lensing, cosmological parameters, and global properties of galaxy populations. *MNRAS*, 346: 746–772, December 2003.

Chapin, E. L., Chapman, S. C., Coppin, K. E., et al. A joint analysis of BLAST 250-500 μm and LABOCA 870 μm observations in the Extended Chandra Deep Field-South. *MNRAS*, 411:505–549, February 2011.

Chapman, S. C., Blain, A. W., Smail, I., and Ivison, R. J. A Redshift Survey of the Submillimeter Galaxy Population. *ApJ*, 622:772–796, April 2005.

Chen, C.-C., Smail, I., Ivison, R. J., et al. The SCUBA-2 Cosmology Legacy Survey: Multiwavelength Counterparts to 10^3 Submillimeter Galaxies in the UKIDSS-UDS Field. *ApJ*, 820:82, April 2016a.

Chen, C.-C., Smail, I., Swinbank, A. M., et al. Faint Submillimeter Galaxies Identified through Their Optical/Near-infrared Colors. I. Spatial Clustering and Halo Masses. *ApJ*, 831:91, November 2016b.

Colless, M., Dalton, G., Maddox, S., et al. The 2dF Galaxy Redshift Survey: spectra and redshifts. *MNRAS*, 328:1039–1063, December 2001.

Condon, J. J., Cotton, W. D., Greisen, E. W., et al. The NRAO VLA Sky Survey. *AJ*, 115:1693–1716, May 1998.

Cooray, A. and Sheth, R. Halo models of large scale structure. *Phys. Rep.*, 372: 1–129, December 2002.

Cooray, A., Amblard, A., Wang, L., et al. HerMES: Halo occupation number and bias properties of dusty galaxies from angular clustering measurements. *A&A*, 518:L22, July 2010.

Cowley, W. I., Lacey, C. G., Baugh, C. M., Cole, S., and Wilkinson, A. Blending bias impacts the host halo masses derived from a cross-correlation analysis of bright submillimetre galaxies. *MNRAS*, 469:3396–3404, August 2017.

Cox, P., Krips, M., Neri, R., et al. Gas and Dust in a Submillimeter Galaxy at $z = 4.24$ from the Herschel Atlas. *ApJ*, 740:63, October 2011.

da Cunha, E., Charlot, S., and Elbaz, D. A simple model to interpret the ultraviolet, optical and infrared emission from galaxies. *MNRAS*, 388:1595–1617, August 2008.

Danielson, A. L. R., Swinbank, A. M., Smail, I., et al. An ALMA Survey of Submillimeter Galaxies in the Extended Chandra Deep Field South: Spectroscopic Redshifts. *ApJ*, 840:78, May 2017.

Davé, R., Finlator, K., Oppenheimer, B. D., et al. The nature of submillimetre galaxies in cosmological hydrodynamic simulations. *MNRAS*, 404:1355–1368, May 2010.

Davis, T. A., Alatalo, K., Bureau, M., et al. The ATLAS^{3D} Project - XIV. The extent and kinematics of the molecular gas in early-type galaxies. *MNRAS*, 429:534–555, February 2013.

de Jong, J. T. A., Verdoes Kleijn, G. A., Boxhoorn, D. R., et al. The first and second data releases of the Kilo-Degree Survey. *A&A*, 582:A62, October 2015.

Dong, C., Spilker, J. S., Gonzalez, A. H., et al. Source structure and molecular gas properties from high-resolution CO imaging of SPT-selected dusty star-forming galaxies. *arXiv e-prints*, January 2019.

Driver, S. P., GAMA Team, Baldry, I. K., et al. Galaxy And Mass Assembly (GAMA). In Andersen, J., Nordströara, m, B., and Bland-Hawthorn, J., editors, *The Galaxy Disk in Cosmological Context*, volume 254 of *IAU Symposium*, pages 469–474, March 2009.

Driver, S. P., Hill, D. T., Kelvin, L. S., et al. Galaxy and Mass Assembly (GAMA): survey diagnostics and core data release. *MNRAS*, 413:971–995, May 2011.

Dunne, L., Eales, S., Edmunds, M., et al. The SCUBA Local Universe Galaxy Survey - I. First measurements of the submillimetre luminosity and dust mass functions. *MNRAS*, 315:115–139, June 2000.

Dunne, L., Gomez, H. L., da Cunha, E., et al. Herschel-ATLAS: rapid evolution of dust in galaxies over the last 5 billion years. *MNRAS*, 417:1510–1533, October 2011.

Dye, S. and Warren, S. J. Decomposition of the Visible and Dark Matter in the Einstein Ring 0047-2808 by Semilinear Inversion. *ApJ*, 623:31–41, April 2005.

Dye, S., Negrello, M., Hopwood, R., et al. Herschel-ATLAS: modelling the first strong gravitational lenses. *MNRAS*, 440:2013–2025, May 2014.

Dye, S., Furlanetto, C., Swinbank, A. M., et al. Revealing the complex nature of the strong gravitationally lensed system H-ATLAS J090311.6+003906 using ALMA. *MNRAS*, 452:2258–2268, September 2015.

Dye, S., Furlanetto, C., Dunne, L., et al. Modelling high-resolution ALMA observations of strongly lensed highly star-forming galaxies detected by Herschel. *MNRAS*, 476:4383–4394, June 2018.

Eales, S., Dunne, L., Clements, D., et al. The Herschel ATLAS. *PASP*, 122:499, May 2010.

Eales, S., Smith, D., Bourne, N., et al. The new galaxy evolution paradigm revealed by the Herschel surveys. *MNRAS*, 473:3507–3524, January 2018.

Eales, S. A. Practical cosmology with lenses. *MNRAS*, 446:3224–3234, January 2015.

Edge, A., Sutherland, W., Kuijken, K., et al. The VISTA Kilo-degree Infrared Galaxy (VIKING) Survey: Bridging the Gap between Low and High Redshift. *The Messenger*, 154:32–34, December 2013.

Engel, H., Tacconi, L. J., Davies, R. I., et al. Most Submillimeter Galaxies are Major Mergers. *ApJ*, 724:233–243, November 2010.

Enia, A., Negrello, M., Gurwell, M., et al. The Herschel-ATLAS: magnifications and physical sizes of 500-μm-selected strongly lensed galaxies. *MNRAS*, 475: 3467–3484, April 2018.

Foreman-Mackey, D., Hogg, D. W., Lang, D., and Goodman, J. emcee: The MCMC Hammer. *PASP*, 125:306, March 2013.

Frayer, D. T., Harris, A. I., Baker, A. J., et al. Green Bank Telescope Zpectrometer CO(1-0) Observations of the Strongly Lensed Submillimeter Galaxies from the Herschel ATLAS. *ApJ*, 726:L22, January 2011.

Freeman, K. C. On the Disks of Spiral and S0 Galaxies. *ApJ*, 160:811, June 1970.

Fu, H., Jullo, E., Cooray, A., et al. A Comprehensive View of a Strongly Lensed Planck-Associated Submillimeter Galaxy. *ApJ*, 753:134, July 2012.

Fu, H., Cooray, A., Feruglio, C., et al. The rapid assembly of an elliptical galaxy of 400 billion solar masses at a redshift of 2.3. *Nature*, 498:338–341, June 2013.

Furlanetto, C., Dye, S., Bourne, N., et al. The second Herschel-ATLAS Data Release - III. Optical and near-infrared counterparts in the North Galactic Plane field. *MNRAS*, 476:961–978, May 2018.

Geach, J. E., Sobral, D., Hickox, R. C., et al. The clustering of Hα emitters at z=2.23 from HiZELS. *MNRAS*, 426:679–689, October 2012.

Geach, J. E., Chapin, E. L., Coppin, K. E. K., et al. The SCUBA-2 Cosmology Legacy Survey: blank-field number counts of 450-μm-selected galaxies and their contribution to the cosmic infrared background. *MNRAS*, 432:53–61, June 2013.

Geach, J. E., Dunlop, J. S., Halpern, M., et al. The SCUBA-2 Cosmology Legacy Survey: 850 μm maps, catalogues and number counts. *MNRAS*, 465:1789–1806, February 2017.

Geach, J. E., Ivison, R. J., Dye, S., and Oteo, I. A Magnified View of Circumnuclear Star Formation and Feedback around an Active Galactic Nucleus at z=2.6. *ApJ*, 866:L12, October 2018.

Gehrels, N. Confidence limits for small numbers of events in astrophysical data. *ApJ*, 303:336–346, April 1986.

George, R. D., Ivison, R. J., Hopwood, R., et al. Far-infrared spectroscopy of a lensed starburst: a blind redshift from Herschel. *MNRAS*, 436:L99–L103, November 2013.

Gladders, M. D. and Yee, H. K. C. The Red-Sequence Cluster Survey. I. The Survey and Cluster Catalogs for Patches RCS 0926+37 and RCS 1327+29. *{ApJS*, 157: 1–29, March 2005.

González-Nuevo, J., Toffolatti, L., and Argüeso, F. Predictions of the Angular Power Spectrum of Clustered Extragalactic Point Sources at Cosmic Microwave Background Frequencies from Flat and All-Sky Two-dimensional Simulations. *ApJ*, 621:1–14, March 2005.

González-Nuevo, J., de Zotti, G., Andreani, P., et al. Herschel-ATLAS: Blazars in the science demonstration phase field. *A&A*, 518:L38, July 2010.

González-Nuevo, J., Lapi, A., Fleuren, S., et al. Herschel-ATLAS: Toward a Sample of ˜1000 Strongly Lensed Galaxies. *ApJ*, 749:65, April 2012.

González-Nuevo, J., Lapi, A., Bonavera, L., et al. H-ATLAS/GAMA: magnification bias tomography. Astrophysical constraints above ˜1 arcmin. *J. Cosmology Astropart. Phys.*, 10:024, October 2017.

Granato, G. L., De Zotti, G., Silva, L., Bressan, A., and Danese, L. A Physical Model for the Coevolution of QSOs and Their Spheroidal Hosts. *ApJ*, 600:580–594, January 2004.

Griffin, M. J., Abergel, A., Abreu, A., et al. The Herschel-SPIRE instrument and its in-flight performance. *A&A*, 518:L3, July 2010.

Gruppioni, C., Pozzi, F., Rodighiero, G., et al. The Herschel PEP/HerMES luminosity function - I. Probing the evolution of PACS selected Galaxies to z $\sim$ 4. *MNRAS*, 432:23–52, June 2013.

Gullberg, B., Swinbank, A. M., Smail, I., et al. The Dust and [C II] Morphologies of Redshift ~4.5 Sub-millimeter Galaxies at ~200 pc Resolution: The Absence of Large Clumps in the Interstellar Medium at High-redshift. *ApJ*, 859:12, May 2018.

Harrington, K. C., Yun, M. S., Cybulski, R., et al. Early science with the Large Millimeter Telescope: observations of extremely luminous high-z sources identified by Planck. *MNRAS*, 458:4383–4399, June 2016.

Harrington, K. C., Yun, M. S., Magnelli, B., et al. Total molecular gas masses of Planck - Herschel selected strongly lensed hyper luminous infrared galaxies. *MNRAS*, 474:3866–3874, March 2018.

Harris, A. I., Baker, A. J., Frayer, D. T., et al. Blind Detections of CO J = 1-0 in 11 H-ATLAS Galaxies at z = 2.1-3.5 with the GBT/Zpectrometer. *ApJ*, 752:152, June 2012.

Hezaveh, Y. D. and Holder, G. P. Effects of Strong Gravitational Lensing on Millimeter-wave Galaxy Number Counts. *ApJ*, 734:52, June 2011.

Hezaveh, Y. D., Marrone, D. P., and Holder, G. P. Size Bias and Differential Lensing of Strongly Lensed, Dusty Galaxies Identified in Wide-Field Surveys. *ApJ*, 761: 20, December 2012.

Hezaveh, Y. D., Marrone, D. P., Fassnacht, C. D., et al. ALMA Observations of SPT-discovered, Strongly Lensed, Dusty, Star-forming Galaxies. *ApJ*, 767:132, April 2013.

Hezaveh, Y. D., Dalal, N., Marrone, D. P., et al. Detection of Lensing Substructure Using ALMA Observations of the Dusty Galaxy SDP.81. *ApJ*, 823:37, May 2016.

Hickox, R. C., Jones, C., Forman, W. R., et al. Host Galaxies, Clustering, Eddington Ratios, and Evolution of Radio, X-Ray, and Infrared-Selected AGNs. *ApJ*, 696: 891–919, May 2009.

Hickox, R. C., Wardlow, J. L., Smail, I., et al. The LABOCA survey of the Extended Chandra Deep Field-South: clustering of submillimetre galaxies. *MNRAS*, 421: 284–295, March 2012.

Hodge, J. A., Carilli, C. L., Walter, F., et al. Evidence for a Clumpy, Rotating Gas Disk in a Submillimeter Galaxy at z = 4. *ApJ*, 760:11, November 2012.

Hodge, J. A., Karim, A., Smail, I., et al. An ALMA Survey of Submillimeter Galaxies in the Extended Chandra Deep Field South: Source Catalog and Multiplicity. *ApJ*, 768:91, May 2013.

Hodge, J. A., Riechers, D., Decarli, R., et al. The Kiloparsec-scale Star Formation Law at Redshift 4: Widespread, Highly Efficient Star Formation in the Dust-obscured Starburst Galaxy GN20. *ApJ*, 798:L18, January 2015.

Hodge, J. A., Swinbank, A. M., Simpson, J. M., et al. Kiloparsec-scale Dust Disks in High-redshift Luminous Submillimeter Galaxies. *ApJ*, 833:103, December 2016.

Hodge, J. A., Smail, I., Walter, F., et al. ALMA reveals evidence for spiral arms, bars, and rings in high-redshift submillimeter galaxies. *arXiv e-prints*, October 2018.

Hogg, D. W. Distance measures in cosmology. *arXiv Astrophysics e-prints*, May 1999.

Holland, W. S., Robson, E. I., Gear, W. K., et al. SCUBA: a common-user submillimetre camera operating on the James Clerk Maxwell Telescope. *MNRAS*, 303: 659–672, March 1999.

Hughes, D. H., Serjeant, S., Dunlop, J., et al. High-redshift star formation in the Hubble Deep Field revealed by a submillimetre-wavelength survey. *Nature*, 394: 241–247, July 1998.

Hung, C.-L., Hayward, C. C., Smith, H. A., et al. Merger Signatures in the Dynamics of Star-forming Gas. *ApJ*, 816:99, January 2016.

Hunter, J. D. Matplotlib: A 2d graphics environment. *Computing in Science & Engineering*, 9(3):90–95, 2007.

Huterer, D., Keeton, C. R., and Ma, C.-P. Effects of Ellipticity and Shear on Gravitational Lens Statistics. *ApJ*, 624:34–45, May 2005.

Huynh, M. T., Emonts, B. H. C., Kimball, A. E., et al. The AT-LESS CO(1-0) survey of submillimetre galaxies in the Extended Chandra Deep Field South: First results on cold molecular gas in galaxies at z ~ 2. *MNRAS*, 467:1222–1230, May 2017.

Inada, N., Oguri, M., Shin, M.-S., et al. The Sloan Digital Sky Survey Quasar Lens Search. V. Final Catalog from the Seventh Data Release. *AJ*, 143:119, May 2012.

Iono, D., Yun, M. S., Aretxaga, I., et al. Clumpy and Extended Starbursts in the Brightest Unlensed Submillimeter Galaxies. *ApJ*, 829:L10, September 2016.

Ivison, R. J., Swinbank, A. M., Smail, I., et al. Herschel-ATLAS: A Binary HyLIRG Pinpointing a Cluster of Starbursting Protoellipticals. *ApJ*, 772:137, August 2013.

Ivison, R. J., Lewis, A. J. R., Weiss, A., et al. The Space Density of Luminous Dusty Star-forming Galaxies at z > 4: SCUBA-2 and LABOCA Imaging of Ultrared Galaxies from Herschel-ATLAS. *ApJ*, 832:78, November 2016.

James, A., Dunne, L., Eales, S., and Edmunds, M. G. SCUBA observations of galaxies with metallicity measurements: a new method for determining the relation between submillimetre luminosity and dust mass. *MNRAS*, 335:753–761, September 2002.

Jin, S., Daddi, E., Liu, D., et al. Super-deblended Dust Emission in Galaxies. II. Far-IR to (Sub)millimeter Photometry and High-redshift Galaxy Candidates in the Full COSMOS Field. *ApJ*, 864:56, September 2018.

Karim, A., Swinbank, A. M., Hodge, J. A., et al. An ALMA survey of submillimetre galaxies in the Extended Chandra Deep Field South: high-resolution 870 μm source counts. *MNRAS*, 432:2–9, June 2013.

Kennicutt, R. C. and Evans, N. J. Star Formation in the Milky Way and Nearby Galaxies. *ARA&A*, 50:531–608, September 2012.

Kochanek, C. S. and White, M. Global Probes of the Impact of Baryons on Dark Matter Halos. *ApJ*, 559:531–543, October 2001.

Koopmans, L. V. E., Treu, T., Bolton, A. S., Burles, S., and Moustakas, L. A. The Sloan Lens ACS Survey. III. The Structure and Formation of Early-Type Galaxies and Their Evolution since z ˜ 1. *ApJ*, 649:599–615, October 2006.

Koopmans, L. V. E., Bolton, A., Treu, T., et al. The Structure and Dynamics of Massive Early-Type Galaxies: On Homology, Isothermality, and Isotropy Inside One Effective Radius. *ApJ*, 703:L51–L54, September 2009.

Kormann, R., Schneider, P., and Bartelmann, M. Isothermal elliptical gravitational lens models. *A&A*, 284:285–299, April 1994.

Kroupa, P. On the variation of the initial mass function. *MNRAS*, 322:231–246, April 2001.

Kuhlen, M., Keeton, C. R., and Madau, P. Gravitational Lensing Statistics in Universes Dominated by Dark Energy. *ApJ*, 601:104–119, January 2004.

Lamarche, C., Verma, A., Vishwas, A., et al. Resolving Star Formation on Subkiloparsec Scales in the High-redshift Galaxy SDP.11 Using Gravitational Lensing. *ApJ*, 867:140, November 2018.

Landy, S. D. and Szalay, A. S. Bias and variance of angular correlation functions. *ApJ*, 412:64–71, July 1993.

Lapi, A. and Cavaliere, A. Self-similar Dynamical Relaxation of Dark Matter Halos in an Expanding Universe. *ApJ*, 743:127, December 2011.

Lapi, A., Shankar, F., Mao, J., et al. Quasar Luminosity Functions from Joint Evolution of Black Holes and Host Galaxies. *ApJ*, 650:42–56, October 2006.

Lapi, A., González-Nuevo, J., Fan, L., et al. Herschel-ATLAS Galaxy Counts and High-redshift Luminosity Functions: The Formation of Massive Early-type Galaxies. *ApJ*, 742:24, November 2011.

Lapi, A., Negrello, M., González-Nuevo, J., et al. Effective Models for Statistical Studies of Galaxy-scale Gravitational Lensing. *ApJ*, 755:46, August 2012.

Larson, R. B. Turbulence and star formation in molecular clouds. *MNRAS*, 194: 809–826, March 1981.

Lawrence, A., Warren, S. J., Almaini, O., et al. The UKIRT Infrared Deep Sky Survey (UKIDSS). *MNRAS*, 379:1599–1617, August 2007.

Leung, T. K. D., Riechers, D. A., Baker, A. J., et al. The ISM Properties and Gas Kinematics of a Redshift 3 Massive Dusty Star-forming Galaxy. *ApJ*, 871:85, January 2019.

Lewis, A., Challinor, A., and Lasenby, A. Efficient Computation of Cosmic Microwave Background Anisotropies in Closed Friedmann-Robertson-Walker Models. *ApJ*, 538:473–476, August 2000.

Li, L.-X. and Ostriker, J. P. Semianalytical Models for Lensing by Dark Halos. I. Splitting Angles. *ApJ*, 566:652–666, February 2002.

Li, L.-X. and Ostriker, J. P. Gravitational Lensing by a Compound Population of Halos: Standard Models. *ApJ*, 595:603–613, October 2003.

Lima, M., Jain, B., and Devlin, M. Lensing magnification: implications for counts of submillimetre galaxies and SZ clusters. *MNRAS*, 406:2352–2372, August 2010a.

Lima, M., Jain, B., Devlin, M., and Aguirre, J. Submillimeter Galaxy Number Counts and Magnification by Galaxy Clusters. *ApJ*, 717:L31–L36, July 2010b.

Limber, D. N. The Analysis of Counts of the Extragalactic Nebulae in Terms of a Fluctuating Density Field. II. *ApJ*, 119:655, May 1954.

Litke, K. C., Marrone, D. P., Spilker, J. S., et al. Spatially Resolved [C II] Emission in SPT0346-52: A Hyper-starburst Galaxy Merger at z~5.7. *ApJ*, 870:80, January 2019.

Lupu, R. E., Scott, K. S., Aguirre, J. E., et al. Measurements of CO Redshifts with Z-Spec for Lensed Submillimeter Galaxies Discovered in the H-ATLAS Survey. *ApJ*, 757:135, October 2012.

Ma, C.-P. Schechter versus Schechter: Subarcsecond Gravitational Lensing and Inner Halo Profiles. *ApJ*, 584:L1–L4, February 2003.

Madau, P. and Dickinson, M. Cosmic Star-Formation History. *ARA&A*, 52:415–486, August 2014.

Maddox, S. J., Dunne, L., Rigby, E., et al. Herschel-ATLAS: The angular correlation function of submillimetre galaxies at high and low redshift. *A&A*, 518:L11, July 2010.

Maddox, S. J., Valiante, E., Cigan, P., et al. The Herschel-ATLAS Data Release 2. Paper II. Catalogs of Far-infrared and Submillimeter Sources in the Fields at the South and North Galactic Poles. *{ApJS*, 236:30, June 2018.

Magliocchetti, M., Lapi, A., Negrello, M., De Zotti, G., and Danese, L. Cosmic dichotomy in the hosts of rapidly star-forming systems at low and high redshifts. *MNRAS*, 437(3):2263–2269, Jan 2014.

Mancuso, C., Lapi, A., Cai, Z.-Y., et al. Predictions for Ultra-deep Radio Counts of Star-forming Galaxies. *ApJ*, 810:72, September 2015.

Marrone, D. P., Spilker, J. S., Hayward, C. C., et al. Galaxy growth in a massive halo in the first billion years of cosmic history. *Nature*, 553:51–54, January 2018.

Marsden, D., Gralla, M., Marriage, T. A., et al. The Atacama Cosmology Telescope: dusty star-forming galaxies and active galactic nuclei in the Southern survey. *MNRAS*, 439(2):1556–1574, Apr 2014.

Martin, D. C., Fanson, J., Schiminovich, D., et al. The Galaxy Evolution Explorer: A Space Ultraviolet Survey Mission. *ApJ*, 619:L1–L6, January 2005.

Mason, C. A., Treu, T., Schmidt, K. B., et al. Correcting the z ~ 8 Galaxy Luminosity Function for Gravitational Lensing Magnification Bias. *ApJ*, 805:79, May 2015.

Massardi, M., Enia, A. F. M., Negrello, M., et al. Chandra and ALMA observations of the nuclear activity in two strongly lensed star-forming galaxies. *A&A*, 610: A53, February 2018.

McMullin, J. P., Waters, B., Schiebel, D., Young, W., and Golap, K. CASA Architecture and Applications. In Shaw, R. A., Hill, F., and Bell, D. J., editors, *Astronomical Data Analysis Software and Systems XVI*, volume 376 of *Astronomical Society of the Pacific Conference Series*, page 127, October 2007.

Messias, H., Dye, S., Nagar, N., et al. Herschel-ATLAS and ALMA. HATLAS J142935.3-002836, a lensed major merger at redshift 1.027. *A&A*, 568:A92, August 2014.

Michałowski, M. J., Dunlop, J. S., Cirasuolo, M., et al. The stellar masses and specific star-formation rates of submillimetre galaxies. *A&A*, 541:A85, May 2012.

Mirabel, I. F., Vigroux, L., Charmandaris, V., et al. The dark side of star formation in the Antennae galaxies. *A&A*, 333:L1–L4, May 1998.

Mitchell-Wynne, K., Cooray, A., Gong, Y., et al. HerMES: A Statistical Measurement of the Redshift Distribution of Herschel-SPIRE Sources Using the Cross-correlation Technique. *ApJ*, 753:23, July 2012.

More, A., Cabanac, R., More, S., et al. The CFHTLS-Strong Lensing Legacy Survey (SL2S): Investigating the Group-scale Lenses with the SARCS Sample. *ApJ*, 749: 38, April 2012.

More, A., Verma, A., Marshall, P. J., et al. SPACE WARPS- II. New gravitational lens candidates from the CFHTLS discovered through citizen science. *MNRAS*, 455:1191–1210, January 2016.

Murray, S. G., Power, C., and Robotham, A. S. G. HMFcalc: An online tool for calculating dark matter halo mass functions. *Astronomy and Computing*, 3:23–34, November 2013.

Myers, A. D., Brunner, R. J., Richards, G. T., et al. First Measurement of the Clustering Evolution of Photometrically Classified Quasars. *ApJ*, 638:622–634, February 2006.

Myers, S. T., Jackson, N. J., Browne, I. W. A., et al. The Cosmic Lens All-Sky Survey - I. Source selection and observations. *MNRAS*, 341:1–12, May 2003.

Narayanan, D., Turk, M., Feldmann, R., et al. The formation of submillimetre-bright galaxies from gas infall over a billion years. *Nature*, 525:496–499, September 2015.

Navarro, J. F., Frenk, C. S., and White, S. D. M. The Structure of Cold Dark Matter Halos. *ApJ*, 462:563, May 1996.

Navarro, J. F., Frenk, C. S., and White, S. D. M. A Universal Density Profile from Hierarchical Clustering. *ApJ*, 490:493–508, December 1997.

Nayyeri, H., Keele, M., Cooray, A., et al. Candidate Gravitationally Lensed Dusty Star-forming Galaxies in the Herschel Wide Area Surveys. *ApJ*, 823:17, May 2016.

Negrello, M., Perrotta, F., González-Nuevo, J., et al. Astrophysical and cosmological information from large-scale submillimetre surveys of extragalactic sources. *MNRAS*, 377:1557–1568, June 2007.

Negrello, M., Hopwood, R., De Zotti, G., et al. The Detection of a Population of Submillimeter-Bright, Strongly Lensed Galaxies. *Science*, 330:800, November 2010.

Negrello, M., Hopwood, R., Dye, S., et al. Herschel -ATLAS: deep HST/WFC3 imaging of strongly lensed submillimetre galaxies. *MNRAS*, 440:1999–2012, May 2014.

Negrello, M., Amber, S., Amvrosiadis, A., et al. The Herschel-ATLAS: a sample of 500 μm-selected lensed galaxies over 600 deg^2. *MNRAS*, 465:3558–3580, March 2017.

Neri, R., Downes, D., Cox, P., and Walter, F. High-resolution C^+ imaging of HDF850.1 reveals a merging galaxy at z = 5.185. *A&A*, 562:A35, February 2014.

Nesvadba, N., Kneissl, R., Cañameras, R., et al. Planck's Dusty GEMS. II. Extended [CII] emission and absorption in the Garnet at z = 3.4 seen with ALMA. *A&A*, 593:L2, August 2016.

Nightingale, J. W. and Dye, S. Adaptive semi-linear inversion of strong gravitational lens imaging. *MNRAS*, 452:2940–2959, September 2015.

Nightingale, J. W., Dye, S., and Massey, R. J. AutoLens: automated modeling of a strong lens's light, mass, and source. *MNRAS*, 478:4738–4784, August 2018.

Norberg, P., Baugh, C. M., Gaztañaga, E., and Croton, D. J. Statistical analysis of galaxy surveys - I. Robust error estimation for two-point clustering statistics. *MNRAS*, 396:19–38, June 2009.

Oguri, M. Constraints on the Baryonic Compression and Implications for the Fraction of Dark Halo Lenses. *ApJ*, 580:2–11, November 2002.

Oguri, M. The image separation distribution of strong lenses: halo versus subhalo populations. *MNRAS*, 367:1241–1250, April 2006.

Oguri, M., Taruya, A., Suto, Y., and Turner, E. L. Strong Gravitational Lensing Time Delay Statistics and the Density Profile of Dark Halos. *ApJ*, 568:488–499, April 2002.

Oguri, M., Inada, N., Pindor, B., et al. The Sloan Digital Sky Survey Quasar Lens Search. I. Candidate Selection Algorithm. *AJ*, 132:999–1013, September 2006.

Oguri, M., Inada, N., Strauss, M. A., et al. The Sloan Digital Sky Survey Quasar Lens Search. III. Constraints on Dark Energy from the Third Data Release Quasar Lens Catalog. *AJ*, 135:512–519, February 2008.

Oguri, M., Inada, N., Strauss, M. A., et al. The Sloan Digital Sky Survey Quasar Lens Search. VI. Constraints on Dark Energy and the Evolution of Massive Galaxies. *AJ*, 143:120, May 2012.

Oliver, S. J., Wang, L., Smith, A. J., et al. HerMES: SPIRE galaxy number counts at 250, 350, and 500 μm. *A&A*, 518:L21, July 2010.

Oliver, S. J., Bock, J., Altieri, B., et al. The Herschel Multi-tiered Extragalactic Survey: HerMES. *MNRAS*, 424:1614–1635, August 2012.

Omont, A., Neri, R., Cox, P., et al. Observation of H_2O in a strongly lensed Herschel-ATLAS source at z = 2.3. *A&A*, 530:L3, June 2011.

Omont, A., Yang, C., Cox, P., et al. H_2O emission in high-z ultra-luminous infrared galaxies. *A&A*, 551:A115, March 2013.

Oteo, I., Zhang, Z.-Y., Yang, C., et al. High Dense Gas Fraction in Intensely Star-forming Dusty Galaxies. *ApJ*, 850:170, December 2017.

Pearson, E. A., Eales, S., Dunne, L., et al. H-ATLAS: estimating redshifts of Herschel sources from sub-mm fluxes. *MNRAS*, 435:2753–2763, November 2013.

Pedregosa, F., Varoquaux, G., Gramfort, A., et al. Scikit-learn: Machine learning in Python. *Journal of Machine Learning Research*, 12:2825–2830, 2011.

Peebles, P. J. E. *The large-scale structure of the universe*. 1980.

Peng, C. Y., Ho, L. C., Impey, C. D., and Rix, H.-W. Detailed Structural Decomposition of Galaxy Images. *AJ*, 124:266–293, July 2002.

Perrotta, F., Baccigalupi, C., Bartelmann, M., De Zotti, G., and Granato, G. L. Gravitational lensing of extended high-redshift sources by dark matter haloes. *MNRAS*, 329:445–455, January 2002.

Perrotta, F., Magliocchetti, M., Baccigalupi, C., et al. Predictions for statistical properties of forming spheroidal galaxies. *MNRAS*, 338:623–636, January 2003.

Pilbratt, G. L., Riedinger, J. R., Passvogel, T., et al. Herschel Space Observatory. An ESA facility for far-infrared and submillimetre astronomy. *A&A*, 518:L1, July 2010.

Planck Collaboration, Ade, P. A. R., Aghanim, N., et al. Planck 2013 results. XXX. Cosmic infrared background measurements and implications for star formation. *A&A*, 571:A30, November 2014.

Planck Collaboration, Aghanim, N., Altieri, B., et al. Planck intermediate results. XXVII. High-redshift infrared galaxy overdensity candidates and lensed sources discovered by Planck and confirmed by Herschel-SPIRE. *A&A*, 582:A30, October 2015.

Planck Collaboration, Ade, P. A. R., Aghanim, N., et al. Planck 2015 results. XIII. Cosmological parameters. *A&A*, 594:A13, September 2016.

Poglitsch, A., Waelkens, C., Geis, N., et al. The Photodetector Array Camera and Spectrometer (PACS) on the Herschel Space Observatory. *A&A*, 518:L2, July 2010.

Popping, G., Decarli, R., Man, A. W. S., et al. ALMA reveals starburst-like interstellar medium conditions in a compact star-forming galaxy at z 2 using [CI] and CO. *A&A*, 602:A11, June 2017.

Porciani, C. and Madau, P. Gravitational Lensing of Distant Supernovae in Cold Dark Matter Universes. *ApJ*, 532:679–693, April 2000.

Prada, F., Klypin, A. A., Cuesta, A. J., Betancort-Rijo, J. E., and Primack, J. Halo concentrations in the standard Λ cold dark matter cosmology. *MNRAS*, 423: 3018–3030, July 2012.

Prugniel, P. and Simien, F. The fundamental plane of early-type galaxies: non-homology of the spatial structure. *A&A*, 321:111–122, May 1997.

Rawle, T. D., Egami, E., Bussmann, R. S., et al. [C II] and ^{12}CO(1-0) Emission Maps in HLSJ091828.6+514223: A Strongly Lensed Interacting System at z = 5.24. *ApJ*, 783:59, March 2014.

Riechers, D. A., Carilli, L. C., Walter, F., et al. Imaging the Molecular Gas Properties of a Major Merger Driving the Evolution of a z = 2.5 Submillimeter Galaxy. *ApJ*, 733:L11, May 2011.

Riechers, D. A., Bradford, C. M., Clements, D. L., et al. A dust-obscured massive maximum-starburst galaxy at a redshift of 6.34. *Nature*, 496:329–333, April 2013.

Rivera, J., Baker, A. J., Gallardo, P. A., et al. The Atacama Cosmology Telescope: CO(J = 3 - 2) mapping and lens modeling of an ACT-selected dusty star-forming galaxy. *ArXiv e-prints*, July 2018.

Robitaille, T. and Bressert, E. APLpy: Astronomical Plotting Library in Python. Astrophysics Source Code Library, August 2012.

Roche, N. and Eales, S. A. The angular correlation function and hierarchical moments of ˜70000 faint galaxies to R=23.5. *MNRAS*, 307:703–721, August 1999.

Rodighiero, G., Daddi, E., Baronchelli, I., et al. The Lesser Role of Starbursts in Star Formation at z = 2. *ApJ*, 739:L40, October 2011.

Ross, N. P., Shen, Y., Strauss, M. A., et al. Clustering of Low-redshift (z > 2.2) Quasars from the Sloan Digital Sky Survey. *ApJ*, 697:1634–1655, June 2009.

Rowan-Robinson, M. and Wang, L. Hyperluminous infrared galaxies from IIFSCz. *MNRAS*, 406:720–728, August 2010.

Rowlands, K., Dunne, L., Dye, S., et al. Herschel-ATLAS: properties of dusty massive galaxies at low and high redshifts. *MNRAS*, 441:1017–1039, June 2014.

Ruff, A. J., Gavazzi, R., Marshall, P. J., et al. The SL2S Galaxy-scale Lens Sample. II. Cosmic Evolution of Dark and Luminous Mass in Early-type Galaxies. *ApJ*, 727: 96, February 2011.

Rujopakarn, W., Daddi, E., Rieke, G. H., et al. ALMA 200-parsec Resolution Imaging of Smooth Cold Dusty Disks in Typical $z \sim 3$ Star-Forming Galaxies. *arXiv e-prints*, April 2019.

Rybak, M., McKean, J. P., Vegetti, S., Andreani, P., and White, S. D. M. ALMA imaging of SDP.81 - I. A pixelated reconstruction of the far-infrared continuum emission. *MNRAS*, 451:L40–L44, July 2015a.

Rybak, M., Vegetti, S., McKean, J. P., Andreani, P., and White, S. D. M. ALMA imaging of SDP.81 - II. A pixelated reconstruction of the CO emission lines. *MNRAS*, 453:L26–L30, October 2015b.

Rybak, M., Calistro Rivera, G., Hodge, J. A., et al. Strong FUV fields drive the [CII]/FIR deficit in z˜3 dusty, star-forming galaxies. *arXiv e-prints*, January 2019.

Sanders, D. B. and Mirabel, I. F. Luminous Infrared Galaxies. *ARA&A*, 34:749, 1996.

Sandstrom, K. M., Leroy, A. K., Walter, F., et al. The CO-to-H_2 Conversion Factor and Dust-to-gas Ratio on Kiloparsec Scales in Nearby Galaxies. *ApJ*, 777:5, November 2013.

Schaller, M., Frenk, C. S., Bower, R. G., et al. Baryon effects on the internal structure of ΛCDM haloes in the EAGLE simulations. *MNRAS*, 451:1247–1267, August 2015a.

Schaller, M., Frenk, C. S., Bower, R. G., et al. The effect of baryons on the inner density profiles of rich clusters. *MNRAS*, 452:343–355, September 2015b.

Schaye, J., Crain, R. A., Bower, R. G., et al. The EAGLE project: simulating the evolution and assembly of galaxies and their environments. *MNRAS*, 446: 521–554, January 2015.

Schneider, P., Ehlers, J., and Falco, E. E. *Gravitational Lenses*. 1992.

Scoville, N., Sheth, K., Aussel, H., et al. ISM Masses and the Star formation Law at Z = 1 to 6: ALMA Observations of Dust Continuum in 145 Galaxies in the COSMOS Survey Field. *ApJ*, 820:83, April 2016.

Scoville, N., Lee, N., Vanden Bout, P., et al. Evolution of Interstellar Medium, Star Formation, and Accretion at High Redshift. *ApJ*, 837:150, March 2017.

Sheth, R. K. and Tormen, G. Large-scale bias and the peak background split. *MNRAS*, 308:119–126, September 1999.

Simpson, J. M., Swinbank, A. M., Smail, I., et al. An ALMA Survey of Submillimeter Galaxies in the Extended Chandra Deep Field South: The Redshift Distribution and Evolution of Submillimeter Galaxies. *ApJ*, 788:125, June 2014.

Simpson, J. M., Smail, I., Swinbank, A. M., et al. The SCUBA-2 Cosmology Legacy Survey: ALMA Resolves the Rest-frame Far-infrared Emission of Sub-millimeter Galaxies. *ApJ*, 799:81, January 2015.

Siringo, G., Kreysa, E., Kovács, A., et al. The Large APEX BOlometer CAmera LABOCA. *A&A*, 497:945–962, April 2009.

Smail, I., Ivison, R. J., and Blain, A. W. A Deep Sub-millimeter Survey of Lensing Clusters: A New Window on Galaxy Formation and Evolution. *ApJ*, 490:L5–L8, November 1997.

Smith, M. W. L., Ibar, E., Maddox, S. J., et al. The Herschel-ATLAS Data Release 2, Paper I. Submillimeter and Far-infrared Images of the South and North Galactic Poles: The Largest Herschel Survey of the Extragalactic Sky. *{ApJS*, 233:26, December 2017.

Smith, R. E., Peacock, J. A., Jenkins, A., et al. Stable clustering, the halo model and non-linear cosmological power spectra. *MNRAS*, 341:1311–1332, June 2003.

Solomon, P. M. and Vanden Bout, P. A. Molecular Gas at High Redshift. *ARA&A*, 43:677–725, September 2005.

Speagle, J. S., Steinhardt, C. L., Capak, P. L., and Silverman, J. D. A Highly Consistent Framework for the Evolution of the Star-Forming "Main Sequence" from z ˜ 0-6. *{ApJS*, 214:15, October 2014.

Spilker, J. S., Aravena, M., Marrone, D. P., et al. Sub-kiloparsec Imaging of Cool Molecular Gas in Two Strongly Lensed Dusty, Star-forming Galaxies. *ApJ*, 811: 124, October 2015.

Spilker, J. S., Marrone, D. P., Aravena, M., et al. ALMA Imaging and Gravitational Lens Models of South Pole Telescope–Selected Dusty, Star-Forming Galaxies at High Redshifts. *ApJ*, 826:112, August 2016.

Spilker, J. S., Aravena, M., Béthermin, M., et al. Fast molecular outflow from a dusty star-forming galaxy in the early Universe. *Science*, 361:1016–1019, September 2018.

Stanford, S. A., Gonzalez, A. H., Brodwin, M., et al. The Massive and Distant Clusters of WISE Survey. II. Initial Spectroscopic Confirmation of z ˜ 1 Galaxy Clusters Selected from 10,000 deg^2. {*ApJS*, 213:25, August 2014.

Strandet, M. L., Weiss, A., Vieira, J. D., et al. The Redshift Distribution of Dusty Star-forming Galaxies from the SPT Survey. *ApJ*, 822:80, May 2016.

Suyu, S. H., Marshall, P. J., Hobson, M. P., and Blandford, R. D. A Bayesian analysis of regularized source inversions in gravitational lensing. *MNRAS*, 371:983–998, September 2006.

Swinbank, A. M., Karim, A., Smail, I., et al. An ALMA survey of submillimetre galaxies in the Extended Chandra Deep Field-South: detection of [C II] at z = 4.4. *MNRAS*, 427:1066–1074, December 2012.

Swinbank, A. M., Simpson, J. M., Smail, I., et al. An ALMA survey of submillimetre Galaxies in the Extended Chandra Deep Field South: the far-infrared properties of SMGs. *MNRAS*, 438:1267–1287, February 2014.

Swinbank, A. M., Dye, S., Nightingale, J. W., et al. ALMA Resolves the Properties of Star-forming Regions in a Dense Gas Disk at $z \sim 3$. *ApJ*, 806:L17, June 2015.

Tacconi, L. J., Neri, R., Chapman, S. C., et al. High-Resolution Millimeter Imaging of Submillimeter Galaxies. *ApJ*, 640:228–240, March 2006.

Tacconi, L. J., Genzel, R., Neri, R., et al. High molecular gas fractions in normal massive star-forming galaxies in the young Universe. *Nature*, 463:781–784, February 2010.

Tacconi, L. J., Genzel, R., Saintonge, A., et al. PHIBSS: Unified Scaling Relations of Gas Depletion Time and Molecular Gas Fractions. *ApJ*, 853:179, February 2018.

Tadaki, K., Iono, D., Yun, M. S., et al. The gravitationally unstable gas disk of a starburst galaxy 12 billion years ago. *Nature*, 560:613–616, August 2018.

Tadaki, K.-i., Iono, D., Hatsukade, B., et al. CNO Emission of an Unlensed Submillimeter Galaxy at z=4.3. *ApJ*, 876:1, May 2019.

Takahashi, R. and Chiba, T. Gravitational Lens Statistics and the Density Profile of Dark Halos. *ApJ*, 563:489–496, December 2001.

Takahashi, R., Sato, M., Nishimichi, T., Taruya, A., and Oguri, M. Revising the Halofit Model for the Nonlinear Matter Power Spectrum. *ApJ*, 761:152, December 2012.

Taylor, M. B. TOPCAT & STIL: Starlink Table/VOTable Processing Software. In Shopbell, P., Britton, M., and Ebert, R., editors, *Astronomical Data Analysis Software and Systems XIV*, volume 347 of *Astronomical Society of the Pacific Conference Series*, page 29, December 2005.

Tinker, J., Kravtsov, A. V., Klypin, A., et al. Toward a Halo Mass Function for Precision Cosmology: The Limits of Universality. *ApJ*, 688:709–728, December 2008.

Tinker, J. L., Robertson, B. E., Kravtsov, A. V., et al. The Large-scale Bias of Dark Matter Halos: Numerical Calibration and Model Tests. *ApJ*, 724:878–886, December 2010.

Tomczak, A. R., Quadri, R. F., Tran, K.-V. H., et al. The SFR-M* Relation and Empirical Star-Formation Histories from ZFOURGE* at 0.5 < z < 4. *ApJ*, 817:118, February 2016.

Toomre, A. On the gravitational stability of a disk of stars. *ApJ*, 139:1217–1238, May 1964.

Turner, E. L., Ostriker, J. P., and Gott, J. R., III. The statistics of gravitational lenses - The distributions of image angular separations and lens redshifts. *ApJ*, 284: 1–22, September 1984.

Valiante, E., Smith, M. W. L., Eales, S., et al. The Herschel-ATLAS data release 1 - I. Maps, catalogues and number counts. *MNRAS*, 462:3146–3179, November 2016.

Valtchanov, I., Virdee, J., Ivison, R. J., et al. Physical conditions of the interstellar medium of high-redshift, strongly lensed submillimetre galaxies from the Herschel-ATLAS. *MNRAS*, 415:3473–3484, August 2011.

van der Walt, S., Colbert, S. C., and Varoquaux, G. The NumPy Array: A Structure for Efficient Numerical Computation. *Computing in Science and Engineering*, 13 (2):22–30, March 2011.

van Kampen, E., Smith, D. J. B., Maddox, S., et al. Herschel-ATLAS/GAMA: spatial clustering of low-redshift submm galaxies. *MNRAS*, 426:3455–3463, November 2012.

Vegetti, S. and Koopmans, L. V. E. Bayesian strong gravitational-lens modelling on adaptive grids: objective detection of mass substructure in Galaxies. *MNRAS*, 392:945–963, January 2009.

Vegetti, S., Koopmans, L. V. E., Bolton, A., Treu, T., and Gavazzi, R. Detection of a dark substructure through gravitational imaging. *MNRAS*, 408:1969–1981, November 2010.

Vieira, J. D., Crawford, T. M., Switzer, E. R., et al. Extragalactic Millimeter-wave Sources in South Pole Telescope Survey Data: Source Counts, Catalog, and Statistics for an 87 Square-degree Field. *ApJ*, 719:763–783, August 2010.

Vieira, J. D., Marrone, D. P., Chapman, S. C., et al. Dusty starburst galaxies in the early Universe as revealed by gravitational lensing. *Nature*, 495:344–347, March 2013.

Viero, M. P., Ade, P. A. R., Bock, J. J., et al. BLAST: Correlations in the Cosmic Far-Infrared Background at 250, 350, and 500 μm Reveal Clustering of Star-forming Galaxies. *ApJ*, 707:1766–1778, December 2009.

Viero, M. P., Wang, L., Zemcov, M., et al. HerMES: Cosmic Infrared Background Anisotropies and the Clustering of Dusty Star-forming Galaxies. *ApJ*, 772:77, July 2013.

Viero, M. P., Asboth, V., Roseboom, I. G., et al. The Herschel Stripe 82 Survey (HerS): Maps and Early Catalog. *{ApJS*, 210:22, February 2014.

Wake, D. A., Sheth, R. K., Nichol, R. C., et al. The 2dF-SDSS LRG and QSO Survey: evolution of the clustering of luminous red galaxies since z = 0.6. *MNRAS*, 387: 1045–1062, July 2008.

Wang, S. X., Brandt, W. N., Luo, B., et al. An ALMA Survey of Submillimeter Galaxies in the Extended Chandra Deep Field-South: The AGN Fraction and X-Ray Properties of Submillimeter Galaxies. *ApJ*, 778:179, December 2013.

Wardlow, J. L., Cooray, A., De Bernardis, F., et al. HerMES: Candidate Gravitationally Lensed Galaxies and Lensing Statistics at Submillimeter Wavelengths. *ApJ*, 762:59, January 2013.

Wardlow, J. L., Cooray, A., Osage, W., et al. The Interstellar Medium in High-redshift Submillimeter Galaxies as Probed by Infrared Spectroscopy*. *ApJ*, 837: 12, March 2017.

Wardlow, J. L., Simpson, J. M., Smail, I., et al. An ALMA survey of CO in submillimetre galaxies: companions, triggering, and the environment in blended sources. *MNRAS*, 479:3879–3891, September 2018.

Warren, S. J. and Dye, S. Semilinear Gravitational Lens Inversion. *ApJ*, 590:673–682, June 2003.

Webb, T. M., Eales, S., Foucaud, S., et al. The Canada-United Kingdom Deep Submillimeter Survey. V. The Submillimeter Properties of Lyman Break Galaxies. *ApJ*, 582:6–16, January 2003.

Weiß, A., Kovács, A., Coppin, K., et al. The Large Apex Bolometer Camera Survey of the Extended Chandra Deep Field South. *ApJ*, 707:1201–1216, December 2009.

White, S. D. M. and Rees, M. J. Core condensation in heavy halos - A two-stage theory for galaxy formation and clustering. *MNRAS*, 183:341–358, May 1978.

Wilkinson, A., Almaini, O., Chen, C.-C., et al. The SCUBA-2 Cosmology Legacy Survey: the clustering of submillimetre galaxies in the UKIDSS UDS field. *MNRAS*, 464:1380–1392, January 2017.

Williams, C. C., Giavalisco, M., Porciani, C., et al. On the Clustering of Submillimeter Galaxies. *ApJ*, 733:92, June 2011.

Wright, E. L., Eisenhardt, P. R. M., Mainzer, A. K., et al. The Wide-field Infrared Survey Explorer (WISE): Mission Description and Initial On-orbit Performance. *AJ*, 140:1868–1881, December 2010.

Xia, J.-Q., Negrello, M., Lapi, A., et al. Clustering of submillimetre galaxies in a self-regulated baryon collapse model. *MNRAS*, 422:1324–1331, May 2012.

Yang, C., Omont, A., Beelen, A., et al. Submillimeter H_2O and H_2O^+emission in lensed ultra- and hyper-luminous infrared galaxies at z 2-4. *A&A*, 595:A80, November 2016.

Yang, C., Omont, A., Beelen, A., et al. Molecular gas in the Herschel-selected strongly lensed submillimeter galaxies at z ~ 2-4 as probed by multi-J CO lines. *A&A*, 608:A144, December 2017.

Yang, C., Gavazzi, R., Beelen, A., et al. CO, H2O, H2O+ line and dust emission in a z = 3.63 strongly lensed starburst merger at sub-kiloparsec scales. *arXiv e-prints*, March 2019.

Zehavi, I., Zheng, Z., Weinberg, D. H., et al. Galaxy Clustering in the Completed SDSS Redshift Survey: The Dependence on Color and Luminosity. *ApJ*, 736:59, July 2011.

Zhang, Z.-Y., Ivison, R. J., George, R. D., et al. Far-infrared Herschel SPIRE spectroscopy of lensed starbursts reveals physical conditions of ionized gas. *MNRAS*, 481:59–97, November 2018.

APPENDIX A

CORRECTION TO THE ANGULAR CORRELATION FUNCTION

One concern that was pointed out by Maddox et al. (2010) is the effect of removing the Galactic cirrus emission, on the measured clustering signal of submillimeter sources. This emission was removed, using the *Nebuliser* algorithm, before trying to detect extragalactic sources with the MADX (Maddox et al. in preparation) algorithm on the *Herschel* images (as discussed in Section 3.2). In addition to the background cirrus emission, *Nebuliser* can also remove any large scale background produced by clustered faint sources that cannot be individually resolved and can ultimately affect the measured clustering signal (Valiante et al., 2016; Maddox et al., 2018).

A.1 Generating Realistic Maps

In order to quantify this effect we create catalogues of clustered source positions on the sky region covered by the *GAMA*-15h field according to an input power-law power spectrum $P_{corr}(k)$[1]. For these catalogues we follow the methodology of González-Nuevo et al. (2005) (G05). We adopt the model by Cai et al. (2013) for the number count distribution of these sources assuming a minimum flux limit of $S_{min} = 5\,\mathrm{mJy}$, unless otherwise stated (we refer the reader to the G05 paper for more details).

---

[1] In the case of a power-law power spectrum $P(k) \propto k^{-1.2}$, the angular correlation function $w(\theta) \propto \theta^{-0.8}$

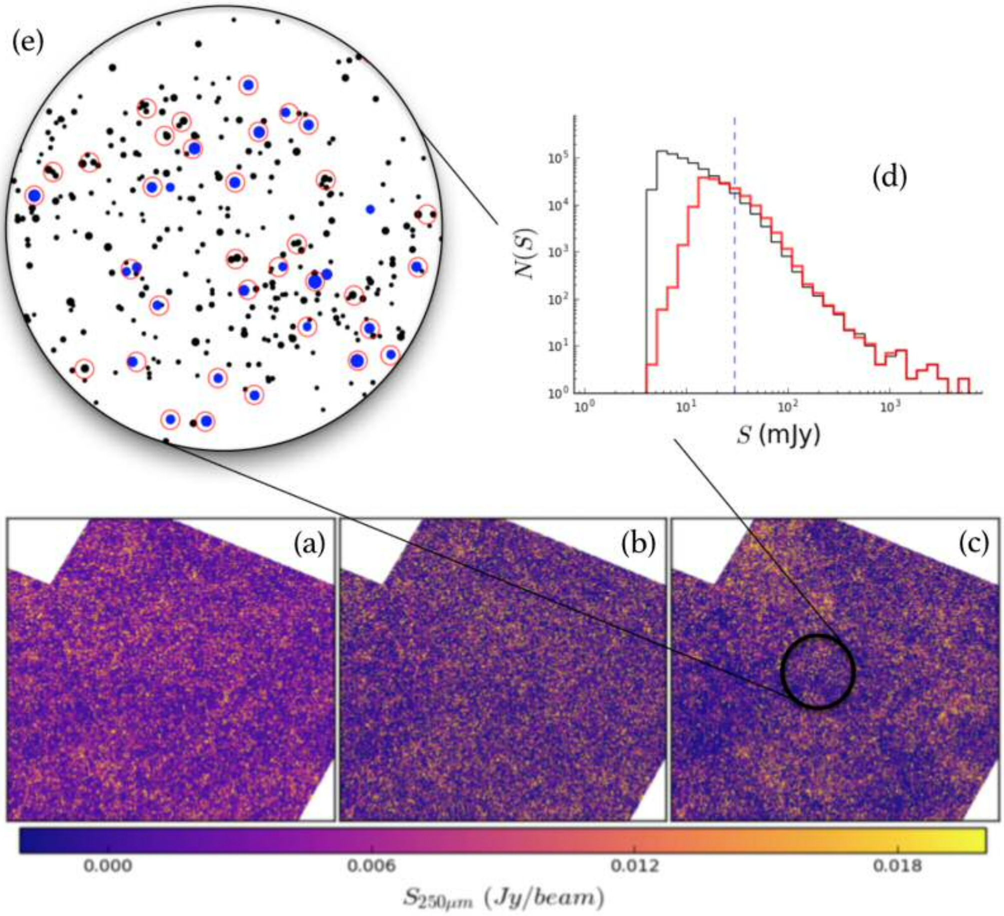

Figure A.1: The different steps illustrating the procedure followed to produce realistic maps of clustered point sources for the *GAMA*-15*h* field (see text for more details). Panel (a) shows the convolved map of our input point sources, panel (b) the noise was added and in panel (c) the background emission from the *Nebuliser* using a pixel scale $N_{pix,b} = 30$ arcmin was added and the mean of the map was set to zero. Applying our source extraction algorithm (MADX) using a pixel scale $N_{pix,f} = 30$ arcmin we obtain the number counts as a function of flux density shown as the red histogram in panel (d), with the input number counts shown as the black histogram respectively. Finally, panel (e) shows a zoomed in region of panel (c) where the black and blue points correspond to the input sources, with the blue being the sources with flux densities >30mJy. The red circles on the other hand correspond to our extracted sources with flux densities >30mJy.

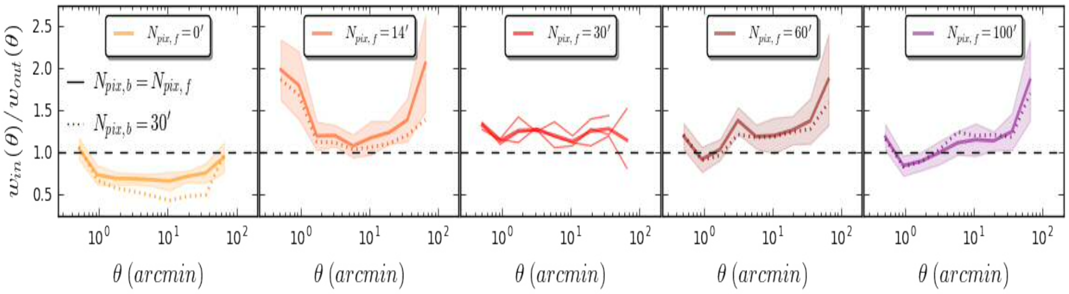

Figure A.2: The ratio of the measured input to the output (after filtering) angular correlation function. The different panels, going from left to right, correspond to a filtering scale of $N_{pix,f} = 0, 14, 30, 60, 100$. In all panels, the dotted lines correspond to a added background emission that was produced by the *Nebuliser* algorithm using a filtering scale $N_{pix,b} = 30$. The continuous lines, on the other hand, correspond to a added background emission using $N_{pix,b} = N_{pix,f}$, where the shaded regions are the 1σ Poisson uncertainties to the measurements. In the middle panel, corresponding to a filtering scale $N_{pix,b} = 30$, we performed this procedure for three realisations of our simulations. These are shown as the thin faded continuous lines where the thick line shows their average.

These catalogues were then used to produce realistic maps of the *GAMA*-15*h* field. We start by creating a high resolution map (1"/pixel) on top of which our simulated sources are laid down. This map is convolved with a PSF (the measured FWHM of the azimuthially average circular PSF is 17.8 at 250μm) and consequently rescaled to the real *Herschel* pixel size at 250 microns (6"/pixel). In panel (a) of Figure A.1 a small patch of this map is shown. Subsequently, the noise map was added to the image. This map was created by assigning each pixel a value drawn from a gaussian distribution with zero mean and standard deviation equal to the corresponding pixel value of the raw instrumental noise map of the *GAMA*-15*h* field (see Valiante et al., 2016). In panel (b), the same patch of the map is shown after the noise was added. Finally, we included the Galactic background cirrus emission that was estimated by *Nebulizer* on our real Herschel image of the *GAMA*-15*h* field, using a filtering scale of N_{pix} pixels. We will use the notation $N_{pix,b}$ when we refer to the background that was added to our simulated map. The last step of the map-making procedure is to set the mean of the map to zero. In panel (c) of Figure A.1 we show the case with $N_{pix,b} = 30$.

Once our simulated map is created we then execute our source extraction algorithm after we filter our map with Nebulizer with a scale in pixels equal to $N_{pix,f}$. We will use the notation $N_{pix,f}$ when we refer to the filtering of our simulated maps prior to source extraction. In Figure A.1 we have used $N_{pix,b} = N_{pix,f} = 30$.

In the right top corner we show the number counts of our input catalogue of simulated point sources as the black histogram along with the number counts of sources extracted from our simulated map as the red histogram. For a visual aid in the left top corner we show the input and output source catalogues in a smaller region of the map. The black and blue points correspond to our input sources (the size of these points is indicative of their flux densities), where blue points are sources with flux densities $S \geq 30\,\mathrm{mJy}$. Equivalently, the open red circles are sources in the output catalogue with flux densities $S \geq 30\,\mathrm{mJy}$. As shown from this Figure, as well as from the histograms, there is a clear flux boosting effect taking place due to the confusion of low flux density sources.

A.2 Determining the correction factor

In order to now quantify the effect in question we compute the ratio of input to the output angular correlation function for sources with $S > 30\,\mathrm{mJy}$, where the results are shown in Figure A.2. The different panels correspond to the different filtering pixel scales used in the analysis $N_{pix,f} = 0, 14, 30, 60, 100$ starting from left to right, respectively. The continuous lines correspond to a background with $N_{pix,b} = N_{pix,f}$ pixel scale, while for the dotted lines we used the same background for all panel of $N_{pix,b} = 30$. The case of $N_{pix,b} = 0$ means that no background emission was added.

In the case where no filtering is being applied prior to the source extraction (first panel of Figure A.2) the resulting clustering strength of our extracted sources is enhanced in all angular scales, whether or not a background is added. This results from the combination of two effects: (i) The low flux density sources of our input catalogue, which constitute the unresolved background, are also clustered. (ii) The added background cirrus emission is also contributing to the enchantment of the clustering signal. In the remaining cases, we filter our simulated map prior to the extraction of sources using the different filtering pixel scales. The aim of filtering the map is to remove the cirrus emission only, but as a consequence some real clustering is also removed.

We determine that the case of $N_{pix,f} = 30$, which is in fact the one used for extracting sources from the H-ATLAS maps, performs best. From the ratio of input to output angular correlation functions we work out that a 25% correction needs to be applied, at all angular scales, to the clustering measurements. In fact, for this case only we performed this procedure for three realisations of our simulation, which are shown as the thin faded red lines in the middle panel of Figure A.2, where the thicker red line is their average. We use this correction factor in our analysis, only when specifically stated. In addition, we see from the different realisations that there is non-negligible scatter, which will contribute to the final error budget of the measured clustering properties presented in Figure 3.9. As a result the quoted errors in Figure 3.9 are slightly underestimated.

A.3 Maddox et al. (2010) vs Cooray et al. (2010)

We pointed out in Section 3.4.2 that our measurement of the angular correlation function is significantly lower compared to the measurement of Cooray et al. (2010). In their case, no filtering was applied prior to source extraction, even though there should be cirrus contamination to some degree in the HERMES fields. This means that their measurement would fall into the case of $N_{pix,b} = 30$ and $N_{pix,f} = 0$. On the other hand, our measurement would corresponds to $N_{pix,b} = 30$ and $N_{pix,f} = 30$. Our simulations in Figure A.2 suggest that there is more than a 50% difference between these two cases. This could be the reason of the disagreement between the two measurements, which was first pointed out by Maddox et al. (2010).

APPENDIX B

FITTING GAUSSIAN PROFILES TO THE RECONSTRUCTED SOURCE

As mentioned in Section 4.5.1 we used a Gaussian profile which we fit to the reconstructed dust continuum emission at 440 μm (ALMA Band 9). The results from our fitting procedure are shown in the first 3 panels of Figure B.2 where we have the original reconstructed source in panel (a), the model in panel (b) and the residuals in panel (c). In this case we can see that we have some significant residuals ($> 3\sigma$) in the East part of the source. We therefore introduce a second Gaussian component to the model and perform the fit again. The double Gaussian profile model and its residuals are shown in panels (d) and (e), respectively, with the two Gaussian components that comprise our model shown in the inset plot

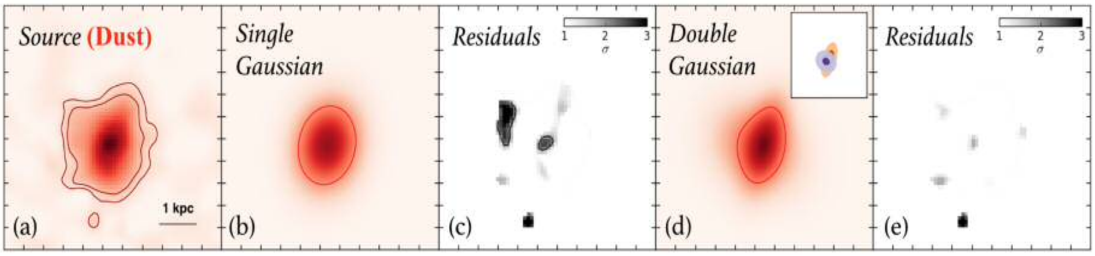

Figure B.1: Results from fitting Gaussian profiles to the reconstructed dust continuum emission at 400 μm (ALMA Band 9). The different panels from left to right show: (a) the original reconstructed source, (b) the best-fit model with a single Gaussian profile, (c) the residuals from panels (a) and (b), (d) the best-fit model with a double Gaussian profile where the inset plot shows the two components, (e) the residuals from panels (a) and (d).

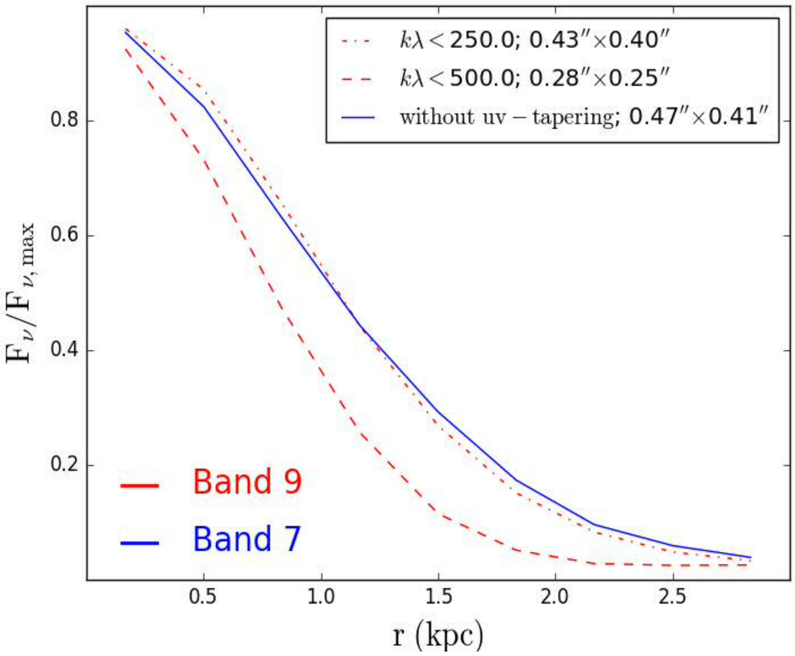

Figure B.2: The normalised surface brightness distribution of the dust continuum as a function of radius (in kpc) from the centre of the emission, where the centre was determined by fitting a 2D Gaussian model. The blue and red lines correspond to the dust continuum in the ALMA bands 7 and 9, respectively. The red dashed and dot-dashed lines correspond to the profiles of the reconstructed sources, where prior to reconstruction we applied a *uv-tapering* of $k\lambda < 250$ and $k\lambda < 500$, respectively. The legend in the figure show the achieved resolution after tapering the visibilities in Band 9.

of panel (d). This simple exercise is to demonstrate that the SLI method (see Section 4.4) captures the true spatial extent of the background source and that sizes and magnifications are more accurately computed in this way (Enia et al., 2018).

In addition, we mentioned in Section 4.5.1 that the spatial extent of dust continuum emission differs in different bands (e.g. see ALMA Bands 7 and 9 in Figure 4.6). In the main text, we attribute this effect to the difference in sensitivity of our observations. To demonstrate that, we taper the visibilities in Band 9 in order to achieve a similar resolution as in Band 7 and then perform the source reconstruction. We fit a single Gaussian profile to the reconstructed source in Bands 7 and 9 for both the original and the uv-tapered source. We plot the normalised radially averaged profiles of the sources in Figure B.2. As we can see surface brightness profiles of the dust continuum in the ALMA Band 7 and in the ALMA Band 9 with a $k\lambda < 250$ uv-tapering, which results in a similar resolution, agree very well.

APPENDIX C

UNDERSTANDING THE SISSA MODEL

In this section we show the effects of the various ingredients that enter the calculation of cumulative image separation distribution. This is calculated from Eq. 5.23 by substituting the Dirac delta function by the Heaviside step function. For this particular calculation only we use the standard method for computing cross-sections as $\sigma = \pi\beta_{cr}^2$, where β_{cr} is the radial caustic within which multiple images are formed.

C.1 Variation in z_s

The source redshift, z_s, predominantly affects the amplitude of the distribution. This is to be expected since a higher source redshift corresponds to a larger volume of the Universe being considered. However, the predicted distributions of image separations in Section 5.4 are normalised and therefore this additional factor cancels out.

C.2 Variation in Halo-Mass Function

The use of different halo mass functions models has very little effect on the distribution of image separations. The T08 and Bocquet mass functions assume the same formalism but their parameters are calibrated from DM only and Hydro cosmological simulations, respectively. Comparing the halo mass functions themselves we find that the effect of baryons is to suppress only slightly the creation of

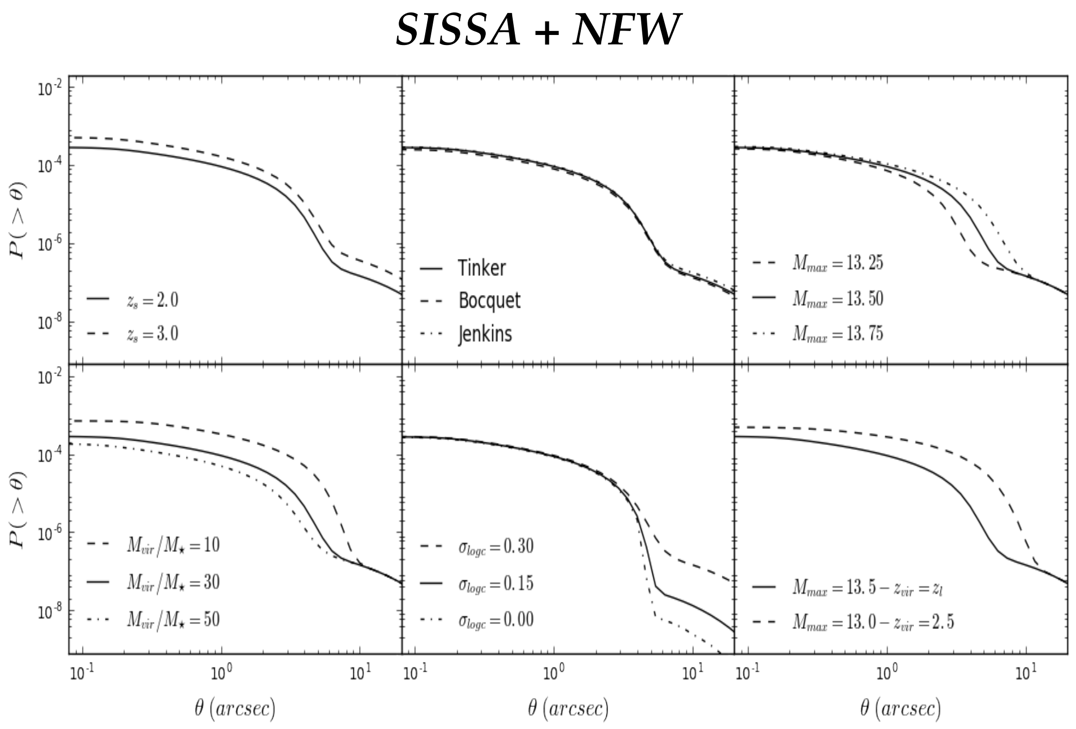

Figure C.1: Effects of parameter variation in the cumulative distribution of image separations.

massive halos but only as small redshifts. At higher redshifts they tend to agree fairly well.

C.3 Variation in M_{max}

The upper transition mass M_{max} parametrizes the change from galaxy-sized SISSA to group- and cluster-sized NFW lenses. This parameter determined the position of the kink in the image separation distribution. For an upper transition mass of $logM_{max} = 13.50$ this transition occurs at $\theta = 7''$. Lowering the transition mass to $logM_{max} = 13.25$ shifts this transition down to $\theta = 4''$, while increasing it to $logM_{max} = 13.75$ this transition shifts up to $\theta = 10''$.

C.4 Variation in $M_{vir}/M_\star$ Ratio

The ratio between the halo and stellar mass $M_{vir}/M_\star$, is an important parameter in the SISSA model and its effect on the distribution of image separations is twofold. First, we see that increasing this ratio from 10 to 50, the abundance of arcsec-scale lenses decreases by almost a factor of ~ 5. Secondly, it affects the kink of the distribution by shifting it from $\theta = 5''$ to $\theta = 10''$.

C.5 Variation in σ_{logc}

The parameter σ_{logc} controls the standard deviation of the distribution of concentration parameters. This distribution is expected to have a scatter that is well described by a lognormal distribution,

$$p(c) = \frac{1}{\sqrt{2\pi}\sigma_{logc}c} exp\left[-\frac{(logc - log\bar{c})^2}{2\sigma^2_{logc}}\right], \tag{C.1}$$

where the $\bar{c}$ is given by Eq. 5.2. The SIS model does not depend on this parameter and therefore arcsec-scale lenses produced by galaxies adopting this model, are not affected by any changes (Takahashi and Chiba, 2001; Kuhlen et al., 2004; Oguri, 2006). However this parameter does enter in the SISSA model through the NFW component. Although, its effect is not as drastic as it is for the wide-separation lenses produce by galaxy groups and cluster adopting a pure NFW model, its still affects the resulting distribution of image separation by shifting the kink by a few arcsec.

C.6 Variation in z_{vir}

As described in Section 5.3.1 the commonly made approximation that the virialization redshift in equal to the observed redshift lead to an overestimation of the halo size and therefore a decrease of the halo's density, making halos less efficient. Adopting a virialization redshift $z_{l,v} = 2.5$ drastically shifts the kink of the distribution to larger angular scales as well as it increases the abundance of galaxy-scale lenses. In this case the virialization redshift is introduced only for the SISSA model, as it would be unrealistic to assume that group- and cluster-scale lenses had beed virialiazed at such high redshift.